Micro-Photoluminescence Studies of $CsPbBr_3$ Based Nanostructures

Guanhua Ying

Oriel College, Oxford

Thesis submitted in fulfilment of the requirements for the degree of Doctor of Philosophy at the University of Oxford

Trinity Term, 2021

Abstract

This thesis summarises the photoluminescence results I have taken on the three different nanostructures of $CsPbBr_3$ perovskite. Due to their microscopic dimensions, interesting physics phenomena under the fields of optical science and quantum mechanics have emerged. With the aid of a confocal micro-photoluminescence setup, detailed sub μm-level features can be retrieved directly for analysis. Although the three topics root from separate branches of specific physics fields, they all demonstrate how this system can be exploited as a general tool for examining the time-integrated and dynamical behaviours. Therefore, the thesis helps build the necessary knowledge for adaptation into different scenarios and external modification for a more specialised measurement. On the other side, much of the content has been devoted into systematic explanation of the relevant concepts in a self-contained fashion. These include the discussion on lasing phenomenon, Gaussian modes and triplet state. These recap or exposure to the different fields will be sufficient for the reader to understand the rest of the content.

The results are selected from the three papers I have written. The first topic is on confined Gaussian modes in $CsPbBr_3$ microcavities. These cavities are naturally formed by the even smaller building blocks of quantum dots. The emission observed depends upon the collective behaviour of the zero-dimensional objects. The second topic is relevant to triplet state and resonant pumping of the $CsPbBr_3$ nanocrystals. Doubly degenerate states associated to the tetragonal phase of the crystal have been presented. A resonantly optimised lasing effect then builds on this triplet signal and shows great potential for device applications. The third topic is about passivated $CsPbBr_3$ nano/micro-rods with $Pb(OH)_2$ cladding. A temperature-tolerant emission and bright stimulated emission from defect sites have been demonstrated. All the three topics have illustrated the potential towards modern optoelectronic applications and the underlying physics can provide further inspiration from a slightly twisted angle for the future structure design.

In the appendix, a guide to the mapping software is introduced. This is a handy tool for analysing the complicated map data, which can be a crucial part of the PL study. The software provides control over the map position and wavelength, as well as a diffusion analyser. It also incorporates a zooming function such that local intensity rescaling is possible.

To the momory of my loving grandmother, Shiying Li. To my dear parents, Huiping Ying and Liangfu Zhang and the love of my life, Dan Song.

Acknowledgements

This thesis can not be completed without the kind contributions from many of my friends and colleagues I have come across during the past years working in the Clarendon Laboratory and here I will acknowledge those I would thank the most for the precious help and guidance they have offered to me.

First, I wish to express my sincere gratitude to Robert Taylor, a great supervisor, who has taken me as a PhD student and guided me all the way through this challenging but fruitful time of study. I have learnt much not only from his expertise in setting up optical systems but also from his deep understanding in solid-state physics and light science. He can always spot any technical problems encountered in my analysis or provide alternative angle of thought when solving difficult situations. Since I came from an engineering background, the courses he recommended to me in my early stage of this PhD life have both equipped myself for the rigorous research work undertaken and also motivated my interest on more in-depth theory learning into the mathematical physics world including field theory and symmetries, which I'm still learning for part time. Besides inspirations into the beauty of science, his knowledge on Latin, wine, European countries and history has also made my learning process multi-dimensional and enjoyable.

Then I wish to thank Tristan Farrow. He has always come up with interesting experimental ideas with rich underlying physics. Among all his help, I am especially grateful that he has offered guidance and support with patience for my first PhD project on organic molecules. This project has shaped my thoughts on the framework of a real research and built my essential skills on optical measurement, sample growth and cryogenic cooling.

I also owe much gratitude to Youngsin Park from Ulsan National Institute of Science and Technology, who has been a kind collaborator and provided all the samples studied in this thesis. He has worked with me on many experiment measurements and contributed extensively to the data analysis. His collaborator, Atanu Jana from Dongguk University, has fabricated all the inorganic perovskite nanostructures and has taken all the transmission electron microscope images, energy dispersive X-ray images and X-ray diffraction images presented in this thesis. Without their contributions, I wouldn't be able to achieve the results enclosed here.

Luke Nuttall, a former PhD student of the group, has taught me many useful skills on handling the helium system and optical system as well as sharing and explaining to me in detail his software programs on Python and Labview. He has solved many of my puzzles during my first two years in the group. I greatly appreciate his enormous help for getting me ready for the PhD study.

In addition, I want to thank other former members/visitors to the group during my

stay in Oxford. Stephen Lennon, Tim Puchtler and Claudius Kocher have all been very kind and warm to me when I first came to the group. I have learnt a lot from them on both experimental operations and physics thoughts. Moreover, I want to thank Vitaly Osokin, a current PhD student in the group, for inputting his original views and assisting the experiments.

Outside the optical laboratory, I want to thank Paul Pattinson for training me on using the clean room facilities. I am also grateful for Robert Storey for supplying the liquid helium essential for the low-temperature measurements.

In the end, I want to mention those who have been and also will be the most tightly binded to my life. My parents and my grandparents, who raised me up and have kept supporting me to explore the greater outside world. They always are my backbone to give me courage whenever depression came into play. Any achievement that I have reached so far is infused with their love and kindness. My grandfather, Zhongfu Ying, is a strict but a lovable mentor to me. He took me into the fantastic world of mathematics while I was still naughty and hated doing homework after school. It was only with his patient teach and guidance, I could slowly pick up a respectful attitude towards science and started seeing the hidden beauty of the logical thoughts. He together with my father, are the shiniest beacons in my life. I am so fortunate to encounter Ms Song, my lovely girlfriend, during my most helpless hours when I was filled with fear and anxiety. I have completed this thesis by her side with all the cares and loves we share together. I wish to accompany her for all the highs and lows in our upcoming future.

List of Publications

First (Co-First) Author

- Youngsin Park, **Guanhua Ying**, Atanu Jana, Vitaly Osokin, Claudius C. Kocher, Tristan Farrow, Robert A. Taylor, and Kwang S. Kim, Coarse and fine-tuning of lasing transverse electromagnetic modes in coupled all-inorganic perovskite quantum dots, *Nano Research* **14**, 108-113, (2020).

- **Guanhua Ying**, Atanu Jana, Vitaly Osokin, Tristan Farrow, Robert A. Taylor, and Youngsin Park, Highly Efficient Photoluminescence and Lasing from Hydroxide Coated Fully Inorganic Perovskite Micro/Nano-Rods, *Advanced Optical Materials* **8**, 2001235, (2020).

- Hanbo Shao, **Guanhua Ying**, Stephen A. Lennon, Frederic S. F. Brossard, Jonathan P. Griffiths, Luke P. Nuttall, Vitaly Osokin, Edmund Clarke, Huan He, and Robert A. Taylor, Purcell enhancement of a deterministically coupled quantum dot in an SU-8 laser patterned photonic crystal heterostructure, *Applied Physics Letters* **117**, 043103, (2020).

- **Guanhua Ying**, Tristan Farrow, Atanu Jana, Hanbo Shao, Vitaly Osokin, Mutibah Alanazi, Youngsin Park, and Robert A. Taylor, Resonantly pumped bright-triplet exciton lasing in caesium lead bromide perovskites, *ACS Photonics* **8**, 2699, (2021). DOI:https://doi.org/10.1021/acsphotonics.1c00720.

- Youngsin Park, **Guanhua Ying**, Robert A. Taylor, and Chan C. Hwang, Exciton dynamics in monolayer graphene grown on a Cu(111) surface, *npj 2D Materials and Applications* **5**, 69, (2021). DOI:https://doi.org/10.1038/s41699-021-00252-x.

Contributing Author

- Youngsin Park, Atanu Jana, Chang W. Myung, Taeseung Yoon, Geungsik Lee, Claudius C. Kocher, **Guanhua Ying**, Vitaly Osokin, Robert A. Taylor, and Kwang S. Kim, Enhanced photoluminescence quantum yield of MAPbBr3 nanocrystals by passivation using graphene, *Nano Research* **13**, 932-938, (2020).

Contents

List of Figures

Glossary

ASE Amplified Spontaneous Emission

BS Beam Splitter

CCD Charge Coupled Device

FWHM Full Width at Half Maximum

IRF Instrument Response Function

NC Nano Crystal

PV Photovoltaic

PL Photoluminescence

μPL micro-Photoluminescence

PMT Photomultiplier Tube

QD Quantum Dot

SE Stimulated Emission

SEM Scanning Electron Microscopy

SF Superfluorescence

SPE Spontaneous Emission

SR Superradiance

TEM mode Transverse Electromagnetic Mode

TRPL Time-Resolved Photoluminescence

Chapter 1

Introduction

Scavenging solar power has been a topical research field in the last decade for perovskite-based semiconductors. However, the prominent photon conversion ability hasn't only trapped the world's interest into the photovoltaic (PV) technologies but also inspired researchers to look into other avenues of potential optoelectronic applications. Light, with much of its beauty revealed from either its macroscopic wave-like nature via Maxwell's equations or its microscopic particle-like identity through bosonic quantum mechanics, provides both a powerful toolbox and a convenient analyser for the underlying material or structural physics. A general framework of this light-in-light-out approach can be established through a micro-photoluminescence (μPL) characterisation especially for nano-scale structures. This also describes the angle of the thesis to investigate the multiple profound aspects of microscopic perovskite geometries.

Chapter 2 introduces the building blocks and different functionalities of a μPL system discussed in an input/output presentation. The characterisations are carried out via photon counting statistics for both time-integrated and dynamical analysis. Fundamental operations of the crucial components are covered in slightly more details for interpretation purposes of the overall system.

Chapter 3 paves the general background concepts relevant to the remaining chapters of this thesis. It starts by discussing the characteristic chemical form of perovskite and the

categories of the composite ions. Then an introduction on quantum confinement naturally leads to the formalism for describing a quantum dot, which further develops into the concept of perovskite nanostructures. After illustrating the material system, discussion focuses on the possible light-matter interaction mechanisms including absorption, recombination and stimulated emission from a microscopic point of view. The chapter ends with a special emphasis on the operating principle of lasers following the discussion on stimulated emission.

Chapter 4 is on transverse electromagnetic modes (TEM modes) observed in self-assembled micro-cavities of colloidal perovskite quantum dots. A thorough mathematical background building on the TEM modes is essential for understanding the experimental results presented later in the chapter and hence it begins with the derivations of Gaussian modes. During the derivation process, the phase term of the mode profile can be spotted explicitly and extracted for simulation of the TEM mode wavelengths given the geometry and material properties of our perovskite nanostructure. The experimentally observed mode PL maps are then presented to match the simulation results and two types of mode tuning mechanisms have been demonstrated through temperature control and power control respectively. They provide a fine and a coarse degree of control over the emission modes.

In chapter 5, triplet state emission from perovskite nanocrystals is demonstrated. The chapter begins with a coherent textbook-style introduction to the concepts of coupled angular momenta and degenerate states in an atomic system. Given the band structure and symmetry properties of the perovskite nanocrystals, these concepts are applied to draw the theoretical framework of the triplet state existing in such a system. To verify that the identity of the experimentally obtained emission indeed matches this prediction, three different PL characterisation techniques including polarisation measurement, Stokes shift and time-resolved PL (TRPL) have been performed to examine the properties of the output signal in a rigorous manner. The second half of this chapter describes how resonant pumping of the triplet state has been achieved using a scanning-wavelength excitation source. This section also demonstrates the optimised lasing performance when bringing the pumping photon energy towards the near-resonant regime, which shows the potential of the perovskite triplet

state emission in device applications.

Chapter 6 turns to perovskite nano/micro-rods encapsulated within a hydroxide passivation coating. Measurements at cryogenic temperatures have shown two PL sites, which are further associated with different emission mechanisms through temperature-dependent and power-dependent characterisations. The shorter-wavelength emission demonstrates a behaviour much less affected by the temperature change compared to any other relevant studies currently in the field, which means the underlying mechanism is less coupled to the thermal bath. The longer-wavelength emission is again proven to be stimulated emission (SE), however, 2D PL maps have shown that the emission comes from localised point-like defect sites instead of the entire rod structure.

Chapter 2

Experimental Setup

2.1 Micro-PL Setup

A μPL system can be described as a generalised framework to study light-matter interaction at micrometre scales. The full system can be broken down into three parts due to their functionality and it consists of input signal, reactor and output signal. Among the three, input signal is associated with the part of the system where the light beam is generated and modulated to cope with a specific requirement for interactions with the sample. The excitation source can be selected from almost all of the typical light emitters including lamp light, white or coloured LED light and a continuous or pulsed laser. To be more specific, all of the main excitation sources discussed here are lasers. They have remarkable advantages over other kinds of light sources due to their spectrally narrow emission linewidth, high photon intensity and their coherent nature. The laser emission can then be modulated based on its properties by adding optical components such as polarisers and waveplates for linear polarisation filtering or conversion between linear/circular polarisation, optical fibre for beam shaping and mode selection, optical filters for allowing a specific wavelength range to pass and etc.

The beam is then fed into a dichroic mirror sitting at 45 degrees to its propagation direction as shown in figure 2.1. The coating on the mirror is chosen in such a way that

the reflectivity at the wavelength for the incident beam is high and thus it assures that most of the excitation light is deflected onto the sample. Conversely, we do not want to collect the PL emission from the sample along the same incident path, therefore, the output signal is expected to have a wavelength matching a high-transmission wavelength for the splitter. To further minimise the 'leaking through' of the excitation signal, an optical filter is placed above the splitter to attenuate any residual component in the output path at the pumping wavelength. In this way, the input and output are well separated and independent manipulations can be made.

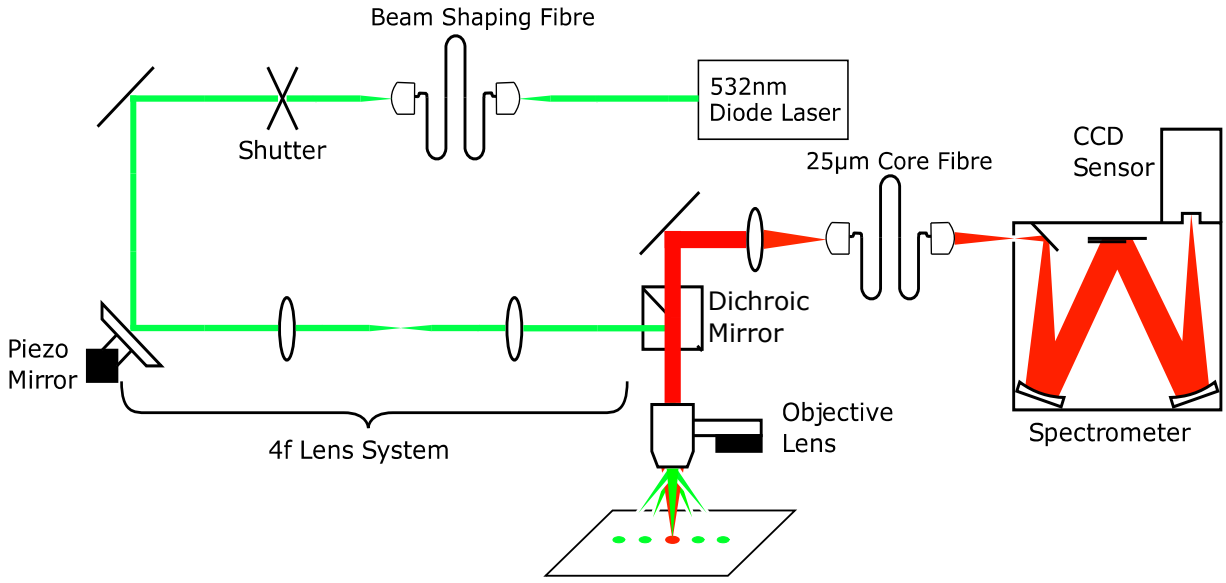

Figure 2.1: The μPL spectroscopy system showing the main functioning parts. The excitation source presented in the schematic is a 532 nm continuous-wave diode laser. This is only for demonstration purposes. In the later discussion of experimental results, the specific pumping sources used will be mentioned explicitly.

The term 'micro-' comes from the use of microscope objective lens, which focuses the reflected excitation beam onto $\sim$1 μm spot on the sample surface. In our setup, the objective is fabricated by the Mitutoyo company and has a magnification of 100$\times$ with numerical aperture of 0.7. This objective works best at visible wavelengths and it is ideal for the green emission from $CsPbBr_3$ at cryogenic temperatures. The detailed introduction of the sample will follow in later chapters.

It is also this focused beam that enables us to resolve structures of sub-μm dimensions op-

tically. As long as the nanostructures are distributed with a separation greater than 500 nm, emission from individual structures can be addressed independently. Another advantage with the μPL system is its ability to perform PL mapping by scanning the objective image over a designated area. This can be done by either moving the objective itself or by tilting a scanning mirror placed before the objective. For the first method, the objective lens is placed on a piezoelectrically actuated stage, which can shift the objective position along x,y or z directions. The module relevant to this chapter is a PI P-733.3CD XYZ Piezo Nanopositioning Stage. The range of travel along the xy-axes is 100 μm and that of vertical z axis is 10 μm. Within this displacement range, the paraxial approximation applies. Since the beam before entering the objective is well collimated and parallel to its length, the position of the focal spot is hence fixed relative to the objective. Thus moving the objective will drive the spot to move together. The objective not only focuses light onto that spot, it also collects from the same spot. Therefore, movement of the objective lens in the xy plane will shift the excitation and collection simultaneously.

The other type of mapping is conducted by operating the scanning mirror. Instead of moving both excitation and collection in a synchronous fashion, it decouples the two. The scanning mirror is a Connex AG-M100D piezo-actuated mirror and it can deflect the incident beam by small angles. However, this will shift the beam away from the central position of the objective lens. To solve this problem, we have adopted a telecentric $4f$ system with a pair of lenses of equal focal distance f between the scanning mirror and the objective as shown in figure 2.2. Starting from the scanning mirror through the two lenses and ending with the objective, the corresponding separation between the optical components are of $1f$, $2f$ and $1f$ respectively. The first lens focuses the deflected beam from scanning mirror onto a middle plane between the two lenses while the second lens picks up the diverging beam and recollimate it onto the objective. Any tilt in the scanning mirror angle will be reflected by a translational movement of the focal spot within the middle plane. The symmetry of this setting ensures that the small tilt is transferred to the incident angle into the objective while keeping the incident position fixed. In addition, the collimated beam size will also replicate that hitting the scanning mirror, therefore, it is only the incident angle that has

been changed. Within the small angle approximation, such change in incident angle will be translated into a shift in position. Detailed explanation on this will be covered in the discussion on diffusion from chapter 6. Apart from full mapping at small steps, these two fine position operations can also be combined with a coarse position control of the cryostat through a micrometer stage for searching and output signal optimisation across the sample surface.

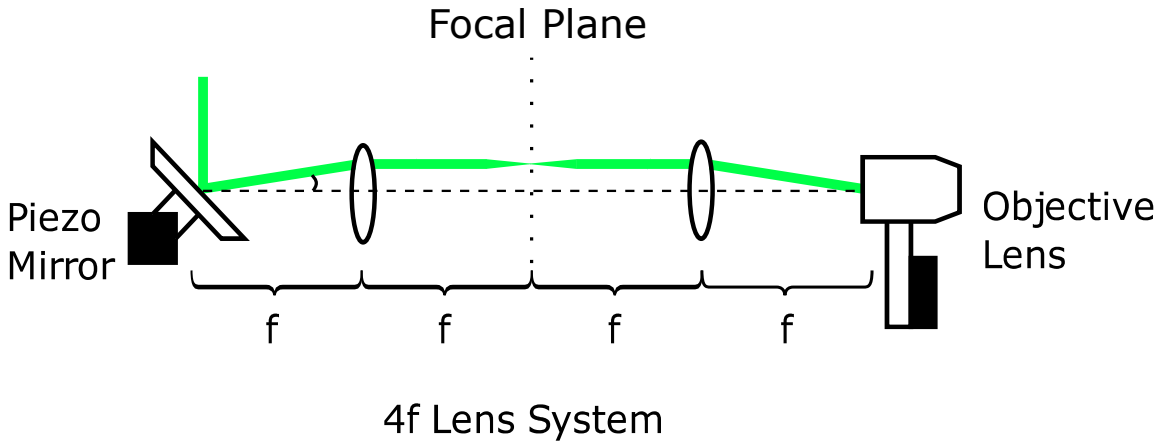

Figure 2.2: An illustration of the $4f$ system. The distance between adjacent components (piezo-scanning mirror, two identical lenses and objective) is equal to the focal distance of the lens. Any angle adjustment at the scanning mirror will move the focal point within the focal plane between the lenses and change the incident angle at the objective lens. However, the incident position onto the objective lens is kept constant.

Now consider the output signal after the optical filter mentioned earlier. The output signal can also be subject to modulations including polarisation manipulation and interferometer measurement (to be discussed in later chapters). The final form of the signal is then focused into a multi mode fibre with $25\,\mu$m core diameter. The reason for using this fibre is to collect from a diffraction-limited spot of a comparable size to the excitation spot given the magnification used and hence a confocal setup is constructed. The other end of the fibre is fed into the spectrometer.

The specific model used for all the work presented in this thesis is an Andor Shamrock 0.3 m imaging spectrometer in a Czerny-Turner configuration. The main functioning sections consist of a rotational reflection grating and a CCD camera. The operation of a reflecting

diffraction grating is shown in figure 2.3.

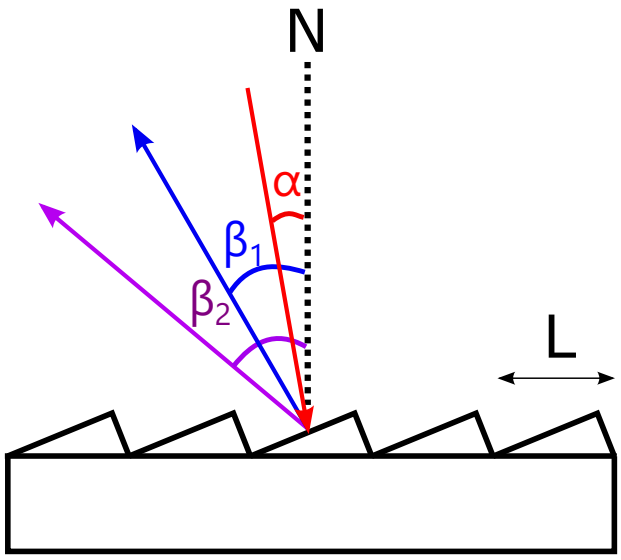

Figure 2.3: The operation of a reflecting diffraction grating. The schematic shows two dispersion angles β_1 and β_2 for outgoing beams of constructive interference.

In the illustration, N defines the normal axis to the grating and α defines the incident angle from this normal axis. Considering only the diffraction effect and taking into account that only two wave paths giving rise to constructive interference remain as an outgoing wave, we can arrive at the general grating equation[1]:

$$L(\sin\alpha + \sin\beta) = m\lambda \tag{2.1}$$

In the above presentation, L is the distance between adjacent line grooves of the grating and m is an integer to represent the spectral order of diffraction. This equation associates the outgoing direction (angle from the normal axis β) to a particular wavelength λ. It is clear from the equation that different wavelengths have been injected into a continuous and finite angular width, which matches the description of a dispersion relationship. By taking an infinitesimal interval $d\lambda$, the dispersed angle can be obtained as:

$$L \times \cos\beta \times d\beta = m \times d\lambda \tag{2.2}$$

The relationship describes the change in the reflected angle corresponding to a change in wavelength, which is of particular interest for retrieving the spatial information of a range of wavelengths. For our spectrometer, we have been limited to the order $m = 1$ set of diffraction lines. The potential concern regarding overlap among multiple orders at the same output angle, *e.g.* existence of order $m = 2$ wave at half the wavelength, can be effectively ruled out with limiting the wavelength window before the spectrometer. This is another reason why a band limiting optical filter has been used.

The spectrometer has three sets of gratings and each of them is blazed. This is shown by the saw-toothed pattern in figure 2.3. Inclusion of such surface structure intends to contain more of the incoming beam into the region of order $m = 1$ for a specific wavelength range. The collection efficiency gradually degrades away from the designated wavelength and hence multiple sets of gratings are required to cope with emission at different wavelengths. The three gratings form a triangle and each sits on one side of it. Their associated line densities are 600, 1200, 1200 lines/mm and the corresponding blaze wavelengths are 1200, 1100, 500 nm respectively. By rotating the gratings the spectrometer can be switched to a different set of wavelengths and a change in the dispersion factor $\frac{d\beta}{d\lambda}$. For the experiments considered within this thesis, only blue/green part of the visible range is relevant and hence a grating choice with line density of 1200 lines/mm and blaze wavelength of 500 nm has been deployed.

The beam is then reflected by two mirrors before eventually arriving at the CCD camera, which accumulates the photon number over a predetermined period of time. The detector of the CCD essentially consists of a 2D array of pixels. Each pixel records photon events restricted to a specific composite area of the beam cross section associated with the distance travelled from the reflective grating. Clearly, the longer the path the more spread along the horizontal direction in space for a particular set of wavelengths (*e.g.* 531.1 nm and 531.2 nm will be better resolved allowing a longer distance from the grating).

The other determining factor of the resolution is the horizontal spatial distribution of the pixel array. The model for our CCD camera is an Andor NewtonEM silicon CCD

equipped with a grid of 1600×200 pixels. Each pixel has the shape of a small square with the side length being 16 μm. Besides photon events, the detector can record dark counts from thermal excitation. Therefore, a thermoelectric cooler module has been adapted to keep the temperature of the CCD at $-60\,^{\circ}$C and suppress the dark count down to a few counts per second. Combining the size effect of the CCD pixels with the angular dispersion of the wavelengths in space at a particular distance, the resolution can be calculated for a selected grating. For the grating picked for the perovskite experiments, the resolution is roughly 0.075 nm.

2.1.1 TRPL

Instead of the CCD camera which integrates the counts of photons over time, TRPL measurement deals with time intervals for photon events at the sub-nanosecond or picosecond scale. The excitation beam ideally comes from a Dirac impulse source of near-zero temporal width. In this way any detected photon events will be post-pumping and they reflect only the dynamics of carriers independent from any ongoing excitation process. However, in a realistic detection system, the detector needs to translate registered photon events into electrical signals and these received signals will be compared with the synchronous electrical input representing pulsed excitation to calculate a temporal delay by a photon counting card. Clearly, this converting procedure requires electrical connection with either coaxial cables or other types of wires carrying a finite complex impedance. Any mismatch of the impedance at a port or joint can either result in a partially reflected wave or a fully-blocked transmission with only evanescent penetration. Although the second case is unlikely, the first case can give rise to back reflected electrical waves happening at a nanosecond scale and can contribute to secondary peaks or postponed reception of a counting event. The distortion to the signal together with an imperfect source, such as the PicoQuant LDH-P-C-450B InGaN laser diode controlled by a PicoQuant PDL 808 'Sepia' box emitting at 450 nm, unavoidably introduces broadening and other features into the ideal excitation impulse function. Each impulse signal triggers a temporal decay of the carriers and hence the final form of the ob-

tained profile is essentially a convolution between the temporally broadened excitation and the characteristic carrier density decay. Since a primary reason for the broadening is due to the finite response time of the detecting equipment, and the temporal function is thus called the instrument response function(IRF).

Further limitation besides finite IRF also exists for the photon counting card. The electronics associated with both the detector and the card have a so-called dead time typically of tens of nanoseconds. This means that it takes a finite amount of time to process and register the input signal corresponding to a photon event and the system will be blind to any subsequent photon events within this dead time. If the temporal separation between two pumping pulses is also of a similar length to it, then there will be on average only one photon event registered during a single excitation cycle. All the other emitted photons within the same cycle will be discarded until the electronics is ready for a new event. Then, by the statistics of large scale sampling, a histogram can be constructed to reproduce the dynamics of a single excitation cycle to present the correlation of the photon events with the synchronous signal. It is worth pointing out that in this scenario, the system will be more sensitive to photon events in the early part of the excitation cycle while the later part is more likely to fall within the dead time region. Therefore, a bias towards the time window immediately after the excitation pulse is likely to be observed.

In order to achieve a high resolution for reconstructing the temporal decay profile, a pulse-picked 100 fs laser emitting at 400 nm is chosen together with a Picoquant PMA Hybrid-42 Photomultiplier Tube. The corresponding IRF is shown in figure 2.4(a). This IRF, as discussed above, has incorporated limiting factors such as the finite temporal width of the laser pulse, the response time and efficiency of the photo-detector and the resolution of the photon counting card. Its overall FWHM has been fitted to be 58.8 ps (with uncertainty of 0.4 ps), which indicates a clean signal of fitting error being only around 1%. With deconvolution of this IRF, it is feasible to measure a lifetime longer than 25 ps under small uncertainty. This setup has been adopted to obtain the short lifetime presented in chapter 5. Because the detector is only recently purchased, the earlier experiments (chapter 4 and chapter 6)

were performed under different apparatus with relevant IRFs provided in each chapter. It is also worth mentioning the IRF associated with another recently-obtained fast detector, MPD 50 μm Avalanche Photodiode, as plotted in figure 2.4(b). The functioning of this detector relies on the avalanche effect: under reverse bias, the photo-generated electron-hole pair in the depletion region is immediately pulled apart and accelerated under the large electric field, they become so fast that upon collision with the lattice more carriers are created and accelerated thereafter to repeat the process. The FWHM is found to be even smaller at 54.5 ps (with uncertainty of 0.6 ps), which means it can also be applied to measure fast decay at 20-25 ps level.

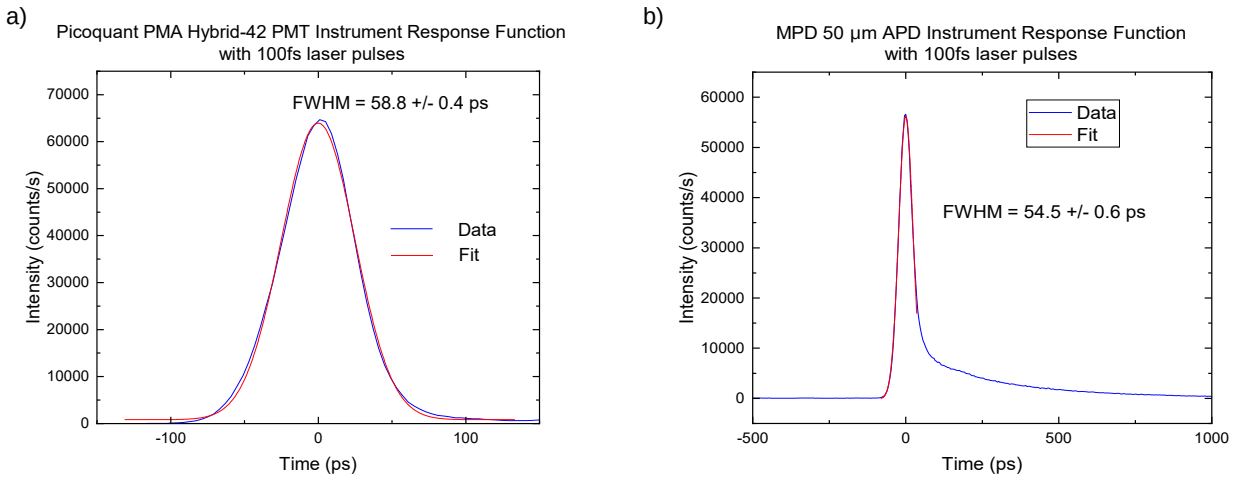

Figure 2.4: IRF responses of 100 fs laser emitting at 400 nm with (a) Picoquant PMA Hybrid-42 Photomultiplier tube and (b) MPD 50 μm Avalanche Photodiode respectively. The fitted FWHM for each curve is shown in the plots with fitting uncertainties.

To integrate the TRPL detection into the μPL system, the detector just needs to be attached to the alternative output port of our spectrometer. The port itself has an adjustable slit, which can be used to trim a customised section of the angular dispersion for a particular wavelength range of the output beam. This intrinsic operation of the spectrometer serves as a band pass filter and it is of great convenience for studying the dynamics associated with a narrow spectral line.

Chapter 3

Background

3.1 Chemical Structure

3.1.1 Unit Cell and Symmetry

Perovskite is now widely recognised for its chemical structure $CaTiO_3$. It is named after the Russian mineralogist Lev Perovski who discovered the mineral. The formula for perovskite is commonly written as ABX_3, where A, B are cations of charge +1 and +2 respectively and X is an anion of charge -1. A variety of combinations can lead to such composition, however, the focus of this thesis will be targeting a specific category of halide-based perovskite.

The unit cell of the perovskite structure is shown in figure 3.1, where the central A site cation is surrounded by 8 connected octahedra of BX_6 groups. The B-X bonds are the determining factors for the electronic properties of the material. Although the A site cation isn't giving direct control over those properties as the electron orbital overlap between the A site and the octahedra is not significant[2][3], it can still interact with the B-X bonding and hence causes distortion to the symmetry. It is worth pointing out that the cubic symmetry is favoured over the others due to its high degree of ionic bonding. Such a crystal formation with a cubic symmetry has a space group of Pm3m and is often called the α-phase.

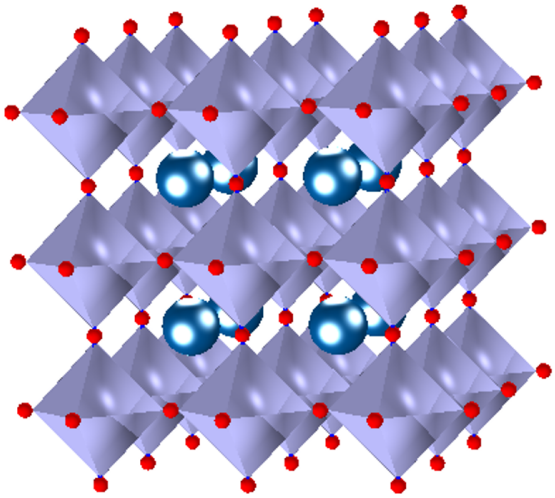

Figure 3.1: Cubic perovskite crystal structure: blue circles are the central A cations and violet octahedrals represent BX_6 groups

An important criterion for checking if the symmetry is within or close to a cubic symmetry is given as a tolerance factor, as shown in equation (3.1), first considered by Goldschmidt[4]. It is a geometrically related reference factor determined from the sizes of all the composite ions, where R_A, R_B, R_X are each the radius of the corresponding ion as mentioned in the last paragraph. Since the interest here is only on halide perovskites, the associated range for having cubic symmetry is estimated to be $0.85 < T < 1.11$[5]. Outside this range the symmetry is not ideal for optimal electronic behaviour. More specifically, for T lower than 0.85, the B-X bonding can produce a shrinkage where the A-X bonds have to extend to maintain structural stability. The process is fulfilled by tilting of the octahedrons and hence bringing down the level of symmetry. The opposite happens when T is greater than 1.11, where a higher symmetry is reached by having relatively bigger A site cation than the B anion compared to the cubic phase.

$$T = \frac{R_A + R_X}{\sqrt{2}(R_B + R_X)} \tag{3.1}$$

Another factor for describing only the geometric structure of the octahedrons is called an octahedral factor, defined by Li *et al*[5]. It is expressed simply as $\frac{R_B}{R_X}$. For halide-based perovskite a stable structure can only emerge at an octahedral factor higher than 0.442. This

factor together with the tolerance factor provide a first baseline for reviewing the feasibility and degree of cubic symmetry for a possible perovskite composition.

3.1.2 Ions

There is a huge variation of possible selections for the AB ions even for halide perovskites, however, within the scope of this thesis the discussion is narrowed down to some specific formations.

The choice of A site throughout this thesis will be Cs^+. However, for optoelectronic applications, especially photovoltaic technology, popular choices for the A site cation are Cs^+, Rb^+, MA^+(Methylammonium) and FA^+ (Formamidinium) with ascending order in structural size. The later two are organic cations each with chemical formula $CH_3NH_3^+$ and $HC(NH_2)_2^+$. While MA^+ has been investigated most for photovoltaic applications its relatively small size makes it fall either within the Schockley-Queisser band gap limit of a single-junction solar cell of $1.1 - 1.4\,eV$[6][7] or the cubic symmetry criterion at room temperature. Having an even smaller ionic size, Cs^+ demonstrates both a band gap towards higher energy and a less symmetric formation of the crystal and hence is a poor choice as a candidate for solar cells on its own. However, by hybridising Cs^+ with another cation FA^+, whose size is larger than MA^+ but occupying an off-centre position leading to distortion of symmetry, with lead halide as the choice for the other two ions the tolerance factor can be engineered close enough to 1 and results in optimal cubic symmetry[8]. Although Cs^+ is not ideal for photovoltaics, it has outstanding stability against moisture, chemical environment, light exposure and temperature change compared to its organic counter parts. For example, $MAPbI_3$ can break down in a reversible reaction under moisture environment as in equation (3.2)[9][10]. With the presence of water and light, the organic product CH_3NH_3I can further dissociate as in equation (3.3). The final product contains water and can in turn boost the rate of the forward reaction in equation (3.2). With FA^+ having a similar path of disassembly to MA^+, mixing with Cs^+ can increase the stability towards water and photochemical breakdown[11]. Picking Cs^+ alone as the A site cation, therefore, has the most

robust inorganic structure and shows advantages in many other optoelectronic applications.

$$CH_3NH_3PbI_3 = PbI_2 + CH_3NH_3I \tag{3.2}$$

$$4CH_3NH_3I + O_2 \longrightarrow 4CH_3NH_2 + 2H_2O + 2I_2 \tag{3.3}$$

As for the B site, IVA metal cations such as Sn^{2+} and Pb^{2+} are of particular interest. Between the two, Pb^{2+} has been applied most in research due to its higher stability. This is as a result of the inert pair effect of post transition metals as first mentioned by Nevil Sidgwick[12]. The electron inert pair corresponds to the outermost s-orbital electrons and for post transition metals they tend to be bonded tightly to the nucleus and hence are less likely to be shared or ionized. The strength of inert pair hence reflects the stability of the metal oxidation state. Pb^{2+} demonstrates an enhanced inert pair effect compared to Sn^{2+} from an increased ionization potential [13], which can be interpreted as relativistic effects in quantum chemistry. Umari *et al.* investigated how such effects affect the electronic properties of $MAPbI_3$ and $MASnI_3$ and showed increased stability with the Pb oxidation state [14][15]. Despite being more stable, an increased bandgap is also witnessed for the structure involving Pb^{2+}. This is due to reduced electronegativity, which makes it harder to attract a bonding pair. Since for optoelectronic applications other than photovoltaics there is no need to optimise the bandgap to match the solar spectrum, stability is our primary consideration here. To further boost the argument above on stability, it is found that Sn^{2+} in $MASnX_3$ oxidises easily into Sn^{4+} with the presence of air [16][17][18]. Therefore, all the material composition discussed in the later context will only involve Pb^{2+} as the B site cation.

The halide group $\left(Cl^-, Br^-, I^-\right)$ has been studied to a great extent as the X site anion. With increasing atomic size from Cl towards I, the bandgap of the perovskite structure shows a red shift due to the reduced electronegativity[19]. This is because the I^- is associated with a more covalent nature. When bonding with Pb^{2+}, I^- forms the most stable structure due to their proximity in the periodic table[20]. By tuning the halide group to incorporate a

smaller effective size for the anion, emission wavelength of the $CsPbX_3$ can be engineered to cover almost the full visible range as shown in figure 3.2. In this thesis the halide is picked to be Br^- and the corresponding perovskite composition $CsPbBr_3$ emits at 532 nm at liquid helium temperature 4 K.

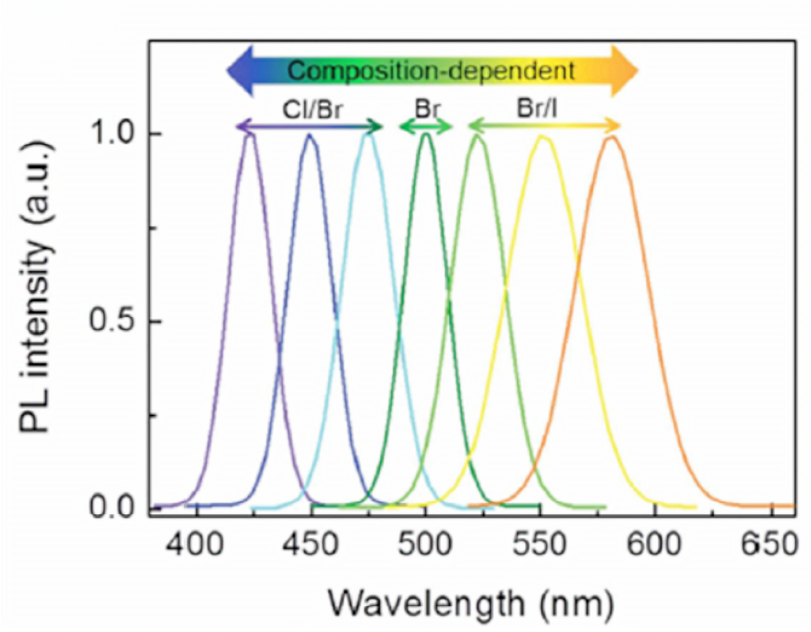

Figure 3.2: Bandgap tuning for changing the halide composition of $CsPbX_3$ perovskite structure.Adapted with permission. Copyright, 2015, American Chemical Society.[21]

3.2 Nanostructures

3.2.1 Quantum Dots

Although not belonging to the classical semiconductor family including binary III/V compounds like GaN or group IV elements such as silicon, inorganic perovskites are a novel material that has drawn great interest for optoelectronic applications due to their semiconductor-like behaviour. For classical semiconductor devices, quantum confinement has always been an important tool for realising certain physical mechanisms, for example, carrier confinement through the implementation of quantum well layers in lasers[22], quantum dot-based light emitting diodes (LEDs)[23] and the inclusion of quantum wells in field-effect transistors[24]. It is therefore attractive to introduce this concept to perovskites.

Just as the name 'confinement' suggests, it is a mechanism to add spatial limitation. The concept can be applied to either photons (a type of bosons) or electrons (a type of fermions). While the treatment in each case differs mostly due to the significant distinction of the relevant material and particle properties, the fundamental principles are analogous and comparable. In this chapter, the focus is on electronic quantum confinement. Generally speaking, the determinants of confinement for electrons include size, shape and electronic band structure of the materials. In order to achieve confinement, first there needs to be a local change in electric potential. This is saying that at least two types of materials with different conduction band energy levels are needed. By having a differential energy band structure along one spatial axis, there will be a tendency of increase in electron density in the region with lower conduction band level. Confinement is only then achieved by bounding the designated region from both sides with materials of higher energy level in a sandwich configuration. Given this setup, quantum effects come into play when the confined region approaches the de Broglie wavelength of the electron. This means that not only the electron is trapped along the confinement axis, but its wavefunction is also localised and bounded.

Depending on how many axes the confinement is applied to, the object can be classified as follows. Without confinement, the electron is free to move in all three spatial directions and the corresponding structure is defined as a 3D object. With confinement along 1 axis, the electron is bound along that direction and the corresponding structure is said to be a 2D object with 1D confinement. This type of structures normally appear as quantum wells or 2D nanosheets. By adding another confinement axis at an orthogonal direction to the existing one, the electron is further bound from another dimension. The resulting object has 2D confinement and is hence a 1D object. A representative case is a quantum wire. In the extreme case, all 3 dimensions are confined and the electron is completely localised if no hopping process is allowed. This object is said to have 3D confinement and is, therefore, a 0D object. The quantum dot is a 0D object and it is the relevant structure to a large part of this thesis. It is worth mentioning that the first creation of a quantum dot was by Ekimov *et al.* [25] and Rossetti *et al.*[26] in classical semiconductors.

Although quantum dots are much larger than the size of their composite atoms, their dimensions are still compatible with the quantum confinement criterion. When the system is excited over its bandgap, an electron-hole pair is generated. The quantum confinement from all dimensions means the electron and hole wavefunctions are localised and largely overlapped. They can not separate into free carriers and hence remain in a electrostatically bound 'exciton' state (discussed in much detail later). This form resembles the atomic structure where electron binds to the positively charged nucleus. Therefore, an exciton can be associated with a Bohr radius which in turn defines the critical dimension to achieve quantum confinement. By reducing the size of the quantum dot, the oppositely charged particles become more squeezed together and the overlap of their wavefunctions gets more significant. As a result, their binding energy is increased and hence higher energy photons are required for the excitation process of smaller quantum dots.

Quantum mechanically, the physical state of an electron can be described by Schrödinger's equation. The most general form of Schrödinger's equation without accounting for special relativity is shown in equation (3.4), where m is the mass of the electron (effective mass in semiconductor), V is the potential and Ψ stands for the wave function in position space.

$$\frac{d}{dt}\Psi(r,t) = V(r,t)\Psi(r,t) - \frac{\hbar^2}{2m}\nabla^2\Psi(r,t) \tag{3.4}$$

Since we are not looking into the dynamics it is helpful to integrate out the time dependence and a simpler form of time-independent Schrödinger's equation is obtained as in equation (3.5). Where the time derivative is replaced by a constant E, which is an eigenvalue of the time-independent Hamiltonian and hence corresponds to the energy of the state.

$$E\Psi(r) = V(r)\Psi(r) - \frac{\hbar^2}{2m}\nabla^2\Psi(r) \tag{3.5}$$

So far it is all about the electron itself while the confinement is introduced through the potential V. We can simply take V to be zero in a small cube of length L in all three directions and towards infinity outside the cube. In this way a three-dimensional confinement is turned

on. Because the space we are working on also possesses three dimensions it essentially represents a zero-dimensional object and leads to the simplest picture for a quantum dot setup where the effects of positively charged holes are not considered. Such a configuration was first brought up by Miller as a 'particle in a box'[27]. The solutions to this model are a collection of sinusoidal standing waves as in equation (3.6) and the corresponding energies are calculated as in equation (3.7).

$$\Psi_{n,m,l}(r) = A \sin\left(\frac{n\pi}{L}x\right) \sin\left(\frac{m\pi}{L}y\right) \sin\left(\frac{l\pi}{L}z\right) \tag{3.6}$$

$$E_{n,m,l} = -\frac{\hbar^2}{2m}\left(\frac{n\pi}{L}\right)^2\left(\frac{m\pi}{L}\right)^2\left(\frac{l\pi}{L}\right)^2 \tag{3.7}$$

Where A is a constant and n,m,l are integers. Comparing the resulting energy spectrum to higher dimensional objects as shown in figure 3.3, including 1D quantum wires and 2D quantum wells, each of reduced degree of confinement, the fully discrete energy spectrum is only witnessed with a 0D structure. When translating to the density of states over energy, the discrete nature is again obtained only in ideal quantum dots. This is because for higher dimensional structures, a lift of constraints allows free movement in the added direction and hence introduces a continuum of states over energy. The spectrum only becomes fully discrete when the movement in all possible directions is confined to quantised modes. This form of the spectrum resembles that of an atom, which is also an 0D object.

The discussion above is still a bit idealistic as it only considers the electron alone. In real semiconductor quantum-confined structures it is essential to take into account the positively charged holes from the valence band. In this case the Bohr model of hydrogen can be used by replacing the nucleus by a hole and the same physics from above can be applied with some adjustments. Now I focus on the specific case of quantum dot (the 0D structure with 3D confinement), a few interesting observations can be taken from equation (3.7). First, by assigning the length of the confinement region 'L' to be the diameter of the quantum dot, it becomes clear that the discrete confinement energies are inversely proportional to the spatial size of the dot, $\frac{1}{L^2}$. Therefore, within the strong confinement regime (small dot size), the

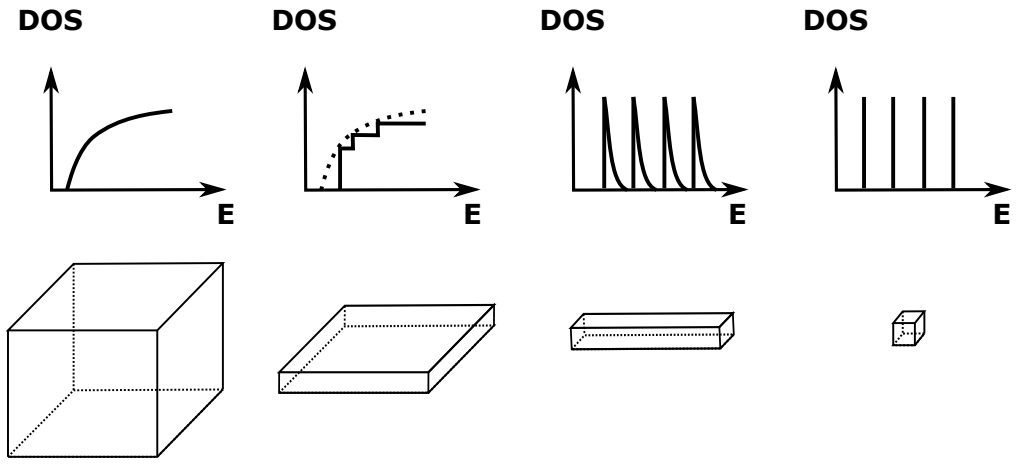

Figure 3.3: Comparison of density of states (DOS) against energy for carriers under different degrees of quantum confinement. From left to right: 3D structure, 2D quantum well, 1D quantum wire and 0D quantum dot. The energy spectra turns more discrete towards higher dimensional confinement.

determination of band gap energy is significantly influenced by the confinement energy along with comparably smaller perturbation to the associated energy levels from the Coulomb attraction between electron and hole, which scales as $\frac{1}{L}$. Additionally, due to its atom-like behaviour, the QD wavefunctions can be described with the familiar quantum numbers characterising the different wavefunctions correponding to the various atomic orbitals (s,p,d-orbitals) and angular momentum(detailed recap of the quantum numbers in chapter 5).

In order to incorporate the semiconductor characteristics into the solutions of the above model (equation (3.6)), following the treatment in the book 'Colloidal Quantum Dot Optoelectronics and Photovoltaics'[28], a periodic Bloch function term '$u_{n,k}(\mathbf{r})$' addressing the periodic potential due to the existence of crystalline lattice is combined with the planewave solution as shown in equation (3.8). The indices 'n' and 'k' are representing the different energy bands and wave vector respectively. [29][30]

$$\Psi_{n,k}(\mathbf{r}) = u_{n,k}(\mathbf{r}) \exp(i\mathbf{k} \cdot \mathbf{r}) \tag{3.8}$$

Because the planewave term is essentially describing the phase change in space, the information on energy bands is effectively contained within the Bloch term. Indeed, the Bloch

function depicts atomic-like orbitals within the unit cell. At point $k = 0$ of the reciprocal lattice, the Bloch function associated with bulk semiconductor is readily applicable to the case of a quantum dot. However, unlike in the bulk semiconductor structure, no translational symmetry is maintained for quantum dot and hence the wavefunction is essentially an 'envelope' of a linear combination of plane waves subject to spherical boundary condition, as shown in equation (3.9), where $C_{n,k}$ are expansion coefficients and f is the envelope function.

$$\Psi_n(\mathbf{r}) = u_{n,0} \sum_k C_{n,k} \exp(i\mathbf{k} \cdot \mathbf{r}) = u_{n,0} f(\mathbf{r}) \tag{3.9}$$

Now by decomposing the overall wavefunction into the associated electron and hole wavefunctions, denoting the conduction and valence bands through subscripts 'c' and 'v' in the Bloch terms, and solving for the spherical boundary condition as in the fundamental atomic model, a self-explainable form of the wavefunction solution can be obtained as:

$$\Psi(\mathbf{r}_\mathrm{e}, \mathbf{r}_\mathrm{h}) = \Psi(\mathbf{r}_\mathrm{e})\Psi(\mathbf{r}_\mathrm{h}) = u_\mathrm{c} f(\mathbf{r}_\mathrm{e}) u_\mathrm{v} f(\mathbf{r}_\mathrm{h}) = C(u_\mathrm{c} j_{l_\mathrm{e}}(kr_\mathrm{e}) Y_{l_\mathrm{e}}^m)(u_\mathrm{v} j_{l_\mathrm{h}}(kr_\mathrm{h}) Y_{l_\mathrm{h}}^m) \tag{3.10}$$

where j_a is spherical Bessel function of ath order and the Y_l^m terms are the spherical harmonics with orbital angular momentum quantum number l and magnetic orbital angular momentum quantum number m. The l_e and l_h are the angular momentum quantum numbers corresponding to the electron and hole respectively. Since the wavefunction vanishes outside the QD, the boundary condition requires that $k_\mathrm{e}{=}\beta_{n_\mathrm{e},l_\mathrm{e}}$ where $\beta_{n_\mathrm{e},l_\mathrm{e}}$ is the n_eth zero of j_{l_e}, the same criterion is also applied to the hole. Summarising the above points, the energy levels observable in a semiconductor quantum dot can be given as equation (3.11).

$$E = E_\mathrm{g} + \frac{\hbar^2 \beta_{n_\mathrm{e},l_\mathrm{e}}^2}{2m_\mathrm{e}^* L^2} + \frac{\hbar^2 \beta_{n_\mathrm{h},l_\mathrm{h}}^2}{2m_\mathrm{h}^* L^2} - E_\mathrm{C} \tag{3.11}$$

where m_e^* and m_h^* are effective masses of electron and hole respectively and E_C is Coulomb adjustment due to electron-hole attraction to the first order.

3.2.2 Inorganic Perovskite Quantum Dots

Besides the discrete spectrum for the density of states, other promising properties including wavelength tuning from size control and large optical oscillator strengths are available with quantum dots[31][32][33][34]. These properties lead to a low threshold for optical gain and hence make quantum dots an ideal choice for light sources. Combining the low-dimensional confinement with the remarkable optical properties of the relatively more stable all-inorganic perovskite, a variety of applications have been seen in the field of optoelectronics including coherent single photon sources[35], quantum dot lasers[36] and many-body effects such as superfluorescence from a coupled superlattice of quantum dots[37].

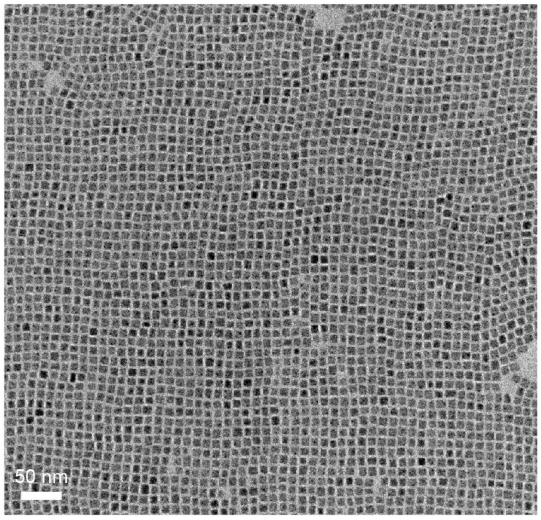

Figure 3.4: Transmission electron microscopy image of the $CsPbBr_3$ nanocrystals prepared under the logic of the above recipe. This TEM image of a superlattice configuration is taken from a paper by Rainò *et al.*Adapted with permission(CCC License number:5265280480515). Copyright, 2018, Springer Nature.[37]

The perovskite quantum dots mentioned above, as well as those described later in the thesis are all classified as colloidal quantum dots, where the naming is associated with their synthesis procedure involving solution processing[38]. In chemistry, 'colloidal' stands for substances that neither precipitate out of the solution nor dissolved in the solution but rather in a suspension state. The general procedure requires the precursor to be heated at high temperature where the reaction breaks the precursor into smaller monomer molecules. It is these monomers that can nucleate and form the nanocrystals as a product. The two key

factors for controlling the quality and size of the nanocrystal formations are temperature and monomer concentration. The nucleation is essentially an atomic annealing effect and hence explains why an increase in temperature is necessary, however, there is an upper bound as the crystal formation can't happen with an over provision of thermal energy which will break the atomic bonding. As for the monomer concentration, there is a critical point for the size distribution of the nanocrystals between shrinkage and growth. When such critical point is kept relatively low, a range of different sizes of nanocrystals can be produced. Nevertheless, due to the difference in the number of atoms involved the rate for different sizes varies. The distribution is biased towards smaller sizes due to the faster growth rate. It is, therefore, important to optimise the monomer concentration such that the mean of the nanocrystal size is only slightly above the critical point.

There are many different methods for producing the $CsPbBr_3$ quantum dots and it is illustrative to briefly go through one specific example conducted by Franziska *et al.*[39] which is also used to produce the single photon source[35]. In the recipe, lead oleate, octadecene and a zwitterionic detergent are initially heated in vacuum. Then nitrogen is filled inside the reaction flask with further heating of raised temperature. Once the set temperature is reached, the reaction flask is cooled with ice bath to room temperature. Centrifugation is then applied to keep the desired precipitate fraction to be dispersed in toluene. The filtered nanocrystals are subject to further purification process in repeated runs of ethylacetate addition followed by centrifugation. Toluene is also used for precipitate dispersion after each repeated cycle to contain the final product. In figure 3.4 an ensemble of cubic $CsPbBr_3$ nanocrystals is presented to have the same morphology as the quantum dots formed from the above recipe.

3.3 Absorption, Spontaneous Emission and Stimulated Emission

Light-matter interaction serves as the fundamental physical driver for the more advanced optoelectronic applications including but not limited to light-emitting diodes, photovoltaic cells and lasers. The most general classification of the mechanisms can be categorised into absorption, spontaneous emission and stimulated emission. In the language of quantum physics, such processes are modelled via transition between states of different energies under the perturbation by a photon. The same idea is further extended to semiconductors where the transition happens across the bandgap.

This section describes light-matter interaction from a quantum mechanical point of view and the content follows the popular textbooks including Quantum Optics by Mark Fox[40], Atomic Physics by C J. Foot[41] and the Physics of Quantum Mechanics by Binney and Skinner[42]. In the simplified picture of a two-level system, the corresponding states are the eigenstates to the static Hamiltonian $\hat{H}_0$ before perturbation. Interaction with light beam is then incorporated by adding a time-dependent potential $V(t)$. Now the wavefunction solved from the overall system Hamiltonian must be in the form of a superposition of the solutions to $\hat{H}_0$ subject to modifications represented by the $a(t)$ terms:

$$\Psi(r,t) = a_i(t)\psi_i(r)e^{-iE_it/\hbar} + a_f(t)\psi_f(r)e^{-iE_ft/\hbar} \tag{3.12}$$

where the subscripts i and f indicate the lower energy and higher energy states respectively. The $a(t)$ terms here are the coefficients to the static eigenstates and they are the probability amplitude for observing the system to be in that particular state at time t. By taking $|a(t)|^2$ the real probability can be calculated to track the evolution of the system. Therefore, it is important to have an explicit expression for each $a(t)$. In order to do this, first apply the static Hamiltonian to the wavefunction for one of its eigenstate 'u', we then have $\hat{H}_0\Psi_u = i\hbar\frac{\partial\Psi_u}{\partial t}$. Similarly, applying the system Hamiltonian to the general solution

given above must satisfy $\hat{H}(t)\Psi = i\hbar\frac{\partial\Psi}{\partial t}$. Splitting $\hat{H(t)}$ into $\hat{H}_0$ and $\hat{V}(t)$, a relationship on the $a(t)$ coefficients is obtained:

$$a_i(t)\hat{V}(t)\psi_i e^{-iE_i t/\hbar} + a_f(t)\hat{V}(t)\psi_f e^{-iE_f t/\hbar} = i\hbar[\dot{a}_i(t)\psi_i e^{-iE_i t/\hbar} + \dot{a}_f(t)\psi_f e^{-iE_f t/\hbar}] \tag{3.13}$$

Orthogonality of the eigenfunctions ψ requires that $\int \psi_u^* \psi_v d^3r = \delta_{uv}$. Therefore, expressions for the $a(t)$ terms can be given as:

$$\dot{a}_i(t) = -\frac{i}{\hbar}(a_i(t)\left\langle i\right|\hat{V}(t)\left|i\right\rangle + a_f(t)\left\langle i\right|\hat{V}(t)\left|f\right\rangle e^{-i(E_f-E_i)t/\hbar}) \tag{3.14}$$

$$\dot{a}_f(t) = -\frac{i}{\hbar}(a_f(t)\left\langle f\right|\hat{V}(t)\left|f\right\rangle + a_i(t)\left\langle f\right|\hat{V}(t)\left|i\right\rangle e^{i(E_f-E_i)t/\hbar}) \tag{3.15}$$

Now it is time to determine the detailed expression for the $\hat{V}(t)$ term to describe the induced oscillating electric dipole. The incoming beam is approximated using the classical theory of EM wave. In order to avoid the nasty computation in the spatial coordinates a further simplification is made to polarise the EM field along the z direction. Following this consideration a neat expression for the potential operator can be specified to be $\hat{V}(t) = er\cdot\mathscr{E}(t) = ez\mathscr{E}_0\cos\omega t$. Given this in mind the matrix element $\left\langle u\right|\hat{V}(t)\left|v\right\rangle$ can be written as $ez\mathscr{E}_0\cos\omega t\left\langle u\right|\hat{z}\left|v\right\rangle$. Substituting this into the set of equations describing $a(t)$ given above:

$$\dot{a}_i(t) = i\frac{\mathscr{E}_0\left\langle i\right|\hat{z}\left|f\right\rangle}{\hbar}\cos(\omega t)e^{-i(E_f-E_i)t/\hbar}a_f(t) \tag{3.16}$$

$$\dot{a}_f(t) = i\frac{\mathscr{E}_0\left\langle i\right|\hat{z}\left|f\right\rangle}{\hbar}\cos(\omega t)e^{i(E_f-E_i)t/\hbar}a_i(t) \tag{3.17}$$

It is worth noting that the diagonal terms of the new matrix elements disappear due to the odd parity of the position operator. The necessity for the remaining matrix elements to be real for physical measurement and the conjugation property of the two off-diagonal elements imply that $\left\langle i\right|\hat{z}\left|f\right\rangle = \left\langle f\right|\hat{z}\left|i\right\rangle$.

Turning to the more general inter-band transitions via a similar approach using Fermi's Golden Rule leads to a direct computation of the transition probability. In this picture the electron is taken to either a continuum or discrete set of final states with the density of states being ρ_f. By solving Schrödinger's equation under this setup, transition probability can be computed and the result is further used to be compared with experimental outcomes. The equation below presents an illustrative description of the composite terms of the transition probability with initial and final states represented by 'i' and 'f'.

$$P_{if} = \frac{2\pi}{\hbar}|M_{if}|^2 g(\hbar\omega) \tag{3.18}$$

The term $g(\hbar\omega)$ gives the density of states around the final state and M_{if} is the matrix element being identical to the one already discussed. It is this matrix element that contains the specific information on the direction of inter-band transition.

Since the matrix element encodes the information of transition probability between different energy states, it is also worth introducing the concept of selection rules to complete the picture. Just as the name suggests, these are rules based on the atomic quantum numbers associated with the initial and final states of a transition. For example, in a simplified picture of single-electron hydrogenic system, consider again the potential operator given above describing the interaction between the light and electric dipole of an atom restated as $\hat{V}(t) = er \cdot \mathscr{E}(t)$, where an electric-dipole operator $\hat{p} = e\mathbf{r}$ can be retrieved. This is clearly an odd function of $\mathbf{r}$ and hence a selection rule of change of parity is imposed to dipolar atomic-like transitions. Based on this, given that the parity of spherical harmonic functions is of the form $(-1)^l$, where l is the orbital angular momentum quantum number, the change of parity requirement then implies that the allowed change in quantum number l is either of ± 1. Similarly, given the chirality of the circularly polarised light or the direction of the polarisation for the linearly polarised light, a corresponding change in the magnetic orbital angular momentum quantum number m of the atomic state is needed to conserve angular momentum.

Although the above rules are for single electron hydrogenic system under dipolar transition, it can be easily adapted to more complicated systems such as quantum dots, due to their atomic-like nature. The optical transitions allowed for quantum dots are again governed by dipolar transition rules. Following the logic above, the parity rule means that these transitions are taking place between electrons and holes of matching n numbers such that $\Delta n = 0$. Using figure 3.5 for illustration, this points to the transitions between a pair of electron-hole states such as between $|0\rangle_{\mathrm{e}}$ and $|0\rangle_{\mathrm{h}}$, between $|1\rangle_{\mathrm{e}}$ and $|1\rangle_{\mathrm{h}}$, etc. corresponding to the conduction band and valence band respectively.

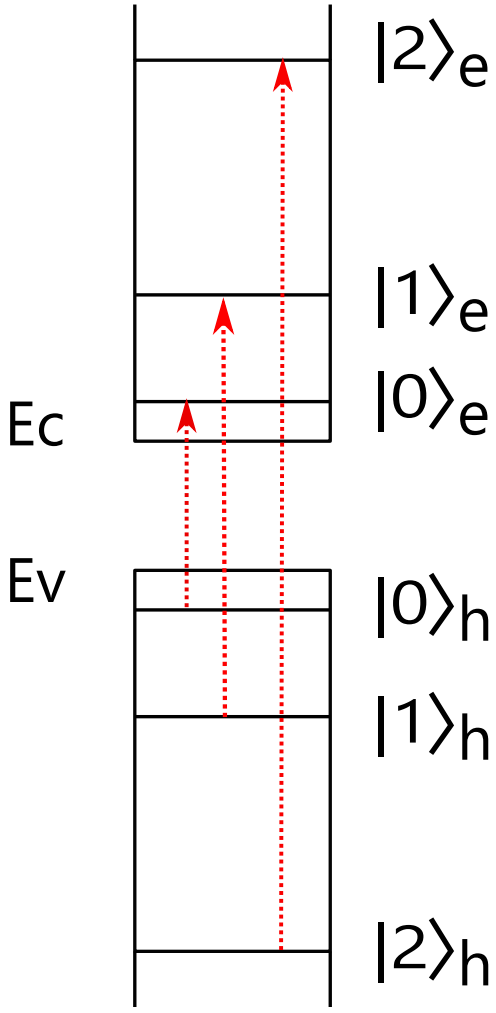

Figure 3.5: Energy level diagram of a quantum dot under spherical approximation with allowed optical transitions under selection rules for illustrative purpose.

Finally turning to the band structure for the specific case of $CsPbX_3$ based quantum dots. As already discussed in the beginning of this chapter, the choice of the A^+ cation

has little influence on the band edges. It is then clear that the combined effects of Pb-X bonding determine the electronic band structure. Regarding the valence band energy, different reports[43][44][45][46] share a consistent view that the band edge energy results from antibonding hybridisation of the Pb 6s and X np orbitals, where the major contribution is from the np orbitals of the chosen halide ion. In contrast, determination of the conduction band edge is predominantly governed by the Pb 6s orbitals with relatively minor contribution from the halide np orbitals. A schematic illustrating the band edge formation from the bonding and antibonding of the Pb-X orbitals can be read out from figure 3.6. With the $CsPbBr_3$ composition, other researches[46][47][48][49] have reported a room temperature bandgap energy of 2.5-2.6 eV (495.9-516.6 nm) for nanocrystals of size around 10 nm. As can be seen later in chapter 6 of this thesis, the red shift in PL emission of this specific perovskite composition without passivation from room temperature to 4K is of a magnitude of 20-30 nm. By taking this factor into account, it can be inferred that the emission wavelength for these nanocrystals of similar sizes should fall close to the range of 520 nm-550 nm. This interval will be used as a benchmark for reference when we discuss the optical transition characteristics of the quantum dots and nanocrystals of comparable sizes in chapter 4 and chapter 5 respectively.

3.3.1 Absorption

Absorption is the 'pumping' process to excite an electron from a ground state or across the band gap. It is also one of the ending processes of the input branch in a PL procedure, where the information of the incoming light beam is encoded into the matter to be characterised. Under this consideration, a modification to the pure reflective PL setup can be adapted, including another output path to be the transmission path through the sample. Retrieving the transmission spectrum in this way and subtracting it from the spectrum of the light source gives an absorption spectrum, serving as the direct measurement of the absorption process.

While the detailed mathematical insight into the mechanism of absorption can be studied

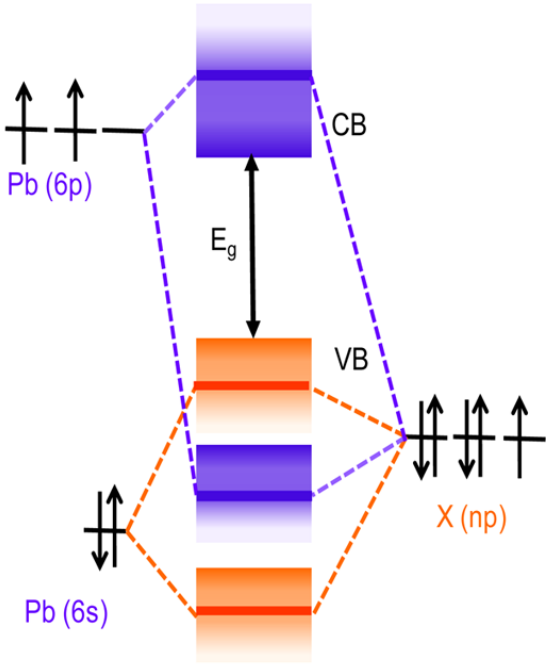

Figure 3.6: Schematic showing the formation of conduction and valence bands (CB and VB respectively) for $CsPbX_3$ based quantum dot resulting from the bonding and antibonding characteristics of the Pb-X group. This figure was taken from a research letter by Vikash *et al.* Adapted with permission. Copyright, 2016, American Chemical Society[46].

through the transition probability given above, it is illustrative to look into the classical propagation equation of the plane wave $\mathscr{E} = \mathscr{E}_0 \exp(-i\omega t + ikr)$. By taking the propagation factor k to be complex, $k = k_{\text{real}} + ik_{\text{img}}$, it is evident that its imaginary part gives rise to a real exponential decay term of the beam amplitude. The corresponding drop in intensity after transmission pins the value of the absorption spectrum at the wavelength specific to that k factor.

As for the sample under study, although the incoming photon provides the energy necessary for the vertical transition in a band diagram, however, for many materials the band gap is not direct. In such cases absorption of a photon is accompanied by a momentum change through lattice vibration, which can be taken as contribution from a phonon.

3.3.2 Excitons and recombination

In semiconductors, instead of immediately generating a freely moving electron and hole, the absorption process initially produces a charge-neutral quasi-particle, 'exciton', a bound state of an electron-hole pair held together via electrostatic attraction. Generally speaking, excitons can be studied depending on the strength of the binding energy and hence classified into two types: strongly bound Frenkel excitons[50] and weakly bound Wannier-Mott excitons[51].

Frenkel excitons are usually found with materials of low dielectric constant, ϵ_r. The dielectric constant is a value associated with the material's permittivity, which measures the electric polarisability of the medium. In the picture of an exciton, the paired electron and hole can be treated as oppositely charged centres. The charge polarised media in between will effectively act as a Coulomb shield and keep them apart, which can be understood as an electrostatic screening process. Hence a weaker effect results in a spatially closer and more tightly bound excitonic state. In the case of Frenkel exciton, the size of the bound carrier pair tends to be at the order of the unit cell. The weakened repulsive screening also indicates a very high binding energy, typically at an order of 0.1-1.0 eV. Moreover, the spatial proximity resulting from tight binding can translate to significant overlap of the electron and hole wavefunctions. Therefore, Frenkel excitons are expected to be localised. This type of exciton is often found in organic molecules, the localisation property means it is normally limited within a single molecule.

Wannier-Mott excitons, on the other hand, are typically found in materials of comparably higher dielectric constant. This type of excitonic states are normally seen in inorganic semiconductors. The enhanced Coulomb screening makes the binding of the electron-hole pair much weaker with their separation being significantly longer than the size of a unit cell. Typically, the binding energy of Wannier-Mott exciton is at the order of 10meV. The weaker binding also implies less spatial restraint on the exciton, which indicates that Wannier-Mott excitons are more delocalised and can move freely.

The setup of the electron-hole system for Wannier-Mott exciton much resembles the atomic structure in the hydrogen model. Therefore, the excitonic state can be treated as an exotic atomic state and a hydrogenic wavefunction is generally accepted to describe its characteristics. However, modifications are required for the Hamiltonian due to the larger size of the exciton along with the lower binding energy comparing to the hydrogen atom both resulting from its weakly bound nature. These effects are incorporated into the energy equation via the inclusion of the dielectric constant. In addition, the effective mass associated with charge carrier in semiconductors is lower than that of an utterly free carrier and hence a reduced mass term is needed. The relevant adjustments mentioned above are incorporated into an effective Rydberg constant R_x as shown in figure 3.7 by multiplying the Rydberg constant R with $\frac{1}{{\epsilon_r}^2}$ and $\frac{\mu}{m_0}$. The energy representation is in the form of the modified hydrogen model to demonstrate the energy of the nth excitonic level. A comparison of the energy dependence with free carriers where the terms associated with electrons and holes are separately considered is also illustrated in the same figure following the treatment in Optical Properties of Solids by Mark Fox[52]. It is evident from the energy spectrum that the excitonic energy levels are lying below the conduction band and inside the bandgap. This is again because of the repulsive Coulomb screening effect which counteracts with the attractive binding of the electron-hole pair. As a result, the excitonic energy levels are lower than that of the unbound electron and hole and this is reflected by the minus sign of the last term for the exciton energy equation. Clearly, the set of excitonic bands associated with different integer number n are corresponding to transitions between different orbitals, these bands are converging towards large n values. In the limiting case when n tends towards infinity, the Rydberg term in the exciton energy equation is negligible and the exciton energy approaches the band gap.

The most direct method for determination of the exciton energy is via absorption spectrum. Given the above knowledge on the modified hydrogen model and assuming a direct bandgap material, the absorption spectrum can be understood with Elliott formula[53]:

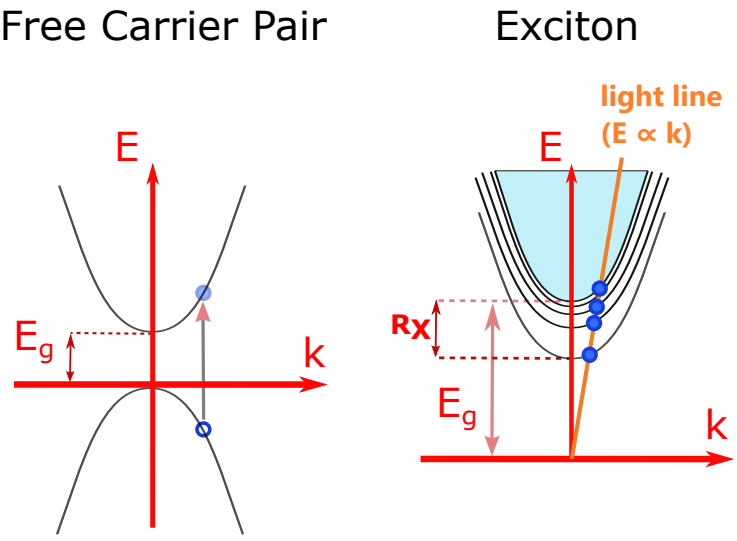

Figure 3.7: Comparison of E-k diagrams for free carriers and weakly bounded excitons. For the excitonic case, the existence for a set of energy bands originate from the choice of integer number n, n =1,2,3..., in the energy calculation.

$$\alpha = [A \cdot \Theta(\hbar\omega - E_g) \cdot D_{cv}(\hbar\omega)] \cdot \frac{\pi x \exp(\pi x)}{\sinh(\pi x)} + A \cdot R \sum_{n=1}^{\infty} \frac{4\pi}{n^3} \cdot \delta\left(\hbar\omega - E_g + \frac{R}{n^2}\right) \tag{3.19}$$

$$x = \sqrt{R(\hbar\omega - E_g)} \tag{3.20}$$

where the first term is from the Sommerfeld model describing the absorption process with the continuum of states above the conduction band. Here Θ is the Heaviside function and D_{cv} is the joint density of states in the conduction and valence band. The combination of the two functions depicts the continuous distribution of states above the conduction band. The second term is associated with the potential different transition paths into the excitonic energy levels, which is represented by the Dirac delta function δ. The familiar form of the exciton energy from figure 3.7 is included here to reveal the discrete nature of the states.

Simplified absorption spectra excluding the effect of broadening showing only the orbitals s1 and s2 as well as conduction band edge can be used to compute the corresponding energy differences and hence the binding energy of the exciton. It is also worth noting that the relative positioning of the energy levels in figure 3.8(a) is consistent with the energy band diagram from figure 3.7.

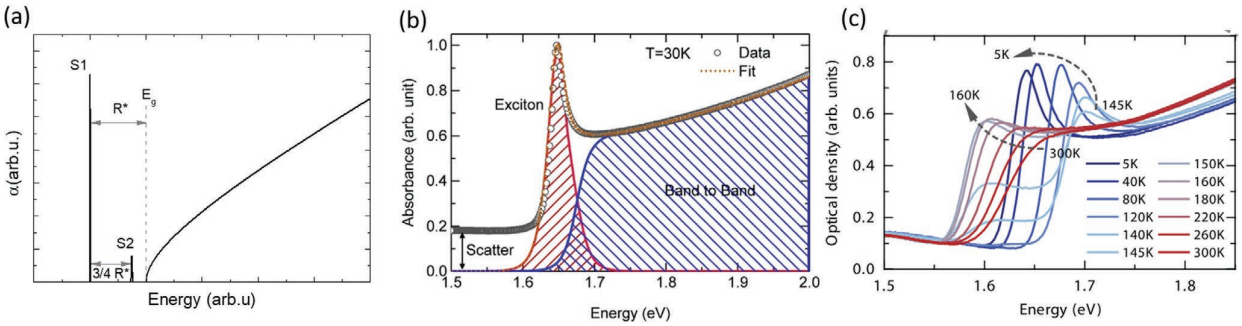

Figure 3.8: (a) Simplified absorption spectra assuming no broadening illustrate the relative positioning of the energy levels for s1 and s2 orbitals (excitonic component) as well as the continuous energy distribution associated with conduction band (band-to-band component) derived from Elliott equation.This figure was taken from a review paper by M. Baranowski *et al.*[54] published under a CC License. (b) Fitting of $MAPbI_3$ absorption spectra at 30 K using the Elliott equation. The contributions from the excitonic component and band-to-band component are overlapped due to broadening at cryogenic temperature. Adapted with permission. Copyright, 2019, American Chemical Society[55].(c) Temperature-dependent absorption spectra for $MAPbI_3$. The two components are indistinguishable above 145K as the broadening effect is significant. Adapted with permission(CCC License number:5265300846655). Copyright, 2019, John Wiley and Sons[56].

However, this is an oversimplified picture. For perovskite bulk structures such as $MAPbI_3$, broadening of the absorption spectra is significant even at cryogenic temperatures, as illustrated in figure 3.8(b)[55]. Clearly, the broadened s1 absorption line is merged with the continuum of the states associated with band to band transition. By increasing the temperature towards room temperature, the excitonic peak becomes almost indistinguishable from the band-to-band transition as indicated by figure 3.8(c)[56]. Therefore, it is proven to be impossible for a direct determination of the excitonic binding energy.

Many approaches have recently been used to approximate a value for the binding energy of excitons in perovskite. Here some of the published results are presented. The first method still focuses on the analysis of the absorption spectrum, by convoluting the Elliott formula with the function of broadening and taking into account the band non-parabolicity,

the binding energy for $MAPbI_3$ is found to fall within the range of 5-29 meV at room temperature and 15-34 meV at cryogenic temperatures[57][58][59][60][61][62][63]. The reason for such a divergent prediction is due to the large number of parameters involved in simulation and fitting procedures, which in the end is more of a numerical optimisation process with little physics insight. And among those reported works, some[60][63] presented explicit temperature dependence of the binding energy while the rest[57][58][59][61][62] have claimed irrelevance to temperature within 10 to 300 K. The second method fits the FWHM of the excitonic line through its dependence on temperature and binding energy[64]. The reported value for $MAPbI_{3-x}Cl_x$ is 55 meV, however, this method is extremely inaccurate at high temperature due to the indistinguishability of the excitonic line. The third method is based on magneto-optical investigations where strong magnetic field is used at room temperature to induce shift in the excitonic transition energy. The binding energy of $MAPbI_3$ under this approach is found to be 16 meV at 4 K and 10-12 meV at room temperature by Miyata et al[65]. Although this technique generates more plausible values at room temperature, its prediction is flawed at low temperatures.

Despite the fact that the results are largely scattered, there are two logical trends that can be extracted to interpret the excitonic behaviour in perovskites. First, as the bandgap increases (e.g. through reducing the size of the halide anion: such as changing I to Cl), the excitonic binding energy also gets larger. This phenomenon is consistent to those observed in typical inorganic semiconductors, where the effective mass of carriers increases as the bandgap gets widened[66]. The second property is to do with the relationship of exciton binding energy to the ambient temperature, as mentioned extensively in the above discussion. Metal-halide perovskites exhibit a large binding energy at cryogenic temperatures while it is reduced significantly towards room temperature. To interpret this, we can use the fundamental concepts introduced at the beginning of this discussion. At low temperatures, the excitons are very localised and the dielectric Coulomb screening is weak. As a result, the electron-hole pair is held closely and a large binding energy is needed to break them up. The excitons in this regime are behaving like Frenkel excitons as in classical semiconductor. With increasing temperature, a large enhancement in Coulomb screening has

been witnessed[67][68]. Therefore, the room-temperature excitons are more weakly bound with comparably lower binding-energy. Another angle to look at this is that the thermalised excitons are also more active, which means the spatial spanning of the quasi-particles are much larger and they can be delocalised inside the crystal lattice. Being coupled to thermal bath also indicates easier separation due to the additional entropy. Within this regime, they are behaving more like Wannier-Mott excitons as in crystal-liquids. The observation is accepted as the dual nature of perovskites[69][70][71]. Following this logic, the excitons found in perovskites at room temperature are generally treated as Wannier-Mott excitons with the exception of those associated with the organic cation, which are taken as their Frenkel counter part.

Another limitation for using the hydrogen model to describe exciton binding energy in perovskites is its negligence of the polaron effect. Excitons live in crystal-like structures and hence interaction with the lattice can have some influence on their properties. Despite the overall charge neutrality of the exciton, it never represents a perfect coincidence of the electron-hole wavefunctions. Therefore, exciton can still be treated as a combination of local positive and negative charge centres. The ionic crystal lattice in the neighbourhood of an exciton can hence interact with it via Coulomb forces. Because the lattice is a connected object, this local interaction will result in its deformation. In the context of condensed matter physics, the lattice vibration modes can be quantised into phonons. Charge carriers in polar semiconductors can hence be described in terms of dressed states incorporating the information of local lattice polarisation, which is represented by the coupled electronic and longitudinal optical phonon states. These dressed states are called polarons. Similar to excitons, the deformation effect can also be classified depending on the size of influence: large polarons are defined with long-range interaction with Coulomb effect extending much longer than the dimension of a single unit cell along the lattice while small polarons usually describe within-unit-cell interactions and even alternations to single bonding. The existence of polaron coupling between the carrier and lattice polarisation gives rise to an increase in the band dispersion adjusted carrier effective mass, which is shown as $m^*_{\mathrm{e,h}} = m_{\mathrm{e,h}} \left(1 + \frac{\alpha}{6}\right)$ for weak coupling in perovskite structures[72]. The modification term α is Fröhlich coupling

constant:

$$\alpha = \frac{e^2}{\hbar}\left(\frac{1}{\epsilon_\infty} - \frac{1}{\epsilon_\mathrm{s}}\right)\sqrt{\frac{m_{\mathrm{e,h}}^2}{2E_\mathrm{LO}}} \tag{3.21}$$

where E_LO is the energy of longitudinal optical phonon and ϵ_s, ϵ_∞ are the static and optical frequency dielectric constants.

In classical semiconductors, the polaron effect is not significant and hence can reasonably be omitted as a modification term. However, its inclusion in calculations associated with perovskites produces a very different exciton spectrum, as reported by Menéndez et al[73]. The reason for this peculiar phenomenon roots from the markedly distinct static and optical-frequency dielectric constants, which are estimated to be around 30 and 5 respectively[67][74][75][76]. The dielectric constant at low and high frequencies do not normally show such a large difference in classical semiconductors. In addition, the phonon energy is also much lower in perovskites compared with traditional semiconductors due to their softness[77]. Taking both factors into account, the Fröhlich constant is significantly higher in perovskites, which means the increase in carrier effective mass is also remarkable. Given the nature of this effect being a coupling interaction, it can be absorbed into the potential term as a modification to the hydrogen model Hamiltonian:

$$-\frac{P^2}{2\mu}\phi + V(R)\phi = E\phi \tag{3.22}$$

where the interacting polaronic potential is in the form presented in the earlier theoretical work by Haken[78] under a later phenomenological modification proposed by Bajaj[79] to correct for the overestimation of the binding energy:

$$V(R) = -\frac{1}{\epsilon_\mathrm{s}}\frac{e^2}{R} - \left(\frac{\epsilon_\infty}{\epsilon_\mathrm{s}}\right)^\gamma\left(\frac{1}{\epsilon_\infty} - \frac{1}{\epsilon_\mathrm{s}}\right)\frac{e^2}{R}(\exp(-R/l_\mathrm{e}) + \exp(-R/l_\mathrm{h})) \tag{3.23}$$

In the interacting potential, the l terms are the polaron radius associated with charge

carrier, they can be expressed as $l_{\mathrm{e,h}} = \sqrt{\hbar^2 m_{\mathrm{e,h}}/E_{\mathrm{LO}}}$. Numerical simulation done by Michal et al[54] using static and optical-frequency dielectric constants of 20 and 5 respectively revealed that the resulting Coulomb potential behaves differently at short range and at long range. At short interacting distance, the Coulomb potential is dominated by the optical-frequency dielectric constant and the screening effect is weak. As for long-range interaction, the effective dielectric constant asymptotes its static value and the Coulomb potential shows relatively strong screening effect. Regarding the binding energy, the simulation indicates that when static and high-frequency dielectric constants are significantly different, the excitonic s1 energy level becomes much lower than that predicted by the bare hydrogen model. This is consistent with a larger s1 and s2 separation and hence a higher binding energy. Moreover, the s2 state lies closer to the conduction band continuum and its relative oscillator strength is much weaker than that of s1[73]. This result explains the invisibility of the s2 spectral line in the absorption discussion and reconciles the abrupt difference between the low and high frequency dielectric constants into the binding energy computation.

All the discussions above are on excitons with perovskites in general. However, the scope of this thesis is much narrower, focusing solely on the $CsPbBr_3$ composition. Due to its lack of organic cations, the material is structurally closer to classical organic semiconductors, which naturally favours the Wannier-Mott excitons. Despite this, the size of the nanocrystals is at the same order as the de Broglie wavelength of the electron wavefunction, which indicates reasonable quantum confinement. In addition, the work presented in chapter 4 and chapter 5 of this thesis was mostly done at 4K on those nanocrystals. Therefore, the optically pumped excitons discussed in those chapters are localised due to both the quantum confinement effect and low thermal energy available. It is hence logical to infer that they have Frenkel characteristics. As the temperature is raised towards room temperature, the Wannier-Mott type will dominate due to increase in Coulomb screening and enhanced delocalisation. In addition, since the nanocrystals are distributed in an array with separation of around 1nm, excitons can hop between neighbouring sites and is hence more mobile and further supports that mainly Wannier-Mott excitons prevail at higher temperatures. For the micro-rod structure discussed in chapter 6, localisation originating from quantum con-

finement is less significant. However, the defect sites are essentially point like confinement centres, which cause self trapping of the excitons and give rise to a Frenkel type behaviour. Even for defect-free rods at 4K, there are still a large amount of Frenkel excitons. However, with raising temperature the Wannier-Mott type will dominate faster than in nanocrystals due to the lack of quantum confinement.

As discussed above, an exciton can reduce to a free carrier pair, however, in the end there will be only two outcomes: recombination or separation of the carriers. Under the picture of recombination, the exciton can hence be thought to bear a finite lifetime. When an exciton recombines, it emits a photon. However, after taking free carrier also into consideration, the possible recombination mechanisms can have several different forms and they are broadly put into two classes, radiative and non-radiative recombination. The former is essentially the inverse of the absorption process and corresponds to the emission term from the computation of transition probability above. Such a process can happen either with an exciton or a free carrier pair and the significance of their difference will become clear soon.

In semiconductors the non-radiative recombination mechanisms are mainly differentiated through the number of carriers involved. There are two categories besides the radiative recombination of free carriers. The first one, Shockley-Read-Hall (trap) recombination, is an one-carrier process where a trap state inside the band gap either captures an electron or a hole before they recombines radiatively with each other[80][81][82]. This process is most prominent with materials of significant defect states. It is an unfavored recombination process and hence needs to be minimised. A most common recipe to reduce such a factor is via passivation[83][84][85]. The other recombination mechanism is Auger recombination, involving an electron-hole pair and another single electron[86][87][88]. The electron-hole pair recombines across the band gap and releases energy. Instead of producing a photon of this energy, it is absorbed by the other electron living in the same band as the electron in the recombined pair. The energy taken drives the electron up the band to an excited level. The following band diagram depicts the three recombination processes involving free carriers.

After demonstrating the classification of recombination process on carrier density, it is

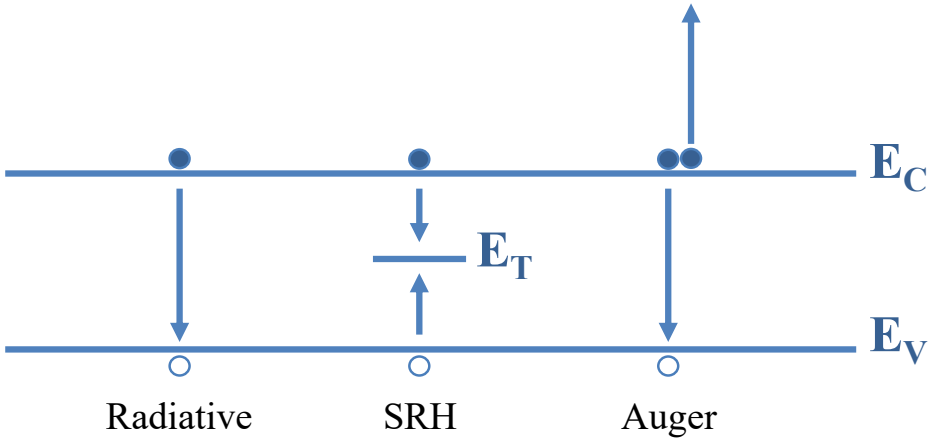

Figure 3.9: Typical recombination mechanisms involved in perovskite materials.

worth mentioning the recombination mechanisms associated with surfaces. Since most of the interesting electronic properties discussed in this thesis are determined by the crystal lattice structure, interruptions to the periodicity of the lattice can cause distortions and result in defect centres to enhance the first-order recombination process. This effect is of particular significance at the surface of the material. In contrast to the well ordered crystal lattice in depth, the formation of dangling bonds at the surface due to the absence of the bonding atom in the neighbourhood can be treated as large local defect centers. Investigations into those dangling bonds has been a profound topic in solid state physics and studies have covered classic semiconductors including Si, GaAs, InAs[89][90][91] towards novel perovskites[92][93][94]. In addition, when layers of two materials with different lattice spacing and bonding natures are joined, the existence of dangling bonding can still be a problem. Although these unpaired bonds can be effectively eliminated through surface passivation by carefully choosing a material to satisfy the interface bonding, even a small mismatch in the lattice constants between the two boundary materials can have a large effect in lattice distortion at a range order of many unit cells. The difference in strain and stress between the lattice at the surface and in depth can eventually result in breaking the superficial bonding and hence produce defect states. The bare perovskite QDs to be discussed in chapter 4 and chapter 5 are 0-dimensional structures, therefore, theoretically they should have no depth. This means that practically these QDs are mostly surface and the carriers under study are best described with surface physics. As a result, the surface recombination is the dominant lossy chan-

nel at low excitation power until the Auger process becomes apparent at higher pumping strength. Whereas the high surface recombination rate means that diffusion is very limited even when the QDs are placed in close proximity, a hopping process of the carriers still ensures a reasonable mobility for a construction of large QD chain or QD lattice[95][96]. On the contrary, the micro/nano-rods discussed in chapter 6 are passivated with lead-hydroxide coating, which not only satisfied the dangling bonds but also provided good lattice matching with the underlying inorganic perovskite lattice. The surface recombination in this case is largely suppressed. Additionally, although some of them are called nano-rods, the dimension of their cross sections is orders larger than the size of the QDs. This implies that the rods have a finite thickness and hence surface effects are of less importance compared to QDs even without passivation. The detailed discussion on the passivation effect will be presented in chapter 6.

As mentioned above, the recombination processes directly affect the concentration of carriers over time and hence can be read out from the lifetime of carriers. Since the focus of this thesis is on perovskite materials, we will limit the scope of discussion only to perovskite. In such a material system, generally all the recombination mechanisms discussed above need to be incorporated[97]. A coupled differential equation is used to describe the decay dynamics. Equation (3.24)(3.25) is the free carrier decay, which is contributed by three recombination mechanisms as discussed. k_{f1}, k_{f2} and k_{f3} are the rates of Shockley-Read-Hall, radiative and Auger recombination. Because the experiments involve measurements at cryogenic temperatures, exciton decay k_{x} can not be neglected. It is now clear that the radiative decay paths for exciton and free carrier pair lead to different orders of their differential terms, as the number of particles involved in each process is different. Here in this model we assume that exciton and free carrier decays are independent of each other. This can be seen through the two separate concentration terms for the exciton procedure and free carrier procedure respectively. The two differential equations are only linked through the initial summation of the two concentration terms at t=0 to be the total carrier concentration. After the initial setup, they become completely independent equations on their own. This is clearly not realistic as excitons can evolve into free carriers over time. However, taking this

factor into account increases the complexity of the computation and the usage of computer power much over the benefit of giving a slight improvement on the accuracy of fitting results.

$$-\frac{dn_{\mathrm{f}}}{dt} = k_{\mathrm{f1}} n_{\mathrm{f}} + k_{\mathrm{f2}} {n_{\mathrm{f}}}^2 + k_{\mathrm{f3}} {n_{\mathrm{f}}}^3 \tag{3.24}$$

$$-\frac{dn_{\mathrm{x}}}{dt} = k_{\mathrm{x}} n_{\mathrm{x}} \tag{3.25}$$

All the lifetime fittings contained in this thesis follow from the model above. I used a customised code to fit the experimental data points using the dynamical model provided above. The code was originally written by a former PhD student Luke P. Nuttall in the group and modified by me to adapt all the different scenarios considered in this thesis.

It is worth to mention the general structure of the fitting algorithm. The code takes into three data files: background, IRF and experimental data. The fitting model relies only on physical parameters relating to the decay process and hence the simulated decay curve needs to be convolved with IRF and added by the dark counts to be comparable to the actual data curve. Another important factor not to be missed out is that the decay does not usually drop to the background level before the second laser pulse hits the sample. The direct outcome of this is that the decay tail of the last excitation cycle is added to the decay curve at the beginning of the current cycle. Given that the excitation cycles are periodic and almost identical, we can assume that a single decay curve is folded. This is saying that the unfinished decay part extruding the one period time window is fed back to the t=0 and added to the decay curve at the beginning. This operation is repeated until the decay hits background level. The process is essentially 'wrapping up' the decay curve to fit in the one period time window. The two operations just interpreted are shown in the figure below for clarity. The resulting decay curve should be in the same form of the data collected from the output of photon detectors (comparable to experimental data file).

In the beginning of the algorithm, initial parameters need to be manually typed in for the coupled differential equations. These parameters generate the first-iteration decay profile to be compared with experimental data. The fitting procedure then optimises the parameters

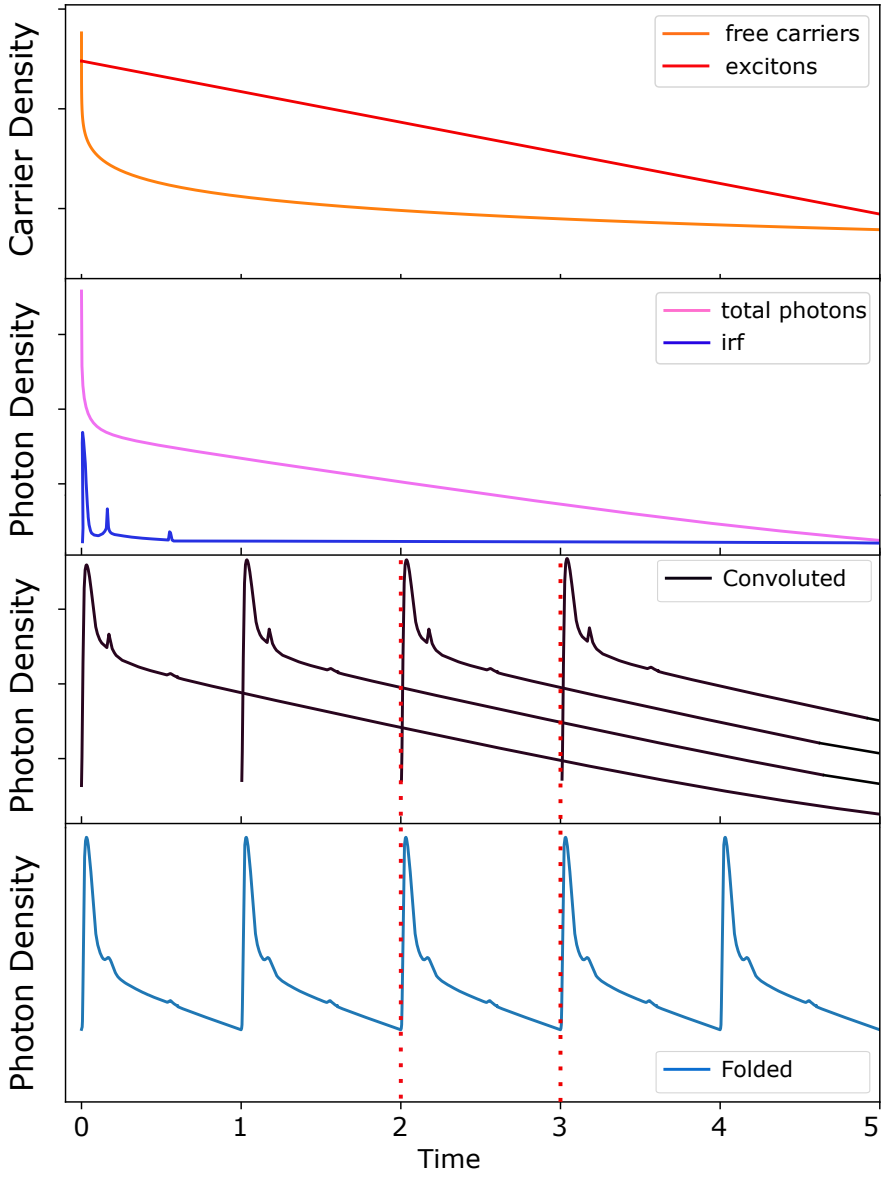

Figure 3.10: Detailed relationship between the fundamental carrier decay dynamics and the actual TRPL data obtained from experiments. The top plot shows the separate decay curves for free carriers and excitons respectively. Summing the two curves gives the total PL photon density after multiplying with a fixed collection efficiency factor and this is plotted in the window below. In the same plot, an IRF function is also presented, which is to be convoluted with the decay curve into the form detectable from a real equipment as shown in the next window. In this third window, a sequence of those independent decay curves following a periodic excitation pattern is demonstrated. By staring at the single period bounded by the red dashed region, it is clear that the unfinished decays from previous pumping cycles will accumulate emitted photons to the current cycle and hence the photon events observed in one excitation cycle is indeed interdependent on the preceding pumping cycles. The bottom window folds the decay tail extruding one period back to the start of the period due to the exact match of a periodic function and thus it generates the final form of the decay event.

by reducing errors at each fitted data point. However, since we are dealing with multi-exponential decay with data points spanning a few orders difference, the absolute error just after the surge of carriers induced through excitation pulse tends to overwhelm that obtained towards the end of the time window. A bias favouring shorter time data points makes the resulting curve diverge at the tail of the decay. In order to remedy this, the time window is truncated into several intervals with each carrying a user specified weight. This customisation step adds flexibility such that different weighting can be applied correspondingly. There are two benefits directly available. First, more weights can be put to the data points of low numerical values and their significance is not overlooked in a fitting process. Second, an interval can be defined around an erroneous region (e.g. contain non physical peak) to have zero weight and the result only concerns data revealing the experimental observation. The squared differences are then scaled through the weighting scheme and summed to give a total error.

The optimisation is based on a basin-hopping scheme[98][99]. The scheme can be easily understood as a composite of two types of operations. The first part is the general error-minimisation process. The dimension of this process is determined by the dimension of the parameter space. A change in the gradient is traced until the a local minimum is found. Due to the potential complex geometry of the multi-parameter function created, many local minima can coexist which makes it very difficult to check if the point found is actually a global minimum or a better minimum for the fitting. This is alleviated by the second part, 'hopping'. After obtaining a local minimum, the parameters are subject to abrupt changes immediately to 'hop out' of the neighbourhood. The minimisation from the first part is then repeated to seek for the minimum in the new region. This combined process will be called for a user-defined number of times and the solution with the least overall error is selected. Because the second step is essentially a random-selection process, the whole algorithm is classified to be a Monte-Carlo algorithm and hence involving more hops will increase the probability to get a more accurate fitting result.

3.3.3 Stimulated Emission and Lasing

In contrast to spontaneous emission, where the initial state is a ground state, the incoming photon can interact with the matter when population inversion is achieved. This is saying that a significant concentration of carriers are already in the excited state when approached by the pumping beam. The interaction process is non-linear as two photons are produced by stimulation using one photon to relax the carrier to the ground state. The two output photons share identical physical properties, they carry the same energy, polarisation and direction of travel. Clearly, stimulated emission serves as an optical amplification mechanism.

The stimulated emission process is most directly reflected in a two level system as shown in figure 3.11(a). In this configuration, the system already sits at its excited state E_2 after population inversion and probing photons exactly matching the transition energy $E_2 - E_1$ stimulates the system to bring it down to the ground state E_1. However, this is not a practical picture of the stimulated emission process as the system can not naturally be in its excited state and hence an explicit pumping process to create population inversion is required. The two level system does not qualify this requisite as pumping for absorption and probing for amplification can not be done in a simultaneous manner. In order to separate the two processes, an additional energy level above E_2 is added as shown in figure 3.11(b). Hence pumping and probing beams are represented by different wavelengths. The resulting higher-energy pumping photons are no longer in resonance with the stimulated emission transition. After population inversion, the higher energy state E_3 follows a fast non-radiative decay path down to energy level E_2. The probing photons then resonantly stimulate the radiative transition to achieve optical amplification. A representative three-level laser system is a Ruby laser first made in Hughes research lab in 1960[100]. A fourth level can also be added by separating the ground state from the lower level of the stimulated emission transition as shown in figure 3.11(c). The pumping process still brings the system from the lowest lying ground state to the highest sitting excited state. Similar to the three-level case, the pumping energy is higher than that of the stimulated emission and hence wouldn't trigger amplification process. Straight after the pumping process the system immediately decays to

level E_2 non-radiatively followed by a resonant optical stimulation down to level E_4. This state quickly reduces to the ground state via another non-radiative decay process. The advantage of adding the fourth level is that the ground state can not consume the probing photons and the resonant beam can only react with the stimulated emission process. As a result, the net gain is high even when the inverted population is low in proportion. The four-level system has been used in Nd:YAG lasers, which was first demonstrated in 1964 at Bell labs [101].

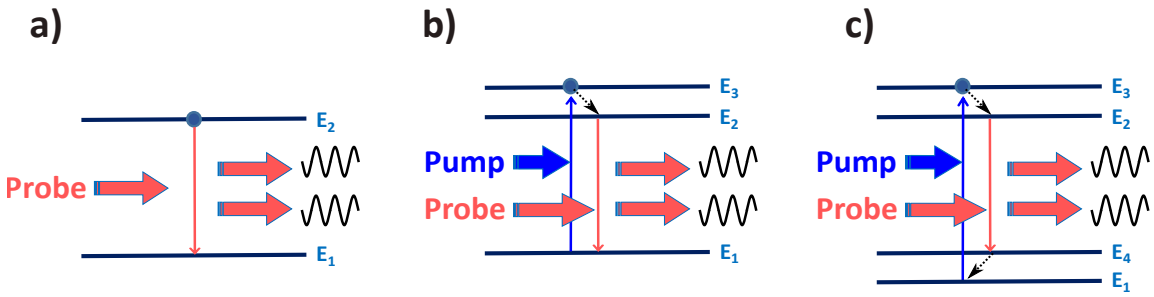

Figure 3.11: Transition mechanisms for stimulated emission processes with a (a) 2-level system, (b) 3-level system and (c) 4-level system. The resonant probing beam for the optical stimulation is shown by the solid red arrow whereas the pumping beam to create population inversion is represented by the blue arrow. The dashed black arrows are associated with fast non-radiative decay processes. After population inversion, the excited state is elastically perturbed by an incoming resonant photon. The emitted photon replicates its physical properties including polarisation and wavelength. The process results in a pair of almost identical photons and can be exploited for optical amplification.

The phenomenon is most widely-applied in developing lasers. The gist of this device is to combine the effect of optical amplification with optical confinement via some physical structure called optical cavity. The confinement can restrict the photons from escaping the gain medium(where the stimulated emission happens) and effectively increase the number of input photons to the stimulated emission process. Another degree of confinement can also be applied to free carriers. Since the stimulated emission only takes place with excited carriers, the same consideration for photons applies here. A heterostructure is normally used(e.g. a quantum well) to design a local energy minimum to limit the carriers inside the gain medium. Therefore, this adds another layer of enhancement to the scale of potential stimulated emissions.

The most fundamental optical cavity is a set of planar mirrors. The idea is to make use of the reflection property of the light beam such that it bounces back and forth between two opposite facing mirrors and hence confinement is realised. However the interference nature of the light can cause most of the beam wavelengths to cancel themselves out during this process. Only the specific wavelengths whose amplitudes are enhanced by constructive interference remain through standing wave configurations. As a result, these wavelengths are the fundamental properties of a laser and they form the modes of the laser operations.

The operation of lasing is best illustrated via the example of a laser diode. Consider a p-i-n junction, where a p-doped layer is followed by an intrinsic region and ends with a n-doped layer. Here p and n types relate to doping the intrinsic semiconductor region with either acceptors or donors respectively. Therefore, the balance between the concentrations of electrons and holes is broken and holes become the majority carriers in p-type semiconductor while the n-type is rich in electrons. By introducing an electric field across the p-i-n junction, more specifically a forward bias, the sloped energy band encourages both electrons and holes to drift away from their dominant regions. Additionally, the slope in concentration of each type of carriers will enhance this migration effect through diffusion. The combined effect will cause significant amounts of electrons and holes to travel into the neutral region, where they recombine radiatively to give out energy via a burst of photons through spontaneous emission. The intrinsic region is hence named active region and it is where the emission is coming from.

Since free carriers are concentrated in the neutral region under a forward bias, our discussion earlier implies that these carriers can be further exploited to undergo stimulated emission with injection of photons at wavelength matching their bandgap energy.

3.4 Rate equation

Since free carriers are concentrated in the neutral region under a forward bias, our discussion earlier implies that these carriers can be further exploited to undergo stimulated emission

with injection of photons at wavelength matching their bandgap energy. It is now appropriate to look into the photon and carrier relationships to understand a microscopic picture of laser operation via rate equations and the following discussion incorporates the presentation used in these references[102][103][104][105]. First considering the structural configuration, applying the optical cavity of length L across the active region, the round-trip optical intensity change is subject to multiplication with a factor $R_1R_2e^{(\gamma g-\alpha)2L}$, where the R terms represent loss due to reflectivity from the end mirrors. The more interesting terms are included in the exponent and contain information on the stimulated emission gain γg and absorption loss α. Clearly the absorption process overwhelms the stimulated emission when gain factor g is relatively low and hence the amplification is not switched on at this level. It is worth mentioning that the coefficient γ is a confinement factor and expressses the ratio of integrated photon energy in active region to that in the optical mode. Alternatively, it can be stated as the volume of active region over the effective optical mode volume, $\frac{V_\mathrm{a}}{V_\mathrm{m}}$. At unity gain of optical intensity, the multiplication to the optical intensity can be rearranged to express the gain factor:

$$\gamma g_\mathrm{th} = \frac{1}{L}\ln(\frac{1}{\sqrt{R_1R_2}}) \tag{3.26}$$

This defines the threshold gain beyond which the optical amplification takes place.

Detailed operation of the lasing process can be illustrated through the dynamics of both photons and free carriers. First look into the rate equation of photon number N_p via stimulated emission :

$$\frac{dN_\mathrm{p}}{dt} = v_\mathrm{g}gn_\mathrm{p}V_\mathrm{a} = v_\mathrm{g}\gamma gN_\mathrm{p} \tag{3.27}$$

It is expressed as a product of group velocity v_g with the photon number after gain. Here n_p is the photon density in the active region. To arrive at the $r.h.s.$ the relationship between γ and the volume ratio is used. However, this equation considers stimulated emission only, the full photon rate equation takes into account both absorption loss and spontaneous emission

gain:

$$\frac{dN_{\mathrm{p}}}{dt} = v_{\mathrm{g}}\gamma g N_{\mathrm{p}} - \frac{1}{\tau_{\mathrm{p}}}N_{\mathrm{p}} + v_{\mathrm{g}}\gamma g N_{\mathrm{sp}} \tag{3.28}$$

The second term in the full equation describes absorption process and is written in terms of the inversed photon lifetime $\frac{1}{\tau_{\mathrm{p}}}$, which states the number of photons lost per second. The third term corresponds to spontaneous emission and it much resembles the stimulated emission gain apart from a spontaneous emission factor N_{sp}. This factor serves as a modification to the gain factor g since the gain is only associated with pure stimulated emission mechanism.

Now consider the change in the density of charger carriers. Since any reaction type considered so far is closely associated with carrier density, its dynamics hence has a direct impact on the photon multiplication process. The rate equation for carrier density n is given as:

$$\frac{dn}{dt} = \frac{\eta I}{qV_{\mathrm{a}}} - R_{\mathrm{r}} - R_{\mathrm{nr}} - v_{\mathrm{g}}g\frac{N_{\mathrm{p}}}{V_{\mathrm{m}}} \tag{3.29}$$

Terms in the above equation can be effectively divided into three types due to the different mechanisms involved. The first type is represented by the first term. It describes the process of carrier injection into the active region due to electric current I flow under an external electric field. η here is an efficiency factor which takes away the portion of current contributed by carriers subject to recombination before arriving in the active region and those have survived through. The second type includes the following two terms and contains information on the net recombination rate less generation. A non-radiative term and a radiative term are separately stated with detailed explanation already given in the last subsection 'recombination' It is also convenient to express out the two terms in carrier density n respectively as $R_{\mathrm{r}} = An^2$ and $R_{\mathrm{nr}} = Bn + Cn^3$. The last type corresponds to carrier reduction from stimulated emission and its form replicates the first term in equation (3.28). However, equation (3.28) is stated in photon number, in order to make it compatible

to the carrier density rate equation it needs to be divided by V_m. The two rate equations are then coupled through the relationship $g = g_0 \log(\frac{n}{n_{\mathrm{tr}}})$. Here n_{tr} is transparency carrier density assuming no reaction is taking place. The direct dependence of the optical gain g on carrier density n implies a mathematical relationship between optical intensity and pumping strength.

With all the ingredients provided, it is convenient to visualise the different operation regions of a laser. The coupled differential equations are solved in steady state and the solutions are rearranged to express the photon density and pumping current, which are the system output and input respectively:

$$N_{\mathrm{p}} = \frac{v_{\mathrm{g}} \gamma g N_{\mathrm{sp}}}{\frac{1}{\tau_{\mathrm{p}}} - v_{\mathrm{g}} \gamma g} \tag{3.30}$$

$$\frac{\eta I}{q V_{\mathrm{a}}} = R_{\mathrm{r}} + R_{\mathrm{nr}} + v_{\mathrm{g}} g \frac{N_{\mathrm{p}}}{V_{\mathrm{m}}} \tag{3.31}$$

At low pumping strength, the gain will be small due to limited carrier injection. As in equation (3.28) the emission gain cannot compensate for the absorption loss and there is little amplification effect. When the pumping strength is increased towards threshold level, the gain factor also scales up and further increases the photon density in the optical mode. However, the emerging net stimulated emission process also causes the last term in equation (3.29) to become significant. As the boost in photon density carries on with higher pumping strength, this rising loss of carriers tames the overall increasing trend in carrier concentration and causes the carrier density to stabilise towards a fixed value at threshold, n_{th}. The gain, therefore, also follows the same pattern and saturates to an upper limit g_{th}. This result is physical as the optical gain cannot move towards infinity.

Now looking back at equation (3.31) again below threshold pumping, the last term can be omitted due to negligible stimulated emission. Following this equation up to threshold level, it can be restated to express the threshold current:

$$\frac{\eta I_{\mathrm{th}}}{qV_{\mathrm{a}}} = R_{\mathrm{r(th)}} + R_{\mathrm{nr(th)}} \tag{3.32}$$

Subtracting this from equation (3.31), which is used for pumping current beyond threshold, a direct relationship between photon density and pumping current can be obtained:

$$\frac{\eta(I - I_{\mathrm{th}})}{qV_{\mathrm{a}}} = v_{\mathrm{g}} g \frac{N_{\mathrm{p}}}{V_{\mathrm{m}}} = \frac{N_{\mathrm{p}}}{V_{\mathrm{m}}\gamma\tau_{\mathrm{p}}} \tag{3.33}$$

The upper boundaries of $n = n_{\mathrm{th}}$ and $g = g_{\mathrm{th}} = \frac{1}{v_{\mathrm{g}}\gamma\tau_{\mathrm{p}}}$ are used with the second relationship used based on the threshold condition from equation (3.30). The result shows a linear dependence between photon density and pumping current and it marks the 'linear region' of laser operation.

3.5 Saturation

However, the optical amplification process is not unlimited with increasing pumping current and gain saturates eventually. The reason for this restriction roots from equation (3.29) where the carrier density stabilises at high photon concentration inside the active region. This in term fixes the gain through the relationship between g and n. As a consequence, the laser enters a steady-state operation stage called 'saturation region'. An alternative but more comprehensive version of equation (3.29) can be used to illustrate the mechanism:

$$\frac{dn}{dt} = J - \frac{1}{\tau} - (\sigma_{\mathrm{absorption}} + \sigma_{\mathrm{emission}}) n n_{\mathrm{p}} \tag{3.34}$$

Here we rewrite the carrier injection term to just include the current density J for convenience and simplify the recombination term to first order only, with its coefficient being the inverse of carrier lifetime. The last term resembles a component in scattering theory. It is in the form of the product of the density of the two classes of particles to 'collide' with each other multiplied by a 'collision cross section' *sigma*, which describes the probability of the

interaction. The cross section is further decomposed into the absorption and emission cross sections as these are the actual interactions happening between the two groups of particles. Taking again the steady state solution at low photon intensity, $n_0 = J\tau$, the overall carrier density can then be written as:

$$n = \frac{n_0}{1 + (\sigma_{\text{absorption}} + \sigma_{\text{emission}})\tau n_{\text{p}}} = \frac{n_0}{1 + \frac{P}{P_{\text{sat}}}} \tag{3.35}$$

with P standing for optical intensity and thus the saturation intensity is written explicitly as $P_{\text{sat}} = \frac{\hbar\omega}{(\sigma_{\text{absorption}} + \sigma_{\text{emission}})\tau}$. At saturation, the gain is half the small signal gain(high frequency gain). This result is commonly found in readings on laser science[106][107][108][109].

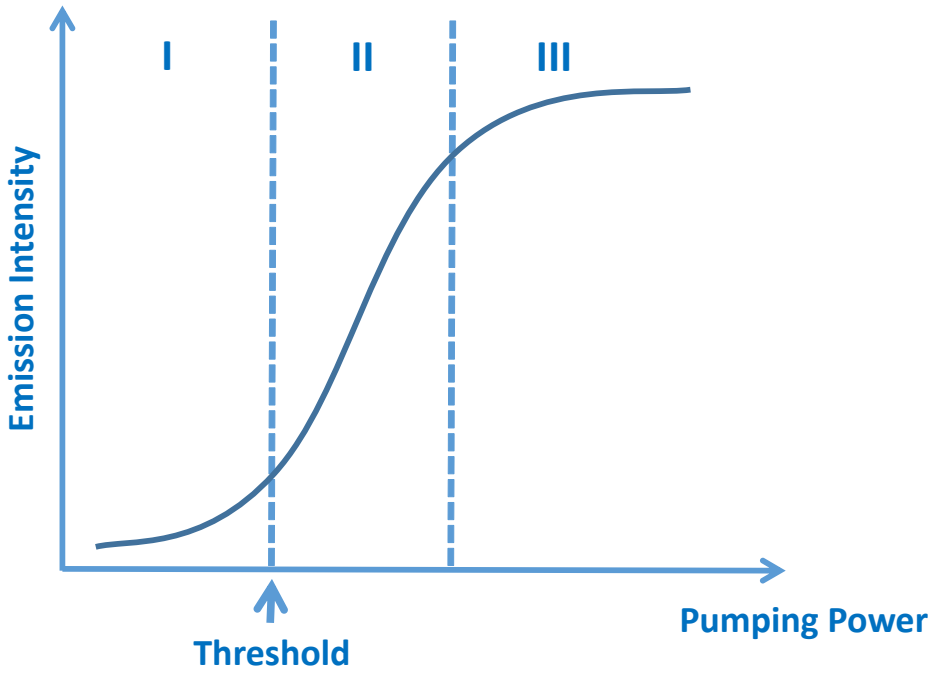

Figure 3.12: Dependence of emitted photon intensity on the pumping strength for a lasing process. The operation is divided into three regions: I, the laser is off when pumping strength is below threshold; II, linear operation region; III, saturation region

Combining the above discussions, it is clear that the operation of a laser can be divided into three regions as shown in figure 3.12. The emission intensity-pumping power dependence follows an 'S' shape and it serves as the most crucial evidence as a proof of the generation of lasing signal. This characteristic is very important in all of the following chapters to verify the nature of the light emission in my samples.

Apart from the S-shape power dependent characteristics, other criteria also need to be checked to verify the identity of stimulated emission. When pumping below the threshold, the excited state will naturally decay into its ground state radiatively at a rate determined by its spontaneous lifetime. However, by increasing the excitation power well above the threshold, the stimulation process essentially interacts with the excited state before it spontaneously decays and hence enhances the rate of emission not only from the non-linearity but also from a shortened lifetime. This can be used as a piece of evidence to support the observation of lasing effect. But this proof is limited by itself. Pumping above threshold means a significant increase in excited carrier density, which results in enhanced multi-carrier non-radiative recombination processes such as Auger recombination. These decay paths are also reflected as shortened lifetime. The localisation effect from confinement further indicates a faster enhancement due to carrier concentration. Therefore, the lifetime shortening can have multiple causes and requires other supporting evidence. Nevertheless, the shortened lifetime can accompany a spectrally narrow lasing mode. In the classical picture, the standing wave theory of the cavity modes favours laser modes at specific wavelengths. Taking into account all the potential broadening mechanisms, the stimulated emission line is still expected to be much narrower than its corresponding spontaneous emission profile. It is hence a better supporting evidence when both lifetime shortening and narrow spectral mode are observed. This argument can be further strengthened when simulation of the cavity structure is in agreement with the experimentally detected mode wavelength. Another proof can root from the coherent nature of stimulated emission. Being a coherent light source, the first order time correlation function of the emitted beam can be retrieved with a Michelson interferometer (to be discussed in detail at chapter 4). A comparison of the extracted coherence time with that of the relevant spontaneous emission process should show a significant enhancement. This is a strong evidence of stimulated emission.

Photon statistics have also been a useful tool to verify the identity of lasing. For conventional laser systems, the laser operation can be distinguished between below-threshold and above-threshold scenarios based on the zero-delay time correlation of two consecutive photon events, $g^{(2)}(0)$ (to see if two photon events are simultaneous or have a finite temporal

separation). When the pumping strength is below or near the threshold level, the emission should exhibit a super-Poissonian distribution consistent with a thermal light source. The corresponding bunching nature is associated with a $g^{(2)}(0)$ greater than 2 and the finite-delay $g^{(2)}(\tau)$ reduces to 1 for temporal separation of the photon pair being longer than the coherence time as shown in figure 3.13(a). By increasing the pumping strength above the threshold, the coherence of the emission is established. Within this regime, the $g^{(2)}(0)$ is expected to be 1 as in figure 3.13(b), revealing the coherent nature of the emission[110][111].

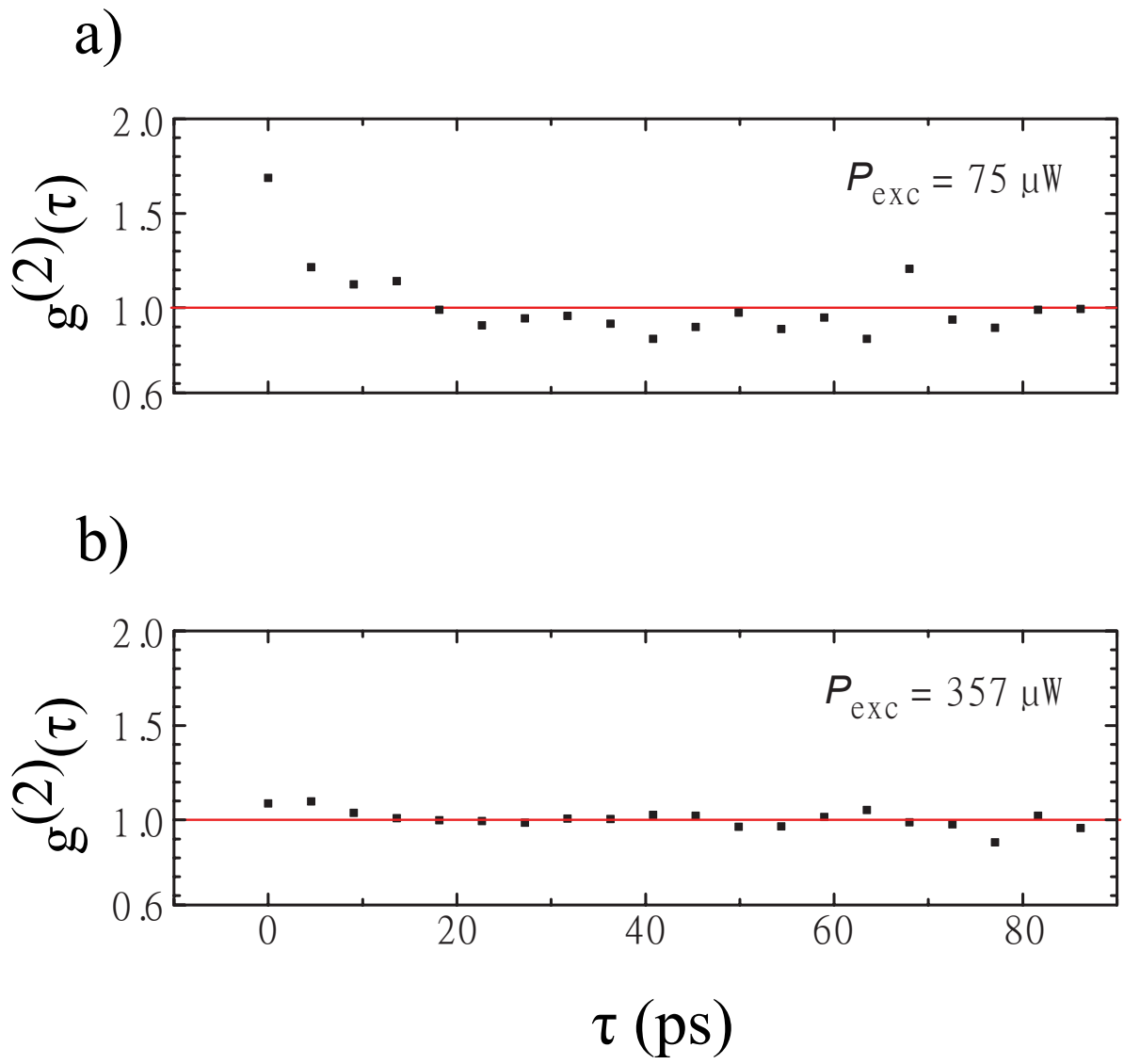

Figure 3.13: Measured second order time correlation function from III-V micropillar cavity of quality factor 9000 embedded with 30 quantum dots for pumping power (a) below threshold and (b) well above threshold. This figure was taken from a research paper by J. Wiersig *et al.* Adapted with permission(CCC License number:5265290700872). Copyright, 2009, Springer Nature.[112]

The above discussions are all under the conventional laser framework, recent development in semiconductor micro-cavity lasers have proven that not only an abrupt threshold is not necessary but also photon antibunching can be witnessed near the threshold[113][114][115][116][117]. Typically, these setups use single-photon emitters including particles or quantum dots and a micro cavity of very high quality factor (larger than tens of thousands). The emitters can couple to the cavity modes either weakly or strongly[40] with the transition wavelength matching that of the cavity mode. However, in the strong coupling regime the photons are oscillating between the emitter and cavity mode with little chance of escaping, which makes it a bad choice for laser design. Only weak coupling is then considered. In this case the cavity electrodynamics induces a change in the density of states where its distribution is significantly enhanced at the wavelength of the cavity mode. The Purcell enhancement factor derived from Fermi's Golden rule can then be used to express the proportion of the total emission rate attributed to the cavity mode. Equivalently, since Purcell effect is on spontaneous emission, a large factor means suppressed emission into non-lasing modes and remarkably enhanced spontaneous emission into lasing modes. This effect reduces the need of very large number of cavity photons and excited states in the gain medium. Consequently, the kink of the threshold in those quantum lasers are smoothed and a more gradual transition into the lasing operation can be demonstrated as in figure 3.14. Regarding photon statistics, Wiersig *et al.*[112] has demonstrated that microlasers with high quality factor (19000) based on very few quantum dot emitters exhibit antibunching statistics during the transition from thermal emission to coherent emission and their second-order correlation function $g^{(2)}(\tau)$ takes on small-amplitude oscillations at threshold pumping strength as shown in figure 3.15(a) and figure 3.13(b), respectively. Although the results are in opposition to those observed in conventional lasers, the authors have demonstrated consistency with recent theoretical developments. They have applied cluster expansion theory to the semiconductor Hamiltonian[118][119] for describing the photon-carrier interactions and the system is coupled to an external reservoir to incorporate photon loss events from cavity. The second order correlation function is then built from the photon number operator and density operator, whose dynamics reproduce the same trend as in the experimental results. The small oscil-

lations in the time correlation function are only visible at near-threshold pumping strength and significantly damped above threshold. The origin of those fluctuations is due to the laser switch-on effect or perturbation to the system's steady state, where the system tends to re-build its equilibrium through relaxation. Therefore, these quantum oscillations are called relaxation oscillations. This effect is only prominent during the transition stage to the lasing operation as the number of photons emitted by the very limited number of quantum dots is small. Therefore, a event of photon loss from the cavity can be treated as a large perturbation to the system and leads to the oscillation ripples. Once the laser is pumped much harder and fully enters the lasing stage, the photon number will be increased significantly and the cavity losses will not produce such huge impact anymore.

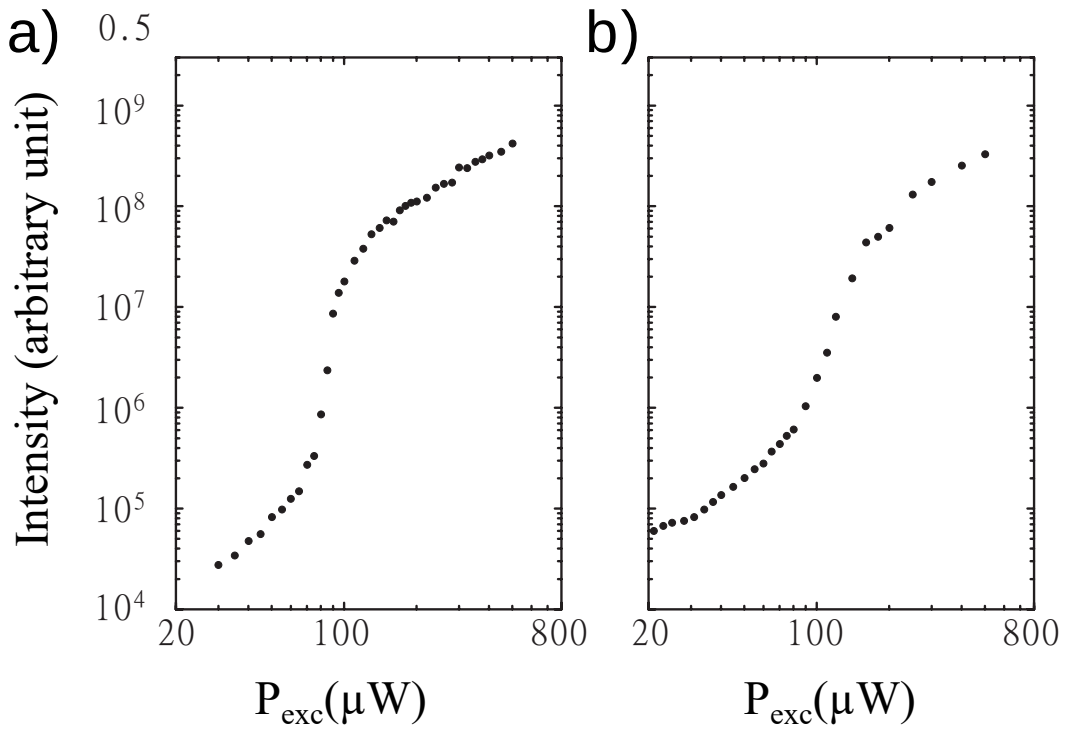

Figure 3.14: Comparison of measured output optical intensity versus the input pumping strength for the 'switch-on' effect of lasing between cavities with (a) relatively low quality factor of 9000 and (b) relatively high quality factor of 19000. The transition associated with the higher quality factor is much smoother where the 'kink' of the threshold almost indistinguishable. This figure was taken from a reserach paper by J. Wiersig *et al.*Adapted with permission(CCC License number:5265290700872). Copyright, 2009, Springer Nature.[112]

This interesting discussion is closely relevant to the quantum dot system to be studied in chapter 4 and chapter 5. However, the density of quantum dots under the scope of this

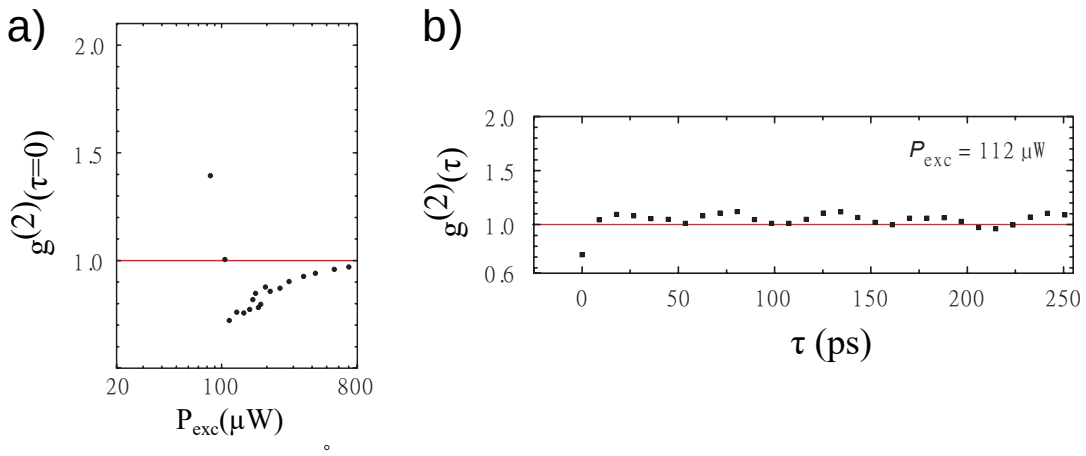

Figure 3.15: Measured second order time correlation function from III-V micropillar cavity of quality factor 19000 embedded with 15 quantum dots. (a) Dependence of the correlation function at zero delay over pumping power shows antibunching at the 'switch-on' transition. (b) Temporal profile of the correlation function exhibits small oscillations near threshold pumping. This figure was taken from a reserach paper by J. Wiersig *et al.* Adapted with permission(CCC License number:5265290700872). Copyright, 2009, Springer Nature[112]

thesis is too large for investigation of any of these effects. Potential future work based on the same perovskite quantum dot system with some dilution process included in the fabrication stage can offer a direction to study these unconventional phenomena in micro-cavity lasers.

Chapter 4

TEM modes in perovskite quantum dots

This section focuses on the stimulated emission given by a unique form of $CsPbBr_3$ based QD cluster. The special characteristics of such structure comes from the fact that the aggregation of the QDs naturally build into a cuboidal shape, which matches the requirement for serving as an optical cavity of $CsPbBr_3$ at 4 K emission wavelength around 530-540 nm. Such effect is essentially a self-assembly process of the QDs and to our surprise that the formation of high-Q micro-cavity through this process is highly reproducible. Further investigation has shown that those cuboidal cavities are actually compatible with TEM modes and two degrees of lasing wavelength control are available to this system.

4.1 Structure and Growth

The QDs was fabricated through a top-down method by Professor Atanu Jana from Dongguk University. First, a solution of $PbBr_2$ in hydrobromic acid is prepared, which is followed by addition of Cs_2CO_3 to produce yellow-orange precipitate. The precipitate is the bulk form of our target chemical and it together with octylammonium bromide are dissolved in dimethylformamide to give out yellowish colloidal solution with the addition of toluene. In this process, the inclusion of octylammonium is to serve as a capping ligand. In nanoparticle preparation, capping ligand is used to coat the surface of nanoparticles to prevent

them from forming agglomeration. Hence the octylammonium catches the individual QDs and isolate them into precipitated nanoparticles. Further separation process is done through centrifuging running at 5000 round per minute for 5 minutes. The sample is preserved in a glass container. Before each characterisation session, the container will be filled with toluene and sonicated for 15 minutes to make a colloidal solution back. The colloidal solution is then spin coated at 2000 round per minute for 2 minutes to reprecipitate onto a glass substrate or lithographically produced marked substrate. No PMMA is used during spin coating process for this sample, however, these structures can last over more than one month by storing in vacuum environment. This robustness potentially arises from both its fully-inorganic nature and the hierarchical structure as discussed in the following paragraphs.

The crystal structure was characterised by professor Atanu Jana using a D/MAX2500V/PC diffractometer, Rigaku with a Cu-rotating anode X-ray source. As for the measurement settings, the Bragg diffraction angle (2θ) was set to be 10-50 degrees and the scan was set to be 2 degree/second. The resulting image was shown in figure 4.1, where orthorhombic or cubic symmetries can be observed[120][121][122][123].

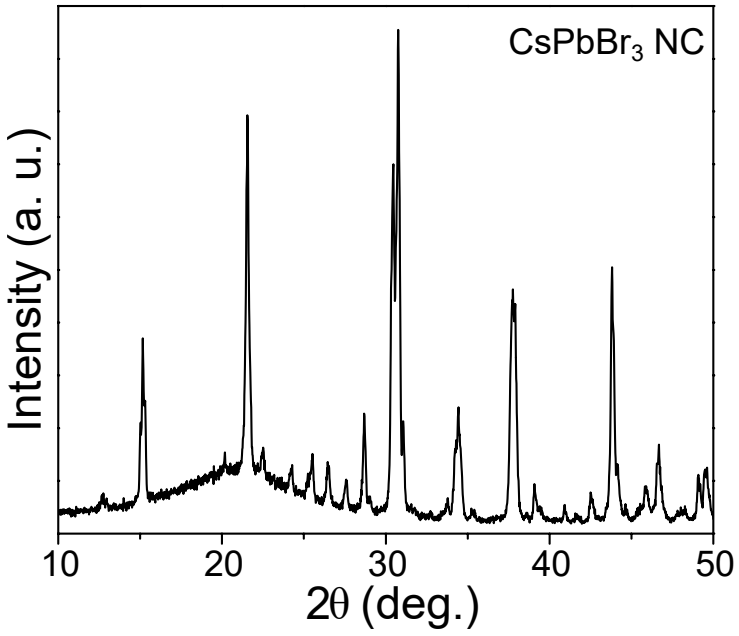

Figure 4.1: Diffraction angle observed for the cluster of CsPbBr3 QDs likewise indicates an orthorhombic crystalline phase similar to its bulk counter part. However, the diffraction result on itself cannot discriminate between a cubic phase and an orthorhombic phase due to the similarity in outcomes.[Image supplied by Atanu Jana from Dongguk University]

The size of the individual QD and lattice fringes were measured also by professor Atanu Jana using a JEOL JEM-2100F electron microscope with a 2000 kV electron source. Figure 4.2(c) and figure 4.3(b) clearly show the individual QDs to have a size of around 5 nm and interplanar lattice fringe distance to be 0.28 nm, which is consistent with that of the (200) plane of $CsPbBr_3$ crystal for QD size being 3.5-7 nm[124][125]. The circular morphology for the QD also matches those reported in other research items[125]. A statistical analysis on the dot size through estimation from the transmission electron microscope images taken with different batches of the sample further shows that majority of the dots are formed within a size range of 4-8 nm as in figure 4.4(a). This means that most of the QDs produced possess dimensions comparable to the Bohr radius associated with excitons in $CsPbBr_3$ structure[124][125] and hence the electron-hole pair is localised and confined spatially. As a result, the energy levels are quantised and spectrally narrow emission at 4 K is expected to focus at a specific wavelength compared to that from a bulk structure. A remark here needs to be made that the dark circles shouldn't be confused with lead precipitate produced by overexposure of the electron beam in a transmission electron microscopy setup[126]. A careful reader must not miss the fact that these are genuine QDs and evidence of individual dots deposited on a copper substrate can also be seen from figure 4.2(a)(b) taken under a transmission electron microscopy. From the same image, it is clear that a nanocrystal (light dark region) of size around 20 nm captures two or three QDs in an encapsulation. Those nanocrystals themselves are further contained in a self-assembled cluster and distributed homogeneously.

Although not possible to statistically determine a precise distribution of the nanocrystal separation, it is evident from the transmission electron microscope images that the adjacent nanocrystals span a distance of 5-25nm. This level of separation means the overlap of electron wavefunctions between two neighbouring nanocrystals is possible but limited. Unlike in the configuration of a superlattice where the distancing between nearby component nanocrystals can be as small as 1-2nm, indicating the strong electron sharing effect due to the large wavefunction overlap, the individual nanocrystals in our case are mostly weakly coupled to each other and can be treated as separate entities when considering their interactions with the

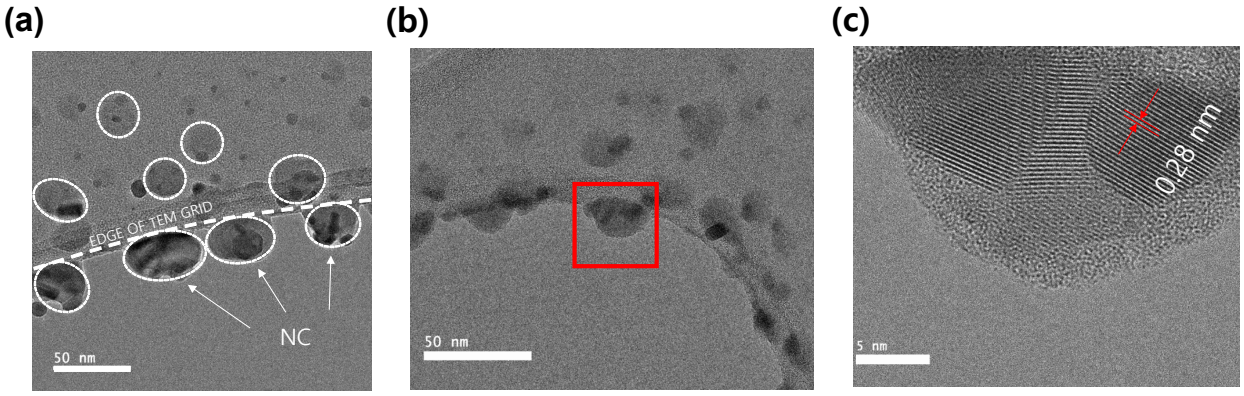

Figure 4.2: Transmission electron microscopy image for $CsPbBr_3$ nanocrystals. (a), (b) Illustration to show the formation of nanocrystals from the more fundamental QDs. These QDs occupy a morphology consistent with the other reported work, including the work by Di *et al.*[125] (c) Zoomed-in image for the single nanocrystal marked in (b) to reveal the crystal lattice. The interplanar spacing is found to be 0.28 nm and it is of a size comparable to that of $CsPbBr_3$ reported elsewhere[124][125]. The QDs are sitting in close distance such that significant interaction among their transition dipole moments is possible. [Image supplied by Atanu Jana from Dongguk University]

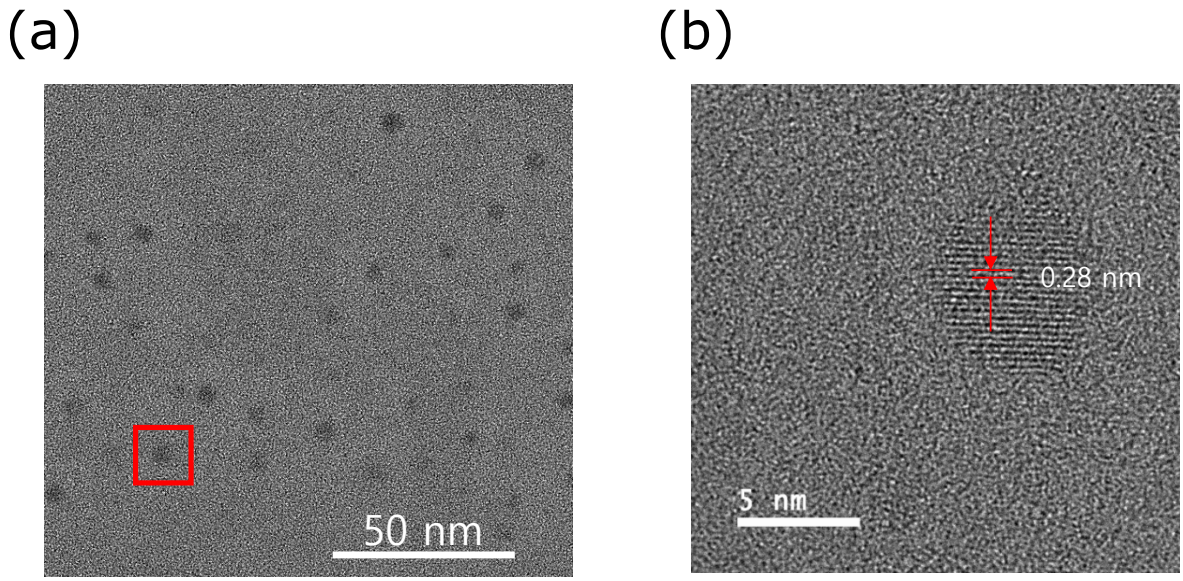

Figure 4.3: (a) Transmission electron microscope image showing the $CsPbBr_3$ QDs embedded inside a cluster structure. The individual QDs are found to be the darker circular regions spanning a diamter of around $\sim$ 5 nm. (b) High-resolution transition electron microscope image zooming into the marked area of a single QD indicated in (a). The detailed crystalline structure reveals a lattice spacing of the size 0.28 nm. [Image supplied by Atanu Jana from Dongguk University]

cavity. As introduced in the cavity coupling discussion of the lasing section in chapter 3, the cavity has effectively modified the density of photon states peaking at the wavelength of the cavity mode (the detailed parameters to be discussed more in the later subsections). Since

our emitters also exhibit bandgap transition peaking between 533-535 nm, closely coinciding with the cavity mode, a large proportion of emitted photons are fed into cavity modes resonantly. This cavity coupling effect provides the basis for optical amplification at a narrow wavelength range.

The cluster is the top-level form of the aggregation and some of them have regular cuboidal shape with opposite facets being around 1-2 μm apart. The schematic of the hierarchy together with a SEM image of a representative cluster are shown in figure 4.5. The cluster of this configuration can act as an intrinsically formed optical cavity for resonance with the behaviour of the corresponding cavity modes discussed more thoroughly in the following subsection. However, not all the clusters formed meet these requirements. Most of the bigger clusters are too large compared to the emission wavelength and they are typically with asymmetric shape. A distribution of the clusters can be read out from figure 4.4(b) which shows that less than 50% of the observed clusters are meeting the size requirement.

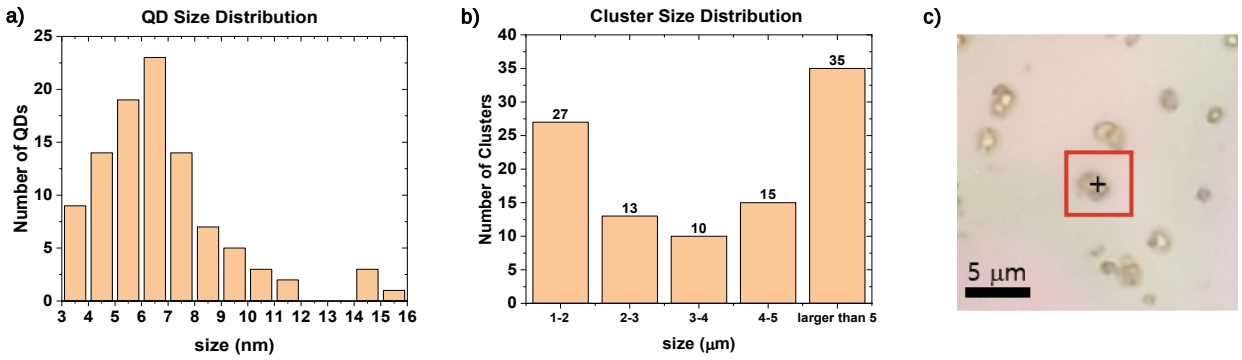

Figure 4.4: (a) Size distribution of the embedded QDs. The sampled statistics closely resembles a normal distribution with majority of the QDs found to fall within the range of 4-8 nm. Outliers at very large sizes (14-16 nm) are also observed. The size of individual dots is estimated from the transmission electron microscope images. (b) Size distribution of the self-assembled clusters. Unlike the case of QDs, the size of clusters is roughly estimated from the 100x microscope optical images, with an example given in (c). Due to the limited resolution of the optical image, very small clusters (smaller than 1 μm) are not observable and are hence not included in the counting. The very large ones (larger than 5 μm) are also excluded due to their irregular shape. The distribution indicates that the target clusters spanning a size of 1-2 μm take a significant but not dominant percentage of all the clusters formed. However, due to the large number of clusters produced (around 5 clusters with size greater than 1 μm per 100 μm^2 area on a 0.5 cm by 0.5 cm substrate) it is easy to find one of the compatible dimension.

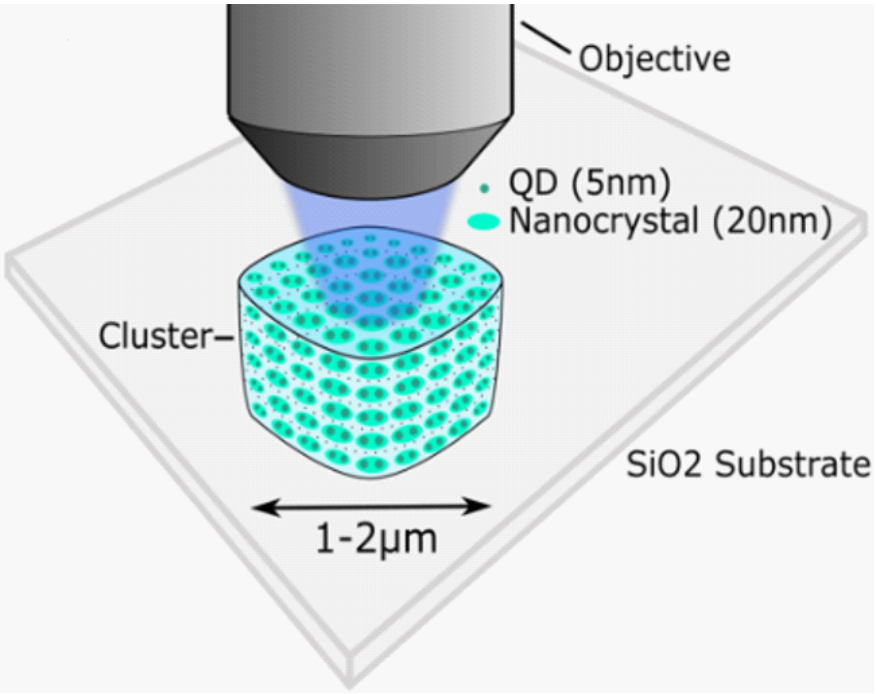

Figure 4.5: Schematics to demonstrate the hierarchical breakdown of the self-assembled cluster system. The typical cluster size is of $\sim$ 1-2 μm, which is built from round shaped nanocrystals with a diameter of $\sim$ 20 nm. These nanocrystals further encapsulate QDs. The area exposed by the pumping laser spot covers thousands of QDs.

4.2 Lasing

As already discussed in the background chapter, the most direct verification of lasing behaviour can be carried out with a pumping strength dependent measurement. For commercial packaged devices, the pump source is normally electric current and hence the dependence of output intensity on current is used for illustration of the working principle. However, the pump source in all the following experiments to be demonstrated will be a photon source, a laser itself. The relationship will be identical to the electrically driven examples and an 'S' curve should be expected in all scenarios.

For demonstration purpose, single mode lasing from a typical cluster of size around 2 μm is presented in figure 4.6(a). The measurement was taken at liquid helium temperature of 4 K, so most of the emission signal is considered to be excitonic. At high pumping fluence above 75 μJcm^{-2} the PL spectrum clearly reveals two components. The broad background emission is the characteristic SPE line for $CsPbBr_3$ nanocrystals at cryogenic temperature.

The other component, the sharp emission emerging at high excitation power is the SE signal. The plot indicates a threshold level of 75 μJcm^{-2}, below which only SPE can be observed. In order to check for the exact dependence on the pumping fluence, areas underneath both SPE and SE emission lines are integrated and plotted for each excitation intensity respectively. The resulting plots are shown in figure 4.6(b), where a neat 'S' shape for the SE emission matches the threshold obtained above and it also marks a saturation level at 300 μJcm^{-2}.

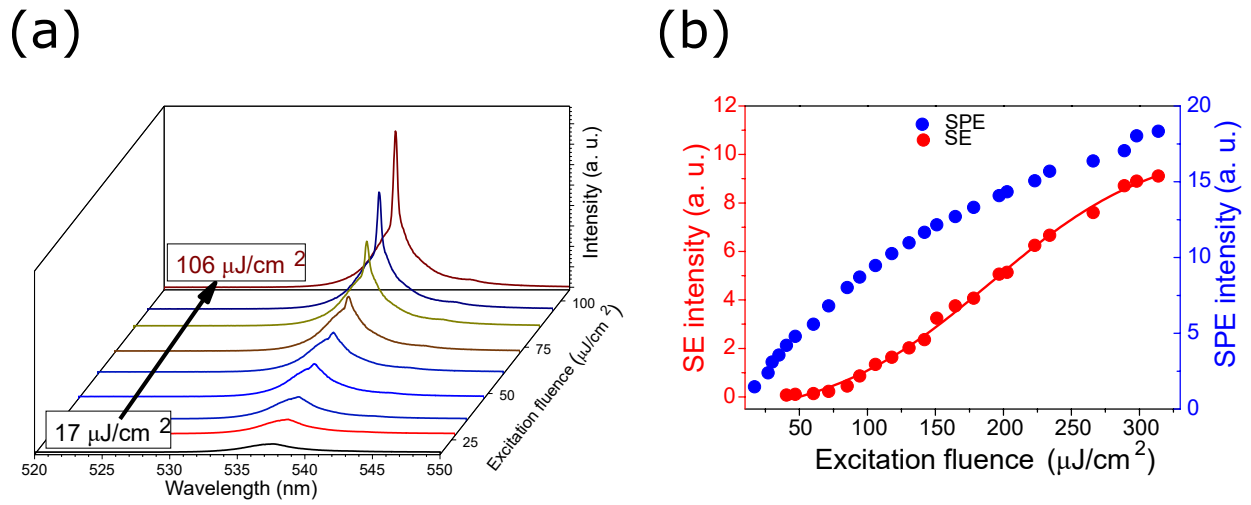

Figure 4.6: (a) Power-dependent PL spectra taken near the onset of lasing process. The SE signal only clearly stems out from the background SPE near a pumping strength of $\sim$ 106 μJcm^{-2}. (b) Dependence of total emission intensity over pumping strength for both SPE and SE signals. A linear dependence is observed for the SPE signal while a characteristic lasing S-shape with a clear threshold and saturation turning points are shown for the SE emission.

Figure 4.7 further compares the dynamics for both SPE and SE decays via TRPL plots. The inset of this figure zooms into the sub-nanosecond resolution to track the fast decay of the lasing signal. The fitting model discussed in the background chapter was adopted here but simplified to include only the lasing component. Due to the short time scale, an accurate IRF deconvolution plays an important role towards fitting accuracy. This is clearly reflected by including the IRF signal as a reference in the inset. The fitting of the SE signal in the inset gives a lasing lifetime of 45 ps (with fitting error of 1.7ps and equivalent uncertainty of 3.8%) and is correct up to 0.4 ns, after which the lasing contribution is submerged into the SPE background and a longer time-scale excitonic fitting is used. The SPE fitting uses a bi-exponential model and gives out a fast lifetime of 310 ps (with fitting error of 6ps and

equivalent uncertainty of 1.9%) and a slower component of 5.96 ns (with fitting error of 243ps and equivalent uncertainty of 4.1%), where the fast component is in good agreement with data reported by other research[127][128]. With such results, it is clear that the SE decay is almost three orders faster than the slower lifetime of the background emission and this again matches the property of fast carrier dilution in a lasing process.

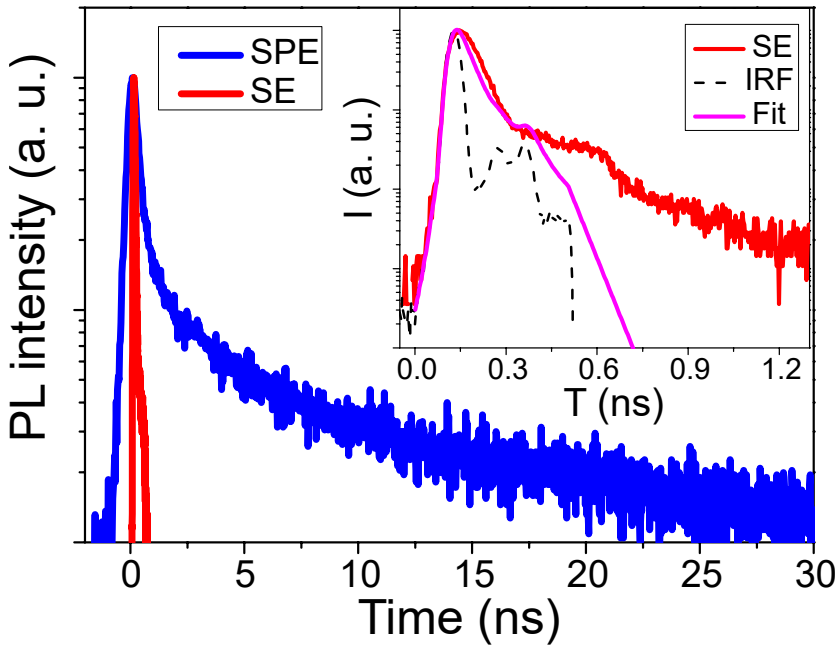

Figure 4.7: Comparison of TRPL decay curves for the SPE and SE emission taken at pumping strength of $\sim 200\,\mu\text{Jcm}^{-2}$ and $\sim 95\,\mu\text{Jcm}^{-2}$ respectively. The inset zooms into the decay dynamics of the first nanosecond for the same plot.

The quality factor of the cavity is also computed from the lasing linewidth at sub-threshold level as in figure 4.8. The excitation fluence is taken at $45\,\mu\text{Jcm}^{-2}$, which is obviously below the threshold level. Having measured a FWHM of around 0.085 nm for the SE peak a Q-factor is calculated to be 6352. However, this linewidth is resolution limited at 1200 grating and 500 blaze level and thus the Q-factor obtained is the minimum possible value. The actual Q-factor is expected to be much higher than this and even the computed value itself is one of the best in the class for $CsPbBr_3$ nanocrystal lasing so far[129][130][131].

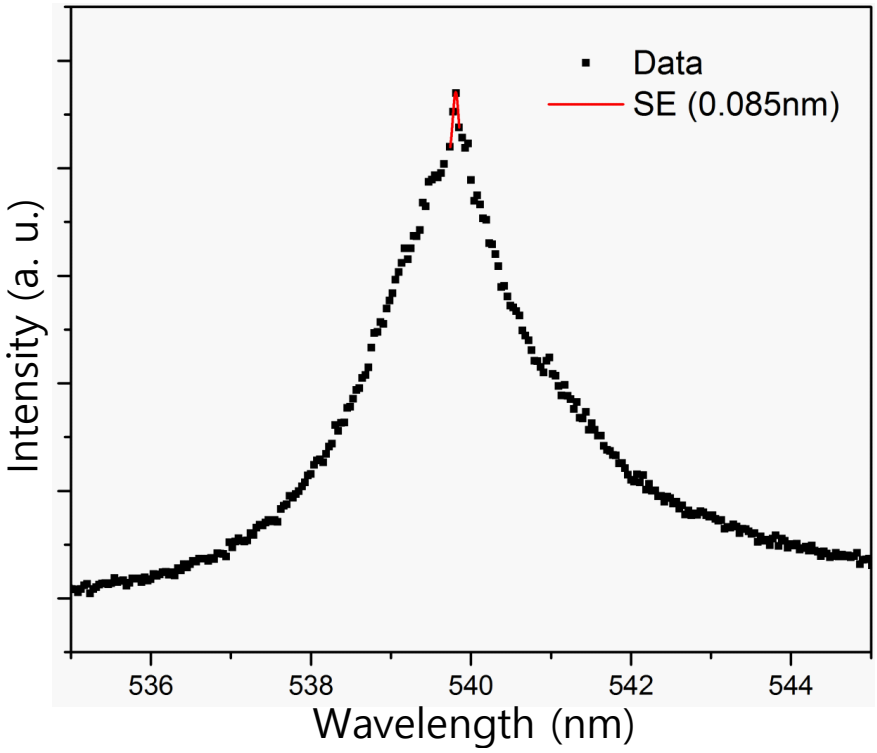

Figure 4.8: Single PL spectrum taken with sub-threshold pumping strength below $\sim 45\,\mu\mathrm{Jcm}^{-2}$. The entire spectrum is fitted with multiple peaks, however, only the fitting to the emergent optical mode is of interest here. To make that fitting clear, the other fitted peaks are removed as they are associated with off-resonant spontaneous emission and none of their information is important to the discussion here. The associated linewidth is 0.085 nm and the corresponding quality factor is found to be 6350.

4.3 TEM Modes

The self-assembly phenomenon of our $CsPbBr_3$ nanocrystal has produced intrinsically formed optical resonators at sub-micron scale. The SEM pictures have revealed that those cavity structures occupy a curved shape, which is compatible with paraboloidal wavefronts for the confined optical modes. Therefore, the class of optical beams giving rise to such wavefront, Gaussian beams, is of particular interest here. The following section discusses extensively the theory of Gaussian beams which is necessary to understand the observed mode structure in our samples. The way of presentation has considered the references[132][133] and [134].

4.3.1 Gaussian Beams

First consider the wave equation on electric field of a propagating wave:

$$\nabla^2 \mathscr{E} + k^2 \mathscr{E} = 0 \tag{4.1}$$

with k being the propagation constant and it is linked to wavelength via $k = \frac{2\pi n}{\lambda}$, where n is the refractive index of the media. The vector decomposition in Euclidean space gives $k^2 = k_x^2 + k_y^2 + k_z^2$. Now define z axis to be the main propagation axis and consider plane wave expansion in the transverse plane of an EM field in the form of a superposition of plane waves with different values of k_x and k_y. The corresponding electric field component can be written as an integration:

$$\mathscr{E} \propto \int \int_{k_x^2 + k_y^2 \leq k^2} \frac{dk_x dk_y}{(2\pi)^2} A(k_x, k_y) \exp(ik_x x + ik_y y + ik_z z) \tag{4.2}$$

where all the composite plane waves satisfy equation (4.1) individually. For laser beams, and the general concept of Gaussian beams introduced earlier, we require the packed wave to have finite transversal extension and moderate propagation spreading. In other words, the beam needs to have a slow change of amplitude along z direction and it is narrow in the width. Therefore, in the equation above the amplitude term $A(k_x, k_y)$ drops fast with k_x and k_y and hence the optical intensity is only significant at values $k_x, k_y << k$. This assumption is under the paraxial wave approximation and it is the fundamental for Gaussian optics[135][136][137].

In order to work out the fundamental mode, further conditions need to be met. The requirement of finite lateral spread naturally leads to the concept of divergence, amplitude spread in wave vector space:

$$D \propto \int_{-\infty}^{\infty} \int_{-\infty}^{\infty} \frac{dk_x dk_y}{(2\pi)^2} (k_x^2 + k_y^2) \mid A \mid^2 \tag{4.3}$$

And also the transversal extension of the intensity in the spatial coordinates:

$$T \propto \int_{-\infty}^{\infty}\int_{-\infty}^{\infty} dxdy(x^2+y^2) \mid \mathscr{E} \mid^2 = \int_{-\infty}^{\infty}\int_{-\infty}^{\infty} \frac{dk_x dk_y}{(2\pi)^2}\left(\left|\frac{\partial A}{\partial x}\right|^2 + \left|\frac{\partial A}{\partial y}\right|^2\right) \tag{4.4}$$

The r.h.s. is arrived by using equation (4.2) and properties of Fourier transform. Minimising both D and T will lead to the expression for the fundamental mode. This can be achieved through minimising their product. To do this a useful technical tool, Schwartz inequality [138][139], can be introduced for two functions $f(\alpha)$ and $g(\alpha)$ with converging integrations:

$$\left(\int_{-\infty}^{\infty} d\alpha \mid f(\alpha) \mid^2\right)\left(\int_{-\infty}^{\infty} d\alpha \mid g(\alpha) \mid^2\right) \geq \left|\int_{-\infty}^{\infty} d\alpha \bar{f}(\alpha) g(\alpha)\right|^2 \tag{4.5}$$

Now the product between divergence and transversal extension can be written as:

$$\begin{aligned}&\left(\int_{-\infty}^{\infty} \frac{dk_x}{2\pi} k_x^2 \mid A \mid^2\right)\left(\int_{-\infty}^{\infty} \frac{dk_x}{2\pi}\left|\frac{\partial A}{\partial x}\right|^2\right) \geq \left|\int_{-\infty}^{\infty} \frac{dk_x}{(2\pi)^2}\frac{1}{2}\left(k_x \bar{A}\frac{\partial A}{\partial k_x} + k_x A\frac{\partial \bar{A}}{\partial k_x}\right)\right|^2 \\ &= \left|\int_{-\infty}^{\infty} \frac{dk_x}{(2\pi)^2}\frac{k_x}{2}\frac{\partial \mid A \mid^2}{\partial k_x}\right|^2 = \frac{1}{64\pi^4} \parallel A \parallel^4\end{aligned} \tag{4.6}$$

The product is simplified to consider the spread only in x due to symmetry property of the wave. Schwartz inequality is then applied and integration by part is used to obtain the expression to the right of the first equality. The minimum is clearly satisfied when equality in the Schwartz relationship is held. This requires that the two functions to be integrated, namely $k_x A$ and $\frac{\partial A}{\partial k_x}$ to differ only by a constant. As a result, A is of exponential form with second order dependence on k_x. Now, including y the expression for the amplitude must take the form $A \propto \exp(-\frac{w_0^2}{4}(k_x^2+k_y^2))$, where w_0 is later to be associated with the width at the waist of the beam.

Inserting the expression for A into equation (4.2), we have:

$$\mathscr{E}_0 \propto \int\int_{-\infty}^{\infty} \frac{dk_x dk_y}{(2\pi)^2} \exp\left(ik_x x + ik_y y + ikz - i\frac{k_x^2 + k_y^2}{2k}z - \frac{w_0^2}{4}\left(k_x^2 + k_y^2\right)\right) \tag{4.7}$$

The square root of k in equation (4.2) is Taylor expanded out up to first order and the A term is absorbed into the exponential. Now using the integration property $\int_{-\infty}^{\infty} \frac{da}{2\pi} \exp(iax - \frac{b}{2}a^2) = \frac{1}{\sqrt{2\pi b}} \exp(-\frac{x^2}{2b})$, where $b \geq 0$, on terms of k_x and k_y:

$$\mathscr{E}_0 = \frac{1}{w_0^2 + \frac{2iz}{k}} \exp\left(ikz - \frac{x^2 + y^2}{w_0^2 + \frac{2iz}{k}}\right) \tag{4.8}$$

after omitting constants. The substitution $\rho^2 = x^2 + y^2$ can be used for simplification. We now have an expression for the fundamental Gaussian mode. However, the terms can be further rearranged to give a more intuitive description of the beam properties.

As illustrated in figure 4.9, the beam waist w_0 represents the beam width at focus where the cross section in the transversal plane is the smallest. It is then useful to define a Rayleigh length, $z_\mathrm{R} = \frac{kw_0^2}{2}$, which is the distance from beam waist to where the area doubles. Now we can introduce a convenient substitution $\zeta = \frac{z}{z_\mathrm{R}}$ as a modified distance in the propagation direction. The following relationship on ζ will be important in the discussions on both fundamental Gaussian modes and its Hermite/Laguerre alternatives later:

$$\frac{1}{1 + i\zeta} = \frac{1 - i\zeta}{1 + \zeta^2} = \frac{\exp(-i \arctan \zeta)}{\sqrt{1 + \zeta^2}} \tag{4.9}$$

Rewriting equation (4.8) using this relationship and recognising that $w_0^2 + \frac{2iz}{k} = w_0^2(1 + i\zeta)$ in the denominator for the ρ^2 term, we obtain the final expression for the electric field of the fundamental Gaussian mode:

$$\mathscr{E}_0 = \frac{1}{w(\zeta)} \exp\left(ikz - \frac{1 - i\zeta}{w^2(\zeta)}\rho^2 - i \arctan(\zeta)\right) \tag{4.10}$$

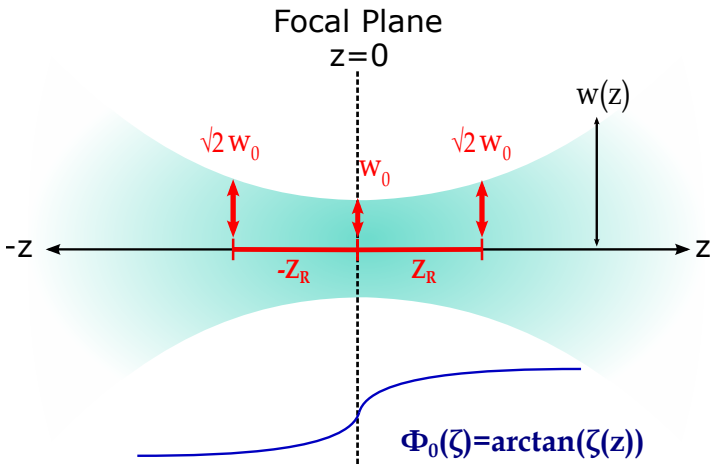

Figure 4.9: Schematic of Gaussian beam near the focal area. The beam waist w_0 is indicated at $z = 0$, where the beam size is the smallest. The Rayleigh length z_{R} is also defined to be the distance from the focal point where the beam area doubles. A Gouy phase $\phi_0(\zeta) = \arctan(\zeta(z))$ is associated with the phase change of the wavefront from its form of coherent phase at the origin, its direct proportionality to the arctan term gives the rapid phase change near the focal point.

where beam width at modified distance ζ is written as $w(\zeta) = w_0\sqrt{1+\zeta^2}$. This is consistent with our definition of beam waist at $\zeta = 0$.

Now the characteristic properties of the Gaussian mode can be directly read out from the expression.

Real term: the optical intensity, from the real term $\exp(\frac{1}{w^2(\zeta)}\rho^2)$, has a Gaussian mathematical form in the xy-plane and hence it is named as a fundamental Gaussian mode.

Dispersion and transversal extension: D is represented in the wave vector space while T lives in the spatial coordinates. x and k are associated through a Fourier transformation similar to that in quantum mechanics. So the minimum is essentially determined through Heisenberg's uncertainty principle. This means that the Gaussian beams are subject to less

dispersion compared to other beams of same size and it sets the lower threshold of diffraction for optical beams.

Gouy phase: the trigonometric phase $\phi_0(\zeta) = \arctan(\zeta)$ is called Gouy's phase. The shape of the corresponding arctan function indicates a rapid phase change around the origin, $\zeta = 0$, where the width equals beam waist (minimum beam extension).

Surface of constant phase: the other phase term $\frac{i\zeta}{w^2(\zeta)}\rho^2$ has dependence on the xy-coordinates. This means that surface of constant phase for the electric field overall is curved due to involvement of both a xy-term and a ζ term.

4.3.2 Hermite Gaussian Mode

Laser modes with rectangular symmetry along the propagation direction are structurally stable optical modes, Hermite Gaussian modes. This class of Gaussian modes are found with modification to the electric field equation (4.2) for the fundamental Gaussian mode, where the z term is rewritten in ζ for simplicity:

$$\begin{aligned}\mathscr{E}^{H}_{m,n} \propto \int\int_{-\infty}^{\infty} \frac{dk_x dk_y}{(2\pi)^2} \left(ik_x + \frac{1}{u}\frac{\partial}{\partial k_x}\right)^m \left(ik_y + \frac{1}{u}\frac{\partial}{\partial k_y}\right)^n \times \\ \exp\left(ik_x x + ik_y y + ikz - (1+i\zeta)\,\frac{w_0^2}{4}\left(k_x^2 + k_y^2\right)\right)\end{aligned} \tag{4.11}$$

The modulation is applied via the k and $\frac{\partial}{\partial k}$ operators with a constant u. It is worth reminding that the effect of having ik_x on the exponential is equivalent to acting with a differential operator $\frac{\partial}{\partial x}$. Inclusion of the $\frac{1}{u}\frac{\partial}{\partial k_x}$ term does not change the nature of the scale wave equation as it commutes with $\frac{\partial}{\partial x}$ and $\frac{\partial}{\partial y}$ where u is arbitrary. Although having only the $ik_{x,y}$ operators can solve the equation correctly, it comes with a complex amplitude. The original motivation for adding the differential-k term is to have a solution of real amplitude with complex components only contained in the exponential. It will become clear later when the equation is solved.

For simplicity, substitute the components in the exponent to be O. We can see easily that $\frac{1}{u}\frac{\partial}{\partial k_x}\exp(O) = [\frac{ix}{u} - (1+i\zeta)\frac{w_0^2}{2u}k_x]\exp(O)$, where the second term essentially also has a $\frac{\partial}{\partial x}$ form. Now combine the $\frac{\partial}{\partial x}$ terms in the modulation function and let $g = 1 - \frac{w_0^2}{2iu}(1+i\zeta)$ being the coefficient to $\frac{\partial}{\partial x}$, the wave equation (4.11) can be written as:

$$\mathscr{E}_{m,n}^{H} \propto g^{m+n}\left(\frac{\partial}{\partial x} + \frac{ix}{ug}\right)^m \left(\frac{\partial}{\partial y} + \frac{iy}{ug}\right)^n \mathscr{E}_0 \tag{4.12}$$

There are now two important identities to use. First introduce the operator identity:

$$\left(\frac{\partial}{\partial x} + bx\right)^c = \left[\exp\left(-\frac{bx^2}{2}\right)\frac{\partial}{\partial x}\exp\left(\frac{bx^2}{2}\right)\right]^c = \exp\left(-\frac{bx^2}{2}\right)\frac{\partial^c}{\partial x^c}\exp\left(\frac{bx^2}{2}\right) \tag{4.13}$$

The first equality in the above equation can be checked by expanding out the exponentials and keep terms only up to the first order. Substituting equation (4.13) into equation (4.12):

$$\mathscr{E}_{m,n}^{H} \propto g^{m+n} exp\left(-\frac{i\rho^2}{2ug}\right)\frac{\partial^m}{\partial x^m}\frac{\partial^n}{\partial y^n}\exp\left(\frac{i\rho^2}{2ug}\right)\mathscr{E}_0 \tag{4.14}$$

Acting the differential operators on both $\exp(\frac{i\rho^2}{2ug}$ and $\exp(-\frac{1-i\zeta}{w_0^2(1+\zeta)^2}\rho^2)$ from equation (4.10) and using the ζ relationship (4.9) gives an amplitude term $\rho^2(-\frac{1}{2iu-w_0^2(1+i\zeta)} - \frac{1}{w_0^2(1+i\zeta)})$. This term becomes real only when complex conjugation between the two terms in the bracket is fulfilled, which means $u = -iw_0^2$. Substitute this into the definition of g gives:

$$g = \frac{1-i\zeta}{2} \tag{4.15}$$

The second identity is the Hermite Polynomial:

$$H_a(x) = (-1)^a \exp(x^2)\frac{d^a}{dx^a}\exp(-x^2) \tag{4.16}$$

Absorb $\exp(\frac{i\rho^2}{2ug})$ into $\mathscr{E}_0$ and take only the real term as relationship (4.15) holds. Then apply the Hermite polynomials to equation (4.14) and include the constants omitted before:

$$\begin{aligned}\mathscr{E}^H_{m,n} &\propto \frac{g^{m+n}}{\pi w_0 w}\exp\left(-\frac{i\rho^2}{2ug}\right)\frac{\partial^m}{\partial x^m}\frac{\partial^n}{\partial y^n}\exp\left(ikz-\frac{2\rho^2}{w^2}+i\phi_0\right)\\ &= \frac{g^{m+n}}{\pi w_0 w}\left[(-1)^{m+n}\left(\frac{\sqrt{2}}{w}\right)^m\left(\frac{\sqrt{2}}{w}\right)^n H_m\left(\frac{\sqrt{2}x}{w}\right)H_n\left(\frac{\sqrt{2}y}{w}\right)\right]\exp\left(ikz-\frac{\rho^2}{w_0^2(1+i\zeta)}+i\phi_0\right)\end{aligned} \tag{4.17}$$

The expression is nasty but some key computation moves will be illustrated here to give a clear picture of the terms. With first move to the right of $\propto$ sign, the simplified real ρ term $\frac{2\rho^2}{w^2}$ in the long exponent exists due to the requirement of having real amplitude as just mentioned above. Then the second move to the right of the equality takes out a component $\frac{i\rho^2}{2ug} = -\frac{\rho^2}{(1-i\zeta)w_0^2}$ from it as an exponent. Also in this step, the terms $(\frac{\sqrt{2}}{w})^m(\frac{\sqrt{2}}{w})^n$ are there to correct the substitution of Hermite polynomial variables x, y by $\frac{\sqrt{2}x}{w}, \frac{\sqrt{2}y}{w}$. These two factors are important since w is linked to ζ and they give rise to $w_0^{m+n}(1+\zeta^2)^{\frac{m+n}{2}}$ in the denominator. Also note that $g^{m+n} \propto (1-i\zeta)^{m+n}$, so the overall outcome is $\exp(-i(m+n)\arctan(\zeta))$ and this is a modifying term to the Gouy's phase. As a result, the final electric field expression is given as:

$$\mathscr{E}^H_{m,n} \propto \frac{1}{w_0^{m+n+1}w}H_m\left(\frac{\sqrt{2}x}{w}\right)H_n\left(\frac{\sqrt{2}y}{w}\right)\exp\left(ikz-\frac{\rho^2}{w_0^2(1+i\zeta)}+i\tilde{\phi}_{m,n}\right) \tag{4.18}$$

where the modified Gouy's phase is equal to $(1+m+n)\arctan(\zeta)$.

4.3.3 Laguerre Gaussian Mode

Another class of Gaussian modes occupying rotational symmetry in the propagation direction are called Laguerre Gaussian modes. This type of modes carry orbital angular momentum and can be solved from the paraxial Helmholtz equation in cylindrical coordinates. It needs

to be clarified that the orbital angular momentum carried by the modes are not similar to polarisation angular momentum, it comes from the field spatial distribution. The intrinsic orbital angular momentum will cause the field to have helical wavefront and hence the beam will have a spiral phase.

The modulation here is in a similar form to the representation of angular momentum operator in quantum mechanics. Separating the amplitude and the phase terms, it can be rewritten as $\sqrt{k_x^2+k_y^2}e^{i\alpha}$. Based on this, generation of a phase $\exp(-in\phi)$ can be accomplished through $(k_x+ik_y)^m(k_x-ik_y)^{n+m}$, with ϕ depending on $\arctan(\frac{y}{x})$. Following the same recipe for the need of real amplitude term, the modulation can be further modified by including $\frac{\partial}{\partial k_x}$ and $\frac{\partial}{\partial k_y}$. Putting this into equation (4.2), we have:

$$\begin{aligned}\mathscr{E}^L_{m,n} \propto & \int\int_{-\infty}^{\infty} \frac{dk_x dk_y}{(2\pi)^2} \left(i\left(k_x+ik_y\right)+\frac{1}{u}\left(\frac{\partial}{\partial k_x}+i\frac{\partial}{\partial k_y}\right)\right)^m \\ & \left(i\left(k_x-ik_y\right)+\frac{1}{u}\left(\frac{\partial}{\partial k_x}-i\frac{\partial}{\partial k_y}\right)\right)^n \exp(O)\end{aligned} \tag{4.19}$$

Use $u=-iw_0^2$ again and define g the same way as in the case of Hermite modes, we arrive at the same expression $g=\frac{1-i\zeta}{2}$ for real amplitude condition. The electric field can now be written in a similar way to equation (4.14):

$$\begin{aligned}\mathscr{E}^L_{m,n} \propto & g^{2m+n}\left(2\partial_{\bar{\omega}}+\frac{i\omega}{ug}\right)^m\left(2\partial_{\omega}+\frac{i\bar{\omega}}{ug}\right)^n \mathscr{E}_0 \\ = & (2g)^{2m+n}\exp\left(-\frac{i\omega\bar{\omega}}{2ug}\right)\partial^m{}_{\bar{\omega}}\left(-\frac{2\bar{\omega}}{w^2}\right)^{m+n}\exp\left(\frac{i\omega\bar{\omega}}{2ug}\right)\mathscr{E}_0\end{aligned} \tag{4.20}$$

where the operator identity introduced before is also applied here in the second step. The term $(-\frac{2\bar{\omega}}{w^2})^{m+n}$ is obtained from applying ∂_{ω}^{m+n} onto $\exp(\frac{i\omega\bar{\omega}}{2ug})\exp(-\frac{\omega\bar{\omega}}{w_0^2(1+i\zeta)})$, with the denominator satisfying $2ug=-i(1-i\zeta)w_0^2$.

Introduce Laguerre Polynomial:

$$L^n{}_m(r)=\frac{e^r r^{-n}}{m!}\frac{d^m}{dr^m}(e^{-r}r^{n+m}) \tag{4.21}$$

Equation (4.20) now equals:

$$\mathscr{E}^{L}_{m,n} \propto (2g)^{2m+n}(-\omega)^{-n-m}m!\left(\frac{2\omega\bar{\omega}}{w^2}\right)^{n}\left(\frac{2\omega}{w^2}\right)^{m}{L^{n}}_{m}\left(\frac{2\omega\bar{\omega}}{w^2}\right)\mathscr{E}_0 \tag{4.22}$$

This equation is again very nasty, here I also provide a correspondence between it and equation (4.21):

- $m!$ corresponds to $m!$
- $(\frac{2\omega\bar{\omega}}{w^2})^n$ corresponds to r^{-n}
- $(\frac{2\omega}{w^2})^m$ corresponds to $\frac{d^m}{dr^m}$, where $\frac{2\omega\bar{\omega}}{w^2} = \bar{\omega}(\frac{2\omega}{w^2})$
- $(-\omega)^{-n-m}$ corresponds to r^{n+m}, where $\frac{2\omega\bar{\omega}}{w^2} = (-\omega)(-\frac{2\bar{\omega}}{w^2})$

Finally, the full expression for the Laguerre mode electric field is given as:

$$\mathscr{E}^{L}_{m,n} = \frac{(-1)^{n+m}2^{n+m}m!e^{-in\phi}}{{w_0}^{2m+n}w^{n+1}}\rho^{n}{L^{n}}_{m}\left(\frac{2\rho^2}{w^2}\right)\exp\left(ikz - \frac{\rho^2}{{w_0}^2(1+i\zeta)} - i{\phi^{L}}_{m,n}\right) \tag{4.23}$$

Again the modified Gouy's phase is ${\phi^{L}}_{m,n} = (n{+}2m{+}1)\arctan(\zeta)$. The modification term is obtained through relationship (4.9) with both $(1{-}i\zeta)^{2m+n}$ from the g^{2m+n} term in equation (4.22) as the numerator and $(\sqrt{1+\zeta^2})^{2m+n}$ from the w^{2m+2n} term in the denominator.

This concludes the detailed mathematical background on the Gaussian modes relevant to this topic.

4.3.4 QD TEM modes

μPL mapping with 0.1 μm scanning step has revealed that the lasing modes observed from the $CsPbBr_3$ nanocrystals indeed occupy circular symmetric optical profiles, as can be seen in figure 4.11. This piece of evidence verifies our conjecture on the potential generation of

TEM modes from the curved-face cavities. This result is quite surprising since the cavity itself is spontaneously constructed by the aggregation of perovskite QDs and the associated stimulated emission has a very high Q value. However, in this research no investigation has been conducted to distinguish if the modes are subject to orbital angular momentum modulations and neither has the propagation-direction spiral phase contribution been tested. It is, therefore, uncertain whether the more specific identity of the TEM modes is either Hermite or Laguerre.

It is also worth verifying here the high spatial resolution of the map. The actual resolving power of the 2D scanning depends on 3 factors. First, it depends on the relative size of the the excitation spot and the nanostructure being scanned. In this case, the laser spot spans a Gaussian shape at a width of $1\,\mu$m while the cluster is of a size between 1-2 μm. To visualise the the process, imagine two circles of comparable diameters. Scanning one of them through the other at a step size greater or equal to 10 percent of the diameter can result in noticeable change in the overlapped proportion of the two circles. Equivalently, the resulting PL is expected to have detectable change in both intensity and shape by varying the overlapped area of the laser spot with the QD. However, when the nanostructure being investigated is much smaller (e.g. 10 nm) compared to the laser spot size, the scanning resolution will be strictly bounded by the dimension of the laser spot of $1\,\mu$m. Second, the resolution depends on the precision of the scanning step of the piezo-stage holding the objective lens. In our setup, the piezo-stage can be controlled to scan at a step smaller than $0.05\,\mu$m. Despite this high precision provided by the scanning system, it is not practical due to the third factor, potential fluctuations in sample position within the cryostat. The cryostat being used is a flow cryostat and hence in the intial cooling-down phase helium needs to be pumped through to bring the temperature close to 4 K. Although the experiment is carried out when a thermal equilibrium is reached, it is never a perfect equilibrium and the system is vulnerable to thermal noise. From our experience, scanning at a step smaller than $0.1\,\mu$m would not accurately reflect the PL profile. Therefore, even the piezo-stage can be set to move at an even smaller step, $0.1\,\mu$m is chosen to give a relatively stable PL image as reflected by the intensity maps shown in this chapter.

In order to characterise the individual modes, mode frequencies need to be extracted from the electric field equation (4.18) for the Hermite modes or equation (4.23) for the Laguerre modes. For a given longitudinal mode, the fundamental mode, higher order TEM modes can be identified through the phase term. Note the two types of Gaussian modes do not hold identical phase contributions and hence it seems a separate analysis is required here. Thankfully, the transversely-symmetric mode profiles for all the modes observed in our self-assembled curved cavities enable us to rule out the asymmetric mode contributions in the Hermite case and hence the phase presentation for both types of Gaussian modes become identical as in the case of Laguerre modes. The exact mode frequencies can then be computed by using the round trip condition $\Delta\Phi{=}2\pi q$, where Φ is the overall phase change and q is an integer. This is the requirement for a mode to be supported by the cavity. Applying this condition, we have:

$$2\pi q = kz + \frac{\zeta\rho^2}{w^2} - (n + 2m + 1)\arctan(\zeta) \tag{4.24}$$

The above equation is simplified by working at the optical axis so $\rho{=}\,0$ and this gets rid of the second term on the right. The propagation constant is also expressed out as $k = \frac{2\pi n\nu}{c}$, where n is the refractive index of the medium. Rearranging the expression gives the characteristic frequency for mode (m, n) as:

$$\nu_{m,n,q} = \frac{c}{2Ln}\left[z + (n + 2m + 1)\frac{2\arctan(\frac{\sqrt{1-g_1g_2}}{1+g_1g_2})}{\pi}\right] \tag{4.25}$$

This equation describes the set of higher order mode frequencies for the q^{th} fundamental Gaussian mode. In this expression, parameter g_i is also introduced to describe the degree of curvature for the cavity surface. Its explicit form is written as $g_i = 1 - \frac{L}{\beta_i}$ with β_i being the curvature factor for cavity mirrors. Substituting the diameter of our clusters at around $1\,\mu m$ and refractive index of $CsPbBr_3$ being 2.2-2.3[130], modal wavelength separation can be calculated to be less than 1nm between a high order TEM mode and a longitudinal mode of greater q index at the target wavelength range. These values are used as a starting basis

to fit the experimentally observed mode structure using equation (4.25) as it is impractical to accurately fix the parameters. The fitting procedure involves three parameters and hence neither a precise determination of each parameter nor their statistical outcomes from multiple fitting rounds is important to the discussion here because of the numerical manipulation involved in the optimisation process. Also due to the existence of irregular background spontaneous emission profile in the actual data, no meaningful fitting error is necessary to be presented. However, the most crucial takeaway from this simulation process is that all the fitting results giving the precise coincidence of the mode peaks are qualified with the size of the cluster and refractive index falling between $1 - 2\,\mu m$ and 2.2-2.3 respectively, which validities our arguments regarding the size and structure of the optical cavity. This explains the small modal line separation presented in figure 4.10 with the corresponding mode profiles demonstrated in figure 4.11.

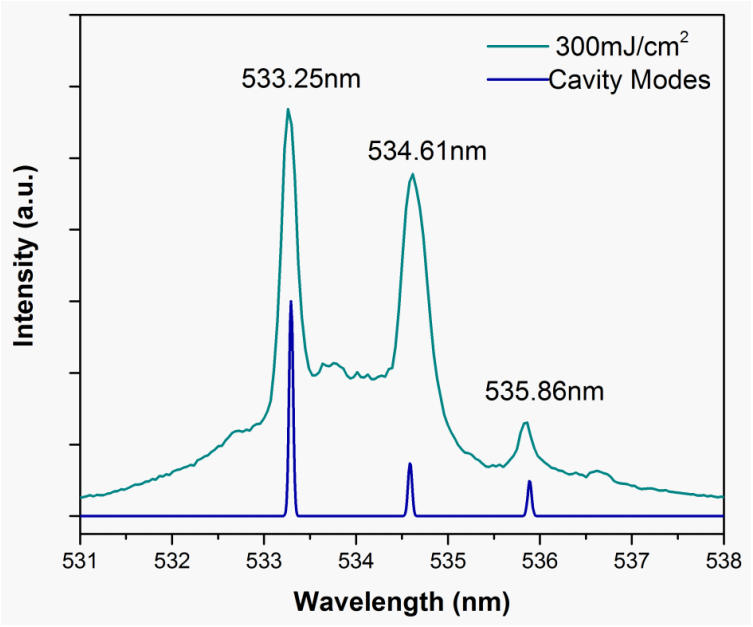

Figure 4.10: TEM mode structure observed in a typical self-assembled cluster of $CsPbBr_3$ QDs under a pumping strength of $\sim 300\,\mu Jcm^{-2}$. The light green lines represent the experimentally observed modes from a PL spectrum and the dark blue lines are the calculated modal wavelengths from Eq.(4.25) via parameter optimisation through a fitting process.

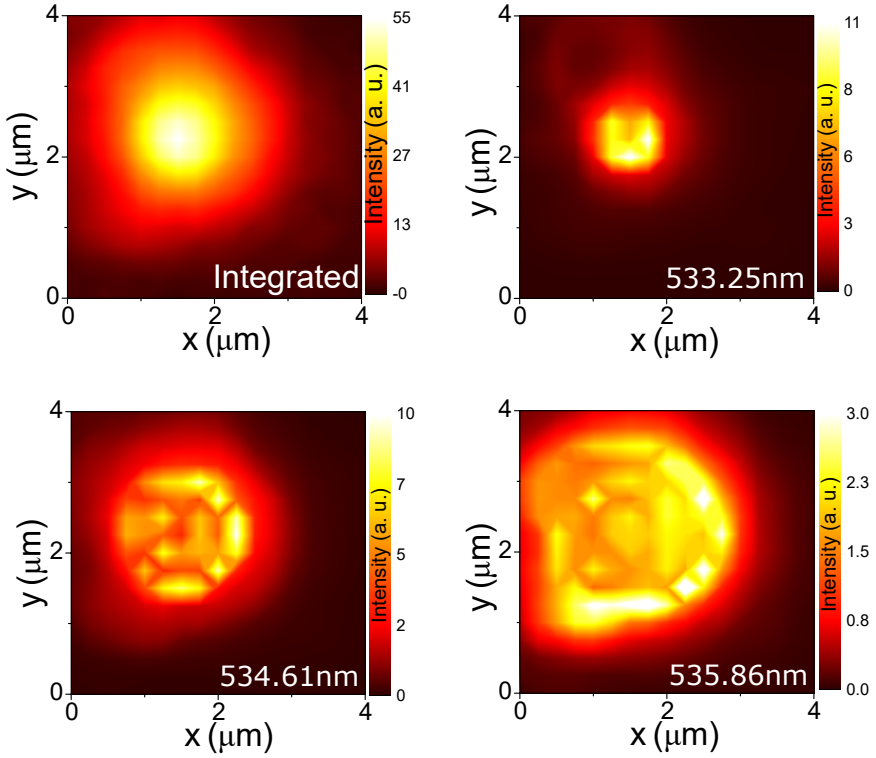

Figure 4.11: 2D PL maps of the modal profiles associated with the modes observed in figure 4.10. A wavelength-integrated map is also plotted at the top-left corner to show the cluster structure and an overall emission profile. Both the fundamental TEM_{00} mode and higher-order $TEM_{i+j\geqslant 1}$ modes are presented.

4.3.5 Mode Tuning with Excitation Power

Using the map viewer python code to customise a wavelength window just around each modal line in the spectrum panel, the individual mode profiles can be filtered out from the full-wavelength integrated spatial map and the plots are shown as each column element of a single row in figure 4.12. The different rows correspond to varying pumping strength and the entire set of plots acts as a matrix containing information on the evolution of TEM modes. With increasing excitation power, new fundamental modes are switched on towards the higher-energy side of the spectrum while the lower-energy modes become fainter. There is a clear overall blueshift of the emission spectrum with higher-order TEM modes being populated along the process. Since the lasing profile is spatially symmetrical, a series of detailed PL spectrum is also taken at $0.25\,\mu m$ step from the centre of the map for each pumping fluence. This is shown in figure 4.13 and illustrates the relative emission strength of the different modes presented in the left panel. It may be questioned here whether these

modes are just all different optical modes of small wavelength variations or they actually come from the fixed frequencies as given by the cavity structure. The proof can be deduced from the observations of figure 4.14(b). This is a waterfall plot of PL spectra taken with fine power tuning (step of around $20\,\mu\mathrm{Jcm}^{-2}$) around a fixed location in a cluster. Overall the plot shows additional peaks are switched on with stronger pumping but the supporting evidence for answering the above question comes from the observation of dashed-lined boxes perfectly aligning along fixed wavelengths. This ensures that the modes witnessed in figure 4.12 actually come from the fixed comb of cavity modes. The switching effect is hence a filling process of those fixed TEM modes determined by the structural properties from the photons of PL emission.

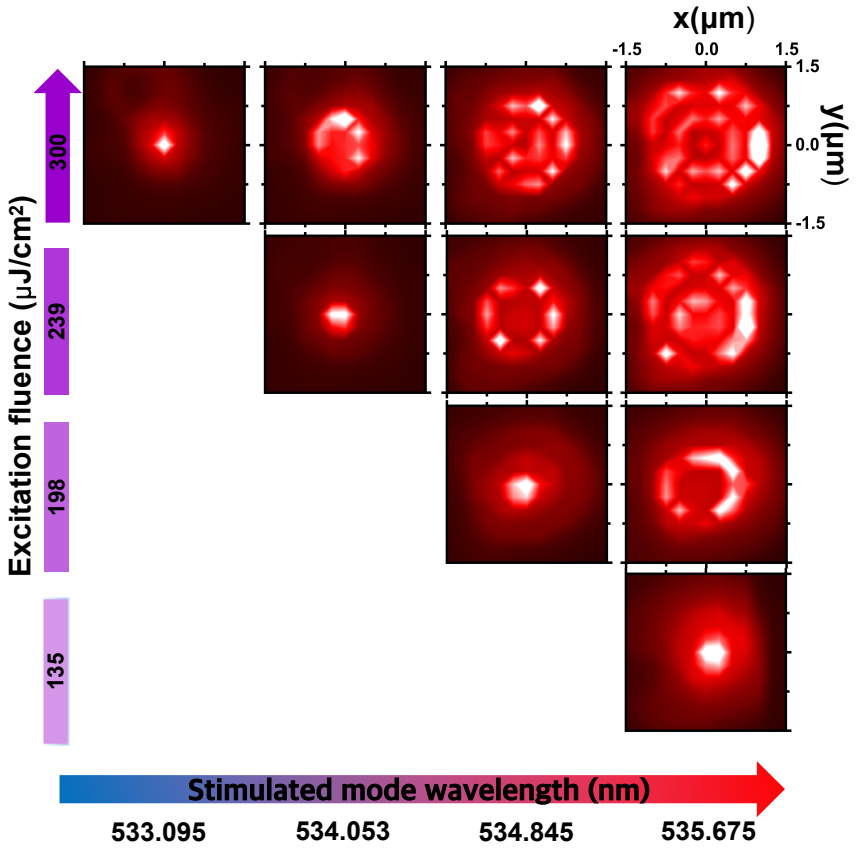

Figure 4.12: PL 2D maps showing the evolution of the TEM modes supported by the QD cluster cavity through cross-sectional cut in the xy-plane. The area taken for the maps has a dimension of $3 \times 3\,\mu$m. At higher pumping strength, higher-energy TEM modes (corresponding to shorter wavelength) are switched on while the lower-energy modes gradually fade away. During the same process, higher-order TEM modes are also observed towards the red side of the spectrum. This observation is repeatable in many other clusters.

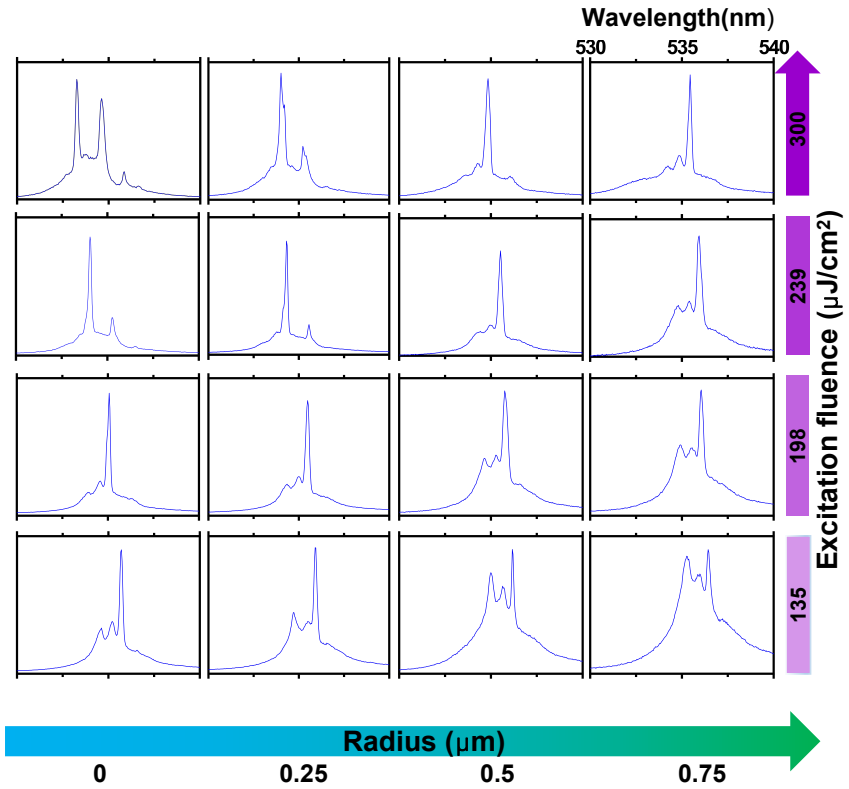

Figure 4.13: PL spectra taken at different radial distance away from the mapping centre of the same cluster as in figure 4.12 under the same set of pumping power.

Exploiting the mode tuning effect with pumping power provides a degree of control over the optical modes. The excitation fluence can hence work as a knob to be continuously adjusted for choosing a desirable modal frequency. This is clear from the 2D counter plot of figure 4.14(b) to demonstrate different sets of modes being switched on along the tuning procedure. The plot a in this figure presents a spectrum slice along an excitation intensity of $582\,\mu\mathrm{Jcm}^{-2}$. Clearly the dominant emission lines at this high pumping fluence are around 539 nm and bluer emissions will start to take over at even greater excitation strength. It is noteworthy that the line width at this pumping power does not appear to broaden at all and all of the lines are around 0.1 nm wide, which is almost the resolution limit of our spectrometer. An opposite argument can go from the direction that the line is broadening but it has just grown from a even narrower original width. This argument can not be directly rejected with evidence due to the limitation of our equipment, however, here it is also saying that our quality factor can be much greater than the calculated value and the lasing performance is of outstanding standard. In either case, the behaviour addresses a

superior property in one aspect.

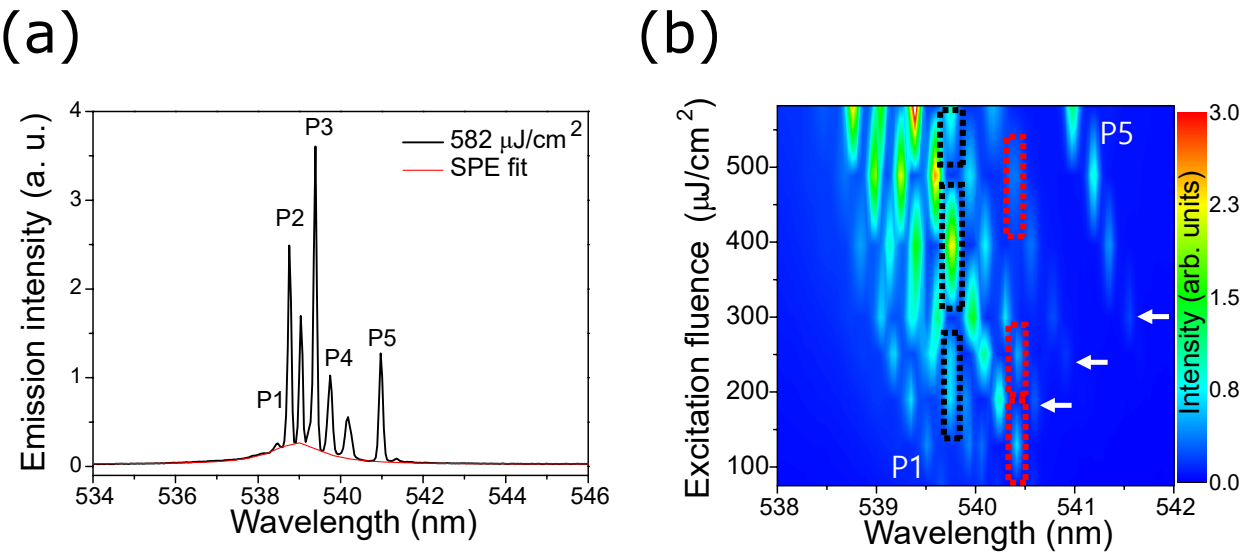

Figure 4.14: (a) Single PL spectrum with a relatively high pumping strength of $\sim 582\,\mu\mathrm{Jcm}^{-2}$ demonstrates the existence of the sharp SE modes over the SPE background fitted to centre at 539 nm. The SE modes are designated with marks P1 to P5. (b) Power-dependent PL 2D counter map presented for the same QD cluster giving the emission spectrum in plot (a). The dashed boxes serve as indicators showing that the SE modes are sitting at fixed wavelengths. As pumping power is increased, new modes are turned on and they are highlighted with white arrows. A correspondence to the mode peaks presented in figure (a) can be followed by using the markers P1 and P5.

On the other hand, the consideration of line width broadening also brings up another concern about the thermalisation induced by the strong pumping intensity. And its potential effect to the blueshift can be lifted with the following discussion. For the pump fluence range shown in figure 4.14(b), the corresponding temperature rise can reach a maximum value of around 1 K given the structure parameters of our cluster. On the other hand, a wavelength shift of 1nm requires an increase in temperature by 10 K as can be directly read out from figure 4.15(b). This is a valid reference since there is only one single mode in this temperature-dependent measurement. A conclusion is then drawn to rule out the cause of the emission blueshift to be thermally induced phase transition. Moreover, this excitation intensity driven blueshift has been spotted in other research works and it is suggested that band filling effect of hot carriers is a possible source for this phenomenon[140][141]. The hot carriers straight after excitation occupy excessive thermal energy through scattering with other carriers and optical phonons. They then gradually cool down but slowly due to their

higher thermal energy compared to that of the crystal lattice, and hence scattering with phonons persists for a while with some residue thermalisation effect. The higher-energy carriers also witness a larger recombination cross section accounting for their active status. This leads to a significant amount of photon emission coming from the blue end of the spectrum where a Boltzmann distribution of the hot carriers is recognised. In addition, increasing pumping strength also facilitates carriers to fill in higher-energy states over the band gap and hence provides a further boost to the blueshift. In contrast, a countering redshift can also be possible. The existence of concentrated carriers can accelerate recombination at a large scale and the higher energy states will be immediately depleted. However, this phenomenon is not prominent in our sample but has been reported by other material systems[141].

4.3.6 Mode Tuning with Temperature

Temperature provides another degree of control to the emission wavelength for the lasing signal. Accompanied by the characteristic blueshift of the perovskite PL emission, a continuous tuneability of the laser emission towards shorter wavelength end is achieved by increasing temperature. This is best illustrated in figure 4.15(a). Being differentiated to the power control, this tuning process does not switch the operation of the laser between various TEM mode. Instead, it relies on the geometric change of the cavity with thermally introduced expansion and the dependence of refractive index on temperature. The detailed relationship requires more sophisticated investigation and lies beyond the scope of this thesis. However, a better intuition into the numerical aspect can assist optimising the fabrication process for obtaining better controllability. As shown in figure 4.15(b) the FWHM has not been observed to broaden at all for the entire temperature range until the lasing disappears at 100 K. The same reasoning as in the pumping control discussion also applies here and it implies that the coherent nature of the emission is not degraded at least up to the capability of our equipment. On the other hand, the intensity of the emission does drop significantly towards 100K and thus the optimal operation temperature is limited within the cryogenic domain.

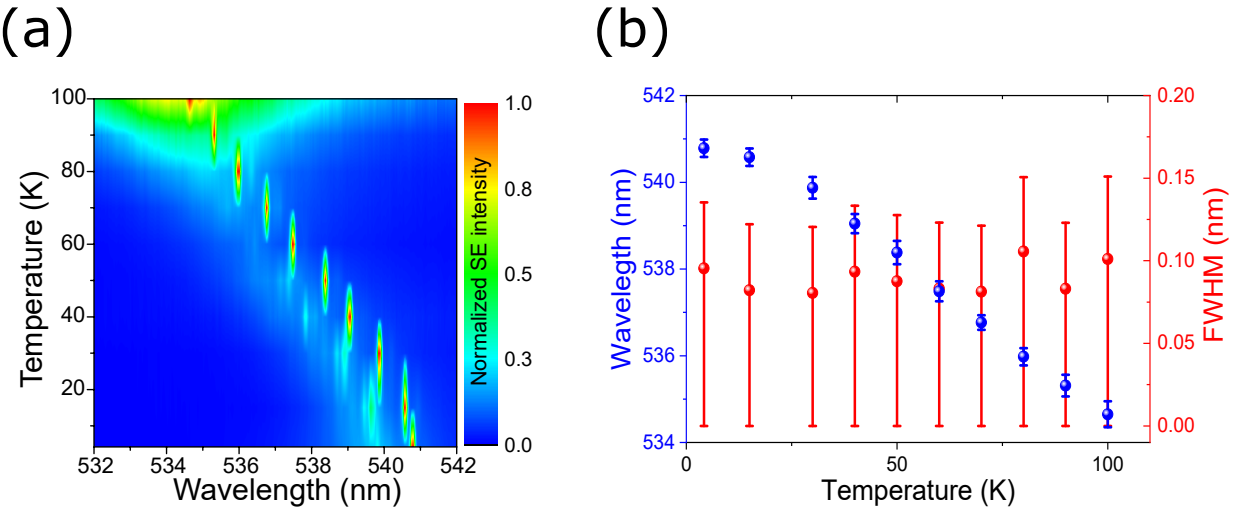

Figure 4.15: (a) Temperature-dependent PL 2D counter map tracing the shift of a single SE mode in a QD cluster. The mode submerges into the SPE background after heating above 100 K. (b) Plots of peak wavelength and FWHM change with temperature for the mode shown in plot (a). The FWHM doesn't demonstrate an obvious pattern of tendency by increasing temperature but rather remained almost fixed within noise level. The errors associated with the peak wavelengths (blue) were obtained through multiple fitting attempts to the PL profiles and by retrieving the standard deviation of the peak position on each trial. As for the errors on FWHM (red), not only the fitting errors are considered but the resolution limit of the spectrometer itself leaves the lower bound of the error bar undetermined.

4.4 Coherence

4.4.1 Michelson Interferometer

Consider a perfectly sinusoidal wave $A\sin(kx-\omega t+\phi)$, it is obvious to see that information is not lost when inspecting at any two temporal points of the wave, no matter how far apart they are. This can be put in another way such that the full wave under study is perfectly predictable if the phase and amplitude are both known at any given spatial-time slice of the wave. Such complete integrity of knowledge of the underlying wave assigns it the property of being perfectly coherent. In real scenarios, however, the waves we observe are normally a cascade of sine waves undergoing distortions to both amplitude and phase. As a consequence, the accumulated effect of noise can be significant enough at large time separation and observations taken can be utterly uncorrelated. Clearly, a measure to the preservation of information is useful and it is conducted through the first-order time correlation of the

wave. The underlying property to be measured, coherence, is the core element to many quantum optical applications and laser design.

In order to verify that our lasing signal preserves coherence, I set up a Michelson interferometer as shown in figure 4.16. Within the setup, the input signal is divided evenly through a 50:50 BS to give two streams of identical waves, propagating towards two adjustable end mirrors. Relative change in the mirror position causes one path to be longer than the other and the corresponding spatial difference is translated into a time delay between the returned beams. They then rejoin at BS to merge into a single output, which is considered to be a superposition of the two beams. If the waves still have some degree of correlation, meaning the original wave is still coherent within the time window, interference patterns can be formed while slightly changing the displacement of one mirror for the intensity extreme of the two to coincide. Keep increasing the relative difference in the path length, at some point no more interference patterns can be seen on the detection plane and the two beams become uncorrelated. The resulting distance travelled between maximum contrast of the interference fringes to the point of diminishing fringes can be converted into a time delay using the speed of light in air and the the corresponding value is a measure of coherence time.

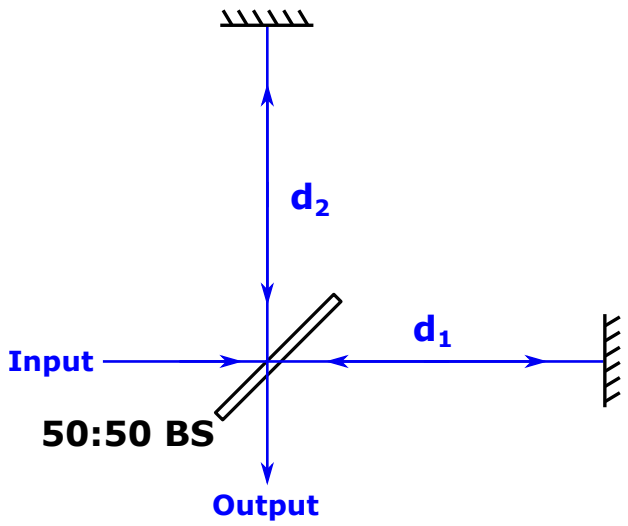

Figure 4.16: Schematics of a Michelson interferometer. The BS divides the incoming signal into two two optical paths. The d_1 and d_2 specify the lengths associated with the two beams each to be reflected by an end mirror. The separate beams rejoin at the BS to become the output signal for studying of the interference patterns.

Inset of figure 4.17(d) presents an image of near zero-point interference pattern for the TEM mode lasing generated by our $CsPbBr_3$ nanocrystal. The first order correlation for SPE and SE signals are plotted via the fringe contrast, using 'Michelson visibility'[142] $\frac{I_{max}-I_{min}}{I_{max}+I_{min}}$ at each measured time delay. Both observations are fitted using Gaussian decays and the extracted SE coherence time of 9.5 ps shows more than two orders improvement from that of the background SPE emission, 41 fs. This coherent lasing emission also corresponds to a spectrally narrow line width of 105 GHz.

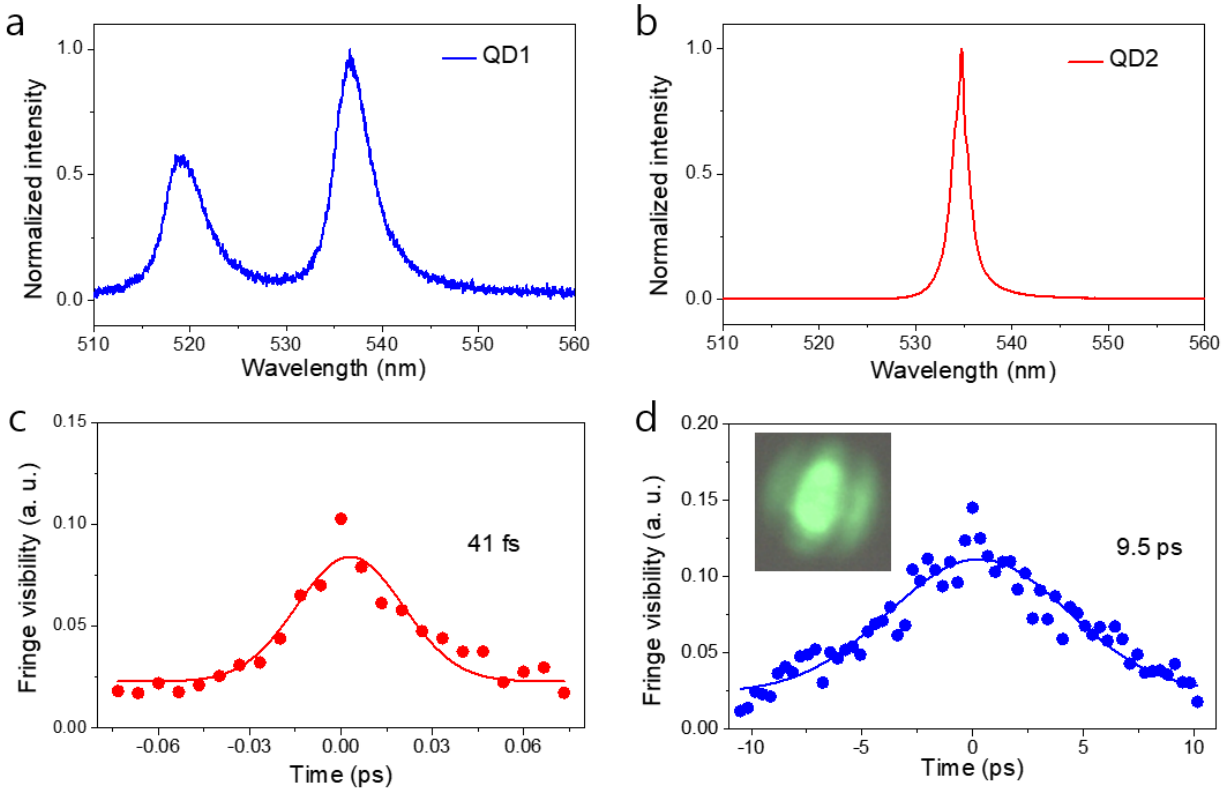

Figure 4.17: (a) PL spectrum taken from a QD cluster shows a longer-wavelength emission peak and a shorter-wavelength peak potentially attribute to the coupled and uncoupled emissions respectively from a collection of QDs. (b) Existence of only one single emission peak at longer wavelength demonstrates a fully coupled collective emission process. (c) and (d) present the fitted first-order time correlation functions for the SPE and SE signals respectively using a Michelson interferometer. Inset in plot (d) shows the interference fringes taken at almost equal separation between the two arms (near zero time delay). The data points are extracted from each interference image taken by a CMOS camera by computing the contrast as a differential in brightness between the intensity maximum and minimum along the fringe pattern. The calculated coherence time for SPE and SE are 41 fs and 9.5 ps respectively.

Since lasing in our sample can be described as a collective emission phenomenon from a group of QDs, it is important to distinguish between the different types of coupled many-

body stimulated emission. As shown in figure 4.18(a), the energy transition diagrams for two of the representative categories are illustrated via a three level system[143]. In both cases, the group of QDs are resonantly pumped to state III, where the induced microscopic dipoles are aligned with the pumping photons after population inversion. The two processes then seek different paths for radiative decay. Amplified spontaneous emission, being fundamentally different from all the rest, has a dephasing time T_2 much shorter than the radiative lifetime τ_R. In the microscopic image, this is saying that individual QDs quickly lose their order and break the overall dipole alignment before giving out light. They then emit photons independently into random directions. Clearly, the emission in this case is incoherent and it is essentially spontaneous emission scaled up by the many-body amplification process, hence the name. On the other hand, with superradiance, the excited QDs have the induced microscopic dipole moment held before dephasing. This eventually leads to the formation of a macroscopic dipole. The macroscopic dipole then emits light into a photon field created inside the lattice-like QD array and the field further interacts back with the dots. This closed feedback is similar to the strong coupling picture in optical cavity and hence similar characteristic properties can be observed here.

A variation to superradiance, superfluorescence, involves off-resonant pumping into an additional excited level at higher energy, level IV. As shown in figure 4.18, this state has a very short lifetime and the QDs immediately decay into state III without maintaining the dipole alignment. However, the microscopic dipoles can still interact in the neighbourhood and after some time τ_S the formation of macroscopic dipole is established. This brings the system back to a coherent state like superradiance and strong light-matter interaction is again manifested. However, a similar consideration of dephasing time is applied here, if the emitters are kept long in the excited state and catch the dephasing time, amplified spontaneous emission happens instead.

Given the incoherent nature of amplified spontaneous emission, the emission observed from the TEM modes clearly have a different coherent origin. This is proven by the significantly prolonged coherent time. However, since the QD array structure doesn't qualify for

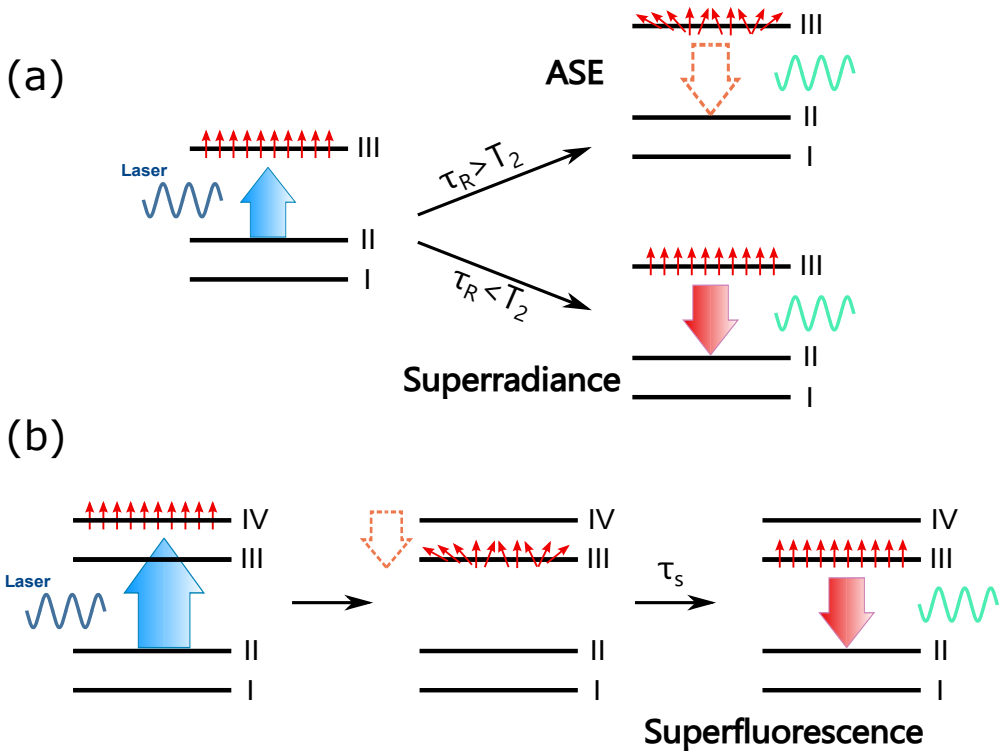

Figure 4.18: Schematics for the SE processes involved in coupled QD system. (a)A three level system initially pumped to level III by an excitation laser source. Depending on the relative length of the dephasing time T_2 and radiative lifetime τ_R, a coherence-preserving SR is observed for the shorter τ_R case while an ASE happens at shorter T_2. (b)A four level system of filled level IV states after population inversion. The system immediately decays to level III followed by a microscopic dipole-realignment time τ_S. The coherent macroscopic state then decays via SF process.

a superlattice, the collective emission hence does not satisfy the requirement of superfluorescence and the existing dipole coupling is weaker in a sub-superfluorescence regime. The self-assembly technique needs to undergo further optimisation such that the size of the QDs can be nearly identical and their associated distribution to become more regular. To this hope, Reino *et al.*[37] has demonstrated superfluorescence in the same nanocrystal system, which both shows the feasibility and the benchmark of achieving strong light-matter interaction with coherent cooperative emission. The potential of combining this into the great tuneability and controllability of lasing discussed in this chapter enables the generation of novel bright coherent laser source as an on-going research direction.

Chapter 5

Resonant probing of perovskite nanocrystal triplet states

Recent reports on triplet state emission in $CsPbBr_3$ nanocrystals have demonstrated them as very bright light sources due to their sub-nanosecond lifetime. The concept of triplet state is closely linked to the quantum physics description of the atomic structure. Since reaching a complete understanding of the corresponding topic requires reading the associated parts in a fragmented way from multiple textbooks, this chapter instead gives a concise and comprehensive picture of the underlying principles in a self-contained manner with some recap of the fundamental knowledge as a basis for carrying on further research in the associated field. We have also utilised the self-assembled micro-cavities to couple to the emission from those triplet states and drive them into coherent SE signals. The other important aspect of this project focuses on the response of the emission through near-resonant pumping of the bandgap. Interestingly, intensity improvement and enhancement of coherence have been demonstrated and reveals the potential of our nanocrystal system for finer optoelectronic applications.

5.1 Growth

Fabrication of the sample was done by professor Atanu Jana from Dongguk University. In order to produce $CsPbBr_3$ nanocrystals, careful treatment is required to obtain both a

Cs-oleate solution and a lead precursor. For preparation of the Cs-oleate, first 32.5 mg, 0.1 mmol Cs_2CO_3 is dissolved in a mixture of 2 ml 1-octadecene and 1 ml Oleic acid inside a glass container with a volume of 15 ml while being stirred. The formed solution is then heated at a temperature of 120 °C to dry for one hour such that Cs_2CO_3 has been used up through reaction with Oleic acid to form Cs-oleate. The other byproducts, water and CO_2, quickly bubble through the solution due to their insolvency at high temperature. Since the solution is likely to transform into solid state over time, to prevent this from happening it has been stored at even higher temperature of 150 °C. Now turning to the preparation of lead precursor, 2 ml 1-octadecene, 42 mg, 0.2 mmol octylammonium bromide, 73 mg, 0.2 mmol lead bromide and 1 ml dimethylformammide are mixed together while being exposed to air and heated to a temperature of 120 °C. The reason for using octylammonium bromide instead of octylamine is due to the potential dynamical equilibrium between the Oleic acid and octylamine effecting on the surface of our nanocrystals[39]. The other remark comes from the mismatch between the number of carbon atoms between the Oleic acid (18 carbon atoms) and octylammonium bromide (8 carbon atoms). In an classical approach, Oleylamin is used instead of the bromide salt for its 18 carbon atoms contained in the molecular structure. The two ligands are both associated with surface passivation of the nanocrystals, their similar structures hence result in a more homogeneous distribution of the cubic shaped products[37]. However, the mismatch of molecular chain lengths in our case generates an embedded system with $CsPbBr_3$ nanocrystals encapsulated inside Cs_4PbBr_6 micro-sized claddings. The mixed solution is the lead precursor, by quickly adding 3 ml of the Cs-oleate solution already prepared and cooling down to room temperature, a crude solution is obtained. It is then subject to centrifuging at 5000 round per minute for 5 minutes before removing the supernatant. Finally, the precipitate is dried at 60 °C to extract the ready-for-deposit form. Before an optical characterisation, this precipitate is dissolved in toluene and then spin-coated at 3000 revolutions per minute with PMMA onto a substrate to separate the microcrystals. Even with the same chemical composition these crystals are more vulnerable than those discussed in chapter 4 even with PMMA coating and they can only maintain their optical property up to a week by storing in vacuum. This may be related

to the lack of the hierarchical structure as a protection layer comparing to the encapsulated QDs demonstrated in chapter 4.

5.2 Triplet state

This section builds up the understanding of triplet state from the fundamental quantum physics concepts of angular momentum and magnetic moment in a fully connected and systematic fashion by a self-contained presentation. The discussion and derivation here have referred to the relevant textbooks [41][42][144] and the undergraduate lecture handouts in quantum mechanics and advanced quantum mechanics taught in the University of Oxford.

5.2.1 Angular momentum

The existence of the triplet state stems from the quantum mechanical concept of angular momentum. In order to have a comprehensive picture of the phenomenon, it is worth recapping some of the most important theoretical background associated with it.

Within the scope of atomic physics, an electron can be characterised with a series of quantum numbers n, l, m_l and s. While the first quantum number n, the principle quantum number, distinguishes the atomic orbitals according to the more significant difference in energy levels, the other three quantum numbers are associated with angular momentum and are thus more relevant to the content of this chapter. The quantum mechanical verification for an operator to be an angular momentum operator requires the commutation relation $[L_x, L_y] = i\hbar L_z$ and the other two obtained from cyclic permutations to be met in space coordinates of x,y,z. This requirement itself is derived by expressing the component angular momentum operator in terms of position and momentum operators $e.g. L_x = YP_z - ZP_y$ similar to the form in classical mechanics and using the commutator $[q, P_{q'}] = i\hbar\delta_{qq'}$ with q and q' being one of xyz. Clearly, the component angular momentum operators L_x, L_y, L_z do not commute with each other and hence they cannot be specified simultaneously. The

squared angular momentum operator L^2, however, commute with each component operators and hence the magnitude of angular momentum can be specified with any of the components in the coordinate directions. Therefore, L^2 and L_z, which represents the projection of angular momentum in a pre-defined z-direction, can be used to characterise a state of angular momentum. Figure 5.1 illustrates this procedure, where the magnitude and z-component of angular momentum are fixed while the xy-plane components are floating within the perimeter of the end circles of the cone.

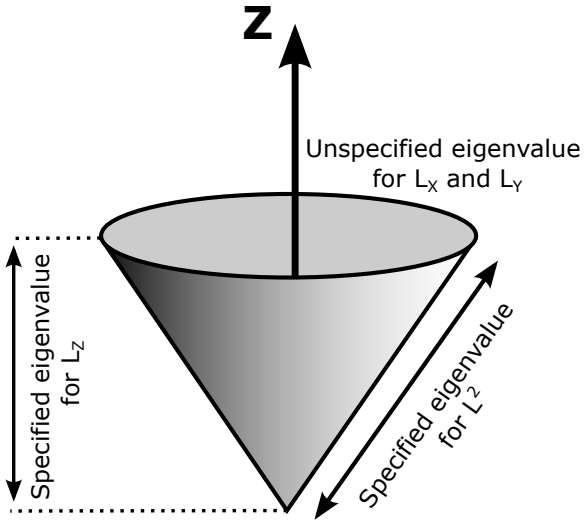

Figure 5.1: Representation of an angular momentum state by a cone. The eigenvalues of L^2 and L_z operators can be specified by the side length and height of the cone, however, the angular momenta in the x and y directions are undetermined at the same time and shown as any possible vector combination in the xy-plane around the perimeter of the circle.

In order to construct the full set of eigenstates of the angular momentum system, a pair of raising/lowering operators can be constructed from the component operators:

$$L_+ = L_x + iL_y \tag{5.1}$$

$$L_- = L_x - iL_y \tag{5.2}$$

It is then straightforward to find the following commutation relations:

$$[L_z, L_+] = \hbar L_+ \tag{5.3}$$

$$[L^2, L_+] = 0 \tag{5.4}$$

An eigenstate of the system can then be specified through the quantum numbers l and m_l. The two numbers are associated with operators L^2 and L_z respectively. To see the detailed correspondence, first consider the case of quantum number m_l and it is defined such that $L_z |l, m_l\rangle = m_l \hbar |l, m_l\rangle$. By using the commutation relationship (5.3) it is easy to see $L_z L_+ |l, m_l\rangle = (m_l+1) L_+ |l, m_l\rangle$, so the raising operator is used to shift a state up to another state of higher m_l value by 1. Similarly, the lowering operator reduces the m_l number by 1. Next, take the state at the top of the m_l ladder and since there is no other state with higher quantum number m_l, the following operation must be fulfilled: $L_- L_+ |l, l\rangle = 0$, where the quantum number l is defined as the maximum possible value of m_l. By decomposing the raising/lowering operators in terms of $L_{x,y,z}$ it is easy to see $L^2 |l, m_l\rangle = l(l+1)\hbar^2 |l, m_l\rangle$. A similar operation can be done by applying lowering operator to the state of the lowest m_l value, which is found out to be $-l$. As a result, the m_l number can only take values from $-l$ with integer steps up to l, and the set of states built correspondingly are all the eigenstates for the specific quantum number l. Here, l and m_l are called orbital angular momentum quantum number and magnetic orbital angular momentum quantum number respectively. They are bounded by the cyclic boundary conditions on the wave functions and hence only integer m_l is possible. There can also be s and m_s, the spin angular momentum quantum number and its magnetic associate. With the boundary condition lifted, the m_s number can take either integer or half-integer values. Lastly, a set of j and m_j can be constructed as total angular momentum from a combination of either orbital angular momentum or spin angular momentum. This last set of quantities will be quoted in the following sections.

5.2.2 Magnetic moment of electron

In a classical picture, an electron moving with some velocity perpendicular to the direction of a uniform magnetic field will circulate in an orbital and hence gain an orbital angular momentum. It is, therefore, intuitive to capture the information on the magnetic strength associated

with such motion, the magnetic moment of an electron. Some background understanding on vector potential is necessary to arrive at this concept. Consider two configurations of vector potential **V** and **W** as in figure 5.2.

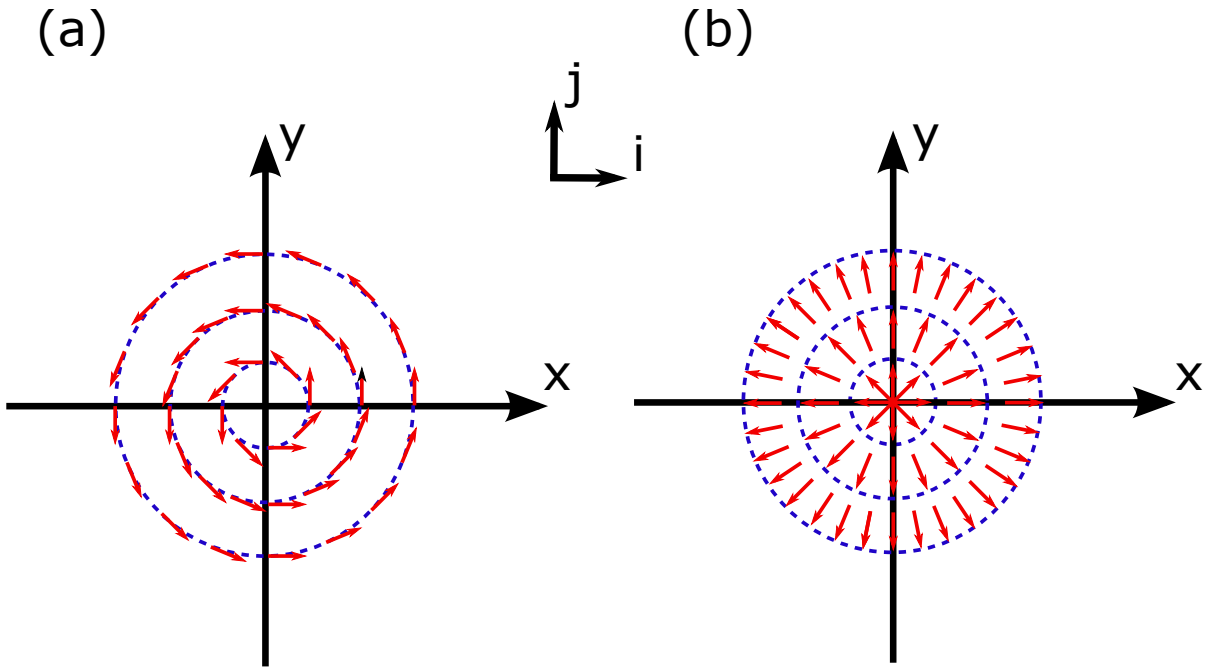

Figure 5.2: Schematics of spatial vector potential configurations **V** and **W**. The dashed counters are perimeters of equal amplitudes and the red arrows indicate the spatial profiles of vector potential. (a)vector potential **V** of zero divergence and non-zero curl. (b)vector potential **W** of none-zero divergence and zero curl.

With **i**,**j**,**k** being unit vectors pointing in the directions of x, y, z correspondingly, the vector calculus gives the following properties:

$$\nabla \cdot \mathbf{V} = 0; \nabla \times \mathbf{V} = 2\mathbf{k} \tag{5.5}$$

$$\nabla \cdot \mathbf{W} = 2; \nabla \times \mathbf{W} = 0 \tag{5.6}$$

A magnetic field strength **B** can be defined from a vector potential **A** as:

$$\mathbf{B} = \nabla \times \mathbf{A} \tag{5.7}$$

Clearly, equation (5.5) implies that a vector potential $\mathbf{A} = \frac{1}{2}\mathscr{B}\mathbf{V}$ generates a uniform magnetic field. Inspecting the relative directions of $\mathbf{r}, \mathbf{B}$ and $\mathbf{A}$ while taking into account the orthogonality of the vectors in a curl operation indicates that the vector potential can be written as $\mathbf{A} = \frac{1}{2}\mathbf{B} \times \mathbf{r}$. The orientations of different components are best illustrated through figure 5.3.

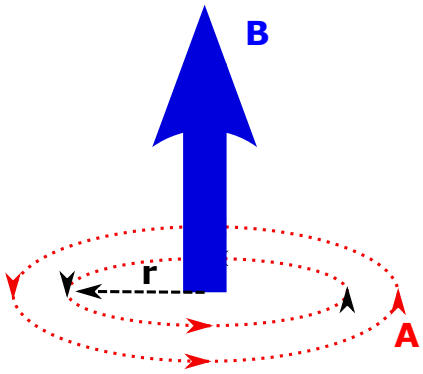

Figure 5.3: The relative directions for the vector potential $\mathbf{A}$, magnetic field strength $\mathbf{B}$ and $\mathbf{r}$. Their mutual orthogonality gives the curl relationship.

Given the above expression for a uniform magnetic field, which is at least a valid approximation locally, an extra term in the form of ∇f, with f being a scalar function, can be added to the vector potential $\mathbf{A}$ without affecting the uniformity of the field. This is the result of the property $\nabla \times (\nabla f) = 0$ in vector calculus. One possible such term can be $\frac{1}{2}\nabla(x^2 + y^2)$, which is essentially $\mathbf{W}$ introduced above. So the magnetic field strength can be written as:

$$\mathbf{B} = \nabla \times (\mathbf{A} + \lambda \nabla f) \tag{5.8}$$

where λ is a constant. In the above example, the divergence of the magnetic field arising from $\mathbf{V}$ is naturally zero. However, a more general vector potential may have a finite divergence. The use of the extra term, which is called a gauge redundancy, can be used to perform a gauge transformation to pull the divergence of the modified vector potential to zero. The associated gauge in this case is the Coulomb gauge.

Now consider the modification to the kinetic term in the electron Hamiltonian under a

uniform magnetic field:

$$(\mathbf{P} + e\mathbf{A})^2 = \mathbf{P}^2 + 2e\mathbf{P} \cdot \mathbf{A} + e^2\mathbf{A}^2 \tag{5.9}$$

where the commutation relationship $[\mathbf{P}, \mathbf{A}]\Psi{=}0$ has been used. The validity of the commutator comes from the zero divergence characteristic of Coulomb gauge. Equipped with this, the overall Hamiltonian can be written as:

$$H = \frac{\mathbf{P}^2}{2m_e} + \text{potential} + \frac{e}{m_e}\mathbf{A} \cdot \mathbf{P} + e^2\mathbf{A}^2 \tag{5.10}$$

Focus on the term with first order in $\mathbf{A}$ and the component Hamiltonian can be written as:

$$H_1 = \frac{e}{2m_e}\mathbf{B} \times \mathbf{r} \cdot \mathbf{P} = \frac{e}{2m_e}\mathbf{B} \cdot \mathbf{r} \times \mathbf{P} = \frac{e}{2m_e}\mathbf{B} \cdot \mathbf{L} \tag{5.11}$$

where $\mathbf{A} = \frac{1}{2}\mathbf{B}{\times}\mathbf{r}$ is used in the first step and the vector calculus property $\mathbf{a}{\times}\mathbf{b}{\cdot}\mathbf{c} = \mathbf{a}{\cdot}\mathbf{b}{\times}\mathbf{c}$ in the second step. The expression can be restated as $H_1 = -\mathbf{B}{\cdot}\mathbf{m}$ with the magnetic moment defined as $\mathbf{m} = \gamma_e\mathbf{L}$. Here the factor $\gamma_e = -\frac{e}{2m_e}$ is the magnetogyric ratio.

The above discussion is on the magnetic moment associated with orbital angular momentum. For spin angular momentum, Dirac equation is required to be solved where matrix in terms of Pauli matrices and relativistic space-time presentation are incorporated. The detailed derivation is out of the scope of this thesis and the result is stated here in a similar form to that from orbital angular momentum:

$$\mathbf{m} = g_e\gamma_e\mathbf{S},$$

where $\mathbf{S}$ is in analogy to $\mathbf{L}$ for orbital angular momentum. The factor g_e here is of particular interest, it is the g-factor of electron and its value of 2.002319304 is determined through quantum electrodynamics, which is a study under the aspect of quantum field theory.

5.2.3 Spin-Orbit Coupling

Now consider an electron moving in an electric field $\mathbf{E}$ with velocity v, there is an induced magnetic field:

$$\mathbf{B} = \frac{\mathbf{E} \times \mathbf{v}}{c^2} = -\frac{1}{rc^2}\frac{d\phi}{dr}\mathbf{r} \times \mathbf{v} = -\frac{1}{m_e rc^2}\frac{d\phi}{dr}\mathbf{L} \tag{5.12}$$

where the electric field is expressed in terms of isotropic electric potential ϕ and clearly the magnetic field is linked to the orbital angular momentum of the electron. Then from the discussion above on the Hamiltonian under magnetic modification, the interaction energy is quoted again here in the same form as:

$$H_{\text{so}} = -\mathbf{B} \cdot \mathbf{m} = \frac{1}{m_e rc^2}\frac{d\phi}{dr}\mathbf{L} \cdot \mathbf{m} = -\frac{e}{m_e^2 rc^2}\frac{d\phi}{dr}\mathbf{L} \cdot \mathbf{S} \tag{5.13}$$

However, the magnetic moment here is associated with the spin angular momentum of the electron, which is describing a magnetic dipole under the effect of a magnetic field. This magnetic field is linked to orbital angular momentum as shown above and hence the interaction is essentially between the spin and orbital angular momenta. The calculation up to now is from a classical point of view and the correct form of the interaction Hamiltonian requires relativistic remedy, Thomas precession[145], which multiplies the result by $\frac{1}{2}$. The final Hamiltonian can be written in the form:

$$H_{\text{so}} = \xi(r)\mathbf{L} \cdot \mathbf{S} \tag{5.14}$$

where $\xi(r) = -\frac{e}{2m_e^2 rc^2}\frac{d\phi}{dr}$. It is also convenient to define a spin-orbit coupling constant $\zeta_{n,l}$ in terms of the expectation value of ξ:

$$hc\zeta_{n,l} = \hbar^2 \langle nlm_l | \, \xi(r) \, | nlm_l \rangle \tag{5.15}$$

Some insights are helpful for a more comprehensive understanding of this factor. First, because $\mathbf{L}\cdot\mathbf{S}$ is in the unit of $\hbar^2$ due to the definition of angular momentum, $hc\zeta_{n,l}$ is thus the expectation value of an energy term. As a result, the spin-orbit coupling constant is a propagation constant/wave number. Second, since the electric potential is isotropic, the orientation of $\mathbf{L}$ is symmetric under spatial rotations. Therefore, the value of ζ is independent of m_l.

Now, take the example of an electron in a hydrogen atom. The electric potential of a hydrogen atom being $\phi = \frac{Ze}{4\pi\epsilon_0 r}$ gives $\xi(r) = \frac{Ze^2}{8\pi\epsilon_0 m_e^2 r^3 c^2}$. The spin-orbit coupling constant is then calculated in terms of the associate Laguerre function:

$$\zeta_{n,l} = \frac{1}{hc}\hbar^2\frac{Ze^2}{8\pi\epsilon_0 m_e^2 c^2}\left\langle nlm_l\right|\frac{1}{r^3}\left|nlm_l\right\rangle = \frac{1}{hc}\hbar^2\frac{Ze^2}{8\pi\epsilon_0 m_e^2 c^2}\frac{Z^3}{n^3 a_0^3 l(l+\frac{1}{2})(l+1)} = \frac{\alpha^2 R Z^4}{n^3 l(l+\frac{1}{2})(l+1)} \tag{5.16}$$

In the above computation, a few quantum mechanical constants have been used. These include: Rydberg constant $R = \frac{m_e e^4}{8\epsilon_0^2 h^3 c}$, Bohr radius $a_0 = \frac{4\pi\epsilon_0\hbar^2}{m_e e^2}$ and fine-structure constant $\alpha = \frac{e^2}{4\pi\epsilon_0\hbar c}$.

5.2.4 Composite angular momentum

Since spin-orbit coupling involves the interaction of two sources of angular momenta, it is now appropriate to extend the discussion into a system of composite angular momentum. For illustration purpose, we denote $J_{1q}, J_{2q'}$ for the angular momenta corresponding to the individual sources and J for total angular momentum. Decomposing J_q into J_{1q} and J_{2q}, it is straightforward to show that $[J_x, J_y] = i\hbar J_z$, which formally confirms the identity of J being angular momentum. Similarly, J^2 commutes with J_1^2 and J_2^2 as the former is the sum of the later two while the individual squared angular momentum can be written in terms of their xyz components and commute with any one of them. The direct result of this indicates that j, j_1, j_2 can all be specified simultaneously while m_j can also be specified. Investigating

further into the commutation relation between the squared total angular momentum J^2 and the z-component of individual angular momentum, we will find:

$$[J_{1z}, J^2] = 2i\hbar(J_{1y}J_{2x} - J_{1x}J_{2y}) \tag{5.17}$$

Clearly, they do not commute and hence j and m_{j1}, m_{j2} cannot be simultaneously specified. There are now two different schemes, specifying m_{j1}, m_{j2} and working in an uncoupled scheme of state $|j_1, m_{j1}; j_2, m_{j2}\rangle$ or in a coupled scheme of state $|j_1, j_2, j, m_j\rangle$ with specified j.

A remark arises from the number of states existing for a specific j number. It is easy to see that for $j = j_1 + j_2$ there will be $2(j_1 + j_2) + 1$ states. However, the full composite system contains $(2j_1 + 1)(2j_2 + 1)$ states for specified j_1, j_2. Therefore, a series of j numbers $(j_1 + j_2, j_1 + j_2 - 1, j_1 + j_2 - 2, ..., |\ j_1 - j_2\ |)$ with their associated m_j ladders designate the states necessary to complete the system. The series is called Clebsch Gordon series. Looking into m_j, the existence of the Clebsch Gordon series also means there are 1,2,3... states corresponding to the m_j value of $j_1+j_2, j_1+j_2-1, j_1+j_2-2$... respectively. Following this knowledge, a coupled state of specified m_j can be created out of the uncoupled states as a superposition where:

$$|j_1, j_2, j, m_j\rangle = \sum_{m_{j1}, m_{j2}} C(m_{j1}, m_{j2})\, |j_1, m_{j1}; j_2, m_{j2}\rangle \tag{5.18}$$

with the coefficient C the Clebsch Gordon coefficient.

Before moving forward, a review on the raising/lowering operator is helpful here. In the discussion earlier, only their functionality has been introduced but not the explicit expression for their matrix element. Consider a state with a single source of angular momentum: $J_+ |j, m_j\rangle = a_+(j, m_j)\hbar\, |j, m_j + 1\rangle$ and $J_- |j, m_j\rangle = a_-\hbar(j, m_j)\, \langle j, m_j - 1|$. Comparing the results of expressing $J_-J_+ |j, m_j\rangle$ in terms of the matrix elements to those expressed in the form of J, J_z as discussed in the section 'angular momentum' it is clear to see:

$$a_-(j, m_j + 1)a_+(j, m_j) = j(j + 1) - m_j(m_j + 1) \tag{5.19}$$

Realising the conjugation relation $\langle j, m_j| J_- |j, m_j + 1\rangle = \langle j, m_j + 1| J_+ |j, m_j\rangle^*$, the individual matrix element for the raising operation can be extracted to be $a_+(j, m_j) = (j(j + 1) - m_j(m_j + 1))^{\frac{1}{2}}$ with that for the lowering operation obtained in the same procedure.

5.2.5 Coupled spin of two particles

Now we can look into the composite spin angular momentum of two spin-$\frac{1}{2}$ particles, where the magnetic spin quantum number of each particle can be $\pm\frac{1}{2}$. The resulting coupled states include a triplet state of total $s = 1$ and a singlet state of total $s = 0$. For the triplet state, we have three configurations of the coupled state where the two sources of spin angular momenta are nearly parallel. With the same way of state representation as in a coupled scheme, $|s_1, s_2, s, m_s\rangle$, it is most straightforward to write down the state of the highest m_s:

$$|\frac{1}{2}, \frac{1}{2}, 1, 1\rangle = |\frac{1}{2}, \frac{1}{2}; \frac{1}{2}, \frac{1}{2}\rangle \tag{5.20}$$

where the r.h.s. is in terms of the uncoupled state $|s_1, m_{s1}; s_2, m_{s2}\rangle$. Then by operating on the state with a total spin lowering operator:

$$S_- |s_1, s_2, s, m_s\rangle = (s(s + 1) - m_s(m_s - 1))^{\frac{1}{2}}\hbar |s_1, s_2, m_s - 1\rangle \tag{5.21}$$

This gives a state $S_- |\frac{1}{2}, \frac{1}{2}, 1, 1\rangle = \sqrt{2}\hbar |\frac{1}{2}, \frac{1}{2}, 1, 0\rangle$. On the other hand, expressing S_- in terms of individual spin lowering operator gives:

$$S_- |s_1, s_2, s, m_s\rangle = (S_{1-} + S_{2-}) |\frac{1}{2}, \frac{1}{2}; \frac{1}{2}, \frac{1}{2}\rangle = \hbar(|\frac{1}{2}, \frac{1}{2}; \frac{1}{2}, -\frac{1}{2}\rangle + |\frac{1}{2}, -\frac{1}{2}; \frac{1}{2}, \frac{1}{2}\rangle) \tag{5.22}$$

So the second triplet state has the form:

$$|\frac{1}{2},\frac{1}{2},1,0\rangle = \frac{1}{\sqrt{2}}(|\frac{1}{2},\frac{1}{2};\frac{1}{2},-\frac{1}{2}\rangle + |\frac{1}{2},-\frac{1}{2};\frac{1}{2},\frac{1}{2}\rangle) \tag{5.23}$$

The parallelism can be reflected from the in-phase superposition, which is obvious in this case. Repeating the procedure a third triplet state can be reached:

$$|\frac{1}{2},\frac{1}{2},1,-1\rangle = |\frac{1}{2},-\frac{1}{2};\frac{1}{2},-\frac{1}{2}\rangle \tag{5.24}$$

An illustration, figure 5.4, shows the three scenarios in spatial coordinates, where the angular momenta from the two sources are not strictly parallel but do form an acute angle of fixed relative geometric position. Although this does not link to the energy of individual particles, the parallelism does imply that the system status is more active at higher energy under stronger interaction.

The singlet state can be directly obtained from the second triplet state introduced above through the orthogonal nature of the states. It is expressed as:

$$|\frac{1}{2},\frac{1}{2},0,0\rangle = \frac{1}{\sqrt{2}}(|\frac{1}{2},\frac{1}{2};\frac{1}{2},-\frac{1}{2}\rangle - |\frac{1}{2},-\frac{1}{2};\frac{1}{2},\frac{1}{2}\rangle) \tag{5.25}$$

For a singlet, the individual spins are perfectly anti parallel and this again is associated to the out-of-phase form of the state.

5.2.6 Coupled spin-orbit

Return to the picture of spin-orbit coupling, again the particle of interest here has a spin of $\frac{1}{2}$. If the orientations of both spin and orbital angular momenta are parallel, the corresponding magnetic moments will also be parallel and hence they interact adversely leading to higher energy similar to the discussion above. Following the same logic, lower energy is obtained with states of anti-parallel spin-orbital angular momenta.

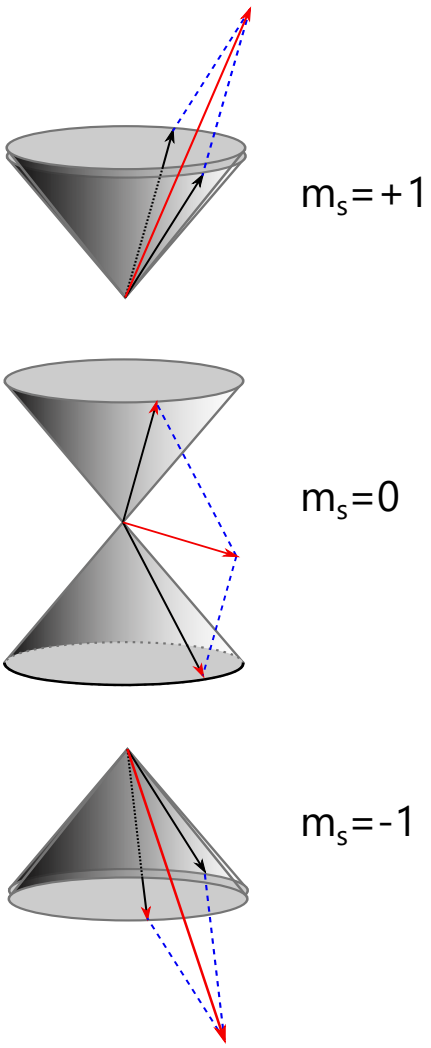

Figure 5.4: The triplet states of quantum number s=1 generated when compositing the spin angular momenta for two spin $-\frac{1}{2}$ particles. The relative angular separation between the two individual angular momenta is fixed in all three cases as an acute angle and it is determined as 70.53°. This is the value of arccos(1/3).

The spin-orbit interaction is naturally described in a coupled scheme of composite system. Consider interaction energy from first order perturbation with H_{so} introduced in the last section:

$$E_{\text{so}} = \langle l, s; j, m_j | \, H_{so} \, | l, s; j, m_j \rangle = \langle l, s; j, m_j | \, \epsilon(r) L \cdot S \, | l, s; j, m_j \rangle \tag{5.26}$$

Because $J = L + S$, the angular momentum operators acting on the state $|l, s; j, m_j\rangle$ can be simplified to be:

$$L \cdot S \left| l, s; j, m_j \right\rangle = \frac{1}{2}(J^2 - L^2 - S^2) \left| l, s; j, m_j \right\rangle = \frac{1}{2}\hbar^2(j(j+1) - l(l+1) - s(s+1)) \left| l, s; j, m_j \right\rangle \tag{5.27}$$

The interaction energy is thus expressed as:

$$\begin{aligned} E_{\text{so}} &= \frac{1}{2}\hbar^2(j(j+1) - l(l+1) - s(s+1)) \left\langle l, s; j, m_j \right| \epsilon(r) \left| l, s; j, m_j \right\rangle \\ &= \frac{1}{2}hc\zeta_{nl}(j(j+1) - l(l+1) - s(s+1)) = Z^4\alpha^2 hcR\frac{j(j+1) - l(l+1) - s(s+1)}{2n^3 l(l+\frac{1}{2})(l+1)} \end{aligned} \tag{5.28}$$

The spin-orbit coupling constant is substituted with the expression obtained in section 'spin-orbit coupling'. In the above computation, the factor $\epsilon(r)$ only depends on r and hence it's expected value is independent from any of the s, j, m_j numbers. Another remark is on interaction energy, absence of its dependence on magnetic quantum number m_j means that it is unaffected by the orientation of the total angular momentum in space. This implies that the spin-orbit induced degeneracy is only $2j + 1$. Now consider the spin $\frac{1}{2}$ particle with p-orbital angular momentum, the antiparallelism configuration of $l = 1, s = -\frac{1}{2}$ results in the lower lying 2-fold degeneracy of states. This example is of particular importance in the following section.

5.3 Triplet exciton in $CsPbBr_3$

Becker *et al.* has demonstrated a thorough study into the fundamental characteristics of bright triplet emission in $CsPbX_3$ nanostructures[128]. As introduced in the background chapter, the electronic properties of perovskite are dominated by the corner octahedrals, the PbX_6 group in this discussion. Under cubic lattice assumption, the bandgap occurs at the R point in the Brillouin zone. Since the emission at cryogenic temperature mainly originates from excitons, both hole and electron angular momenta need to be addressed at this point.

It is worth recalling here that both particles are subject to a spin number of $\frac{1}{2}$.

First consider the holes living in the valence band, the overall s-symmetry[146][147] of the mixture of Pb 6s and Br 4p orbitals means there can exist two Bloch states $|\uparrow\rangle_h = |l=0\rangle|\uparrow\rangle$ and $|\downarrow\rangle_h = |l=0\rangle|\downarrow\rangle$ for the spin-up state and spin-down state in a similar way of presentation to that in the paper. Then for the conduction band, the Pb 6p electrons match our earlier example on the coupled spin-orbit system in the last subsection and hence a 2-fold degeneracy for the lowest lying states apply here:

$$|\Uparrow\rangle_e = -\frac{1}{\sqrt{3}}((|X\rangle + i|Y\rangle)|\downarrow\rangle + |Z\rangle|\uparrow\rangle) \tag{5.29}$$

$$|\Downarrow\rangle_e = \frac{1}{\sqrt{3}}(-(|X\rangle - i|Y\rangle)|\uparrow\rangle + |Z\rangle|\downarrow\rangle) \tag{5.30}$$

where the spatial components for the Bloch state have been quoted in a consistent representation to the paper.

The two sets of states corresponding to the two spin $\frac{1}{2}$ particles now much resemble our earlier discussion on coupled spin of two particles in the last subsection. The same logic leads to a structure formed by a triplet state and a singlet state. The representation in the last subsection is duplicated here for the triplet state:

$$|\frac{1}{2},\frac{1}{2},1,1\rangle = |\Uparrow\rangle_e|\uparrow\rangle_h \tag{5.31}$$

$$|\frac{1}{2},\frac{1}{2},1,0\rangle = \frac{1}{\sqrt{2}}(|\Downarrow\rangle_e|\uparrow\rangle_h + |\Uparrow\rangle_e|\downarrow\rangle_h) \tag{5.32}$$

$$|\frac{1}{2},\frac{1}{2},1,-1\rangle = |\Downarrow\rangle_e|\downarrow\rangle_h \tag{5.33}$$

The probability for radiative recombination is found to be finite for the triplet state and zero for the singlet state and hence only the emissive triplet state in the $CsPbBr_3$ is of particular interest for optical applications[128][148].

5.3.1 Verification of triplet state emission

The final form of the triplet state requires Rashba effect to be considered, which is significant in the $CsPbBr_3$ systems[149][150][151][152]. The Rashba effect is associated with inversion symmetry breaking and results from the combined effects of strong spin-orbit coupling and asymmetric electric field[152][153][154]. The orthorhombic distortion and inhomogeneous electric field of the cubic shape are then taken into account and the final states are:

$$|\Psi_x\rangle = \frac{1}{\sqrt{2}}(|\Uparrow\rangle_e |\uparrow\rangle_h - |\Downarrow\rangle_e |\downarrow\rangle_h) \tag{5.34}$$

$$|\Psi_z\rangle = |\frac{1}{2}, \frac{1}{2}, 1, 0\rangle \tag{5.35}$$

$$|\Psi_y\rangle = \frac{1}{\sqrt{2}}(|\Uparrow\rangle_e |\uparrow\rangle_h + |\Downarrow\rangle_e |\downarrow\rangle_h) \tag{5.36}$$

The detailed calculation is not within the scope of this thesis and the three states are corresponding to the alignment of dipole to the three orthorhombic axes. However, with tetragonal symmetry, which describes the structure of our nanocrystal system, only 2-fold degenerate states $|\Psi_x\rangle$ and $|\Psi_y\rangle$ exist. Another remark here is to do with the relative energy between the singlet and triplet states. The triplet states after Rashba effect are now sitting at the band edge and hence give much faster emission than other crystal system with a lowest lying dark singlet state. This now brings up a full fine-structure splitting picture for a tetragonal phase $CsPbBr_3$ nanocrystal system, as shown in figure 5.5. Because the two-peak spectra obtained from our samples match the qualitative description of a triplet state, a thorough verification is necessary.

First, the relative position between the spectrum lines needs to be in a close match to the reported data. From figure 5.7, the energy separation between the two peaks can be found out to be 2meV. This value is consistent to the fine-structure splitting of the 2-fold triplet state found in tetragonal colloidal perovskite nanocrystals[155].

Then, since the dipole direction is of significant importance in distinguishing a triplet, the polarisation properties play a key role in the verification process. As long as the states are

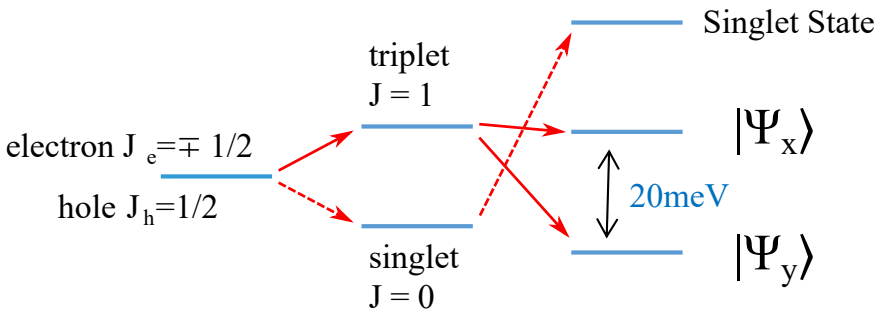

Figure 5.5: Excitonic energy fine structure

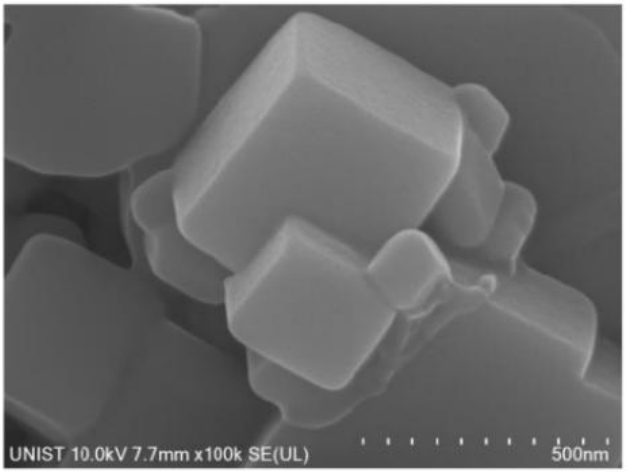

Figure 5.6: SEM of encapsulated CsPbBr3 nanocrystals.[Image supplied by Tristan Farrow from University of Oxford]

resolved in the spectrum, the linear polarisability resulting from the dipole emission and the orthogonality arising from the symmetry axes in the tetragonal phase should be observed. With this in mind, we have characterised the polarisation behaviour of the two emission lines. A linear polariser with extinction ratio at the level of 10^5 will provide sufficient discrimination between the two orthogonal polarisation directions. However, since the spectrometer grating has some intrinsic degree of polarisation, the linear polariser is fixed to give maximum coupling efficiency for the collected signal. A half-wave plate is then placed before the linear polariser for the optical axis of the emission to be adjusted so that only its component aligning with the polariser will be filtered through to pass into the detector. The result taken at 4 K is shown in figure 5.7 with a near-resonant excitation power of around 50 μW. The spectra spanning a full revolution of 120 ° for the polarisation angle of the emitted signal at a step of 20 ° are illustrated. It is evident that the emissions at 2.335 eV and 2.337 eV demonstrate

linear polarised light for both sites while their directions of polarisation are orthogonal. This is because the red peak gradually decreases from its maximum until near extinction while the blue peak emerges towards its upper extreme within the polarisation adjustment of the first 90 °. Such a pattern is also observed to reverse for the next 30 ° of rotation. The inset plot shows a comparison of the integrated intensity under the two peaks from a Gaussian fitting via a polar plot. Both sets of integrated intensities are normalised with respect to their own maximum value in order to provide a higher contrast in the relative polarisation directions for verifying the orthogonality nature. In addition, by using the relationship $\frac{I_{max}-I_{min}}{I_{max}-I_{min}}$ for measuring the degree of linear polarisability, the values are found to be almost 100% for the 2.337 eV peak and around 85% for the 2.335 eV peak, again revealing the quality of linear polarisation.

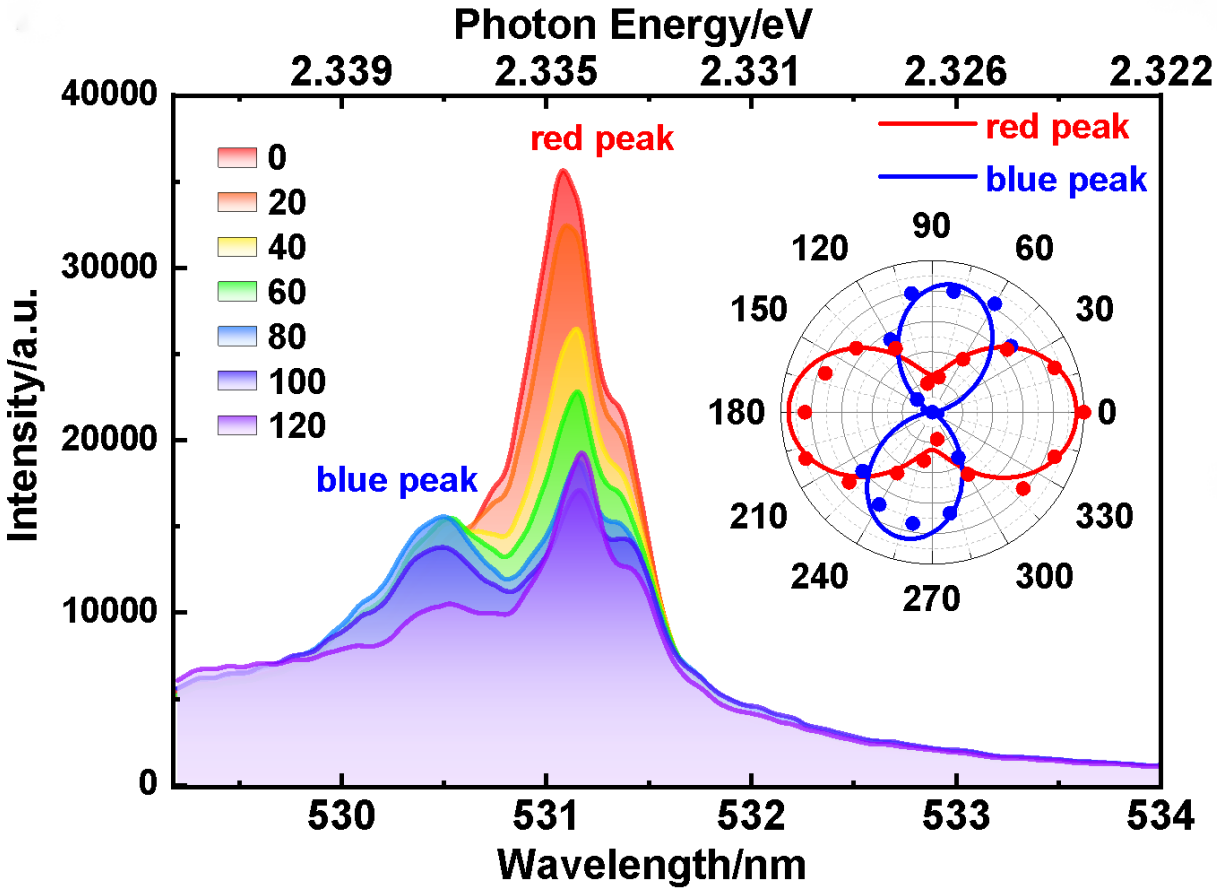

Figure 5.7: Polarisation dependent PL spectra of the PNC measured at 4 K with an excitation power of $\sim 50\,\mu$W near-resonant laser excitation. The inset depicts the polar angle diagram of the two emission peaks using a linear polariser in tandem with a half-wave plate to select a narrow polarisation angle of the emission spectrum and align it with the spectrometer gratings. Each peak's maximum intensity on the polar plot is self-normalised.

A comparison of the polarisability between the designated red peak and those of the other higher energy states have also been presented in figure 5.8(a) via a polar plot. Clearly, the emission from the other states shows very weak polarisability, which is almost negligible compared to that of the red peak. Further investigation into the difference of polarisability between on- and off-resonant (2.505 eV) pumping has been carried out for the red site, as in figure 5.8(c). Resonant pumping in general decreases the depolarisation effect. On the contrary, Stokes shift associated with above-resonance pumping shows a slight but observable distortion to the polarisability. This depolarisation effect comes from phonon scattering and broadening of the confinement potential of the dipoles along the orthogonal polarisation axes in the lattice. (Refer back to the three orthogonal axes mentioned above in triplet discussion where the oscillation now has components shared in the other two directions besides the main oscillating axis)

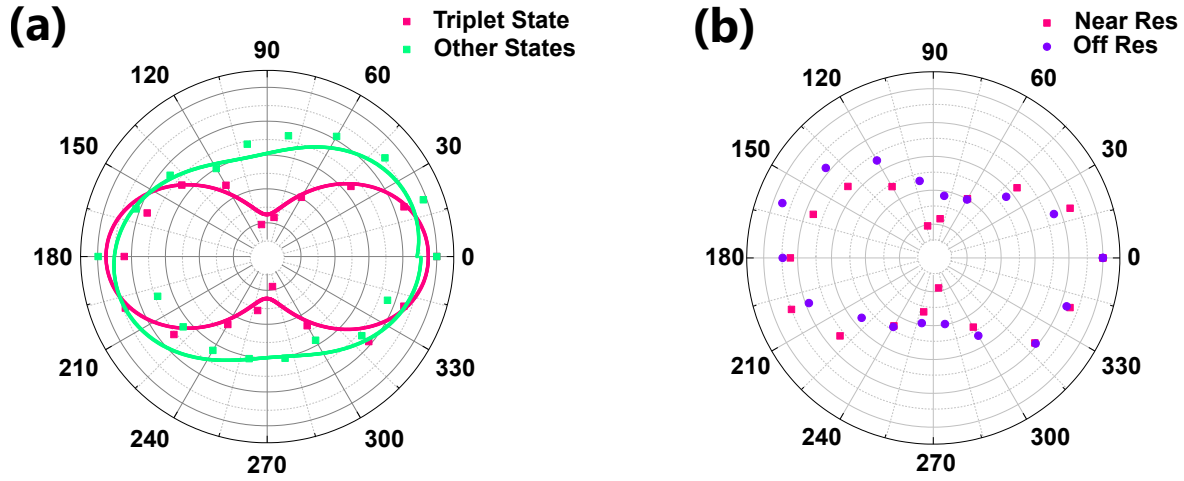

Figure 5.8: (a) A comparative study of the polarisation-dependence revealed that the triplet state emission is markedly more polarised than the background signal from other higher-energy states. (b) Polarisation-dependence of the on- and off- resonance polarisation signals generated with a 2.505 eV (495 nm wavelength) pump.

Finally, a TRPL measurement is conducted to extract the emission lifetime. The reason for this characterisation is that there have been established study on the size-lifetime correspondence[156], which is related to the Bohr radius of the system. Figure 5.9 reveals the exciton dynamics and shows a fast decay component of 49 ps (with fitting error of 0.4ps and equivalent uncertainty of 0.8%) owing to the lasing effect with also a slower component of 268 ps (with fitting error of 8ps and equivalent uncertainty of 3.0%) for radiative recom-

bination. The latter matches our expectation for weakly confined exciton of a size around 10 nm[35][128]. Referring to the Stokes shift of 18 meV from a later figure, reference to other research reports[157] has also confirmed the size to be of the same range. Therefore, we have reassured the nanocrystal dimension to be the one stated above.

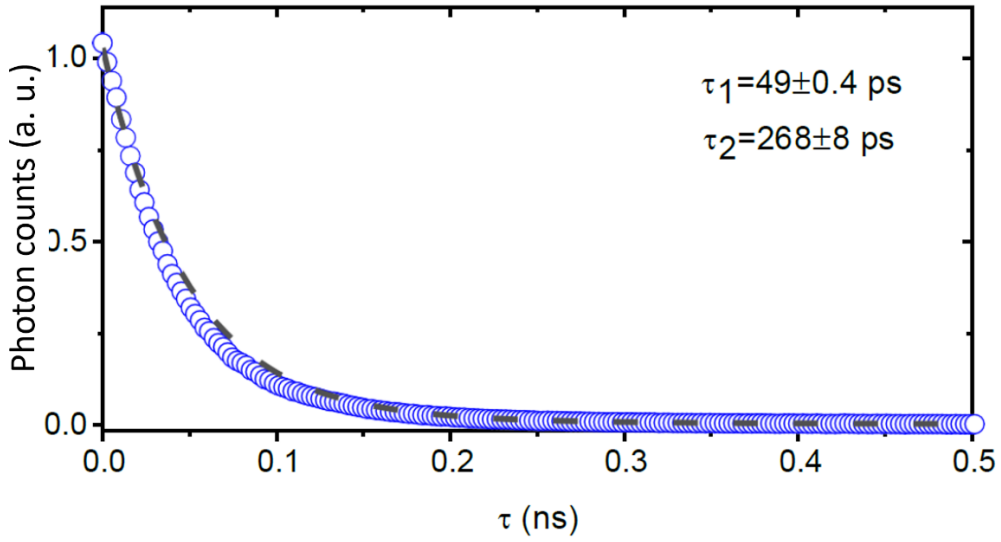

Figure 5.9: Time-resolved PL decay of $CsPbBr_3$ nanocrystal pumped quasi-resonantly.

In conclusion, the identity of the two emission lines have been proven to come from the triplet state with a rigorous verification process and reference to the paper by Becker *et al.*[128]. The stimulated emission from such source is hence interesting for bright nano-laser applications.

5.4 Resonant Pumping

With a supercontinuum white pulsed laser source, customisation is available for construction of an excitation signal not only capable of emitting photons with energy over the bandgap but can also be tuned to interact with the sample in a resonant fashion. The laser is from FIANIUM SuperK Extreme series produced by NKT Photonics and it has an operating frequency of 78 MHz with 10 ps pulse width. The wavelength selection and filtering procedure is achieved by directing the broadband source into a controllable transmission grating. The Fianium active filter is computer controllable and uses two transmission gratings working

in tandem in subtractive mode to produce a tuneable laser excitation. Figure 5.10 demonstrates a series of these spectra taken for the excitation signal after wavelength adjustment. After fitting with Gaussian profiles, an average FWHM is found to be 1.421 nm with a standard deviation of 0.013 nm. Although full information for an entire wavelength scan is not included, it does prove that the change in linewidth of the source signal is small and the excitation is indeed spectrally narrow. The filtered beam is coupled into a multi-mode fibre for beamshaping before being sent into the μPL system.

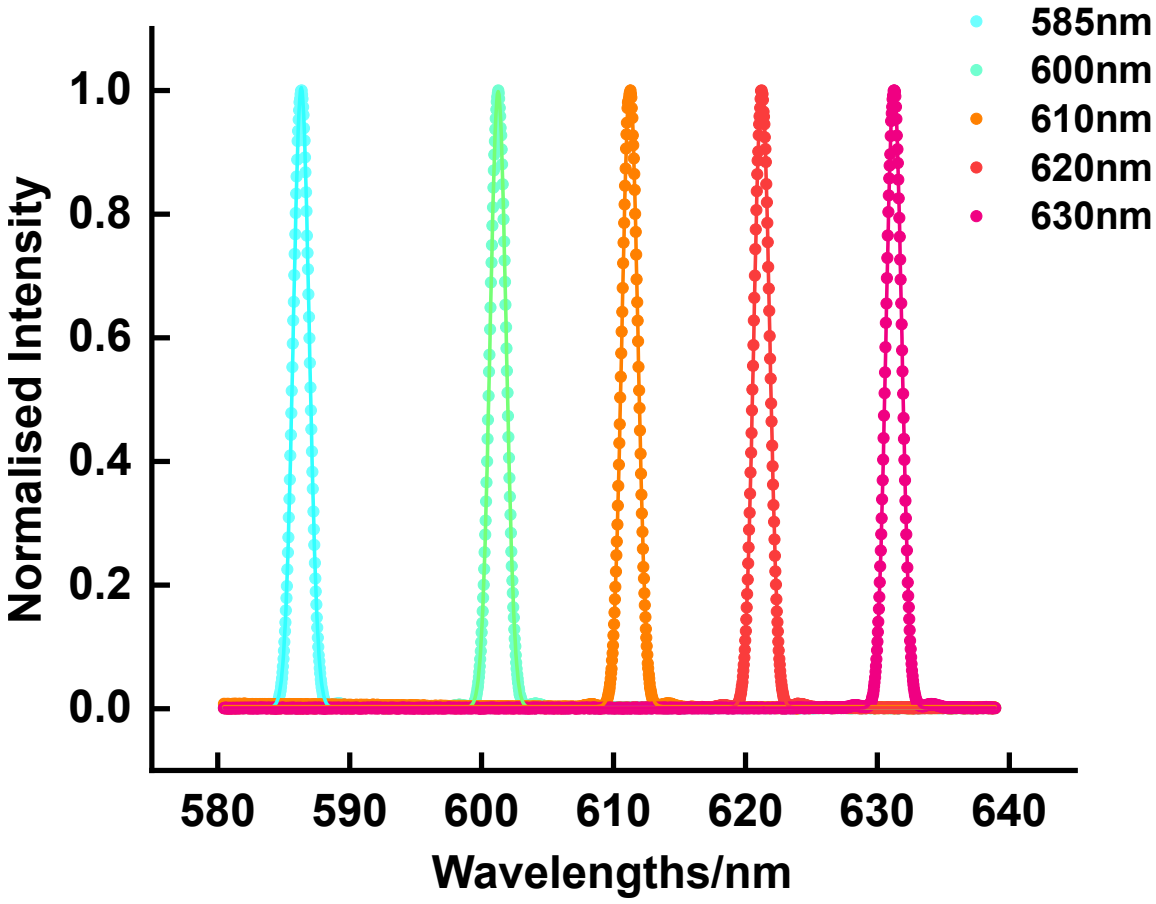

Figure 5.10: Normalised spectra taken by tuning the peak of the excitation source to wavelengths of 585 nm, 600 nm, 610 nm, 620 nm and 630 nm. Gaussian fits produce FWHM values of 1.430 nm, 1.439 nm, 1.419 nm, 1.414 nm, 1.402 nm respectively.

The continuous tuneability enabled us to gradually shift the excitation wavelength towards quasi-resonance with the higher energy split of the triplet state (detailed discussion and verification of the triplet splitting will follow in the next subsection) at 2.335 eV, 531 nm on the spectrum. The triplet state is pumped hard and fixed at 50 μW into SE regime and the intensity peaks at an excitation wavelength of 526.8nm as reflected by the wavelength

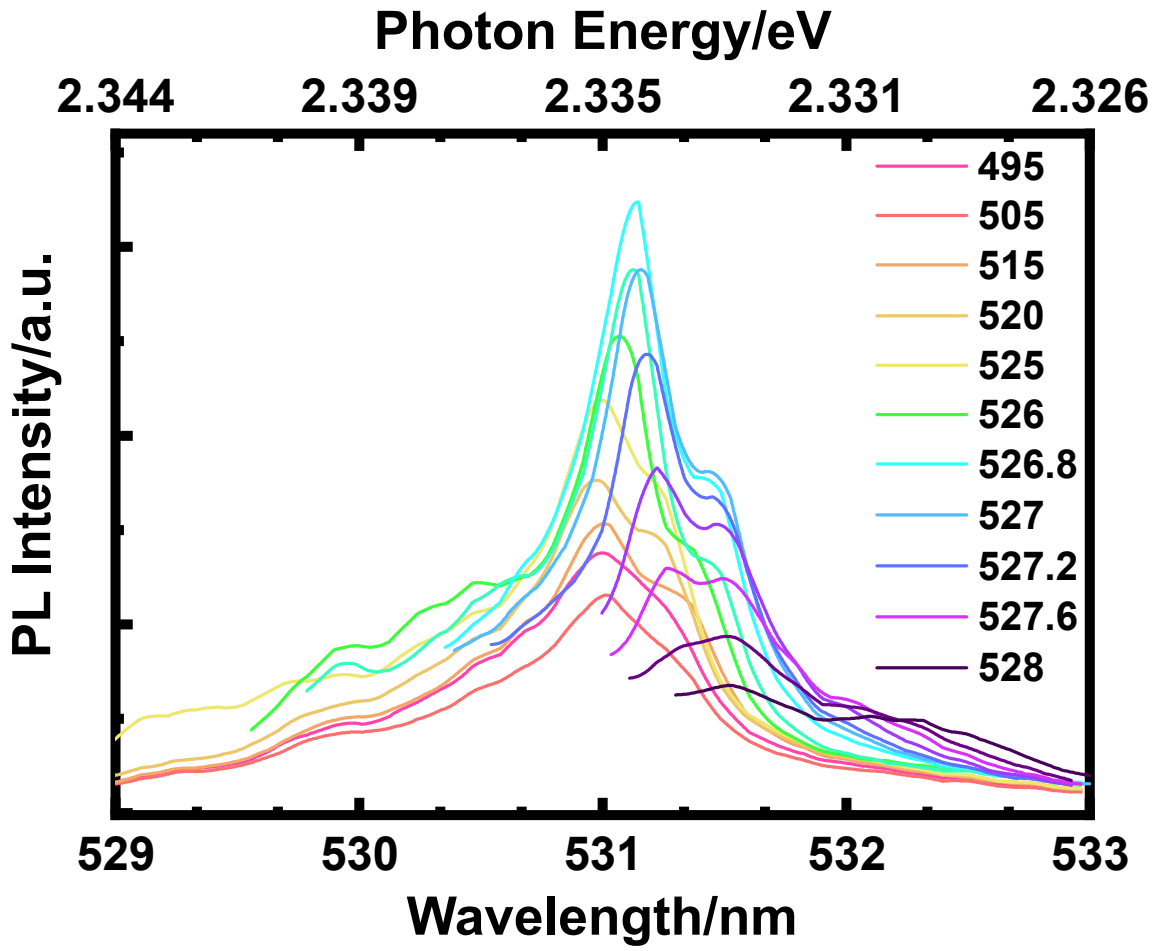

Figure 5.11: PL spectra of excitation wavelength scan using a super-continuum white laser in conjunction with an adjustable grating. The fluence can be controlled and the scan is only performed over a narrow wavelength range where the excitation intensity is kept constant.

sweep in figure 5.11 and also from the associated change in the integrated intensity from a Gaussian fit of the underlying line as shown by figure 5.12(a). In addition, a 1.1 μeV red shift of the SE peak is observed and plotted explicitly in figure 5.12(b) when pumped with longer-wavelength excitation beam. This is an expected result since near-resonant excitation will only pump carriers into lower lying energy states and hence the overall energy distribution will be tilted towards the red side when recombination takes place. The schematic in figure 5.13 compares the different carrier dynamics in off-resonant and near-resonant excitation regimes. When pumping with higher-energy photons, there exist multiple decay paths including trap-assisted decay into a mid-gap dark state and 2-step decay with phonon interaction. A significant proportion of the photons emitted are incoherent and add to the

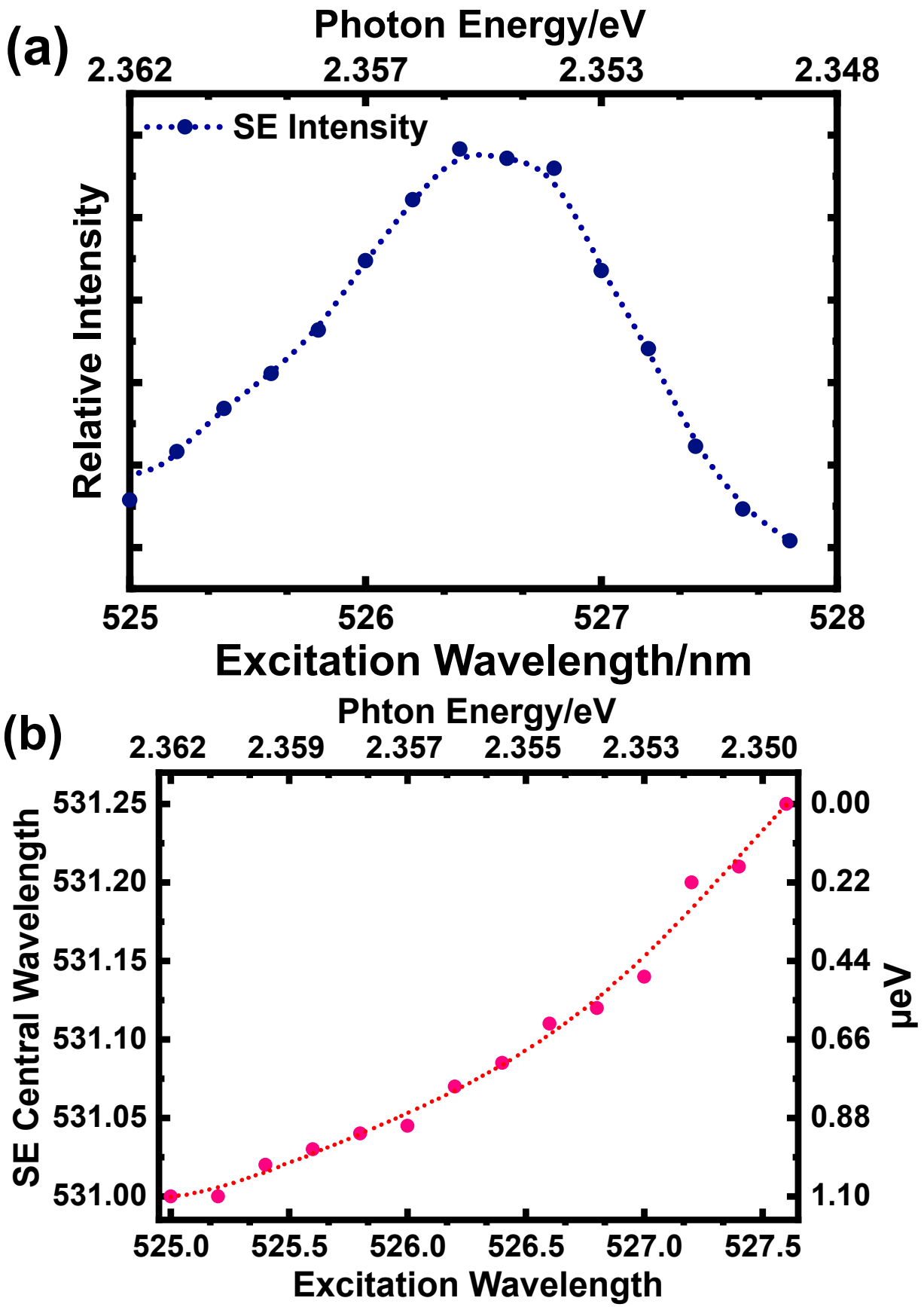

Figure 5.12: (a) Integrated SE intensity over the excitation wavelength.(b) Red shift of the SE peak after the excitation wavelength exceeds the resonant pumping wavelength.

spectrum via higher-energy states. On the other hand, near-resonant excitation increases the relative weighting of coherent emissions and hence a suppressed blue shoulder together with an augmented SE peak is witnessed in the wavelength sweep, figure 5.11.

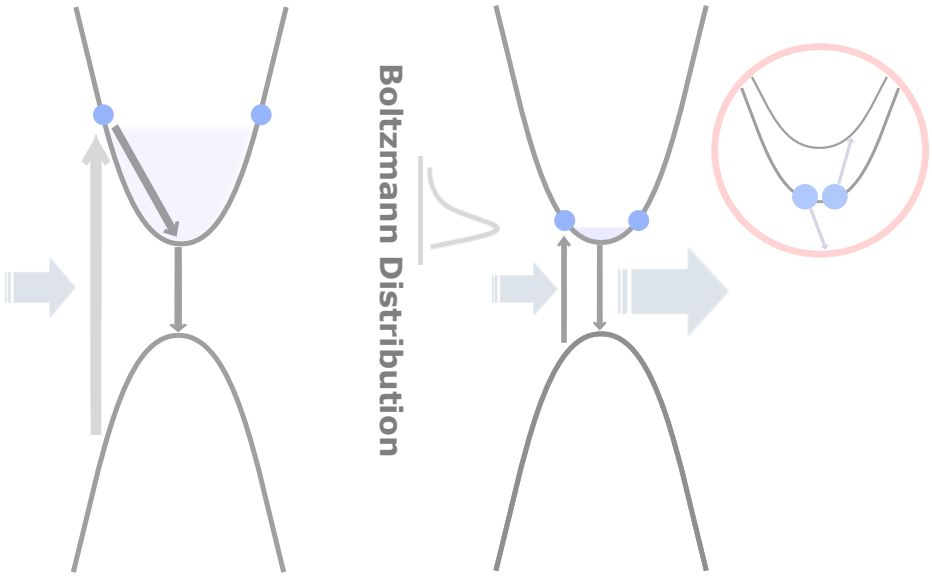

Figure 5.13: Schematics showing the possible transition paths from a generalised picture. In non-resonant excitation of an electron-hole pair, radiative and non-radiative phonon-scattering decay pathways can generate spontaneous emission resulting in an incoherent background signal on top of the stimulated signal. For excitations near the excitonic transition, the absorption coefficient increases, resulting in brighter PL and a suppression of the incoherent decay pathways as the intensity of the coherent signal increases. The inset shows an Auger mechanism when excess carriers concentrate in a small region.

In order to verify the identity of the 'SE' signal discussed above, the near-resonant and off-resonant behaviours of the emission are further investigated with excitation power dependence measurement. The off-resonant pumping is set at a wavelength of 495 nm (2.505 eV energy) while that of the near-resonant case is 526 nm. For the off-resonant pumping illustrated in figure 5.14(a), as discussed above, a major portion of the PL spectrum is contributed by the photons with energy over the bandgap. When the pumping strength is less than 10 μW, there is only a broad emission line spanning a wavelength range of around 4 nm. This is purely from SPE effect originating from incoherent emission. As the excitation power is increased, a new narrower line starts to emerge from the SPE emission and becomes more prominent in the spectrum.

The relative contributions from the two components can be visualised via decomposition

of the overall emission. Figure 5.16 shows the multi-Gaussian fit for a single spectrum taken at 25 μW. The fitted two parts present a good match to the PL components. By extracting the central wavelength and integrated area under the Gaussian fits, properties for each signal can be evaluated and compared. Considering the integrated area for the fitting of the newly emerging signal, its identity is verified to stem from SE as proven by the S-shape excitation dependence curve illustrated in figure 5.15. This is the characteristic property of lasing and the corresponding threshold pumping strength is found to be 15 μW. The threshold level is comparably lower than some of the reported $CsPbBr_3$ based lasers[158][159] and hence shows some behavioural advances. In the case of central wavelength, blue shift of the SE wavelength is observed again with higher pumping strength. This is consistent to the blueshift mentioned in last chapter of TEM modes and the corresponding mechanism also applies here.

Although the SE signal has demonstrated shortened lifetime, S-shape power dependence and narrow spectral width, its coherence identity can be further verified using an interference experiment to test the first-order time correlation function. The relevant experimental techniques and principles are already discussed in chapter 4 under the subsection 'Michelson Interferometer'. Since the SE and SPE peaks are well distinguishable as shown from the PL spectra presented earlier in this chapter, it is hence feasible and ideal to carry out this interference measurement. Unfortunately, the full characterisation was done during an early breakout of the Covid in 2020 and access to lab was restricted. Therefore, I didn't have enough time to finish this test before the sample went bad and it has to be considered as part of future work when a new sample arrives.

By bringing the excitation wavelength closer to resonance, an excitation power run of the same incremental steps to that in figure 5.14(a) is illustrated in figure 5.14(b), for a direct comparison. The enhanced contrast between SE and SPE emission is obvious even from low excitation fluence just above threshold. Different from the off-resonant case, the profiles associated with the two mechanisms present sharper boundaries and the SE emission looks more outstanding from the SPE background. This is a clear indication of a more dominant

coherent emission where the overall proportion of the incoherent recombinations are significantly reduced. When pumping photons are on-resonant with the dipole moments formed by the lower lying carrier near band edge, they tend to scatter elastically and motivates the SE mechanism. However, for higher-energy pumping photons, although they can still stimulate the higher lying carriers in the energy band, a comparable proportion of the carriers will also follow a decay path assisted by the interchange of momentum with phonons. This fact discriminates the behaviour from resonant scattering and hence blurs the boundary between SPE and SE. The direct impact is reflected by the unsuppressed incoherent decay paths. In contrast, near-resonant pumping cuts out a much cleaner SE and casts more coherence into the radiation. For application purposes, such improvement on SE line purity enables the generation of a spectrally purer signal.

Figure 5.17, from another angle, tracks the increase in signal intensity towards resonance for both SE and SPE. From the plot, the SE intensity enhancement is of more than nine times than that witnessed for SPE. By comparing these micro-PLE patterns with the μPL spectrum, a Stokes shift of 18meV can be computed by taking the difference between the two peaks in the SPE plot as shown in figure 5.18. Clearly, the optimisation of the signal quality is not limited to the effect of Stokes shift, but more as a result from the resonant phenomenon introduced above.

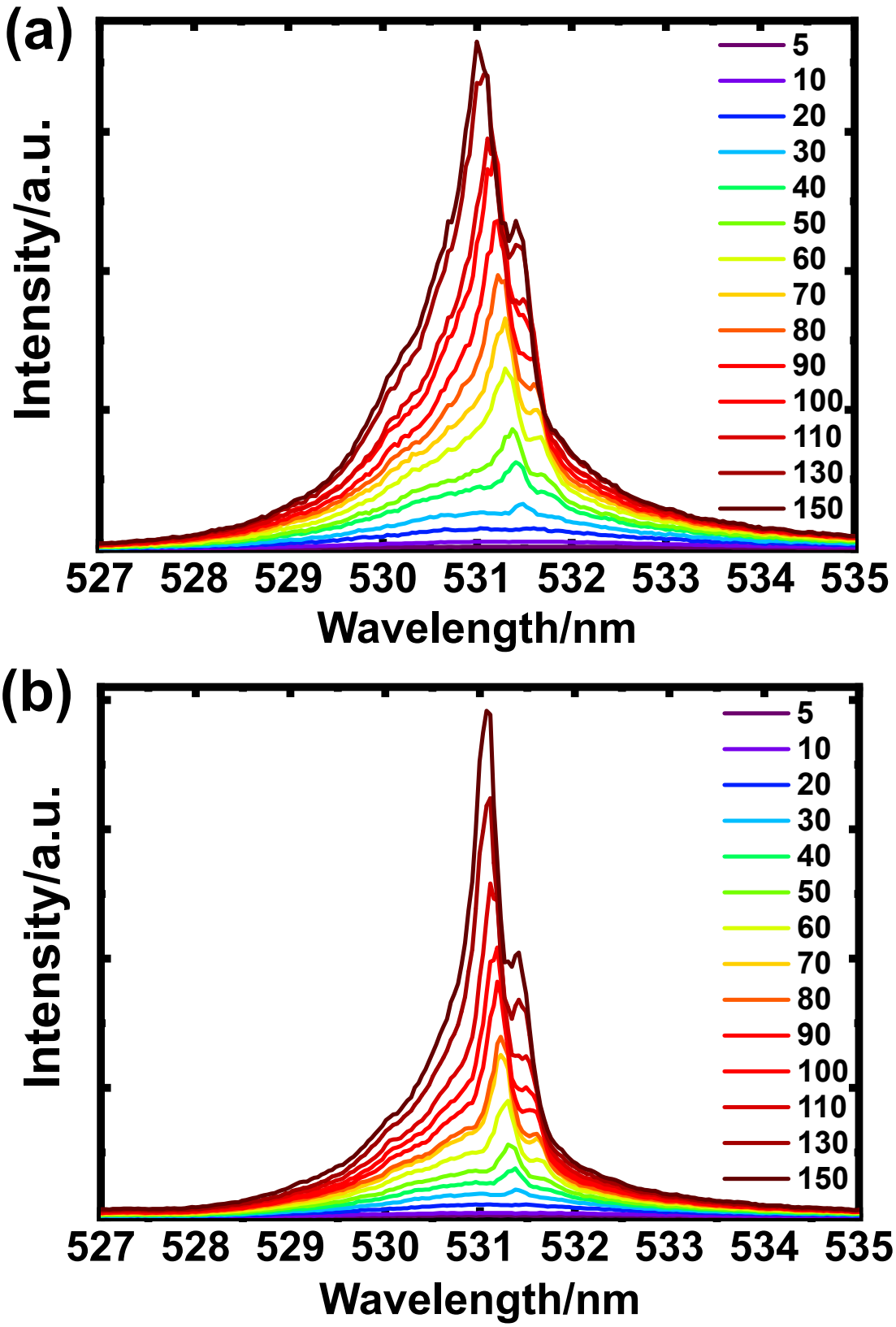

Figure 5.14: Excitation power dependent PL spectra of the $CsPbBr_3$ PNC measured at 4 K. (a) Intensity dependence on excitation power using an off-resonant optical pump (495 nm). (b) Intensity dependence on excitation power using a near-resonant optical pump (526 nm). The excitation fluence is controlled to give the same density of pumping photons. Importantly, the contrast between the SE and SPE peaks is significantly higher even at near-threshold pumping.

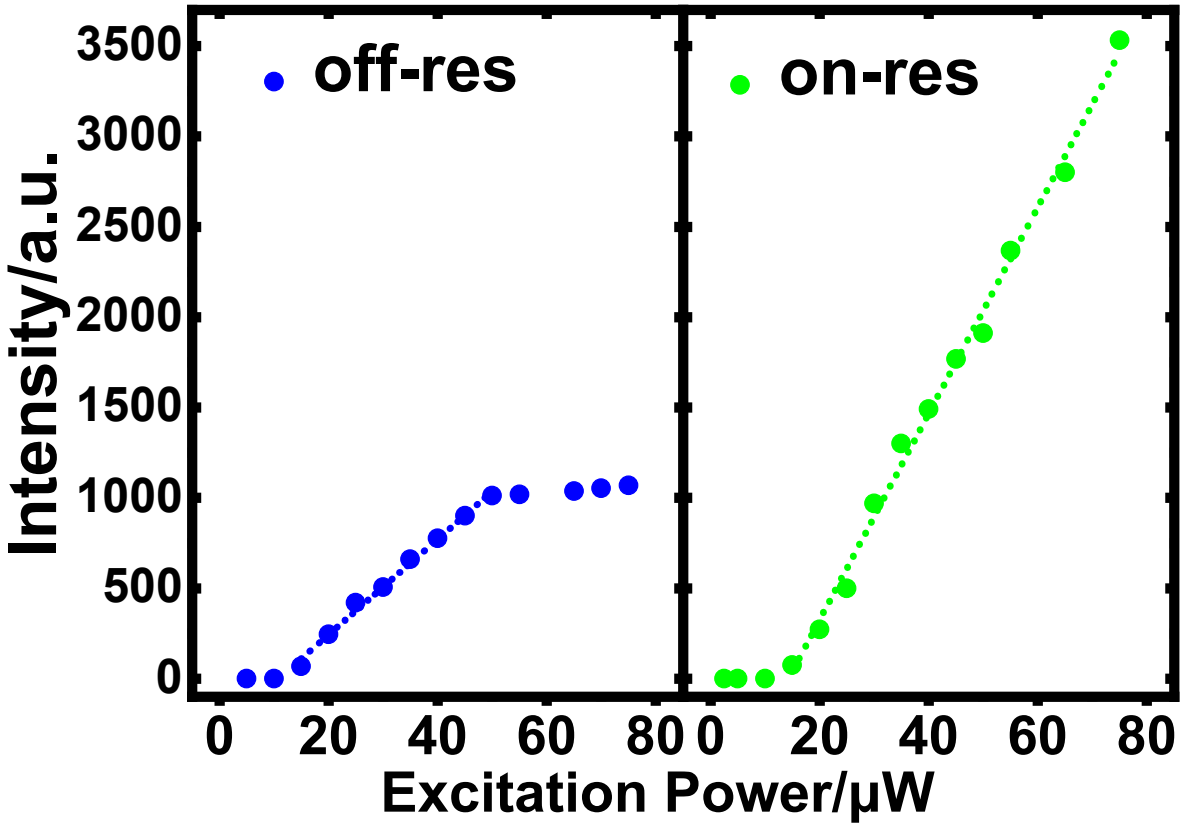

Figure 5.15: Integrated SE intensity versus pumping strength for non-resonant (left panel) and near- resonant (right panel) pumping plotted on the same scale for emission intensity. Over the same range of pump-photon density, the near-resonant pumping regime produced a significantly steeper linear lasing intensity increase, while saturation is not reached even at the highest pumping fluence available. In the off-resonant pumping regime, a shallower linear intensity increase is observed, reaching saturation at 50 μW.

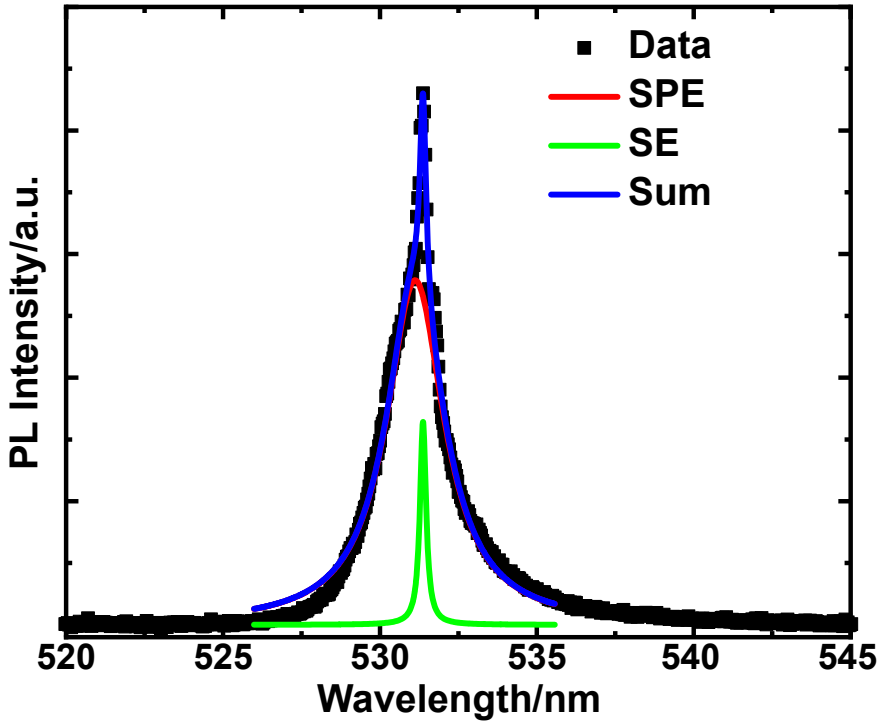

Figure 5.16: Fitting of off-resonant PL emission using Gaussian function measured at 25 mW pump power.

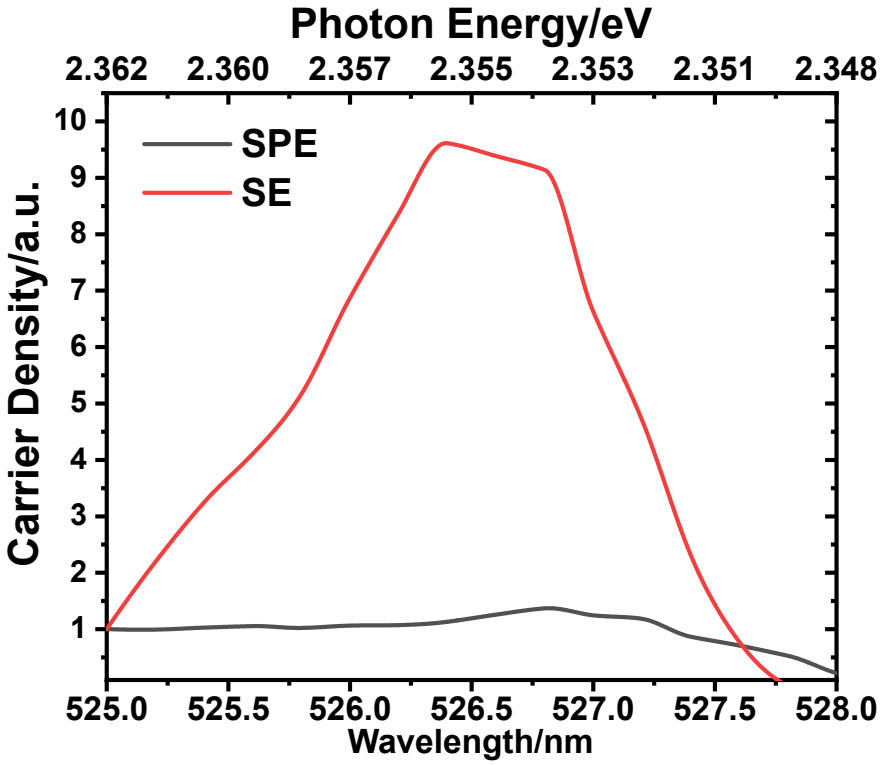

Figure 5.17: Percentage carrier density change associated with SE compared to that contributing to SPE over the range of the excitation wavelength scan from 525 nm until 528 nm. Both densities are assigned '1'(100 percent) at the starting point of the scan. The difference between the two curves indicates a 9 times more relative density increase for the carriers associated with SE.

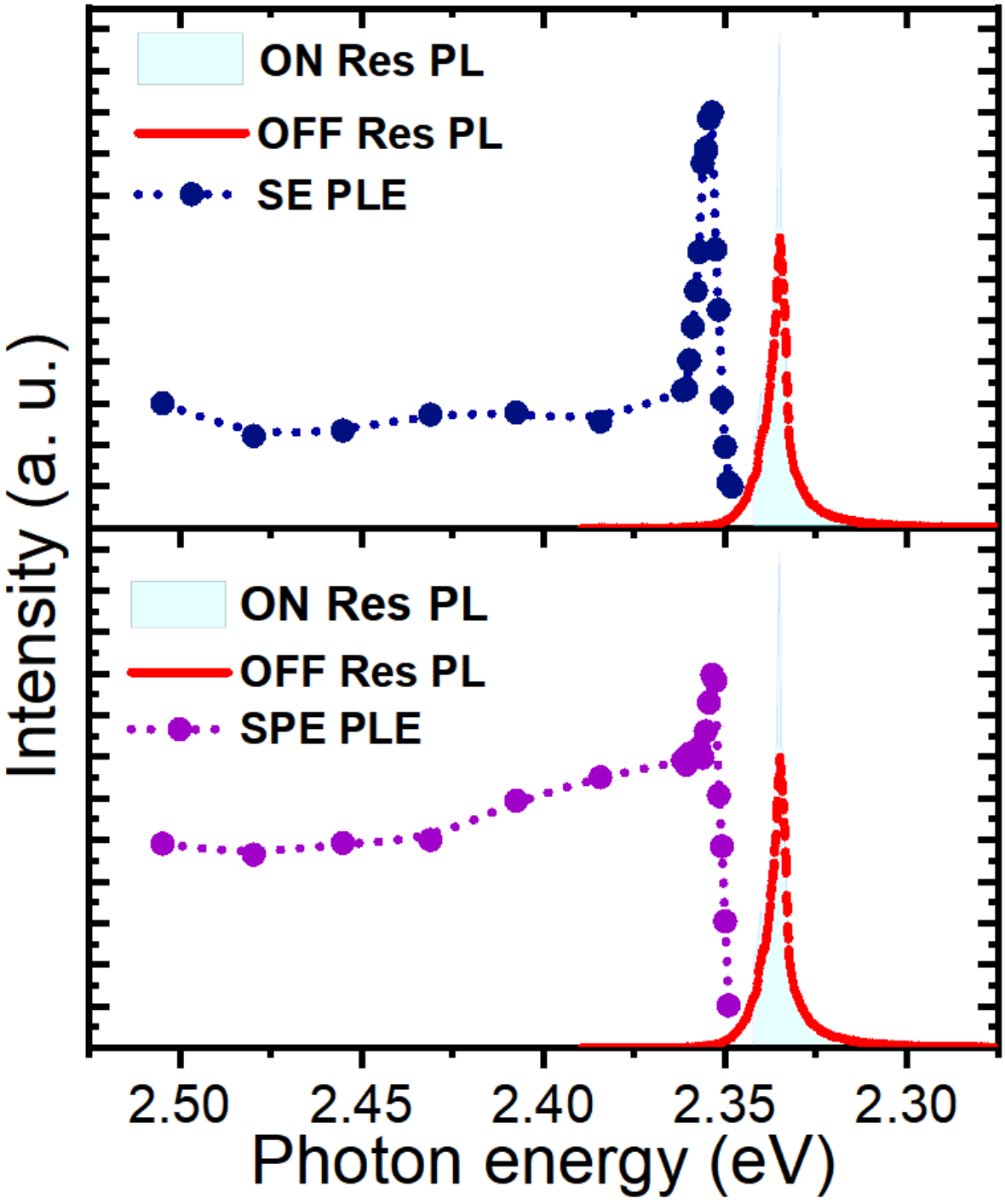

Figure 5.18: PLE and PL plot on – and off resonance. PLE plot for SE (dark blue dotted line) and SPE (violet dotted line) signals respectively. The red profile shows the PL emission from non-resonant pumping and the light blue shadow indicates that obtained from near-resonant excitation. The SE PLE peak is Stokes-shifted by 18 meV with respect to the SE PL peak, and suggests small losses due to vibrational relaxation.

Chapter 6

Hydroxide coated perovskite nano μ-rods

Instead of the cubic shaped nanocrystals discussed earlier, this chapter discusses my research on the PL emission given by $CsPbBr_3$ micro/nano-rods coated with $Pb(OH)_2$ cladding for surface passivation at cryogenic temperature. Such configuration is subject to high quantum yield and high environmental stability. There are two types of emissions, where one of them is associated with excitons generated at the passivation interface and the other originating from the defect sites for SE. The two emissions are characterised via diffusion analysis to compare their corresponding carrier dynamics.

6.1 Growth

The process for fabricating the micro-/nano-rods can be decomposed into several stages as shown in figure 6.1 according to our collaborator professor Atanu Jana's paper on the growth procesure[160]. In the initial phase, 500 mg, 1.5 mmol Cs_2CO_3 is mixed with 1 g, 2.7 mmol $PbBr_2$ that has already been dissolved in 2 mL HBr solution inside a container of relatively small size. Immediately after the mixing, a bright yellowish crystallised precipitate forms to be recognised as bulk $CsPbBr_3$ for further processing. The container will then be filled with MAm(methylamine) vapour and left at room temperature for roughly 24 hours until the colour has turned greenish white. This colour change indicates formation of $Pb(OH)_2$

layer onto the surface of the bulk perovskite structure. The underlying mechanism involves diffusion of the MAm into the solution to form MA^+ ions, which then react with water to produce hydroxide ions floating in the solution. Further reaction takes place between these hydroxide ions and $CsPbBr_3$ to bond at the surface for the generation of $Pb(OH)_2$ cladding. However, at this stage the sample is not completely dried out. MA^+ and H_2O both present in the perovskite (proven through X-ray diffraction and infrared spectroscopy done by professor Atanu Jana)[160] and hence surface passivation is not properly done at this stage. Due to the existence of void spaces in the interface, there is a reversible process which either incorporates or removes water from the compound via hydrating or heating the sample respectively. A co-existence of $CsPbBr_3$ and Cs_2PbBr_6 is also confirmed and they balance in proportion leading towards a dynamical equilibrium. Cubic shape $CsPbBr_3$ also appears along with rod-like structures, but they will break down upon heating. The final water-stable $CsPbBr_3$ structure can be obtained by leaving the sample to dry for 10 days. There are no more water or MA^+ residue remaining and the result is verified through Fourier Transform Infrared Spectroscopy[160] performed by professor Atanu Jana. This concludes the final stage of the growth by showing that $Pb(OH)_2$ now properly passivates the surface as demonstrated in figure 6.2.

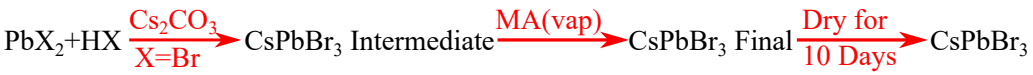

Figure 6.1: The fabrication procedure for $CsPbBr_3$ rods coated with $Pb(OH)_2$ cladding.

Size tuning is also possible by changing the number of days for the reaction. The related study has demonstrated the relationship for different rod diameters produced with respect to the time spent during the growth. Moreover, keeping the rods in closed environment for longer than one month will generate more uniform distribution of the sample sizes. Apart from time, temperature is also a crucial factor influencing the reaction. For the growth procedure mentioned so far, the temperature is fixed at 20 °C for keeping the reaction in a controlled and moderate speed.

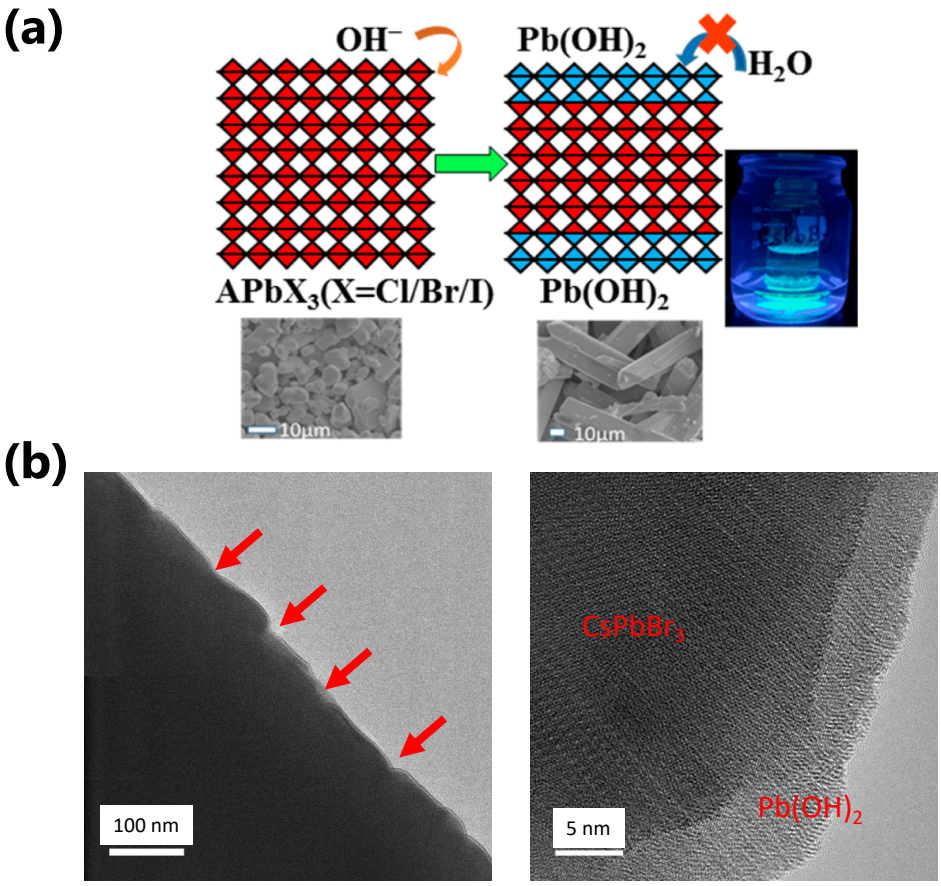

Figure 6.2: (a) Schematic showing the crystalline joint between the $CsPbBr_3$ rod centre core and $Pb(OH)_2$ cladding. (b) Transverse electron microscope image demonstrating the coated interface of the hydroxide group onto the perovskite surface. The cladding layer has a thickness of around 5nm in this case. [Image supplied by Atanu Jana from Dongguk University]

6.2 PL

In order to investigate the emission characteristics of the $CsPbBr_3$ micro/nano-rods modified with the hydroxide coating, we have picked up three different sizes spanning widths of 1, 2.5 and 4 μm to represent small, medium and big size groups among our samples. From now on, they will be labeled rod A, rod B and rod C respectively. All the three rods have regular structures and are deposited in isolation to any other rods. As for the pumping source, we have chosen a 450 nm pulsed laser due to our experience with the 4 K $CsPbBr_3$ emission wavelength as demonstrated in the preceding chapters. The beam was focused onto the centre of each rod as shown in the top schematics of each subplot in figure 6.3. For $CsPbX_3$ based nanorod systems, many other studies have reported witness of lasing emission from the

guided modes of the structure[131][161][162][163]. Therefore, we have performed a power-dependent characterisation of the emission spectrum at 4.5 K and have also taken optical microscopy pictures over the sample while pumping the crystal. It is clear from figure 6.3 that radiation from the ends of the rods are visible in all three cases. The spatial separation of the excitation spot from these emissions verifies that they actually originate from the waveguide modes. Despite this, the colours observed in the camera after filtering out the pumping wavelength are obviously bluer compared to the characteristic $CsPbX_3$ green emission at 4K, which falls within the range 520-540nm[39][131][164][165][166] for other nanostructures and thin films. The wavelength of this blue-shifted emission is confirmed from the PL spectrum to be at around 495nm as shown by rod A in the left-hand side panel of figure 6.3, where no other emission wavelength is observable. For consistency check, the same emission line has also been spotted in the other two cases without a shift in wavelength. Therefore, this blue radiation is less likely to be size-dependent but more closely linked to the surface modification from the hydroxide coating. Extracting the integrated areas from Gaussian fits of the power dependent measurements taken at this blue site from all three cases exhibit a linear dependence. This matches the description of single exciton emission.

For larger rods, well-distinguished new greener emission lines become available. In the case of rod B, an emission site at 515 nm is clear from the spectrum when pumping with a power over 0.17 $mWcm^{-2}$ as shown in the middle plot of figure 6.3. Interestingly, while at low excitation strength this green emission is almost completely submerged into the red shoulder of the blue site it eventually becomes dominant over stronger pumping. This much faster intensity growth with an onset level resembles a SE process. Again, by plotting the total intensity under the Gaussian fit, a characteristic S-shape is obtained revealing lasing. For the bigger size rod C, another greener emission site at 530 nm is observable while the PL peaks for the other two sites are still maintained at their respective wavelengths. Figure 6.4 also shows the excitation power dependence for this emission site follows an S-like character. The existence of multiple SE modes possibly stems from the fact that mode confinement can be established along both lateral and axial directions. A schematic illustration of the confined axes on a rod is presented in figure 6.5. Another possibility is from localisation of

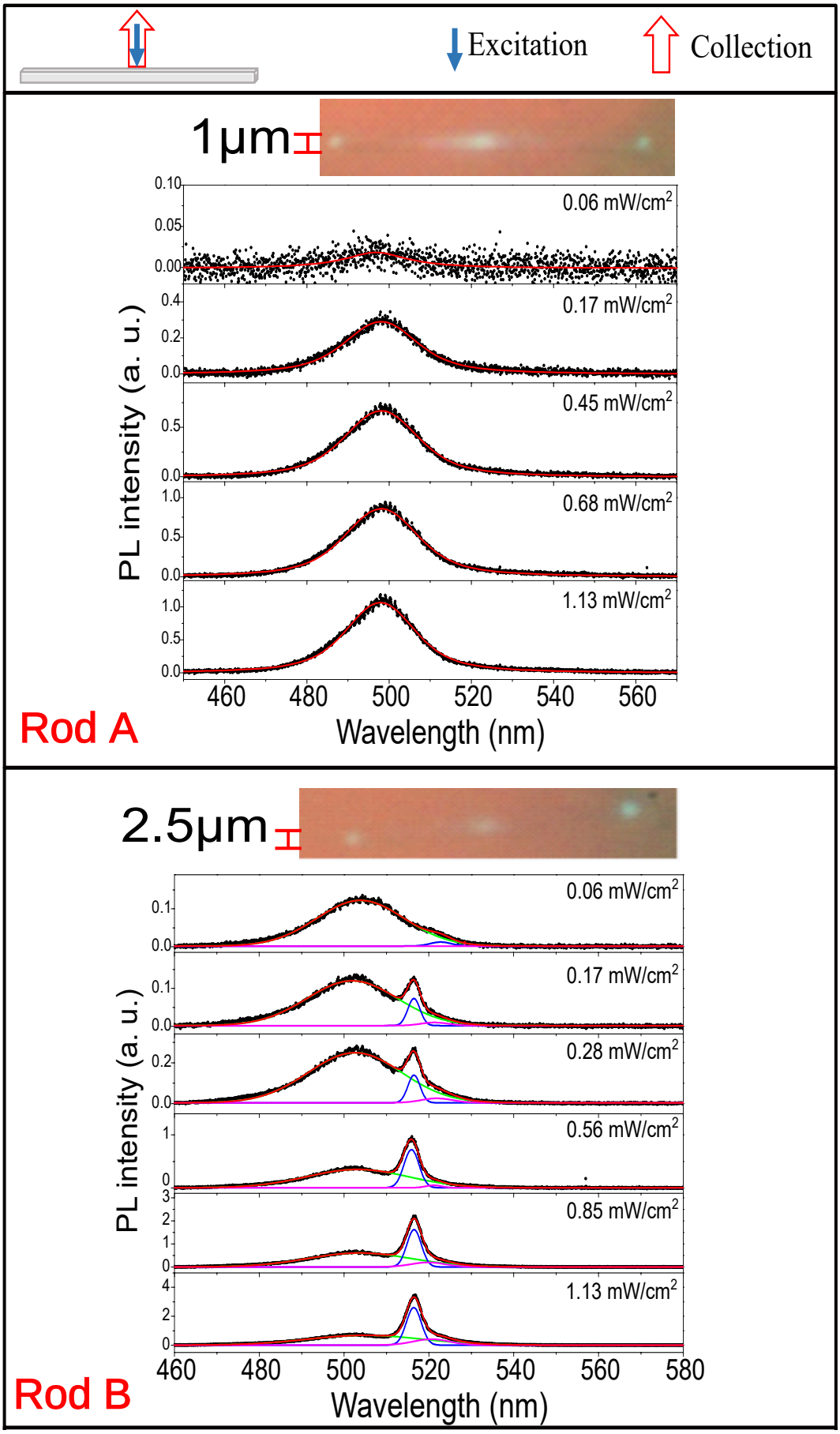
Excitation
Collection
1μm
0.06 mW/cm2
0.17 mW/cm2
0.45 mW/cm2
0.68 mW/cm2
1.13 mW/cm2
PL intensity (a. u.)
Wavelength (nm)
Rod A
2.5μm
0.06 mW/cm2
0.17 mW/cm2
0.28 mW/cm2
0.56 mW/cm2
0.85 mW/cm2
1.13 mW/cm2
PL intensity (a. u.)
Wavelength (nm)
Rod B

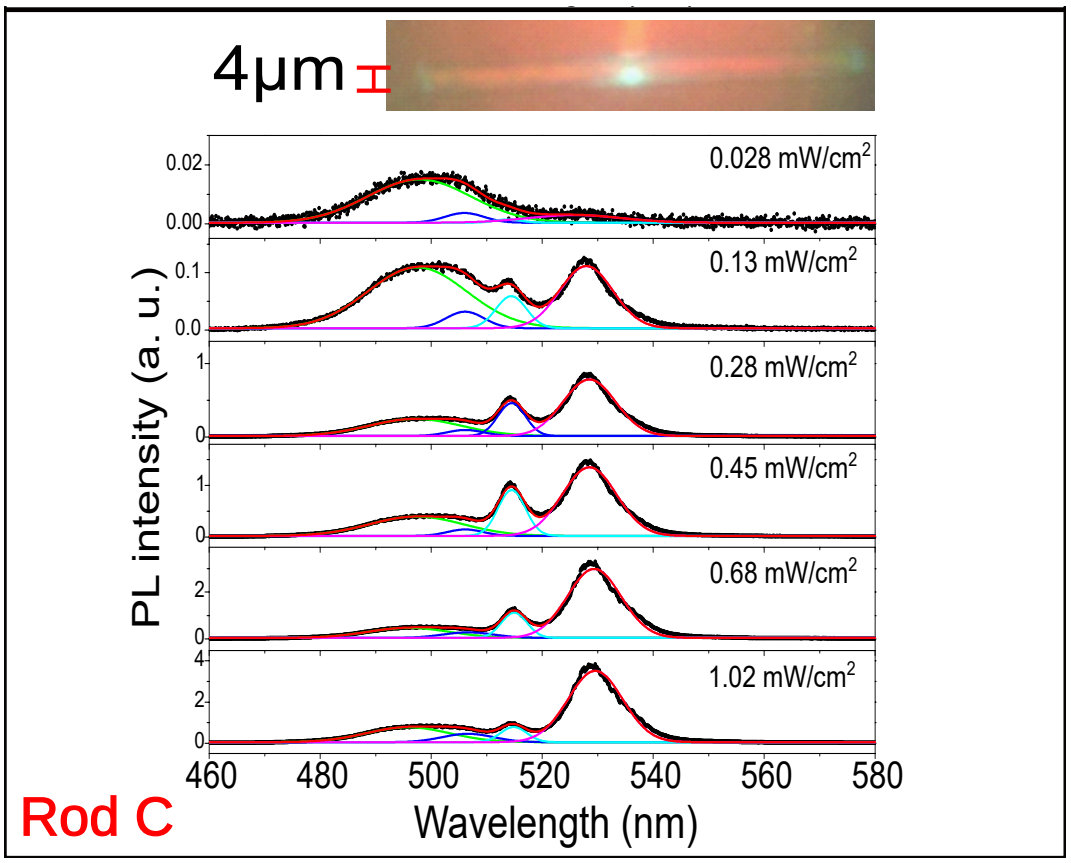

Figure 6.3: Power-dependent PL spectra taken at 4.5 K for $CsPbBr_3$ rods with cross-sectional diameters of $\sim 1\mu$m (left panel), $\sim 2.5\,\mu$m (middle panel) and $\sim 4\,\mu$m (right panel) respectively by having both the excitation and collection spots at the centre of the rod. Solid lines are Gaussian fits to the individual emission peaks.

carriers. Areas of concentrated carriers after population inversion are active for SE to take place at their designated wavelengths.

Although lasing can lead to many interesting optical phenomena including those mentioned in the preceding chapters, the unique feature in this system is actually on the non-SE emission at 495 nm. Before discussing the technical advantage of this blue site radiation, it is worth thinking about the underlying mechanism. As discussed above, we have already demonstrated that this emission exists with the presence of $Pb(OH)_2$ cladding. Arriving at this exact conclusion also requires ruling out the possible contribution to the blue shift of the emission wavelength from the MA^+ cations left over as residual after the fabrication process. There are two pieces of evidence directly supporting our argument. First, the significantly larger size of the MA^+ cations compared to Cs^+ will result in a red shift to the characteristic emission wavelength rather than a blue shift after hybridisation. Second, upon completion

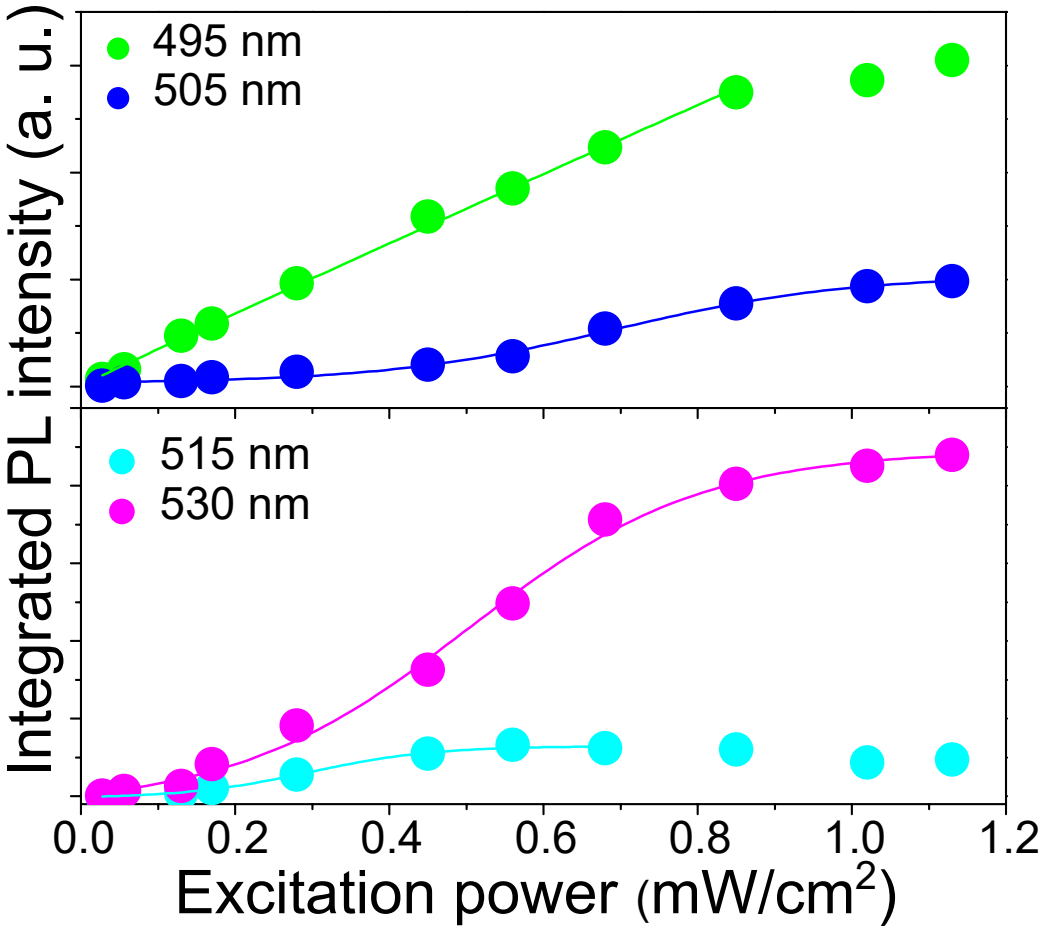

Figure 6.4: Plots showing the dependence of integrated PL counts over the excitation pumping strength for the four peaks fitted out of the spectra taken for the $\sim 4\,\mu$m-wide rod shown in figure 6.3.

of the growth stage a Fourier Transform Infrared Spectroscopy measurement was performed indicating no sign of existence for the MA^+ cation[160]. Therefore, the only possible cause to such shift in wavelength is limited to the $Pb(OH)_2$ cladding. However, the contribution from the $Pb(OH)_2$ on its own is also not possible since its transition energy is too high and out of the range of our consideration. Clearly, it is now narrowed down to the interface effect that gives the shift. The bonding process between the perovskite core and the cladding is from the interaction with the OH^- group. This is realised by replacing the labile peripheral $[PbX_6]^{4-}$ octahedrals of perovskite with $Pb(OH)_2$ bonded interface. The surface modulation will enhance the stability against chemical conditions and water as well as introducing passivation effect[160]. It has been demonstrated that these coated perovskite rods can live for more than 6 months while maintaining the bright PL emission even in a water-rich en-

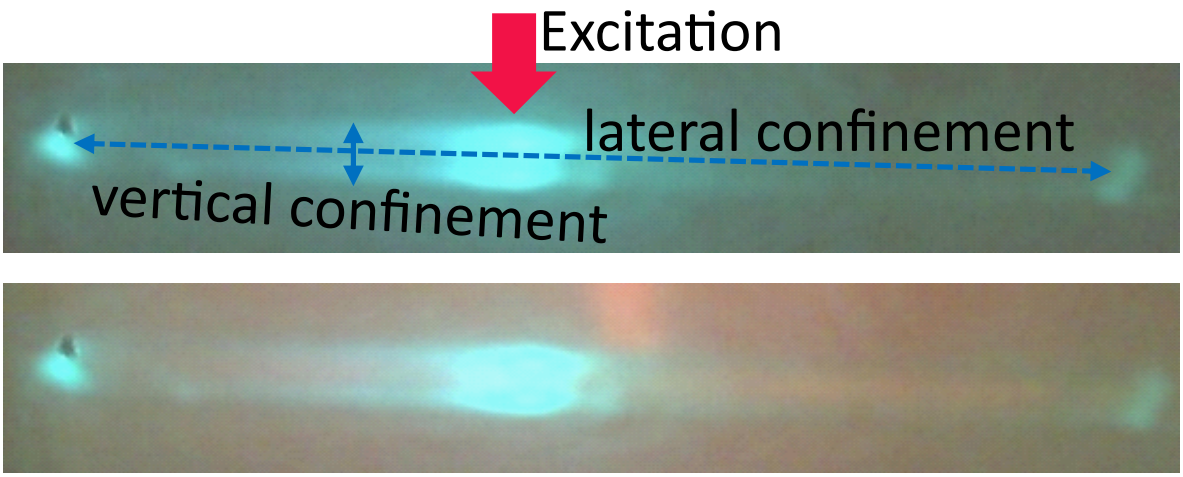

Figure 6.5: Coloured CCD camera images taken for rod C demonstrating the spatial profile of the PL emission. The upper image is obtained dark while the bottom image is taken with the illumination from a LED light source. Both lateral and vertical axes of the rod can potentially support cavity modes.

vironment. The surface cladding also plays a key role in shaping the nanostructures during fabrication. The coating suppresses the growth of the perovskite along lateral directions and hence forces the structure into rod-like shapes instead of the natural cubic configuration for $CsPbBr_3$ nanocrystal. This also leads to the smaller cross-sectional dimension of the actual perovskite region compared to the width witnessed from microscopy image. On the other hand, the reduced core size also brings up concerns on whether the cladding completely eats away the perovskite in the centre for small size rods. This concern is lifted by inspecting the spatial distribution of the various chemical composites involved from energy dispersive X-ray imaging taken by professor Atanu Jana for a relatively thin rod of width between 1-2 μm as shown in figure 6.6. The technique relies on the fact that different atomic structures occupy their own characteristic emission spectra. Therefore, the process can be used to filter out the emission from different atoms to monitor their locations respectively. The measurement was compared to a SEM image of the structure presented in the same spatial coordinates. It is evident from plots (c) and (d) that both Pb and Br are found to fill in the region along the rod. This verifies that the octahedrals still remain in the core region and hence the original $CaPbBr_3$ is well preserved even for thinner rods.

The discussion so far concludes the structural configuration of the rods and also explains the origin of the new emission site at 495 nm. The following paragraphs will look into the

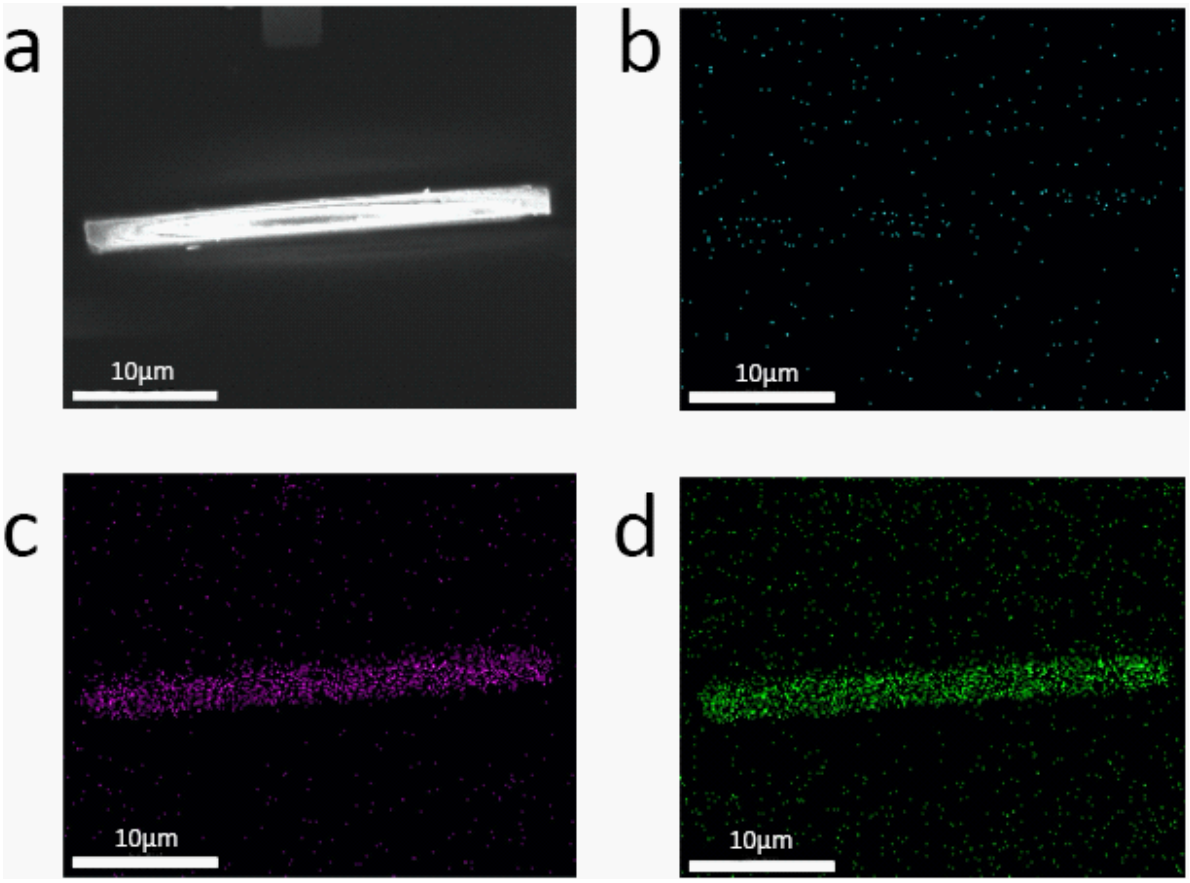

Figure 6.6: (a)SEM image for $CsPbBr_3$ rod coated with $Pb(OH)_2$. Plots (a), (b) and (c) illustrate the energy dispersive X-ray images taken at Cs L , Pb M, and Br L.[Image supplied by Atanu Jana from Dongguk University]

properties of the blue and green emissions in our structure to exploit their potential for device applications. Starting with temperature dependence for the two types of PL signal, figure 6.7 illustrates a comparison between rod A and rod C. At 4.5 K, the behaviours exhibited by the two rods are identical to the discussion above. A homogenous broad blue emission peaking between 495-510 nm is presented in both cases while a narrow line at 540 nm is only seen for rod C with its identity proven to be SE. By increasing the temperature towards room temperature, 298 K, different trends are observed for the two peaks. The green emission in rod C follows the typical temperature-dependent pattern for uncoated $CsPbBr_3$ as in previous chapters, it blue shifts at higher temperatures. Since it is a lasing process, its intensity drops much faster than that of the excitonic blue site emission. This is because the increas in temperature can be translated into a rise in entropy, which represents disorder and randomness. For lasing process, these are unfavourable conditions as the multiplication pro-

cess prefers ordered dipole alignment and coherence with the only exception being random laser, which requires disordered material system and clearly not matching the description of our sample[167][168][169]. On the other hand, the interface-induced blue site emission exhibits an opposite trend, it red shifts with temperature. From a close inspection on the series of plots in figure 6.7(b), it is not hard to see that the two emission sites are merging together and only one peak can be seen from 150 K onwards. For both rods, the trends for PL are similar after 150 K and the room-temperature spectra both peak at a wavelength around 510 nm. These room temperature behaviours are consistent to other reports of pure $CsPbBr_3$ systems[170][171]. Now focusing on the temperatures below 150 K, the blue site emissions observed for the two rods both show an asymmetric Gaussian shape with more states distributed towards the shorter-wavelength end. The merging process of the two peaks with increased temperatures for rod C can be now viewed instead as a splitting process into the two peaks towards lower temperatures. This can be understood as a split of transition energies between the states corresponding to radiative recombination happening at the interface with hydroxide claddings and the states associated with recombination in unpassivated $CsPbBr_3$ regions. In the case of thinner rods including rod A, the carrier recombination process is dominant in the interface and hence only the blue peak is observable at cryogenic temperatures. However, the more remarkable observations for the blue site emission are associated with the almost unbroadened energy distribution at increasing temperature and reduction of peak intensity only by a factor of 1.5 between 4.5 K and 298 K as shown in figure 6.8. The down scaling factor of peak intensity with temperature change in a similar range for all perovskite systems studied so far are over 100 and our observation hence sets a benchmark. This result has proven that the interface states can tolerate the thermalisation effects more than the unpassivated states and serves as an angle to interpret the enhanced quantum efficiency in our systems.

Further investigation exploiting the spatially-resolved 2D PL intensity maps has been performed on both rod A and rod C at 4.5 K and 298 K to generate the spatial profiles for different emission sites as shown in figure 6.9. The left-hand side panel of figure 6.9 demonstrate the overall wavelength-integrated intensity and the intensity at the peak of the

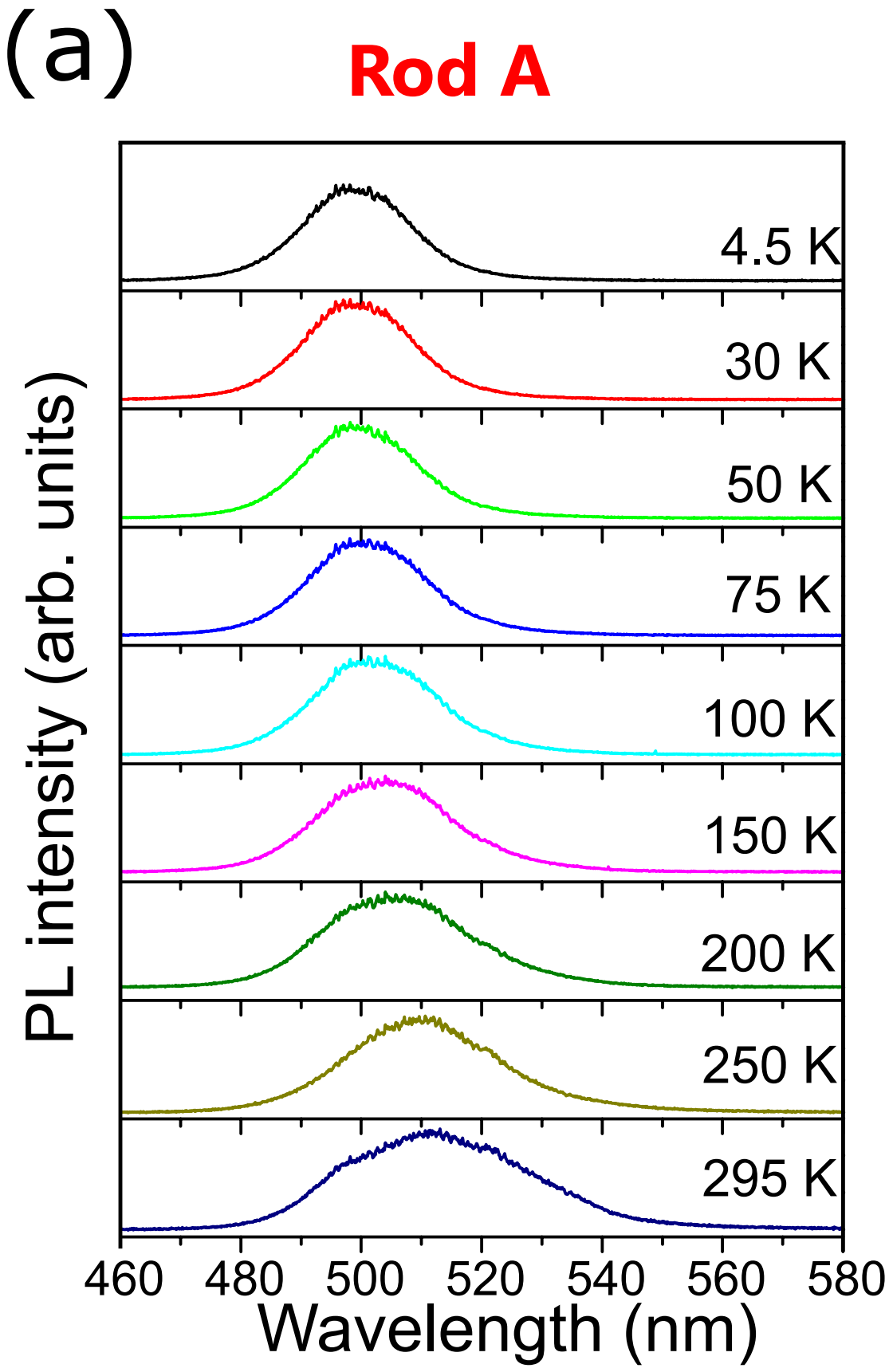
(a)
Rod A
4.5 K
30 K
50 K
75 K
100 K
150 K
200 K
250 K
295 K
PL intensity (arb. units)
460
480
500
520
540
560
580
Wavelength (nm)

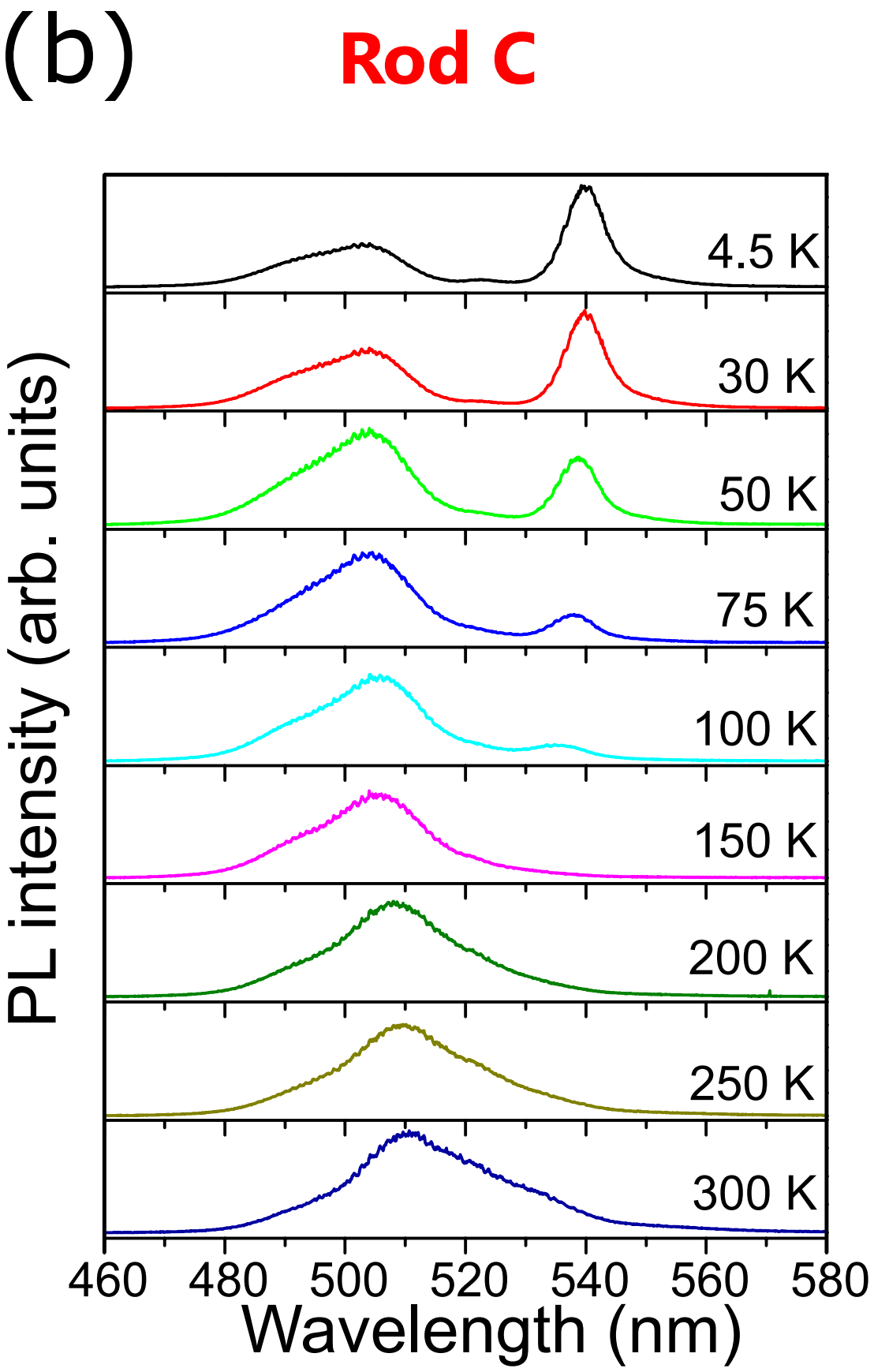

Figure 6.7: Temperature-dependent PL spectra taken for rod A in plot (a) and rod C in plot (b).

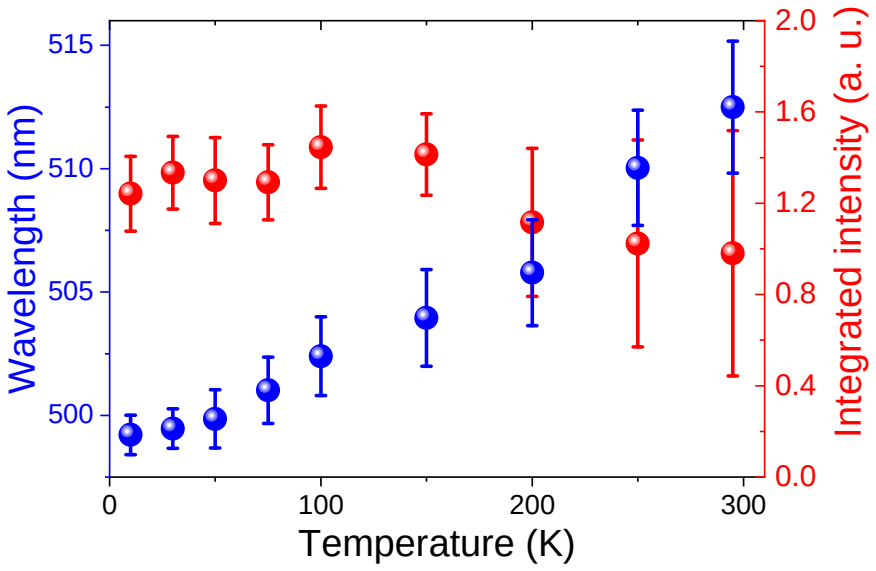

Figure 6.8: Dependence of PL peak position and integrated intensity for the blue-site emission as a function of temperature. The peak wavelength exhibits a redshift with increasing temperature while the total counts of the entire spectrum only drops by a factor of ∼1.5 at room temperature. The errors on both peak wavelengths (blue) and integrated intensity (red) were obtained through multiple fitting attempts to the PL profiles with standard deviations taken at each temperature.

blue site for rod A at cryogenic and room temperatures respectively. The wavelengths for the peak of the blue emission has been chosen to be 495 nm at 4.5 K and 510 nm at 298 K such that it has taken into account the red shift with temperature consistent with the discussion from last paragraph. All of the intensity maps appear to be quite uniform and similar to each other. This serves as another piece of evidence to support our argument on the origin of this blue site to come from interface emission and suggests that the hydroxide cladding has been coated uniformly around the surface and along the length of the rod. This conclusion has also been verified from the blue-site emission profiles with the larger rod C in the right-hand side panel of figure 6.9. However, the SE profile at 540 nm exhibits completely discrete and localised emission. This is reasonable for rods with bigger core region due to the increased likelihood of lattice mismatch at the interface between hydroxide cladding and the inner perovskite. This mismatch can build up the strain along the bonding surface and eventually lead to discontinuity in the lattice and introduce local defect states. The localisation effect mentioned earlier can originate from these defect sites and they will act as trapping centres

to capture excitons. In contrast, limited core size for thinner rods to fall within hundreds of nanometers means that strain can be distributed more smoothly along the hydroxide interface. This implies that any built-in strain can be easily soothed in the neighbourhood and hence no localised green emission is observed.

6.3 Diffusion

The existence of localisation and waveguide mode emission makes it intriguing to look into the kinematic behaviours of carriers. Following this consideration, it is worth introducing the important concept of diffusion in some detail before moving forward.

Since many of the perovskite-based optoelectronic devices for power management applications require efficient collection or injection of charge carriers, diffusion length thus becomes a fundamental factor for evaluation of the performance in the related studies. The effect of diffusion is witnessed when a concentration difference of a single particle type exists across a connected spatial region and the density tends to rebalance via driving particles from more concentrated area towards where they are scarce in number. This implies that a system of uniform density distribution subject to no external force will have no tendency for redistribution and it is hence regarded as the final steady state for an unbalanced system. From this prospective, it is intuitive to write down Fick's first law:

$$J = -D\nabla\Phi \tag{6.1}$$

where J is called diffusion flux, which essentially describes the differential density, $\nabla\Phi$, of particles in the spatial coordinates. The diffusion coefficient D encodes other properties of the specific type of particles linked to their kinematic behaviours. These factors include the velocity of the particles in a specific medium and the associated viscosity. An explicit expression linking the diffusion coefficient D to carrier mobility μ is also stated via the Einstein relation: $D = \mu k_B T$. This relationship also incorporates the potential for increased

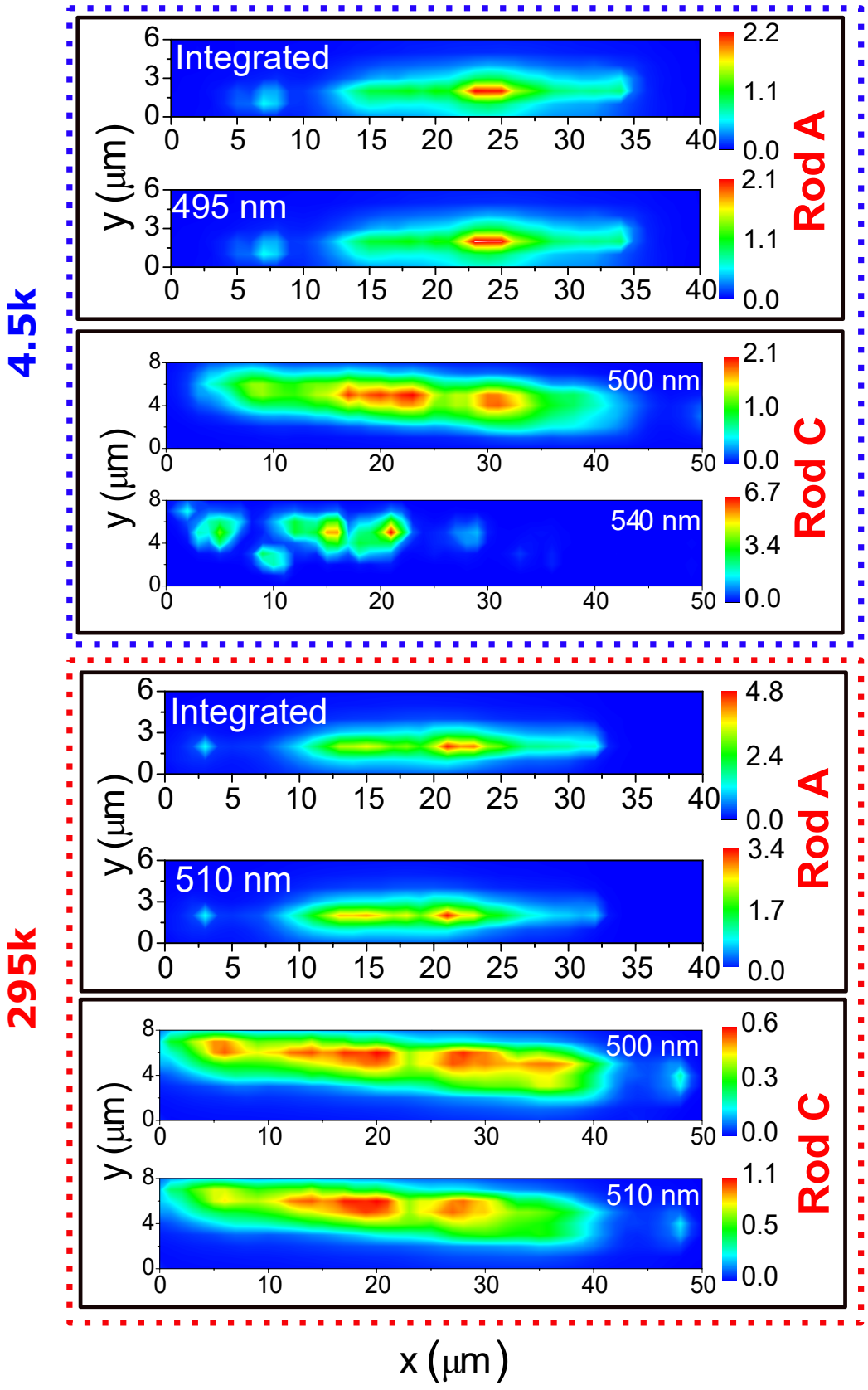

Figure 6.9: 2D PL maps taken for rod A (left panel) and rod C (right panel) at 4.5 K (top blue panel) and 295 K (bottom red panel). For rod A, due to the existence of a single peak at the blue site, only the wavelength-integrated map and the map at the peak wavelength for the blue site (taking into account the blue shift of the peak with increasing temperature) are demonstrated. As for rod C, a comparison between the blue and green-site emissions are shown for both temperatures.

kinetic energy of each individual particle at higher temperature. In order to look further into the dynamical characteristic of a diffusion process, Fick's second law is helpful:

$$\frac{d\Phi}{dt} = D\nabla^2\Phi \tag{6.2}$$

The equation itself is intuitive, the second order spatial differential reflects the difference between local changes in particle density for a pair of infinitesimal regions adjacent to each other. This indicates the degree of diffusion required to fill up the lower density in a farther area after first injecting particles into the immediate neighbouring region. Therefore, it describes the tendency for change in particle density over time.

Another representative factor relating to diffusion can be constructed as $L = \sqrt{D\tau}$ and it is a distance unit, called diffusion length. This factor is more useful for performance analysis in perovskite systems as it also includes carrier lifetime term τ. Lifetime is a good indicator for the extent of recombination mechanism, which is a lossy process for carriers. Combining this with the diffusion coefficient will hence serve as a more realistic measure of the actual distance travelled by free carriers after excitation.

6.3.1 Scanning Excitation and Fixed Collection

The most direct observation of a diffusion profile is obtained by looking into the distance travelled by a carrier before it recombines radiatively to give out a photon. Such a measurement can be achieved through spatially separating the excitation and collection spots in a μPL system. Given a confocal setup, the collection area can be limited to a region of $1\,\mu\text{m}^2$ with the help of a $25\,\mu$m core multi-mode fibre and it is aligned to coincide with the excitation laser spot via intensity maximisation. Starting with overlapped excitation and collection, customised positioning between the two is available from the combined operations between objective lens and piezoelectrically controlled scanning mirror. As introduced in the experimental setup chapter, shifting the objective lens itself will move both the excitation and collection spots simultaneously and hence only produce an on-spot excitation PL inten-

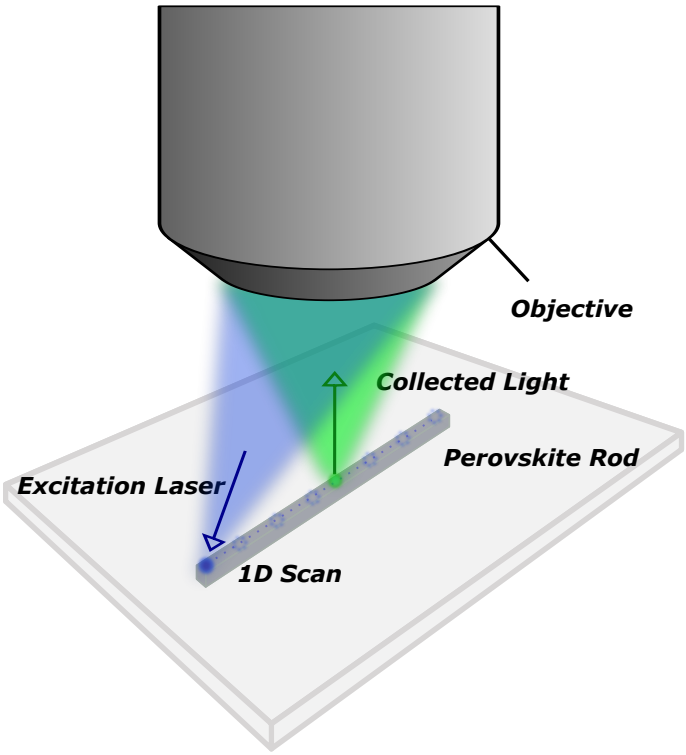

Figure 6.10: Schematic of separable excitation and collection μPL setup. The blue excitation spot is shifted with a piezo-controlled scanning mirror while the collection position is fixed by the objective lens.

sity map. Clearly, this doesn't contain much information on diffusion. It is the scanning mirror that can alter the angle of the incident beam and move the excitation spot around the sample surface. As long as the tilt on the mirror falls within the small angle approximation of the objective, the angle change can be translated linearly into a translational interval in the horizontal plane. The operation only involving the scanning mirror is hence associated with a fixed collection and scanning excitation measurement and its corresponding schematic is illustrated in figure 6.10. On the other hand, after shifting the excitation and collection spots together with a movement of the objective lens, a following tilt on the scanning mirror can be used to bring the excitation back to its original position without further changing the collection site. Such a process essentially scans the collection at fixed excitation. The two methods can both be used to study the diffusion characteristics while the former is for carriers to diffuse to a single position to recombine and the later is for carriers to diffuse from a single position of excitation. Because excitation depends on the local band structure and recombination relies on environmental factors, the two methods are each preferred in a

different situation and they can be combined for a full picture of carrier diffusion analysis.

Equipped with these techniques, we have performed another two sets of power run on rod C to compare the results of on-spot excitation and separated excitation/collection. In the case where both excitation and collection are at the end of the rod (left-hand side panel of figure 6.11), two emission sites at 522 nm and 538 nm are observed. The power dependent measurements indicate that the two emission signals again arise from SE despite that they are positioned at slightly different wavelengths to those seen near the centre of the rod from figure 6.3. However, the more interesting observation here is the absence of the blue site emission near 495-500 nm. This is an expected result due to the less effective $Pb(OH)_2$ coating near the end of a rod. As shown in figure 6.6(a) the structural morphology close to the end facet is less regular and hence it is hard to sustain a smoothly bonded interface. Moreover, the fact that the green lasing signal has appeared without the blue site also means that the existence of the two emissions are not coupled and it supports our theory on their different origins. A conjecture at the carrier level attributes the green emission to the creation of hot electron-hole plasma. Such a guess stems from valid bases since the initial stage of plasma formation before the cooling phase presents a wide energy distribution. This matches the relatively broad-band SE spectrum for our green signal. In addition, coupling to plasmon resonance can also lower the transition energy necessary for achieving population inversion as reported by[172], which possibly explains the red shift of the SE central wavelength from the characteristic $CsPbBr_3$ band gap at around 520 nm. We have also ruled out other possible mechanisms including exciton-polariton and bi-excitonic emission. For exciton-polariton, our pulse energy is too high to keep such bonded states. In the case of bi-exciton, the mechanism produces narrow spectrum line sitting far from the band gap energy, which is certainly not consistent with our results.

For the other set of power run (right-hand side panel of figure 6.11), the collection was kept at the end of the rod while moving the excitation to the centre. A schematic illustrates this setting. The blue site that has disappeared in the last scenario becomes visible again. Since there is no interface emission at the end and excitation/collection are

now well separated, the detected blue site emission must come from diffusion. Its relatively bright intensity indicates a long diffusion length for the generated excitons along the coating surface and it further confirms the smoothness and strength of the hydroxide bonding. The other two green emission sites from on-spot excitation are preserved. However, the green SE sites observed in the right-hand side panel of figure 6.3 at 515 nm and 530 nm are still missing. This is a clear evidence that all these four sites are associated with wave function overlapping for carriers at locally confined regions. These carriers lose energy very quickly from carrier-carrier interactions due to their high concentration before having a chance to escape from the area. Therefore, there is no sign to trace the two emission sites located at the centre. As for the other two green sites, diffused carriers with higher energy can be captured by the defect states living near the end of the rod and their emitted photons are reabsorbed here to follow the same decay paths as in the case of on-spot excitation.

In order to extract the full diffusion profile for carriers at 4.5 K, a scan of the collection spot has been performed along the rod at a pumping fluence of 0.28 μWcm^{-2} while keeping the excitation at the centre. As discussed earlier, this procedure can translate a set of time-integrated PL spectra each for carriers diffusing through a specific distance into a single diffusion curve as shown in figure 6.12. Both the blue and green site emissions are fitted with Gaussian functions since it is the natural solution to describe a diffusion process given the second order spatial derivative involved in equation (6.2). The corresponding diffusion lengths are obtained to be 5.70 μm for the blue peak and 1.12 μm for the green SE peak. As mentioned before, this number is a calibration for the capability of carriers to move in matters before they settle down or get transformed and thus it can be used to represent an average distance travelled by a particular type of carriers. The green site diffusion length approaching the size of the laser spot hence directly reflects the restriction for carrier movements outside the defect region and it has quantified the associated localisation strength. Since this length is comparable to our spatial resolution limit, it is likely that the actual confinement area is even smaller. In contrast, the diffusion length for the interface excitons falls within the reported range spanning 290 nm to 9.2 μm for $CsPbBr_3$ based nanocrystal systems. Clearly, it is not only a valid result but also sits in the long-diffusion length part among all those

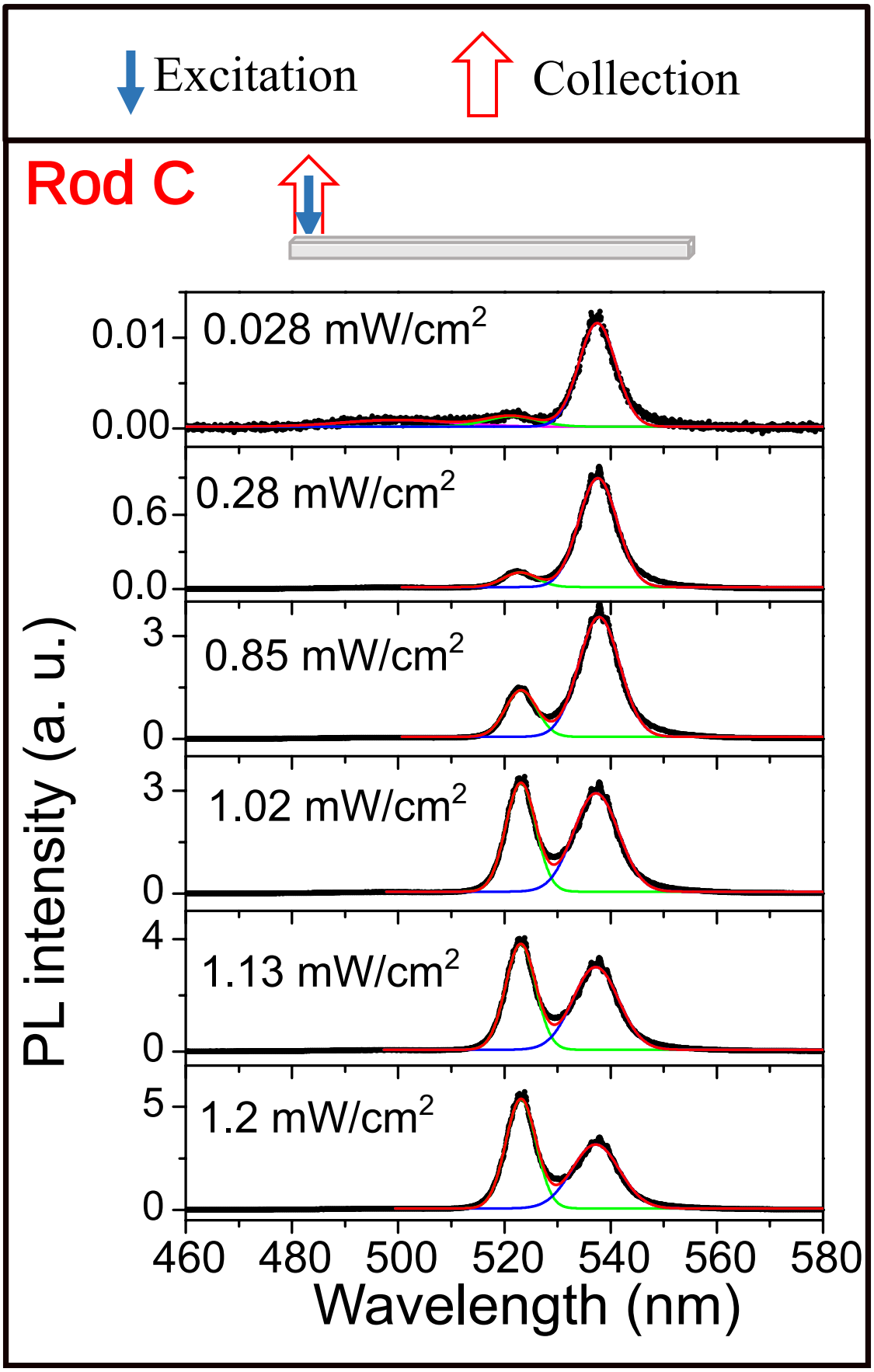
Excitation
Collection
Rod C
0.028 mW/cm2
0.28 mW/cm2
0.85 mW/cm2
1.02 mW/cm2
1.13 mW/cm2
1.2 mW/cm2
PL intensity (a. u.)
Wavelength (nm)

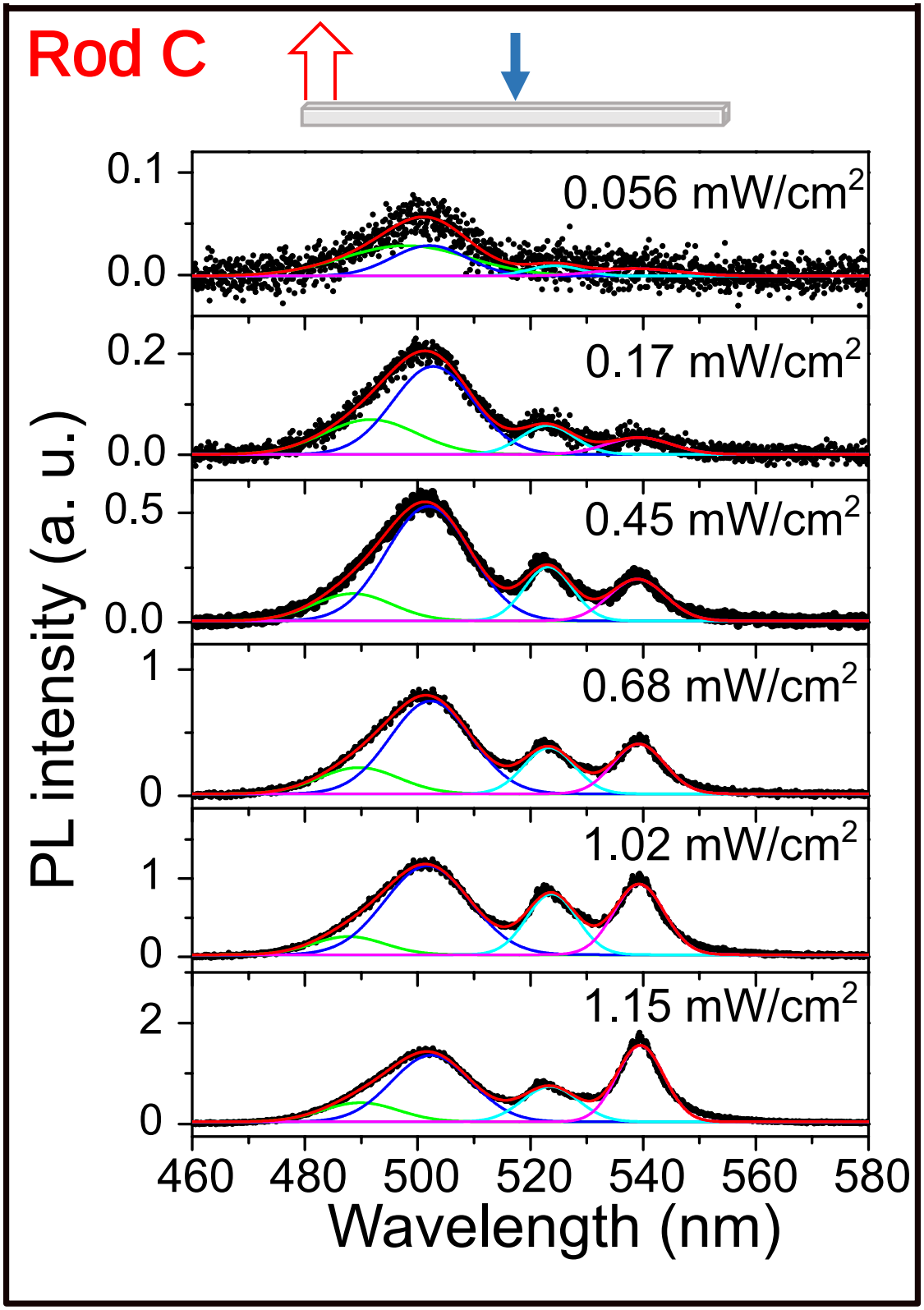

Figure 6.11: Power-dependent separable excitation-collection μPL spectra taken at 4.5 K for rod C. The left panel shows the measurement results obtained by fixing both excitation and collection beams at one end of the rod. In the right panel, the excitation has been moved to the centre of the rod while the position for collection spot is unchanged. The emission peaks are all fitted with solid lines.

reported numbers. These results are consistent to the discussion from last paragraph and they have brought up a much finer view into the detailed diffusion characteristics.

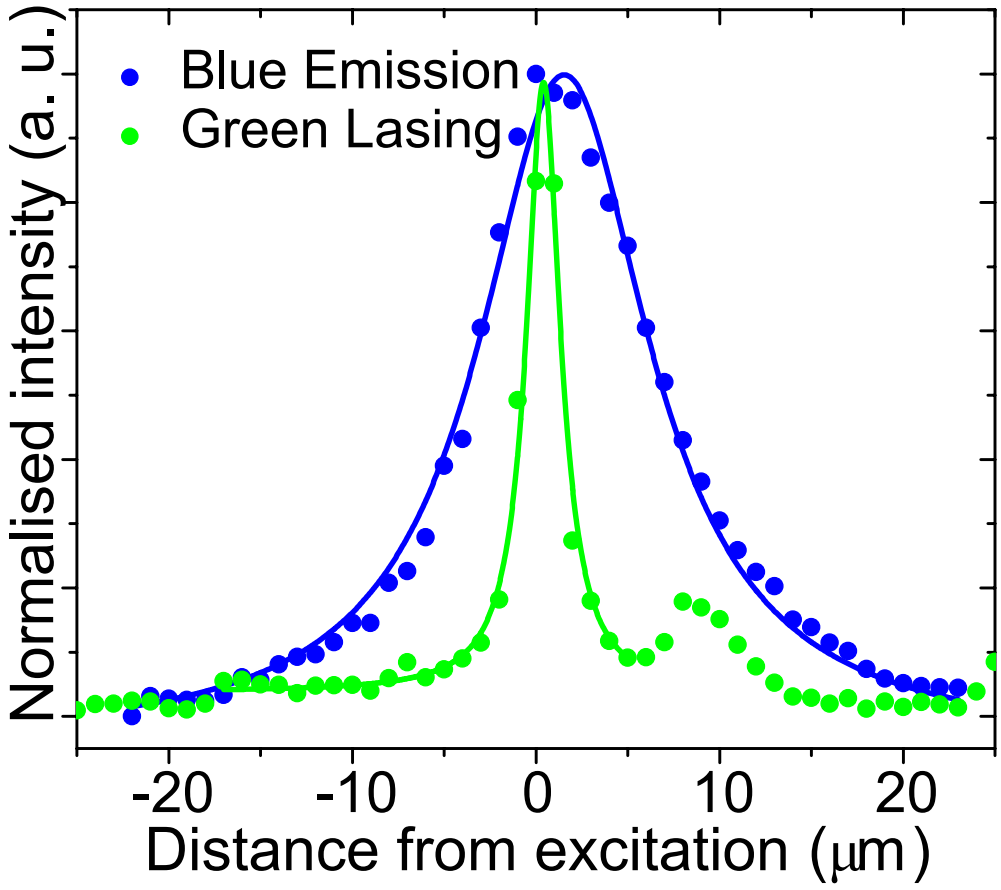

Figure 6.12: 1D μPL scan of the collection spot along the rod while fixing excitation at the centre. Dependence of integrated PL counts against separation distance is plotted for both the interface site and defect site. The two dataset are both fitted with a Gaussian function to extract diffusion lengths of 5.70 μm and 1.12 μm respectively.

Finally, figure 6.13(a) has exhibited a set of TRPL plots for the two sites to extract their lifetimes. Although lifetime has already been absorbed into diffusion length by the form of equation (6.2), it still contains some important information on its own to isolate solely the temporal length that a carrier lives. The associate values obtained for the blue site and green SE site are 865 ps and 182 ps respectively. Since both lifetimes are very short, in the sense that they are in the same order of magnitude to IRF, convolution with IRF has been applied while fitting the result (see chapter on background). The significantly shorter lifetime at defect states (green site) stems from the enhancement on the SE mechanism due to the increased carrier density from the localisation effect. An electron-hole plasma is

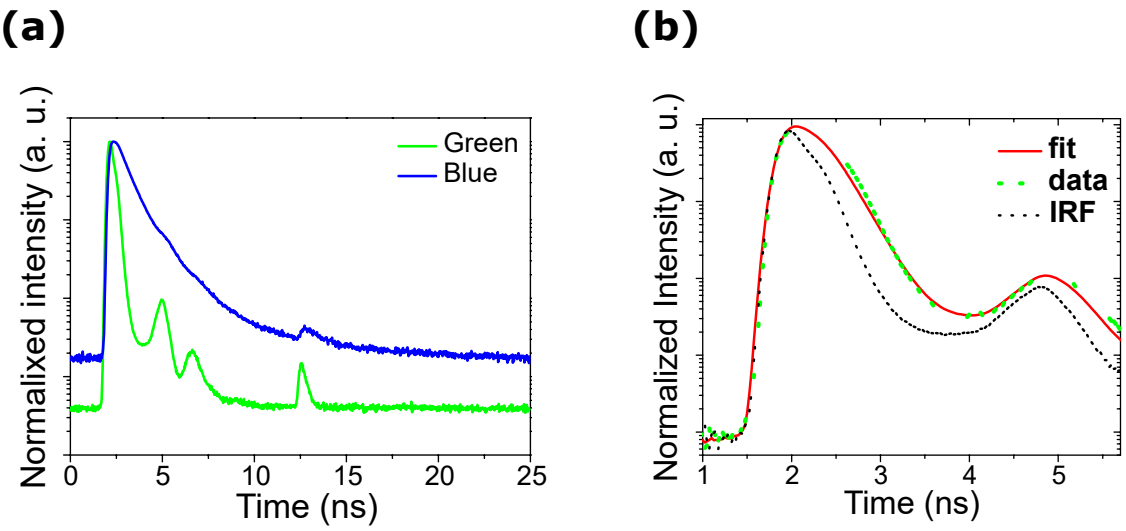

Figure 6.13: (a) TRPL decay curves for the blue emission at the hydroxide interface and green emission from the defect sites. The defect state exhibits a fast decay response due to the SE mechanism involved, hence spiky features are observed for the green decay curve which attributes to the IRF function of the TCPC system.(b) Zoomed-in image of the first 5 ns for the defect decay curve. An IRF response is also plotted explicitly.

initially formed near the excitation laser spot after the energetic short-pulse pumping. The optical amplification process is then boosted with a dense pool of excited carriers restricted in space. Therefore, they have very limited chance to survive the interaction with other carriers and escape the spot. This can be understood with their very fast decay time and it also gives an explanation to the resolution-limited diffusion length. As for the blue site emission, stabilisation of the peripheral structure has been achieved via hydroxide coating along the perovskite surface and it has led to passivation of the edge states. The blue excitons are hence moving with less resistance and no local concentration of carriers is expected. This means these carriers can live longer and effectively help build a more uniform carrier density distribution along the rod through diffusion before they eventually recombine, which explains the increased lifetime and a longer distance travelled associated with the blue curves.

Chapter 7

Conclusion

This chapter summarises the key experimental results encountered in this thesis.

Chapter 4 presents a clear demonstration of the symmetric Gaussian modes, including a fundamental longitudinal mode and a series of higher order TEM modes, directly observed in self-assembled cavities formed by $CsPbBr_3$ QDs. The identity of these modes are verified through mode wavelength simulation using material and structural parameters and the symmetric mode profiles can be directly seen from the sub-μm 2D PL maps. At cryogenic temperatures, the linewidths of the modes are measured to be 0.085nm, which hits the resolution power of the spectrometer. This signals a potentially much higher quality factor over 6000 might be present. The coherent nature of the SE signal has also been examined via a first-order correlation measurement using a Michelson interferometer. The extracted coherence time of 9.5ps is more than 230 times longer than that of the SPE background. All these information can support a high-quality lasing source with promising device applications.

Further investigation on these modes via temperature and pumping strength tuning has revealed two degrees of control over the specific modes currently in operation. The temperature tuning continuously shifts the mode wavelength without causing the linewidth to broaden beyond the resolution of our spectrometer. On the other hand, pumping strength can switch on new modes while shutting down the currently existing modes. These intrinsic degrees of control sheds light on the potential development of such crystal system into

functional microlasers or ultrafast optoelectronics.

Chapter 5 looks into the triplet emission from a tetragonal-phase $CsPbBr_3$ nanocrystal system. Verification of the degenerately split states with an energy separation of 2meV is successfully carried out by showing the orthogonal linear-polarisation relationship between the two emission lines. TRPL measurement indicating a lifetime of 268ps along with the observed Stokes shift of 18meV further support that the nanocrystals are each of 10nm size and can give rise to the expected bright triplet state. It is also demonstrated that lasing emission has been developed based on the distinguished triplet line and this signal can be optimised by tuning the pumping wavelength towards the near-resonant regime. The resonantly pumped emission not only exhibits faster intensity response to the pumping strength but also shows higher contrast over the background emission. This behaviour is ideal for building a spectrally-pure and bright coherent light source.

A general limitation in the work above stems from the fact that all the results were obtained at cryogenic temperature. Industry-standard applications require both reliable and outstanding operation at room temperature and hence these results are far from being adopted in a real system. However, they do provide an angle of thought for designing the nanostructures to exploit the fundamental physics and this is already a step beyond sole observation of the phenomena. For these two examples, more chemistry manipulation such as encapsulation or ligand related operations can be added for enhancing the stability of the system and maintaining these behaviours towards a higher temperature.

Chapter 6 shows how surface passivation with $Pb(OH)_2$ coating onto the $CsPbBr_3$ nano/micro-rods can produce a blue-shifted excitonic emission site which is robust against temperature change. A comparison study on rods of various diameters has indicated that such emission is from the interface layer between the hydroxide cladding and inner perovskite core. Any defect sites arising from lattice mismatch for bigger rods can locally trap the carriers and exhibit SE at high pumping strength within the expected pure perovskite emission wavelength. These behaviours have been thoroughly characterised from temperature-dependent comparison, pumping strength-dependent comparison, 2D PL map comparison and TRPL

study to form a complete picture of the underlying reasoning for the emissions. However, further investigation is still required to understand the splitting into the two emission sites at cryogenic temperature. This can be investigated using a dynamics study possibly combined with a more detailed electronic property characterisation of the structure at low temperatures. The decoupling from the thermal bath may inspire new thoughts into fabrication of efficient devices in the field of optoelectronics.

Appendix A

2D Map Viewer

In chapter 2, the concept of 2D mapping has been introduced as a functionality of the μPL system. The operation is essentially taking single time-integrated spectra associated with a set of different spatial coordinates. Equipped with this knowledge, it is obvious that the resulting data is actually a three-dimensional data array with indices spanning x coordinates, y coordinates and wavelengths. The analysis hence becomes complicated at this point due to the existence of four variables including the photon counts and there is no way to present all the four orthogonal axes in a single three-dimensional picture. Therefore, a map viewer UI (user interface) has been developed specifically for this type of data analysis. The prototype was initially created by a former PhD student Luke P. Nuttall and further developed by myself to enclose all the following functions on the map data. All the map results discussed in this thesis are demonstrated by this software.

Figure A.1 illustrates the UI. The program consists of three panels from left to right and they are the map/figure panel, button panel and data panel. Out of the three, the most important is the map/figure panel. Within this panel, the top window exhibits a 2D colour map from the associated dataset. Upon loading the data file, the software can either recognise an ASCII format or a custom-defined binary format with JSON metadata specifying the detailed experimental parameters. Another piece of python code 'binmap.py' will be called and sorts all of these parameter into variables. This process will also extract

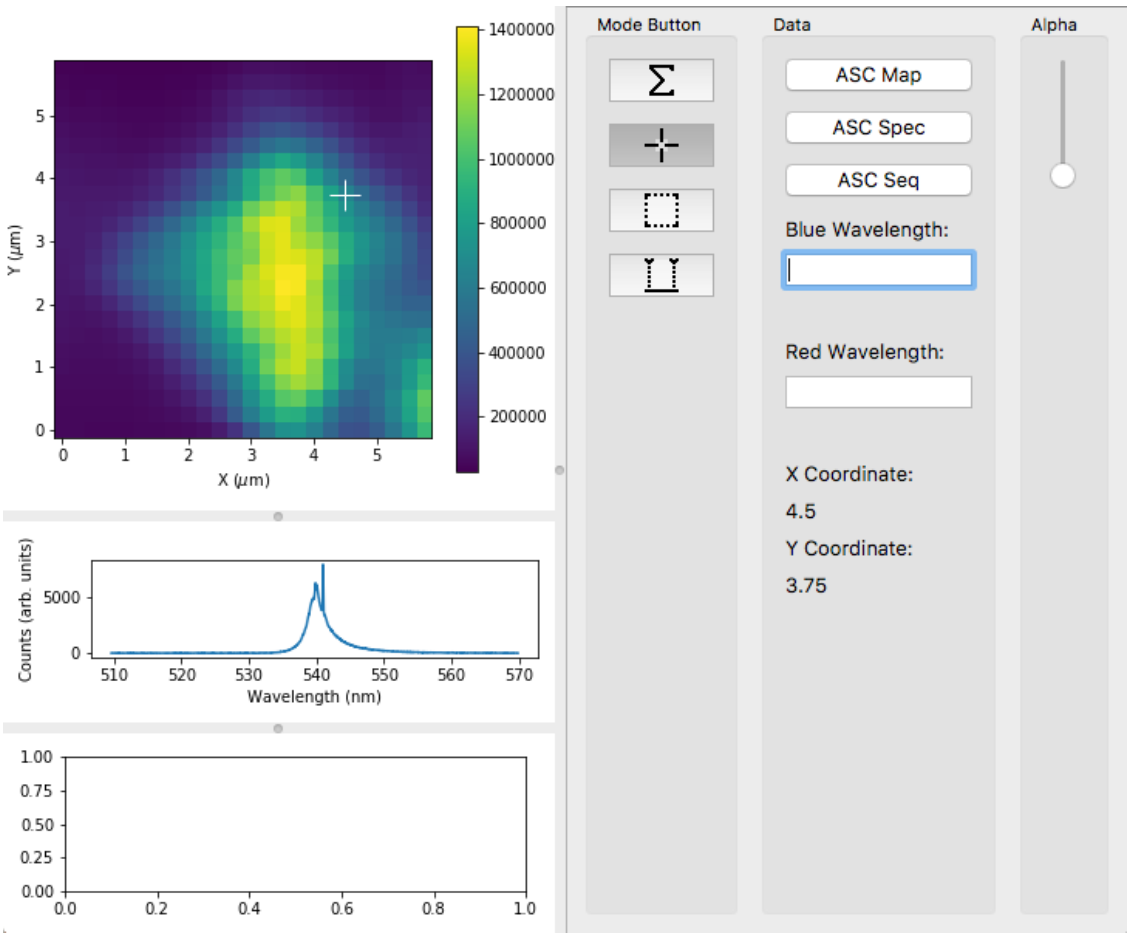

Figure A.1: The user interface for the 2D map viewer. The entire software consists of three panels, from left to right, are figure panel, button panel and data panel (including the alpha control for the case of two wavelength selection regions) respectively. In the figure panel, from top down, the windows are correspondingly map window, spectrum window and diffusion analysis window. The operations for the buttons are introduced in the text. This particular illustration is from an initial loading of the mapping file into the software, where the map window shows full wavelength-integrated map and no wavelength selection is enabled in the spectrum window.

the three independent variables 'x', 'y' and 'wavelength' and create an array of predefined class structure to contain all these information for a single data point. The reason for incorporating the alternative binary format is to reduce the stored data size as the saving process of large ASCII maps can crash the LabView program controlling the experiment. After the initialisation stage, the top window will be automatically filled to print a 2D map of the xy-coordinate matrix. The intensity at each pixel is integrated over the entire wavelength range and hence one degree of freedom has been removed. A colour bar to the right of the map is used to compare the relative intensity among the pixels to reveal local

intensity plateau and valleys. The white cross sitting at a single pixel can be thought of as a pointer to a specific spatial coordinate (like the pointer in C++ used to link to a stack of memory), where the detailed coordinate information can be read out from the Data panel 'X Coordinates' and 'Y Coordinates' in predefined units. The associated spectrum to this location is then presented in the second window from the top of the panel. By left clicking with the mouse at different locations in the 2D map, a spectrum corresponding to the nearest pixel will be updated in the second window. Therefore, the wavelength information lost in the 2D map is restored at this spectrum window.

The spectrum window itself actually has three operation modes. Right clicking on the mouse can cycle through these three modes. The first mode is the one illustrated above, where no operation can be done on the spectrum. By right clicking once, the window will be switched to the second mode as shown in figure A.2(a). In this mode, a wavelength selection tool bounded from both sides has appeared on the spectrum window. A simultaneous change on the 2D map in the map window will also be updated to show a colour map for the same set of pixels but with intensity at each pixel only integrated from the counts within the bounded wavelength region. The two boundaries of the coloured wavelength region can each be dragged with the left button of the mouse to travel along the wavelength axis such that any wavelength interval can be chosen within the wavelength limit of the data. There is also no problem by dragging the left boundary over the right boundary as the code will automatically correct for this action. Again the actual wavelengths of the two boundaries can be read out from 'Blue Wavelength' and 'Red Wavelength' on the Data panel. The names are associated with the relative wavelengths for the two colours in the spectrum, where blue stands for the shorter wavelength (left boundary) and red stands for longer wavelength (right boundary). This action enables the 2D map to show the spatial distribution for a specific spectral structure, *e.g.* lasing mode(see chapter 4) or to select from multiple Gaussian profiles(see chapter 6).

Right clicking on the spectrum window once more brings up another wavelength selection region in red colour. Each bounded region is still subject to automatic wavelength correction

itself for potential cross of boundaries but the different colours of the region is only for labelling purpose. The 2D map, in the mean time, has automatically changed to a blue-red colour map with the colours corresponding to the colours labelling the two wavelength regions in the spectrum window. The 2D map actually contains two layers of monochromatic colour map each plotted with a transparency 'α' scale of range [0,1] representing the change in intensity for its designated wavelength region. Therefore, the blue and red colours appearing on the 2D map are essentially individual 2D maps for the two separately bounded wavelength regions. Presented in this way, a comparison between two different spectral structures can be visualised directly. In addition, spatially dependent studies including diffusion analysis of different wavelengths can be made possible. It is worth noting that the Data panel now only indicates the boundary wavelengths for the blue panel at the moment.

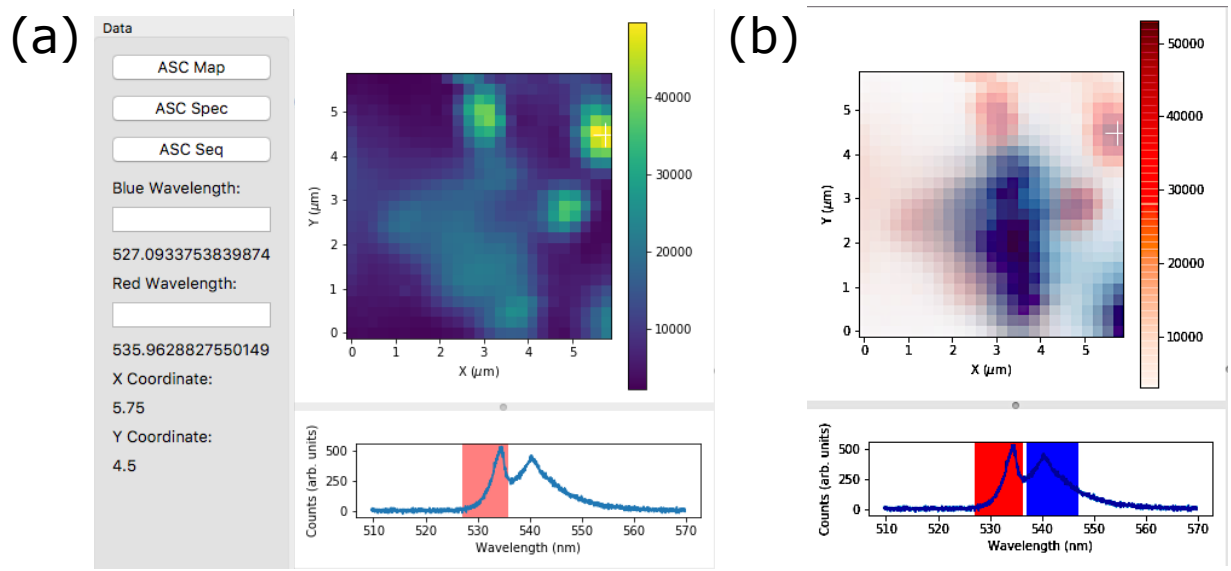

Figure A.2: Wavelength selection modes for the spectrum window. (a) Single wavelength selection region to illustrate an intensity map of the chosen wavelength range. (b) Two wavelength selection regions to compare the relative spatial distribution of PL intensity for the two identified peaks.

Now we have a combined operation of spatial selection on the 2D map window and wavelength selection on the spectrum window. This has converted the extra dimension of the data to a degree of control by the user in an embedded fashion and hence the full content of the underlying physical feature can be more easily retrieved.

Now turning back to the map window, it also has three different operation modes. Similarly, switching between the modes is done by right clicking on the map window. The first mode is with coordinate clicking operation with the white cross discussed above. When switching to the second mode, the white cross disappears and instead a white box shows up as shown in figure A.3(a). All the four sides of the white box can be dragged to adjust the size of the box. In addition, dragging with the left button of the mouse near the centre of the box can shift it around the map as a whole. The more important operation is associated with middle clicking inside the white box such that it will replot the 2D map only to the most closely resolved region bounded by its sides. This action can be seen from figure A.3(b) and it is essentially a 'zoom in' action, and it will replot the colour map with a scale according to the regional maximum and minimum intensities. Any effects from big intensity change outside the region or the global extrema will be discarded. Middle clicking the map window again can bring the user back to the global picture of the dataset.

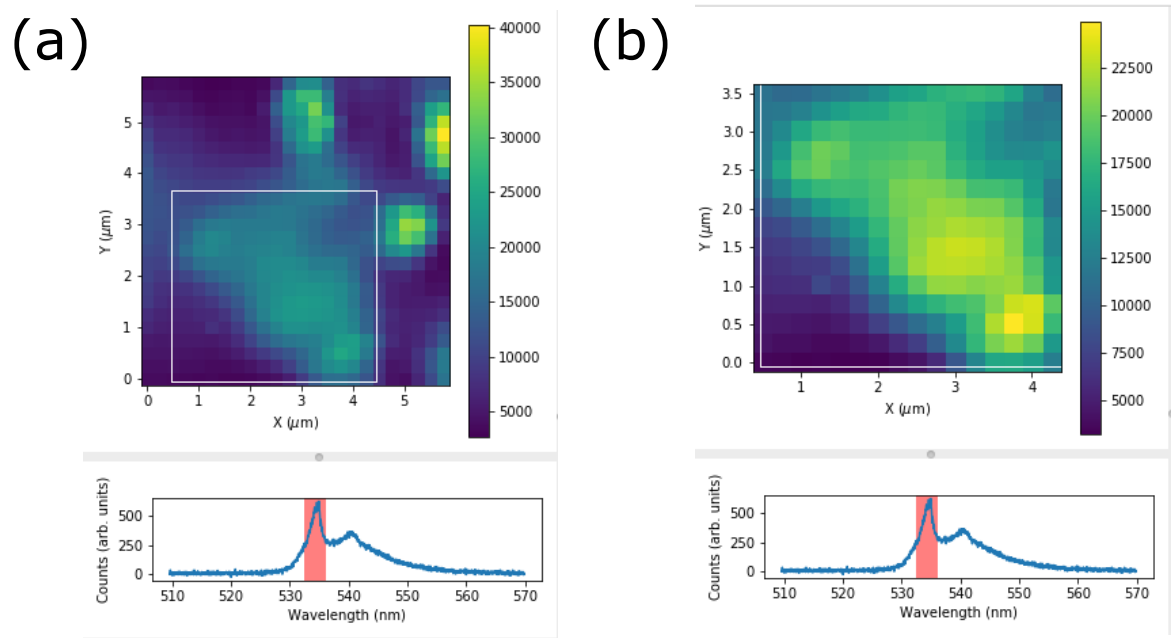

Figure A.3: 'Zoom' operation on the PL map window. (a) Box mode to select a region over the entire 2D map for detailed inspection. (b) The 'zoom in' view of the selected region in subplot (a), where the intensity map is replotted and rescaled only according to the specific local characteristics.

The last mode available in the map window is helpful for a diffusion analysis. Upon

entering this mode the white cross reappears and it becomes a node of a big white triangle. Middle click will change among the three nodes of the triangle and thus specifying the coordinate of each node determines the location and shape of the triangle. This operation will again select all the data points inside the bounded region but instead of zooming, it converts the Cartesian coordinates to polar coordinates with the white cross defining the origin. By including a property 'r' in the data class structure, all the data points encircled by the white triangle can now be sorted based on their spatial distance to the origin. The third window down from the top in the map/figure panel now exhibits the PL intensity plot of these selected points against their distance from the origin. Another remark here is to do with the intensity at each point, these values are determined by the mode currently employed in the spectrum window as discussed above. This type of analysis is particularly useful in scenarios of separate excitation and collection, as will become clear in section 'diffusion' of chapter 6.

There are currently four buttons in the button panel. Buttons at the top and the bottom are corresponding to the first mode and second mode of operation for the spectrum window. Left clicking these buttons can switch to the designated mode. Similarly, the second and third buttons are linked to the first and second mode in map window. Although the program is still under further development, the main necessary analysis and operations have already been built in and it has provided some of the key results for the experimental chapters of the thesis.

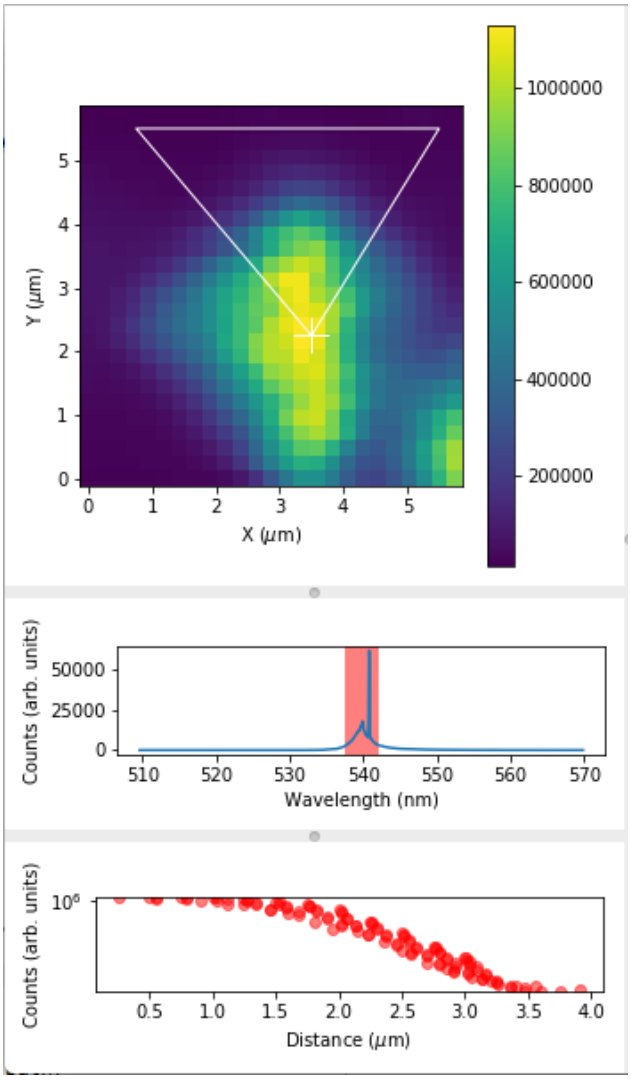

Figure A.4: A regional selection operation to convert the spatial coordinates of all the points encircled to a distance 'r' from a designated point in the map. The intensity is then plotted for those points against 'r' as in the bottom diffusion analysis window to show the change in PL counts away from this point.

Bibliography

[1] Neumann, W. *Fundamentals of dispersive optical spectroscopy systems* (Spie Press, 2014).

[2] Chang, Y. H., Park, C. H. & Matsuishi, K. First-principles study of the structural and the electronic properties of the lead-halide-based inorganic-organic perovskites $(CH_3NH_3)PbX_3$ and $CsPbX_3(X = Cl, Br, I)$. *Journal of the Korean Physical Society* **44**, 889 (2004).

[3] Umebayashi, T., Asai, K., Kondo, T. & Nakao, A. Electronic structures of lead iodide based low-dimensional crystals. *Physical Review B* **67** (2003).

[4] Goldschmidt, V. M. Krystallbau und chemische zusammensetzung. *Berichte der deutschen chemischen Gesellschaft (A and B Series)* **60**, 1263–1296 (1927).

[5] Li, C. *et al.* Formability of ABX_3 $(X = F, Cl, Br, I)$ halide perovskites. *Acta Crystallographica Section B: Structural Science* **64**, 702–707 (2008).

[6] Pang, S. *et al.* $NH_2CH{=}NH_2PbI_3$: An alternative organolead iodide perovskite sensitizer for mesoscopic solar cells. *Chemistry of Materials* **26**, 1485–1491 (2014).

[7] Eperon, G. E. *et al.* Formamidinium lead trihalide: a broadly tunable perovskite for efficient planar heterojunction solar cells. *Energy and Environmental Science* **7**, 982 (2014).

[8] Li, Z. *et al.* Stabilizing perovskite structures by tuning tolerance factor: Formation of formamidinium and cesium lead iodide solid-state alloys. *Chemistry of Materials* **28**, 284–292 (2015).

[9] Abdelmageed, G. *et al.* Mechanisms for light induced degradation in $MAPbI_3$ perovskite thin films and solar cells. *Applied Physics Letters* **109**, 233905 (2016).

[10] Niu, G., Guo, X. & Wang, L. Review of recent progress in chemical stability of perovskite solar cells. *Journal of Materials Chemistry A* **3**, 8970–8980 (2015).

[11] Lee, J.-W. *et al.* Formamidinium and cesium hybridization for photo- and moisture-stable perovskite solar cell. *Advanced Energy Materials* **5**, 1501310 (2015).

[12] Sidgwick, N. V. *The electronic theory of valency* (Oxford Univ.-Press, 1927).

[13] Madan, R. D. *Satya Parkash's modern inorganic chemistry* (S. Chand, 1987).

[14] Umari, P., Mosconi, E. & De Angelis, F. Relativistic gw calculations on $CH_3NH_3PbI_3$ and $CH_3NH_3SnI_3$ perovskites for solar cell applications. *Scientific Reports* **4**, 4467 (2014).

[15] Pyykko, P. Relativistic effects in structural chemistry. *Chemical Reviews* **88**, 563–594 (1988).

[16] Stoumpos, C. C., Malliakas, C. D. & Kanatzidis, M. G. Semiconducting tin and lead iodide perovskites with organic cations: Phase transitions, high mobilities, and near-infrared photoluminescent properties. *Inorganic Chemistry* **52**, 9019–9038 (2013).

[17] Hao, F., Stoumpos, C. C., Cao, D. H., Chang, R. P. H. & Kanatzidis, M. G. Lead-free solid-state organic–inorganic halide perovskite solar cells. *Nature Photonics* **8**, 489–494 (2014).

[18] Bernal, C. & Yang, K. First-principles hybrid functional study of the organic–inorganic perovskites $CH_3NH_3SnBr_3$ and $CH_3NH_3SnI_3$. *The Journal of Physical Chemistry C* **118**, 24383–24388 (2014).

[19] Ogomi, Y. *et al.* $CH_3NH_3Sn_xPb_{1-x}I_3$ perovskite solar cells covering up to 1060 nm. *The Journal of Physical Chemistry Letters* **5**, 1004–1011 (2014).

[20] Butler, K. T., Frost, J. M. & Walsh, A. Band alignment of the hybrid halide perovskites $CH_3NH_3PbCl_3$, $CH_3NH_3PbBr_3$ and $CH_3NH_3PbI_3$. *Materials Horizons* **2**, 228–231 (2015).

[21] Protesescu, L. *et al.* Nanocrystals of cesium lead halide perovskites (($CsPbX_3$ $X = Cl, BrandI$)): Novel optoelectronic materials showing bright emission with wide color gamut. *Nano Letters* **15**, 3692–3696 (2015).

[22] Zory, P. S. Quantum well lasers. *Academic Press* 1–13 (1993).

[23] Liu, Z. *et al.* Micro-light-emitting diodes with quantum dots in display technology. *Light: Science & Applications* **9**, 83 (2020).

[24] Datta, K. & Khorsru, Q. D. M. Iii–v tri-gate quantum well mosfet: Quantum ballistic simulation study for 10 nm technology and beyond. *Solid-State Electronics* **118**, 66–77 (2016).

[25] Ekimov, A., Efros, A. & Onushchenko, A. Quantum size effect in semiconductor microcrystals. *Solid State Communications* **56**, 921–924 (1985).

[26] Rossetti, R., Nakahara, S. & Brus, L. E. Quantum size effects in the redox potentials, resonance raman spectra, and electronic spectra of cds crystallites in aqueous solution. *The Journal of Chemical Physics* **79**, 1086–1088 (1983).

[27] Miller, D. A. B. Optoelectronic applications of quantum wells. *Optics and Photonics News* **1**, 7–14 (1990).

[28] Konstantatos, G. *Colloidal quantum dot optoelectronics and photovoltaics* (Cambridge Univ. Press, 2013).

[29] Sercel, P. C. & Vahala, K. J. Analytical formalism for determining quantum-wire and quantum-dot band structure in the multiband envelope-function approximation. *Physical Review B* **42**, 3690–3710 (1990).

[30] Ashcroft, N. W., Mermin, N. D. & Company, B. P. *Solid state physics* (Brooks/Cole Cengage Learning Learning, 2018).

[31] Klimov, V. I. *et al.* Optical gain and stimulated emission in nanocrystal quantum dots. *Science* **290**, 314–317 (2000).

[32] Cooney, R. R., Sewall, S. L., Sagar, D. M. & Kambhampati, P. Gain control in semiconductor quantum dots via state-resolved optical pumping. *Physical Review Letters* **102** (2009).

[33] Dang, C. *et al.* Red, green and blue lasing enabled by single-exciton gain in colloidal quantum dot films. *Nature Nanotechnology* **7**, 335–339 (2012).

[34] Gaponenko, S. V. *Optical properties of semiconductor nanocrystals* (Cambridge University Press, 1998).

[35] Utzat, H. *et al.* Coherent single-photon emission from colloidal lead halide perovskite quantum dots. *Science* **363**, 1068–1072 (2019).

[36] Wang, Y. *et al.* All-inorganic colloidal perovskite quantum dots: A new class of lasing materials with favorable characteristics. *Advanced Materials* **27**, 7101–7108 (2015).

[37] Rainò, G. *et al.* Superfluorescence from lead halide perovskite quantum dot superlattices. *Nature* **563**, 671–675 (2018).

[38] Murray, C. B., Kagan, C. R. & Bawendi, M. G. Synthesis and characterization of monodisperse nanocrystals and close-packed nanocrystal assemblies. *Annual Review of Materials Science* **30**, 545–610 (2000).

[39] Krieg, F. *et al.* Colloidal $CsPbX_3$ ($X = Cl, Br, I$) nanocrystals 2.0: Zwitterionic capping ligands for improved durability and stability. *ACS Energy Letters* **3**, 641–646 (2018).

[40] Fox, M. *Quantum optics : an introduction* (Oxford University Press, 2006).

[41] Foot, C. J. *Atomic physics* (Oxford University Press, 2005).

[42] Binney, J. & Skinner, D. *The Physics of Quantum Mechanics* (Oxford University Press, 2013).

[43] Umebayashi, T., Asai, K., Kondo, T. & Nakao, A. Electronic structures of lead iodide based low-dimensional crystals. *Physical Review B* **67** (2003).

[44] Filippetti, A. & Mattoni, A. Hybrid perovskites for photovoltaics: Insights from first principles. *Physical Review B* **89** (2014).

[45] Brandt, R. E., Stevanović, V., Ginley, D. S. & Buonassisi, T. Identifying defect-tolerant semiconductors with high minority-carrier lifetimes: beyond hybrid lead halide perovskites. *MRS Communications* **5**, 265–275 (2015).

[46] Ravi, V. K., Markad, G. B. & Nag, A. Band edge energies and excitonic transition probabilities of colloidal $CsPbX_3$ ($X = Cl, Br, I$) perovskite nanocrystals. *ACS Energy Letters* **1**, 665–671 (2016).

[47] Kojima, A., Teshima, K., Shirai, Y. & Miyasaka, T. Organometal halide perovskites as visible-light sensitizers for photovoltaic cells. *Journal of the American Chemical Society* **131**, 6050–6051 (2009).

[48] Schulz, P. *et al.* Interface energetics in organo-metal halide perovskite-based photovoltaic cells. *Energy & Environmental Science* **7**, 1377 (2014).

[49] Ryu, S. *et al.* Voltage output of efficient perovskite solar cells with high open-circuit voltage and fill factor. *Energy Environ. Sci.* **7**, 2614–2618 (2014).

[50] Frenkel, J. On the transformation of light into heat in solids. i. *Physical Review* **37**, 17–44 (1931).

[51] Wannier, G. H. The structure of electronic excitation levels in insulating crystals. *Physical Review* **52**, 191–197 (1937).

[52] Fox, M. *Optical properties of solids* (Oxford University Press, 2012).

[53] Elliott, R. J. Intensity of optical absorption by excitons. *Physical Review* **108**, 1384–1389 (1957).

[54] Baranowski, M. & Plochocka, P. Excitons in metal-halide perovskites. *Advanced Energy Materials* 1903659 (2020).

[55] Singh, S. *et al.* Effect of thermal and structural disorder on the electronic structure of hybrid perovskite semiconductor $CH_3NH_3PbI_3$. *The Journal of Physical Chemistry Letters* **7**, 3014–3021 (2016).

[56] Panzer, F., Li, C., Meier, T., Köhler, A. & Huettner, S. Impact of structural dynamics on the optical properties of methylammonium lead iodide perovskites. *Advanced Energy Materials* **7**, 1700286 (2017).

[57] Saba, M. *et al.* Correlated electron–hole plasma in organometal perovskites. *Nature Communications* **5** (2014).

[58] Yang, Y. *et al.* Low surface recombination velocity in solution-grown $CH_3NH_3PbBr_3$ perovskite single crystal. *Nature Communications* **6** (2015).

[59] Yang, Y. *et al.* Observation of a hot-phonon bottleneck in lead-iodide perovskites. *Nature Photonics* **10**, 53–59 (2015).

[60] Yamada, Y., Nakamura, T., Endo, M., Wakamiya, A. & Kanemitsu, Y. Photoelectronic responses in solution-processed perovskite $CH_3NH_3PbI_3$ solar cells studied by photoluminescence and photoabsorption spectroscopy. *IEEE Journal of Photovoltaics* **5**, 401–405 (2015).

[61] Sestu, N. *et al.* Absorption f-sum rule for the exciton binding energy in methylammonium lead halide perovskites. *The Journal of Physical Chemistry Letters* **6**, 4566–4572 (2015).

[62] Ruf, F. *et al.* Temperature-dependent studies of exciton binding energy and phase-transition suppression in $(Cs, FA, MA)Pb(I, Br)_3$ perovskites. *APL Materials* **7**, 031113 (2019).

[63] Even, J., Pedesseau, L. & Katan, C. Analysis of multivalley and multibandgap absorption and enhancement of free carriers related to exciton screening in hybrid perovskites. *The Journal of Physical Chemistry C* **118**, 11566–11572 (2014).

[64] D'Innocenzo, V. *et al.* Excitons versus free charges in organo-lead tri-halide perovskites. *Nature Communications* **5** (2014). URL `https://www.nature.com/articles/ncomms4586`.

[65] Miyata, A. *et al.* Direct measurement of the exciton binding energy and effective masses for charge carriers in organic–inorganic tri-halide perovskites. *Nature Physics* **11**, 582–587 (2015).

[66] Galkowski, K. *et al.* Excitonic properties of low-band-gap lead–tin halide perovskites. *ACS Energy Letters* **4**, 615–621 (2019).

[67] Anusca, I. *et al.* Dielectric response: Answer to many questions in the methylammonium lead halide solar cell absorbers. *Advanced Energy Materials* **7**, 1700600 (2017).

[68] Onoda-Yamamuro, N., Matsuo, T. & Suga, H. Dielectric study of $CH_3NH_3PbX_3(X = Cl, Br, I)$. *Journal of Physics and Chemistry of Solids* **53**, 935–939 (1992).

[69] Guo, Y. *et al.* Dynamic emission stokes shift and liquid-like dielectric solvation of band edge carriers in lead-halide perovskites. *Nature Communications* **10** (2019).

[70] Miyata, K. *et al.* Large polarons in lead halide perovskites. *Science Advances* **3** (2017).

[71] Egger, D. A. *et al.* What remains unexplained about the properties of halide perovskites? *Advanced Materials* **30**, 1800691 (2018).

[72] Feynman, R. P. Slow electrons in a polar crystal. *Physical Review* **97**, 660–665 (1955).

[73] Menéndez-Proupin, E., Beltrán Ríos, C. L. & Wahnón, P. Nonhydrogenic exciton spectrum in perovskite $CH_3NH_3PbI_3$. *physica status solidi (RRL) - Rapid Research Letters* **9**, 559–563 (2015).

[74] Sendner, M. *et al.* Optical phonons in methylammonium lead halide perovskites and implications for charge transport. *Materials Horizons* **3**, 613–620 (2016).

[75] Melissen, S. T. A. G., Labat, F., Sautet, P. & Le Bahers, T. Electronic properties of $PbX_3CH_3NH_3(X = Cl, Br, I)$ compounds for photovoltaic and photocatalytic applications. *Physical Chemistry Chemical Physics* **17**, 2199–2209 (2015).

[76] Wilson, J. N., Frost, J. M., Wallace, S. K. & Walsh, A. Dielectric and ferroic properties of metal halide perovskites. *APL Materials* **7**, 010901 (2019).

[77] Létoublon, A. *et al.* Elastic constants, optical phonons, and molecular relaxations in the high temperature plastic phase of the $CH_3NH_3PbBr_3$ hybrid perovskite. *The Journal of Physical Chemistry Letters* **7**, 3776–3784 (2016).

[78] Haken, H. Die theorie des exzitons im festen körper. *Fortschritte der Physik* **6**, 271–334 (1958).

[79] Bajaj, K. Effect of electron-phonon interaction on the binding energy of a wannier exciton in a polarizable medium. *Solid State Communications* **15**, 1221–1224 (1974).

[80] Shockley, W. & Read, W. T. Statistics of the recombinations of holes and electrons. *Physical Review* **87**, 835–842 (1952).

[81] Street, R. A., Schoendorf, M., Roy, A. & Lee, J. H. Interface state recombination in organic solar cells. *Physical Review B* **81** (2010).

[82] Tzabari, L. & Tessler, N. Shockley–read–hall recombination in p3ht:pcbm solar cells as observed under ultralow light intensities. *Journal of Applied Physics* **109**, 064501 (2011).

[83] Wu, X. *et al.* Efficient perovskite solar cells via surface passivation by a multifunctional small organic ionic compound. *Journal of Materials Chemistry A* **8**, 8313–8322 (2020).

[84] Chen, B., Rudd, P. N., Yang, S., Yuan, Y. & Huang, J. Imperfections and their passivation in halide perovskite solar cells. *Chemical Society Reviews* **48**, 3842–3867 (2019).

[85] Li, C. *et al.* Perovskite passivation strategies for efficient and stable solar cells. *Solar RRL* **5**, 2000579 (2020).

[86] Kao, K. C. *Dielectric phenomena in solids.* (Elsevier, 2004).

[87] Kirk, A. P. *Solar photovoltaic cells : photons to electricity* (Academic Press, An Inprint Of Elsevier, 2015).

[88] Li, S. S. *Semiconductor physical electronics* (Springer, 2010).

[89] Zhang, S. B. & Wei, S.-H. Surface energy and the common dangling bond rule for semiconductors. *Physical Review Letters* **92** (2004).

[90] Komsa, H.-P. & Pasquarello, A. Dangling bond charge transition levels in AlAs, GaAs, and InAs. *Applied Physics Letters* **97**, 191901 (2010).

[91] Warren, W. L., Robertson, J. & Kanicki, J. Si and n dangling bond creation in silicon nitride thin films. *Applied Physics Letters* **63**, 2685–2687 (1993).

[92] Wang, F. *et al.* Iodine-assisted antisolvent engineering for stable perovskite solar cells with efficiency 21.3%. *Nano Energy* **67**, 104224 (2020).

[93] Kang, J. & Wang, L.-W. High defect tolerance in lead halide perovskite $CsPbBr_3$. *The Journal of Physical Chemistry Letters* **8**, 489–493 (2017).

[94] Fang, Z. *et al.* Dual passivation of perovskite defects for light-emitting diodes with external quantum efficiency exceeding 20%. *Advanced Functional Materials* **30**, 1909754 (2020).

[95] Giovanni, D. *et al.* Origins of the long-range exciton diffusion in perovskite nanocrystal films: photon recycling vs exciton hopping. *Light: Science & Applications* **10** (2021).

[96] Penzo, E. *et al.* Long-range exciton diffusion in two-dimensional assemblies of cesium lead bromide perovskite nanocrystals. *ACS Nano* **14**, 6999–7007 (2020).

[97] Herz, L. M. Charge-carrier dynamics in organic-inorganic metal halide perovskites. *Annual Review of Physical Chemistry* **67**, 65–89 (2016).

[98] Li, Z. & Scheraga, H. A. Monte carlo-minimization approach to the multiple-minima problem in protein folding. *Proceedings of the National Academy of Sciences* **84**, 6611–6615 (1987).

[99] Olson, B., Hashmi, I., Molloy, K. & Shehu, A. Basin hopping as a general and versatile optimization framework for the characterization of biological macromolecules. *Advances in Artificial Intelligence* **2012**, 1–19 (2012).

[100] MAIMAN, T. H. Stimulated optical radiation in ruby. *Nature* **187**, 493–494 (1960).

[101] Geusic, J. E., Marcos, H. M. & Van Uitert, L. G. Laser oscillations in nd-doped yttrium aluminum, yttrium gallium and gadolinium garnets. *Applied Physics Letters* **4**, 182–184 (1964).

[102] Rana, F. Lecture 11: Basics of semiconductor lasers. URL `https://courses.cit.cornell.edu/ece533/Lectures/Lectures.htm`.

[103] Hooker, S. & Webb, C. E. *Laser physics* (Oxford Univ. Press, 2011).

[104] Renk, K. F. *BASICS OF LASER PHYSICS : for students of science and engineering.* (Springer, 2019).

[105] Staelin, D. H. 6.013 recitation 25: Gain saturation, laser oscillators and fabry-perot filters gain saturation in optical amplifiers and lasers (2002). URL `http://www2.myoops.org/twocw/mit/NR/rdonlyres/Electrical-Engineering-and-Computer-Science/6-013Electromagnetics-and-ApplicationsFall2002/ED9EE666-7EED-4FD5-81C7-0C5FD79F71A7/0/Rec25\_Notes.pdf`.

[106] Paschotta, R. *Field guide to lasers* (Spie Press, 2008).

[107] Koechner, W. *Solid state laser engineering* (Berlin Heidelberg New York Barcelona Budapest Hong Kong London Milan Paris Santa Clara Singapore Tokyo Springer, 1996).

[108] Parvin, P., Zaeferani, M. S., Mirabbaszadeh, K. & Sadighi, R. Measurement of the small-signal gain and saturation intensity of a xef discharge laser. *Applied Optics* **36**, 1139–1142 (1997).

[109] Matsuzaka, F., Yokozawa, T. & Hara, H. Saturation parameter and small-signal gain of a laser-diode-pumped tm:yag laser. *Applied Optics* **37**, 5710–5712 (1998).

[110] Smith, A. W. & Armstrong, J. A. Laser photon counting distributions near threshold. *Physical Review Letters* **16**, 1169–1172 (1966).

[111] Chang, R., Detenbeck, R., Korenman, V., Alley, C. & Hochuli, U. Photon bunching in a laser at threshold. *Physics Letters A* **25**, 272–273 (1967).

[112] Wiersig, J. *et al.* Direct observation of correlations between individual photon emission events of a microcavity laser. *Nature* **460**, 245–249 (2009).

[113] Strauf, S. *et al.* Self-tuned quantum dot gain in photonic crystal lasers. *Physical Review Letters* **96** (2006).

[114] Ulrich, S. M. *et al.* Photon statistics of semiconductor microcavity lasers. *Physical Review Letters* **98** (2007).

[115] Vahala, K. J. Optical microcavities. *Nature* **424**, 839–846 (2003). URL `https://www.nature.com/articles/nature01939`.

[116] Reitzenstein, S. *et al.* Single quantum dot controlled lasing effects in high-q micropillar cavities. *Optics Express* **16**, 4848 (2008).

[117] Rice, P. R. & Carmichael, H. J. Photon statistics of a cavity-qed laser: A comment on the laser–phase-transition analogy. *Physical Review A* **50**, 4318–4329 (1994).

[118] Fricke, J. Transport equations including many-particle correlations for an arbitrary quantum system: A general formalism. *Annals of Physics* **252**, 479–498 (1996).

[119] Kira, M., Jahnke, F., Hoyer, W. & Koch, S. Quantum theory of spontaneous emission and coherent effects in semiconductor microstructures. *Progress in Quantum Electronics* **23**, 189–279 (1999).

[120] Protesescu, L. *et al.* Nanocrystals of cesium lead halide perovskites ($CsPbX_3$, $X = Cl, Br, I$): Novel optoelectronic materials showing bright emission with wide color gamut. *Nano Letters* **15**, 3692–3696 (2015).

[121] Swarnkar, A. *et al.* Colloidal $CsPbBr_3$ perovskite nanocrystals: Luminescence beyond traditional quantum dots. *Angewandte Chemie (International Ed. in English)* **54**, 15424–15428 (2015).

[122] Stoumpos, C. C. *et al.* Crystal growth of the perovskite semiconductor $CsPbBr_3$: A new material for high-energy radiation detection. *Crystal Growth & Design* **13**, 2722–2727 (2013).

[123] Chen, X. *et al.* $CsPbBr_3$ perovskite nanocrystals as highly selective and sensitive spectrochemical probes for gaseous hcl detection. *Journal of Materials Chemistry C* **5**, 309–313 (2017).

[124] Xuan, T. *et al.* Highly stable $CsPbBr_3$ quantum dots coated with alkyl phosphate for white light-emitting diodes. *Nanoscale* **9**, 15286–15290 (2017).

[125] Di, X. *et al.* Use of long-term stable $CsPbBr_3$ perovskite quantum dots in phosphosilicate glass for highly efficient white leds. *Chem. Commun.* **53**, 11068–11071 (2017).

[126] Dang, Z. *et al.* In situ transmission electron microscopy study of electron beam-induced transformations in colloidal cesium lead halide perovskite nanocrystals. *ACS Nano* **11**, 2124–2132 (2017).

[127] Zhu, H. *et al.* Lead halide perovskite nanowire lasers with low lasing thresholds and high quality factors. *Nature Materials* **14**, 636–642 (2015).

[128] Becker, M. A. *et al.* Bright triplet excitons in caesium lead halide perovskites. *Nature* **553**, 189–193 (2018).

[129] Møller, C. K. Crystal structure and photoconductivity of cæsium plumbohalides. *Nature* **182**, 1436–1436 (1958).

[130] Zhang, Q., Ha, S. T., Liu, X., Sum, T. C. & Xiong, Q. Room-temperature near-infrared high-q perovskite whispering-gallery planar nanolasers. *Nano Letters* **14**, 5995–6001 (2014).

[131] Du, W. *et al.* Strong exciton–photon coupling and lasing behavior in all-inorganic $CsPbBr_3$ micro/nanowire fabry-pérot cavity. *ACS Photonics* **5**, 2051–2059 (2018).

[132] Deng, D. & Guo, Q. Elegant hermite–laguerre–gaussian beams. *Optics Letters* **33**, 1225–1227 (2008).

[133] Pampaloni, F. & Enderlein, J. Gaussian, hermite-gaussian, and laguerre-gaussian beams: A primer. *arXiv:physics/0410021* (2004).

[134] Hedse, A. Applications of orbital angular momentum of light in attosecond science. *FYSK02 20181* (2018). URL `https://lup.lub.lu.se/student-papers/search/publication/8954522`.

[135] Rhodes, D. R. On the stored energy of planar apertures. *IEEE Transactions on Antennas and Propagation* **14**, 676–683 (1966).

[136] Rhodes, D. On a fundamental principle in the theory of planar antennas. *Proceedings of the IEEE* **52**, 1013–1021 (1964).

[137] Carter, W. H. Electromagnetic beam fields. *Journal of Modern Optics* **21**, 871–892 (1974).

[138] Steele, J. M. *The Cauchy-Schwarz master class : an introduction to the art of mathematical inequalities* (Cambridge University Press, 2010).

[139] Strang, G. *Linear algebra and its applications* (Thomson, 2006).

[140] Zhou, C. *et al.* Cooperative excitonic quantum ensemble in perovskite-assembly superlattice microcavities. *Nature Communications* **11**, 329 (2020).

[141] Fu, J. *et al.* Hot carrier cooling mechanisms in halide perovskites. *Nature Communications* **8** (2017).

[142] Michelson, A. A. & Morley, E. W. On the relative motion of the earth and the luminiferous ether. *American Journal of Science* **s3-34**, 333–345 (1887).

[143] Dai, D. C. Brief comment: Dicke superradiance and superfluorescence find application for remote sensing in air. *arXiv:1108.5360 [physics]* (2011).

[144] Atkins, P. W. & Friedman, R. *Molecular quantum mechanics* (Oxford University Press, 2011).

[145] Thomas, L. I.the kinematics of an electron with an axis. *The London, Edinburgh, and Dublin Philosophical Magazine and Journal of Science* **3**, 1–22 (1927).

[146] Bir, G. L., Pikus, G. E., Shelnitz, P. & Louvish, D. *Symmetry and strain-induced effects in semiconductors* (Halsted Press, 1974).

[147] Even, J., Pedesseau, L., Jancu, J.-M. & Katan, C. Importance of spin–orbit coupling in hybrid organic/inorganic perovskites for photovoltaic applications. *The Journal of Physical Chemistry Letters* **4**, 2999–3005 (2013).

[148] Koster, G. F. & Al, E. *Properties of the Thirty Two Point Groups* (Mit Press, 1963).

[149] Kim, M., Im, J., Freeman, A. J., Ihm, J. & Jin, H. Switchable s = 1/2 and j = 1/2 rashba bands in ferroelectric halide perovskites. *Proceedings of the National Academy of Sciences* **111**, 6900–6904 (2014).

[150] Zheng, F., Tan, L. Z., Liu, S. & Rappe, A. M. Rashba spin–orbit coupling enhanced carrier lifetime in $CH_3NH_3PbI_3$. *Nano Letters* **15**, 7794–7800 (2015).

[151] Kepenekian, M. *et al.* Rashba and dresselhaus effects in hybrid organic–inorganic perovskites: From basics to devices. *ACS Nano* **9**, 11557–11567 (2015).

[152] Mosconi, E., Etienne, T. & De Angelis, F. Rashba band splitting in organohalide lead perovskites: Bulk and surface effects. *The Journal of Physical Chemistry Letters* **8**, 2247–2252 (2017).

[153] Bychkov, Y. A. & Rashba, E. I. Oscillatory effects and the magnetic susceptibility of carriers in inversion layers. *Journal of Physics C: Solid State Physics* **17**, 6039–6045 (1984).

[154] Yaffe, O. *et al.* Local polar fluctuations in lead halide perovskite crystals. *Physical Review Letters* **118** (2017).

[155] Fu, M. *et al.* Neutral and charged exciton fine structure in single lead halide perovskite nanocrystals revealed by magneto-optical spectroscopy. *Nano Letters* **17**, 2895–2901 (2017).

[156] Rashba, E. & Gurgenishvili, G. E. Edge absorption theory in semiconductors. *Soviet Physics - Solid State* **4**, 759–760 (1962).

[157] Brennan, M. C. *et al.* Universal size-dependent stokes shifts in lead halide perovskite nanocrystals. *The Journal of Physical Chemistry Letters* **11**, 4937–4944 (2020).

[158] Yakunin, S. *et al.* Low-threshold amplified spontaneous emission and lasing from colloidal nanocrystals of caesium lead halide perovskites. *Nature Communications* **6** (2015).

[159] Wu, K., Park, Y.-S., Lim, J. & Klimov, V. I. Towards zero-threshold optical gain using charged semiconductor quantum dots. *Nature Nanotechnology* **12**, 1140–1147 (2017).

[160] Jana, A. & Kim, K. S. Water-stable, fluorescent organic-inorganic hybrid and fully inorganic perovskites. *ACS Energy Letters* **3**, 2120–2126 (2018).

[161] Eaton, S. W. *et al.* Lasing in robust cesium lead halide perovskite nanowires. *Proceedings of the National Academy of Sciences* **113**, 1993–1998 (2016).

[162] Evans, T. J. S. *et al.* Continuous-wave lasing in cesium lead bromide perovskite nanowires. *Advanced Optical Materials* **6**, 1700982 (2017).

[163] Park, K. *et al.* Light–matter interactions in cesium lead halide perovskite nanowire lasers. *The Journal of Physical Chemistry Letters* **7**, 3703–3710 (2016).

[164] Fu, Y. *et al.* Broad wavelength tunable robust lasing from single-crystal nanowires of cesium lead halide perovskites ($CsPbX_3, X = Cl, Br, I$). *ACS Nano* **10**, 7963–7972 (2016).

[165] Zhang, Q. *et al.* High-quality whispering-gallery-mode lasing from cesium lead halide perovskite nanoplatelets. *Advanced Functional Materials* **26**, 6238–6245 (2016).

[166] Yantara, N. *et al.* Inorganic halide perovskites for efficient light-emitting diodes. *The Journal of Physical Chemistry Letters* **6**, 4360–4364 (2015).

[167] Noginov, M. *Solid-state random lasers.* (Springer, 2010).

[168] Lawandy, N. M., Balachandran, R. M., Gomes, A. S. L. & Sauvain, E. Laser action in strongly scattering media. *Nature* **368**, 436–438 (1994).

[169] Cao, H. *et al.* Ultraviolet lasing in resonators formed by scattering in semiconductor polycrystalline films. *Applied Physics Letters* **73**, 3656–3658 (1998).

[170] Chen, Q. *et al.* All-inorganic perovskite nanocrystal scintillators. *Nature* **561**, 88–93 (2018).

[171] Ming, Y. *et al.* Room-temperature synthesis of $CsPbBr_3$ and $CsPb(Br/Cl)_3$ with narrow FWHM and high fluorescence intensity. *Journal of Materials Science: Materials in Electronics* **32**, 12793–12799 (2020).

[172] Schlaus, A. P. *et al.* How lasing happens in $CsPbBr_3$ perovskite nanowires. *Nature Communications* **10** (2019).